Microfabricated Sampling Probes for Monitoring Brain Chemistry at High Spatial and Temporal Resolution

by

Thitaphat Ngernsutivorakul

A dissertation submitted in partial fulfillment
of the requirements for the degree of
Doctor of Philosophy
(Chemistry)
in The University of Michigan
2018

Doctoral Committee:

Professor Robert T. Kennedy, Chair
Professor Zhan Chen
Emeritus Professor Michael D. Morris
Professor Euisik Yoon

Thitaphat Ngernsutivorakul

nonngern@umich.edu

ORCID iD: 0000-0002-3474-3545

Dedication

To my family and friends

Acknowledgements

First and foremost, I am grateful to my advisor, Dr. Robert Kennedy, for his continuous guidance and encouragement throughout my graduate career. Thank you for all the support as well as the opportunity to explore the fields of miniaturization and microfluidics.

I would also like to thank my dissertation committees, Dr. Zhan Chen, Dr. Michael Morris, and Dr. Euisik Yoon, for contributing their time and providing invaluable feedback. Besides being willing to serve on my committee, Dr. Chen guided me throughout my first research rotation. Dr. Morris generously allowed me to work in his lab on the miniature fiber optic probe project. I gained the bulk of my knowledge of miniaturized bioanalysis systems from Dr. Yoon's BioMEMS class. These experiences and knowledge during the early stage of my PhD study proved to be greatly valuable to my research. I also extend my gratitude to Dr. Nikos Chronis, who formerly served on my dissertation committee.

I extend a special thanks to my previous mentor, Dr. Jill Venton, at the University of Virginia, who introduced me to brain chemistry research. She also encouraged me to continue pursuing a chemistry career. I would not be here today without her previous guidance.

Thank you to all the members of the Kennedy Group, past and present, for the friendship and help. Particularly, I thank Dr. Cynthia Cipolla for my initial training; Dr. Woonghee Lee for training me in microfabrication of sampling probes; Dr. Omar Mabrouk, Dr. Jenny Wong, and Alec Valenta for their help with animal surgeries; Dr. Coleen Dugan

for help with COMSOL modeling; Dan Steyer for help with droplet-based MS assay; Dr. Erik Guetschow for sharing his droplet-based CE expertise; Dr. Tom Slaney for useful discussions on low-flow push-pull perfusion; Dr. Shi Jin, Dr. Shusheng Lu, Dr. Mohamed Dawod, and Clair Ouimet for many helpful discussions related to microchip CE; Thomas White for assistance in the two-step AAO process lately; and Dr. Jim Grinias, Dr. Katy Nesbitt, and Dr. Alex Zestos for their suggestions on several various topics.

Outside of the group, I thank Dr. Francis Esmonde-White for his guidance on the fiber optic probe project. I thank Dr. Sam Pappas for help with histology. I also thank Dr. Onnop Srivannavit, Dr. Ning Gulari, and Dr. Rob Hower for several useful discussions related to microfabrication of Si neural probes. I extend my gratitude to the staffs at the Lurie Nanofabrication Facility; their expertise has been helpful throughout my time in the cleanroom.

I gratefully acknowledge the funding supports from the National Institutes of Health, the Chemistry Departmental Fellowship, and the George Ashworth Analytical Fellowship. I also extend my acknowledgement to the Royal Thai Government Scholarship; I would not have an opportunity to come to study in the U.S. without their previous support. Finally, I would like to thank my family in Thailand, and my friends in Ann Arbor and all over the world. This journey would not have been possible without their support and encouragement.

Table of Contents

List of Figures

List of Tables

List of Appendices

List of Abbreviations

3MT	3-methoxytyrosine
5HIAA	5-hydroxyindole-3-acetic acid
5HT	serotonin
AAO	anodic aluminum oxide
ACh	acetylcholine
Amp	amperometry
AMPH	amphetamine
Asp	aspartate
aCSF	artificial cerebrospinal fluid
BHF	buffered hydrofluoric acid
BSA	bovine serum albumin
BzCl	benzoyl chloride
DA	dopamine
CCD	charged coupled device
CE	capillary electrophoresis
Ch	choline
cps	centipoise
CSF	cerebrospinal fluid
DMSO	dimethyl sulfoxide
DOPA	3,4-dihydroxyphenylalanine
DOPAC	3,4-dihydroxylphenylacetic acid
DRIE	deep-reactive ion etching
ED	electrochemical detection
EOF	electroosmotic flow

ESI	electrospray ionization
fMRS	functional magnetic resonance spectroscopy
FITC	fluorescein isothiocyanate
FSCV	fast-scan cyclic voltammetry
GABA	gamma-amino butyric acid
Gln	glutamine
Glu	glutamate
Gluc	glucose
Hist	histamine
HPLC	high performance liquid chromatography
HVA	homovanillic acid
i.d.	inner diameter
i.p.	intraperitoneal
IPA	isopropyl alcohol
LED	light-emitting diode
LC	liquid chromatography
LIF	laser induced fluorescence
LPCVD	low pressure chemical vapor deposition
LOD	limit of detection
m/z	mass-to-charge ratio
MALDI	matrix-assisted laser desorption/ ionization
MEMS	microelectromechanical systems
MRM	multiple reaction monitoring
MS	mass spectrometry
NDA	naphthalene-2,3-dicarboxyaldehyde
o.d.	outer diameter
PDMS	polydimethylsiloxane
PEG	polyethylene glycol

PET	positron emission tomography
PFA	perfluoroalkoxy alkane
PFD	perfluorodecalin
PFO	perfluorooctanol
Phe	phenylalanine
PMT	photon multiplier tubing
psi	pound per square inch
PVD	physical vapor deposition
RIE	reactive ion etching
RSD	relative standard deviation
S/N	signal-to-noise
Ser	serine
SEM	scanning electron microscopy
SEM	standard error of the mean (depends on the context)
Tau	taurine
Tyr	tyrosine

Abstract

Monitoring neurochemical dynamics has played a crucial role in elucidating brain function and related disorders. An essential approach for monitoring neurochemicals is to couple sampling probes to analytical measurements; however, this approach is inherently limited by poor spatial and temporal resolution. In this work, we have developed miniaturized sampling probes and analytical technology to overcome these limitations.

Conventional sampling probes were handmade and have several disadvantages, including large sizes (over 220 μm in diameter) and limited design flexibility. To address these disadvantages, we have used microfabrication to manufacture sampling probes. By bulk micromachining of Si, microchannels and small sampling regions can be fabricated within a probe, with an overall dimension of ~100 μm. For development of a dialysis probe, nanoporous anodic aluminum oxide was adapted for monolithically embedding a membrane. Coupling the probe to liquid chromatography-mass spectrometry, multiple neurochemicals were measured at basal conditions, including dopamine and acetylcholine. Comparing to conventional dialysis probes, the microfabricated dialysis probe provided at least 6-fold improvement in spatial resolution and potentially had lower tissue disruption.

Furthermore, we have continued the development of a microfabricated push-pull probe. We enhanced functionality of the probe by integrating an additional channel into the probe for chemical delivery. Further, we demonstrated that the probe can feasibly be coupled to droplet microfluidic devices for improved temporal resolution. Nanospray ionization mass spectrometry was used for multiplexed measurements of neurochemicals in nanoliter droplet

samples. Utility of the integrated system was demonstrated by monitoring in vivo dynamics during potassium stimulation of 4 neurochemicals, including glutamate and GABA. The probe provided unprecedented spatial resolution and temporal resolution as high as ~5 s. Additionally, we highlighted versatility of the method by coupling the probe to another high-throughput assay, i.e., droplet-based microchip capillary electrophoresis for rapid separation (less than 3 s) and measurement of multiple amino acid neurochemicals.

This collection of work illustrates that development of the microfabricated sampling probes and their compatible microfluidic systems are highly beneficial for studying brain chemistry. The integrated miniaturized analytical technology can potentially be useful for solving other problems of biological significance.

Chapter 1
Introduction

Submitted, in part, as a review article in *ChemPhysChem*, Special Issue on Neurochemistry and Neuroengineering. Editorial contributions from co-authors: Thomas S. White and Dr. Robert T. Kennedy

Brain chemicals are highly diverse. Over two hundred different compounds have been identified as neurotransmitters, including amino acids, peptides, purines, lipids, monoamines, and other small molecules (e.g., acetylcholine)[1,2]. These chemicals participate in neural activity and are involved in various physiological functions, such as learning, memory, mood, and movement[3–5]. Abnormal levels or dynamics of neurotransmitters also link to mental illnesses and neurological disorders, such as Alzheimer's[6,7] and Parkinson's diseases[8–11]. It is therefore of interest to study dynamics of neurotransmitters and their metabolites in the brain extracellular space. Besides these compounds, other chemicals including metabolic intermediates and drugs are also important for brain functions. Energy metabolites (e.g., glucose) provide fuel for neurons[12], and measuring their concentrations has proven useful for diagnostics in traumatic brain injury[13–15]. Drugs or psychopharmacological substances can have effects on neurotransmission in many different ways, such as enhancing or inhibiting transmitter release[16].

Measuring brain chemistry in vivo has proven indispensable in better understanding chemical neurotransmission, which can be correlated to brain functions, behavior and pharmacology[17–20,16]. Probe techniques, such as electrochemical sensors[21–23] and microdialysis sampling[24–28], have remained predominant for in vivo neurochemical

monitoring. In these techniques, needle-like probes are implanted into live brain tissues for direct chemical measurements. First generation probes were handmade and have several limitations, including variability, low reproducibility, and limited design flexibility. The probe size can be bulky for the sampling probes in particular, leading to poor spatial resolution and substantial tissue damage. To overcome these limitations, several efforts have been devoted to using microfabrication. Microfabrication techniques ultimately allows development of miniature, multiplexed and highly-precise probes for studying brain chemistry. Other advantages also include a wide choice of materials, scalability, and batch fabrication[29]. Furthermore, microfabrication offers unique opportunities for incorporating multiple functions into a single probe, such as electrophysiological recording, drug delivery, and optical stimulation[30–34].

The objective of this chapter is to provide a background and a review on microfabricated probes for monitoring brain chemistry. While this dissertation focuses on microfabricated sampling probes, this chapter will also discuss microfabricated electrochemical sensors as the two techniques offer complementary strengths and weaknesses. Moreover, assays coupled to sampling probes for improving temporal resolution will be highlighted. Finally, an overview of this dissertation will be given.

Current Monitoring Technology

Criteria for evaluating methodology for in vivo neurochemical monitoring include sensitivity, selectivity, spatial resolution, temporal resolution, and multiplexing[23,25,35–38]. Sensitivity and selectivity are crucial to neurochemical measurements as the brain extracellular space is a complex mixture of chemicals with concentrations from picomolar (pM) to millimolar (mM). Spatial resolution is important due to the heterogeneity and small

size of the brain structures. Temporal resolution is essential because neurochemical levels can alter rapidly (i.e., on millisecond time scale during exocytosis[39,40] or second time scale during behavior or stimuli[41–44]). Finally, simultaneous measurement of multiple chemicals is often needed when one would like to study multiplexed transmission or interactions between neurotransmitters, metabolites and drugs[45]. Therefore, it is desirable to develop technology that allows multiplexed neurochemical monitoring with long-term stability and high spatial and temporal resolution. In vivo neurochemical monitoring has been performed by non-invasive imaging techniques, such as positron emission tomography (PET), functional magnetic resonance spectroscopy (fMRS), and genetically-encoded biosensors, or by invasive techniques, such as electrochemical sensors and microdialysis sampling, that involve probe insertion into brain tissue.

Non-invasive Imaging Techniques

Predominant neurochemical imaging techniques include PET and fMRS. In PET, radioactive tracers (i.e., positron-emitting radionuclides) are intravenously injected into the bloodstream for labeling interested molecules in the brain prior to scanning[46–48]. Even though this technique is highly effective, it has limited spatial (2 - 3 mm at state of the art[49,50]) and temporal resolution (several seconds to minutes)[51–53]. fMRS uses a magnetic field to resolve ^{1}H spectra for identification and measurement of brain chemicals[54,55]. This technique has spatial[55] and temporal resolution[56–58] within the scales that are comparable to those of PET. The advantage of fMRS mainly stems from its non-requirement of tracers, but this technique suffers inherently poor sensitivity. Although administration of a contrast agent may improve

sensitivity, it still remains insufficient for detecting many neurotransmitters at basal concentration.

Imaging brain chemicals via genetically-encoded biosensors is an emerging technology based on introduction of fluorescent markers into the tissue of interest[59–61]. This technique allows chemical measurement with superior spatial (µm-scale) and temporal resolution (ms to s). Despite this advantage, this technology is still in its infancy. Thus far only glutamate can be studied in vivo by this approach with a sub-micromolar (µM) limit of detection (LOD). Engineering a marker to efficiently yield a fluorescent signal for a specific molecule is also a long and difficult process. Due to several limitations of the imaging techniques, the probe techniques remain popular for in vivo neurochemical monitoring.

Electrochemical Sensors

Electrochemical detection of neurotransmitters relies on use of microelectrodes. Commonly, a microelectrode is made by aspirating a carbon fiber or a metal wire (~10 µm diameter) into a glass capillary before pulling the glass capillary and manually trimming the electrode site to a length of 50 - 100 µm (Figure **1.1**A & D). Using electrochemical methods[23,62], such as amperometry or fast-scan cyclic voltammetry (FSCV), electroactive molecules (e.g., dopamine and serotonin) can be detected directly via a redox reaction at the exposed electrode site. For detection of non-electroactive molecules (e.g., glutamate and glucose), the surface of electrode is treated with a selective enzyme/ membrane to generate an electroactive product[63,64], such as H_2O_2 via oxidase reaction, or nicotinamide adenine dinucleotide (NADH) via dehydrogenase reaction. Microelectrodes can allow in vivo monitoring with high spatial (10 - 100 µm) and temporal resolution (ms to s). Due to this advantage, electrochemical sensors are popularly used for real-time monitoring of transient

neurochemical changes during behavior and/or stimulation. Selectivity, sensitivity, and LODs of the electrochemical sensors rely on several factors, such as electrode design, materials for electrode and selective-membrane, fabrication procedures, and detection method. Advances in technique and instrumentation, better control of electrode surface chemistry, and development of new materials and methods for electrode modification have improved overall selectivity and sensitivity. This improvement has allowed detection of neurochemicals with lower LODs (e.g., below 500 nM for glutamate[65], and below 20 nM for dopamine[66,67]). Despite this improvement, development of sensors with sufficient sensitivity and selectivity for in vivo monitoring has remained challenging for many neurochemicals. Furthermore, electrochemical sensors are generally incapable of multiplexed neurochemical measurements.

Development of microelectrode arrays has become a topic of interest since it allows study of networks and chemical heterogeneity[68] within singular closely-spaced brain regions. Moreover, the multisite platform can be useful in multiplexed monitoring if each electrode has a different selectivity. Traditionally, multisite in vivo monitoring may be performed by implanting several individual microelectrodes with the aid of a stereotaxic system for manual alignment[69]. An alternative approach is to create electrode arrays either by bundling of microwires or placing carbon fibers into multi-barrel pulled glass capillaries[39,70]. Although these two approaches seem to be effective, they have limitations in term of reproducibility and spatial control. Scalability has remained a challenge. Simultaneous recording at vertically-spaced different spots is also not possible highlighting the inflexibility of design of manually prepared electrodes. Several efforts have resorted to microfabrication to overcome these problems.

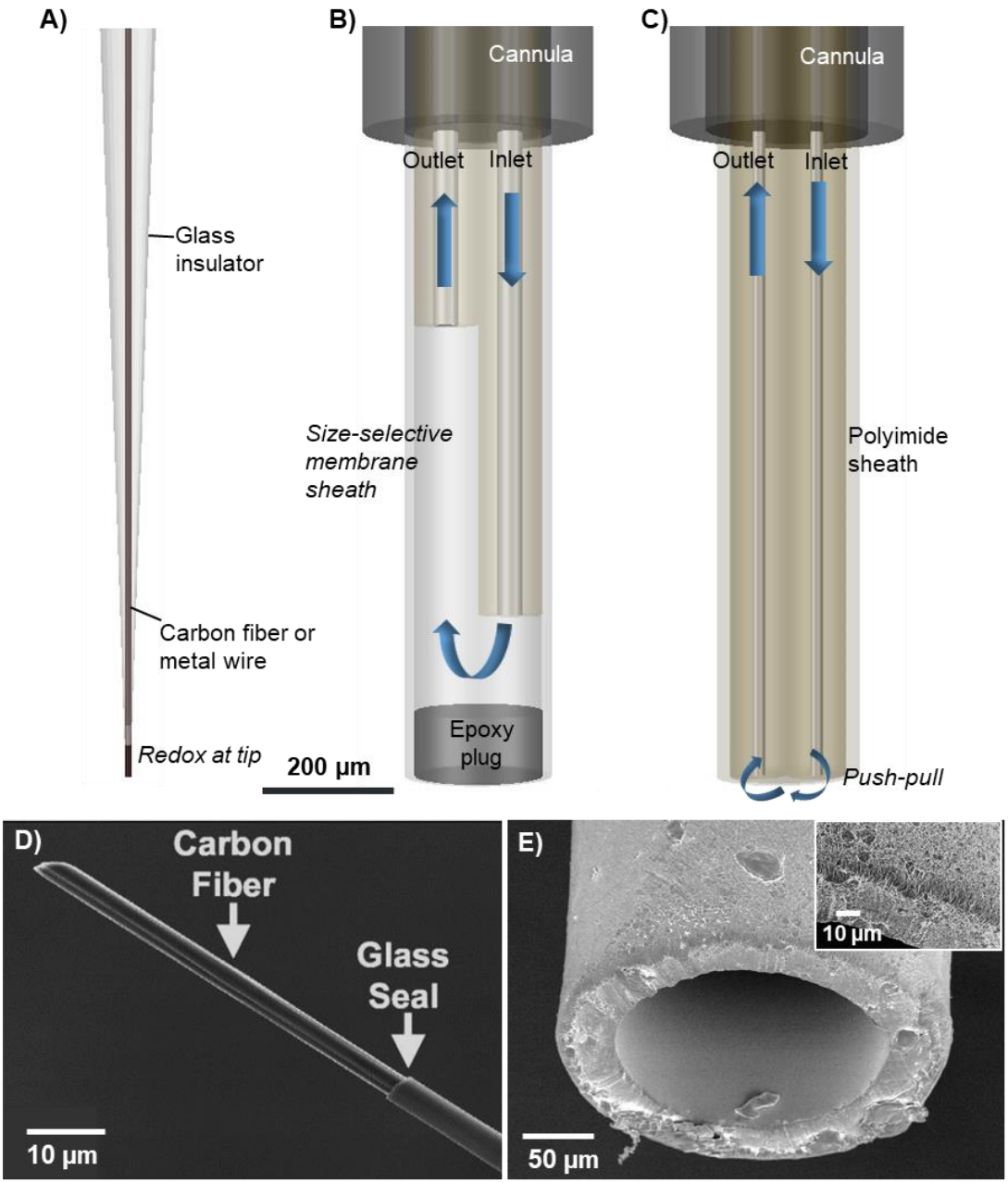

Figure 1.1 (A - C) Schematic of conventional probes for in vivo neurochemical monitoring with comparison of probe sizes. A) Electrochemical microelectrode with 10 µm diameter, 50 µm long. B) Concentric microdialysis probe with 1 mm long polyacrylonitrile (PAN) membrane with 230 µm o.d. C) push-pull probe, made by assembly of 20 µm i.d./90 um o.d. capillaries side-by-side, sheathed with 180 µm i.d./220 µm o.d. polyimide tubing. Models were drawn to scale for comparison of probe size and regions of chemical monitoring (at exposed electrode surface for (A), membrane surface for (B), and space between orifices for (C). (D - E) Exampled SEM images of a cylindrical carbon fiber microelectrode (D), highlighting a tip size of < 10 µm diameter (reproduced with permission from[22]); and a concentric dialysis tubing (E), AN 69 membrane, the inset shows a zoom in highlighting tortuous paths.

Sampling Methods

Microdialysis is a popular sampling method for in vivo studies. In microdialysis, an implantable probe (Figure **1.1**B & E) is constructed by sheathing inlet and outlet capillaries with a hollow-fiber, semi-permeable membrane which is plugged at one end (220 - 500 µm in diameter, 1 - 4 mm long)[25–27]. During sampling, the inlet is infused with a buffer that matches the ionic composition of extracellular fluid at 0.1 - 3 µL/min. Sampling occurs at the membrane where analytes are extracted from the extracellular space according to their concentration gradients. The buffer with extracted analytes, called dialysate, is collected in fractions before chemical analysis with an appropriate analytical technique. Microdialysis sampling is widely used for in vivo chemical monitoring due to its versatility and feasibility for coupling to various analytical techniques[37,71], such as liquid chromatography with mass spectrometry (LC-MS), immunoassay, and capillary electrophoresis with laser-induced fluorescence (CE-LIF). This feature allows measurement of any neurochemicals and drugs with high sensitivity and selectivity, and multi-analyte capability.

An inherent weakness of microdialysis sampling is poor spatial resolution due to a large size of membrane tubing, which correlates to an active sampling region. An alternative sampling method with higher spatial resolution is miniaturized push-pull sampling or "low-flow push-pull perfusion"[72,73]. In this approach, the probe (Figure **1.1**C) is constructed by mounting two 20 µm inner diameter (i.d.)/ 220 µm outer diameter (o.d.) fused-silica capillaries side-by-side, then sheathed with a 180 µm i.d./ 220 µm o.d. polyimide tubing. Sample is pulled from one capillary using low flow rates (typically at 50 nL/min) and a make-up fluid is pushed from another capillary at the same flow rate. The push-pull probes consequently sample only from the probe tip, resulting in substantially better spatial

resolution, as compared to microdialysis probes. However, the overall size of the push-pull probe remains bulky due to the assembly process. This large size precludes experiments in many small brain regions. It can also cause tissue damage that may confound measurement in vivo[74]. These size limitations highlight the need for use of microfabrication to construct sampling probes. Another traditional weakness of the sampling methods is poor temporal resolution (order of mins); however, advancement in analytical methods and microfluidic technology has allowed in vivo neurochemical monitoring with temporal resolution of less than 10 s. This subject will be discussed further in the later section, "Assays for Improved Temporal Resolution".

Microfabricated Electrochemical Sensors

The field of neuro Microelectromechanical Systems, or "neuroMEMS" (see historical reviews and recent technological advancement[32,33,75,76]) has well-established technologies for fabricating neural probes to investigate electrical activity at multiple different sites. Advancement in microfabrication tools and materials allowed development of small, highly reproducible, highly integrated, and high density neural probe arrays (see Figure **1.2**A for an example of 256-site probes; up to 1024 sites have been made[75,77]). The microfabrication process has more recently been adopted to construct probes with sensor arrays for neurochemical recording. Careful considerations of material for substrate and electrodes, and surface architectures are required to achieve desired performance[78].

Electrodes

A key component in electrochemical detection is the electrode site. By microfabrication, electrodes can be deposited as thin films (less than a few hundred nm) by various techniques, such as sputtering and low pressure chemical vapor deposition (LPCVD), prior to insulation. Choices of materials for insulating the electrodes include SiO_2, Si_3N_4, SU-8, and polyimide. For detection of the H_2O_2 product from enzyme sensors, Pt is normally used due to its electrocatalytic property, long-term biocompatibility, and ease of fabrication. For direct detection of electroactive molecules (monoamines in particular), carbon is a more suitable material because it has less charging current, more favorable electrocatalytic properties for these molecules, and relatively wide potential window. Since direct deposition of carbon (i.e., via sputtering or evaporation) typically resulted in low-quality film, it is preferable to use pyrolysis of photoresists in the microfabrication of carbon electrodes[79,80]. The surface area of an electrode is also another important parameter in designing neurochemical probes. Enlarging this surface area increases sensitivity; however, a large surface area can increase probe size and compromises spatial resolution. In the microfabricated probes[79,81–94], electrode surface areas ranged from 500 - 1000 μm^2 for direct electrochemical detection of dopamine, and 5000 - 10000 μm^2 for detection of non-electroactive species by enzyme-coated electrodes. Methods to increase surface roughness without overall size are an approach to increase sensitivity for a given size electrode. The gap between electroactive sites was typically kept at 50 – 200 μm in order to limit cross-talk.

Surface modification of electrodes, with selective membranes, is generally required to improve selectivity and sensitivity. For detection of non-electroactive molecules, enzymes mixed with bovine serum albumin (BSA) are typically immobilized on electrodes by crosslinking with glutaraldehyde. Thickness of the enzyme coating is critical to performance

of the electrode as the substrates and products must move through the membrane layers. Excessive thickness could lead to slow response time[95] of the electrode and higher degree of cross-talk between electrodes[96]. On the other hand, overly thin membranes may lead to insufficient sensitivity and non-uniformity; that could be detrimental to stability and reliability of the electrode. Therefore, the thickness of the membrane should be well-controlled and optimized. For example, the enzyme thicknesses on the microfabricated electrodes were reported to be approximately 5 – 10 μm thick[84,91]. Rise times of the microfabricated electrodes ranged from ~1 – 8 s[79,81–94]. Microfabrication techniques (i.e., lithographic patterning of polymers/ resists) also made it possible to create microwells which encompassed the planar electrodes (for example, see Figure 1.2C, inset). Not only did these microwells act as an effective insulator, but they also allowed precise immobilization and stable formation of the selective membranes[86,94,97].

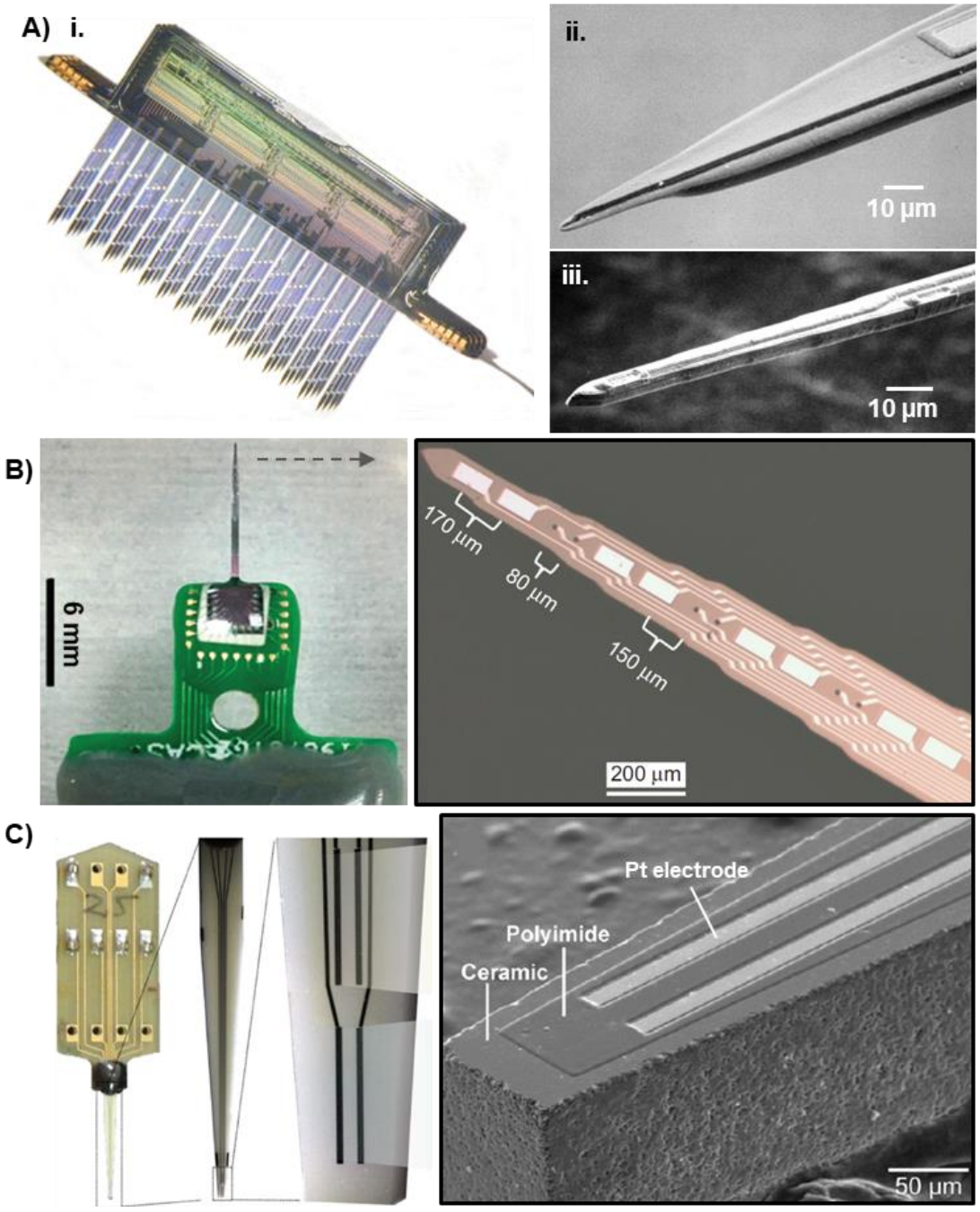

Figure 1.2 Examples of probes with multisite electrochemical sensors. A, i) Multi-channel (256-site 32-channel array) "Michigan Probes" for electrophysiological recording; SEM images of probe tips fabricated by using wet etching with boron-etch stop (A,ii) or dry etching (A, iii). The developed fabrication process for the Michigan probes formed the basis for development of other neural interfaces, including electrochemical probes; B) Silicon probe for neurochemical monitoring (white rectangular sites) integrated with electrophysiological recording sites (small black dots). C) Ceramic probe for neurochemical recording. The shank length is ~10 mm. The recording sites are 15 µm × 333 µm. The inset shows an SEM image of the probe tip. A, © 2008 IEEE, reproduced with permission from[77]; B, reproduced with permission from[87]; C, reproduced with permission from[92,97].

Stiff Probe

Si is the most widely used substrate due to its mechanical and electrical properties, and relatively simple processing. Standard lithography allows patterning of microprobe structures and recording sites with fine features. Wet etching or dry etching, particularly deep-reactive ion etching (DRIE) based on the "Bosch process"[98], are employed in defining probe outline and thickness[99]. Ultimately, silicon micromachining allows fabrication of very thin neural probes (~10-15 µm, see Figure **1.2**A) with precisely-defined tapered tip[77]. Different designs of microfabricated Si probes have been developed by several groups for monitoring several neurochemicals, including dopamine[79,81], glutamate[82–84], lactate and glucose[86] with LODs of sub-µM. In all of these probe designs, at least 4 electrode sites were integrated on a single probe, enabling concurrent recording of a target analytes at high spatially different locations. For example, the microfabricated probes were employed in recording stimulated dopamine in 4 different sites (at 100 – 200 µm vertically spaced) in rat striatum by FSCV[79] or amperometry[81]. These results revealed heterogeneity of the stimulant effect on dopamine release, indicating necessary use of the microfabricated probes. With multi-site probes, simultaneous detection of multiple analytes in different target areas could also be achieved precisely[84,86]. At an additional electrode site, direct integration of a reference electrode can be performed via electrodeposition[83,84]. Further, parallel electrophysiological recording was also made feasible by adding extra electrodes[81,87]. Figure **1.2**B shows an example of a single probe consisting of 8 electrochemical sites (60 µm × 125 µm) and 6 electrophysiological sites (15 µm diameter). This microfabricated probe was used for concurrent recording of glutamate and electrophysiology in rat striatum.

Other types of stiff substrates for microfabricating neurochemical probes have also been explored. The Gerhardt group has extensively developed probes with electrode arrays based on 125 µm thick ceramic wafers (Figure **1.2**C)[100]. Probe shapes with ultra-fine tip were created by using a diamond dicing saw and a laser cutter. Although thinner ceramic wafers (25 – 50 µm) were also commercially available, they were too fragile and difficult to process. The ceramic-based probes were treated with specific enzymes for monitoring glutamate[88,89], lactate[90], choline, acetylcholine[91], and glucose[92]. A self-referencing recording approach was also used to remove interferents[101]. Chronic measurements in freely moving animals were also demonstrated with adequate sensitivity and selectivity, illustrating a potential advantage of biocompatibility with this substrate[102].

Polymer Probe

Interest in developing neural probes using "soft" materials like polymers, has recently grown as matching the Young's modulus of the probe material to the soft brain is thought to minimize tissue damage[103–106]. Choices of soft materials in order of their respective stiffness (from high to low) included polyimide, SU-8, parylene, and polydimethylsiloxane (PDMS). However, soft implants normally require the use of needle guide or stiff coating (such as polyethylene glycol (PEG)[107,108] or biodegradable silk[109,110]) for aiding tissue penetration and trajectory to deep brain tissue. Otherwise, soft implants were designed for primary use at the brain surface, or at depths up to a few millimeters (in the case of polyimide and SU-8). At present, only a few studies have been reported on using polymeric substrates to microfabricate neurochemical probes[93,94]. One example was to microfabricate polyimide-based probes for detecting glutamate and lactate[94]. The polymer probe consisted of Pt

electrodes with integrated reference and counter electrodes. The final probe size was 500 µm wide × 100 µm thick, and 5.5 mm or 16 mm long. Utility of the more durable probe (5.5 mm long) was demonstrated in vivo by monitoring glutamate in rat cortex at 1.7 mm depth.

Microfabricated Sampling Probes

Microfabrication has been employed to embed microfluidic channels into neural probes[30,111,112]. Small channels with different shapes and material types can be constructed by a variety of techniques, such as surface micromachining using sacrificial layer, and bulk micromachining using buried channel technology[113,114] or wafer bonding. Using microfabrication technologies, various microfluidic neural probes have been developed for neurological studies and treatments. Their features as well as manufacturing processes are well summarized in a recent review by Sim et al[34]. Most of the work in microfabricating fluidic probes aimed to improve microinjection or chemical delivery to brain tissues. Nevertheless, the similar technology can be adapted to fabricate sampling probes.

Push-pull/ Direct Sampling

Over the past few years, our group has developed the first, functional sampling probes for in vivo monitoring of brain chemistry[115]. Based on the buried channel technology, microfabrication in Si was used to construct push-pull sampling probes with 20 µm diameter channels. The microfabricated push-pull probes are 85 µm wide × 70 µm thick × 11 mm long, consisting of two 20 µm orifices at the probe tip for push-pull sampling (Figure **1.3**). The overall size of the microfabricated probes was 6-fold smaller than the capillary-based probes, thus potentially reducing tissue damage. Sampling at 50 nL/min from rat striatum, the

microfabricated push-pull probe was coupled to a benzoyl-chloride LC-MS assay[45] for monitoring of multiple neurotransmitters and metabolites (Figure 1.3C). Despite the advantage of small probe size, the requirement of low flow rate compromised on temporal resolution. In our previous report, to collect 1 µL fractions required for the LC-MS assay, temporal resolution was limited to 20 min.

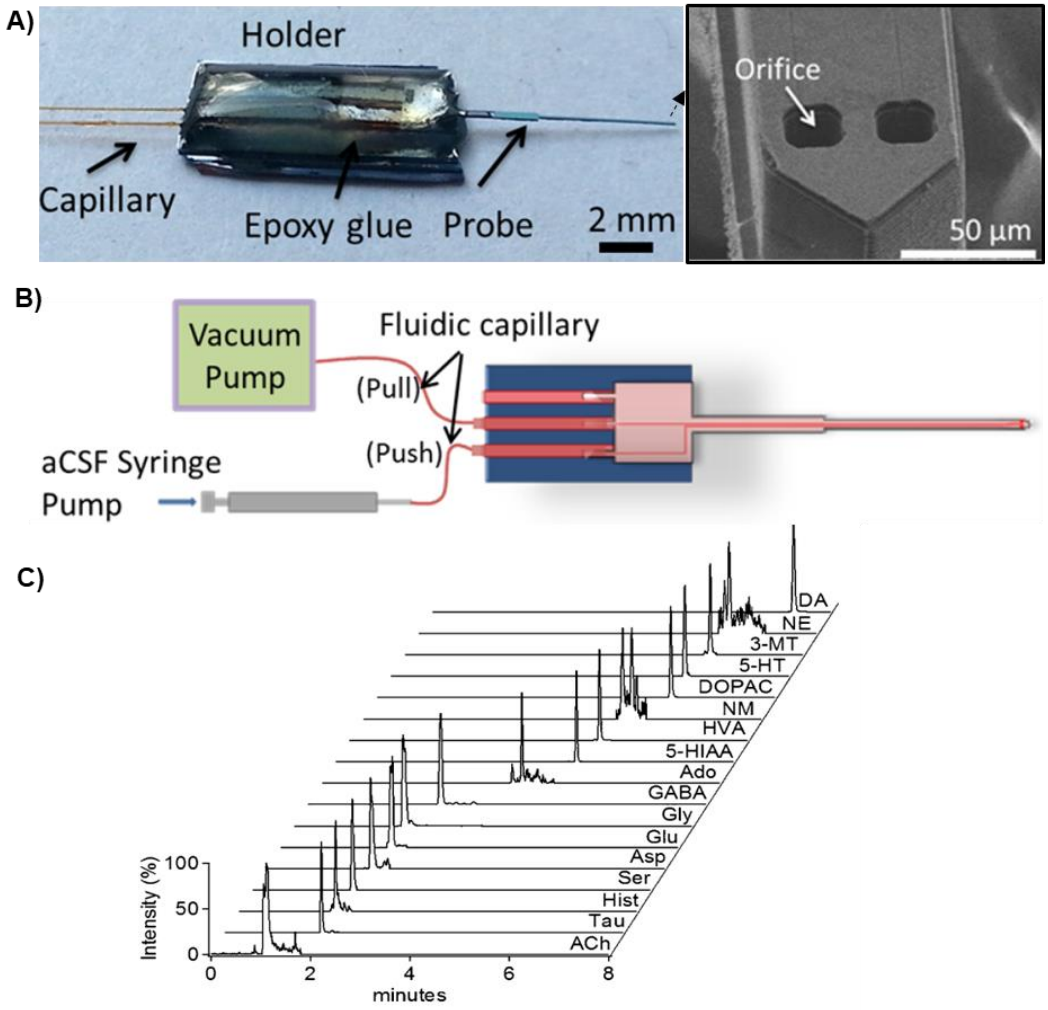

Figure 1.3 Microfabricated push-pull probe for in vivo neurochemical monitoring. A) Packaged sampling device including the probe and connected standard fused-silica capillaries for sample collection. The inset shows a SEM image of the probe tip consisting of two orifices for push-pull sampling. B) Schematic of an experimental setup for low-flow push-pull perfusion. A vacuum pump was used to withdraw the sample while a syringe pump was used to add a make-up aCSF. Perfusion rates were 50 nL/min for push and pull modes. C) Representative chromatogram of in vivo monitoring. The assay allowed multiplexed monitoring of various neurotransmitters and metabolites. Reproduced with permission from[115]. © 2013 American Chemical Society

Other groups have recently also investigated microfabrication of sampling probes. Besides sampling, other features were further implemented in these probes. One such probe was a silicon-based probe designed for sampling with three integrated electrodes for sensing[116]. Another work showed a probe that contained microfluidic channels for sampling as well as electrodes for stimulating and recording in one package[117] This probe was constructed by polyimide and SU-8. The resulting shank size of 240 μm wide × 86 μm thick. Through a single inlet, direct sampling was performed at 300 nL/min without adding a makeup fluid into the sample. In vitro tests revealed the probe capable of segmented-flow sampling, on-chip detection, and functional electrical capabilities. Both designs sought to miniaturize sampling probes with integrated functions through microfabrication techniques. However, it remains to be determined how these probes will function for monitoring neurochemicals in vivo.

Membrane Integration

Although microfabricated push-pull probes allow sampling with high spatial resolution, they are more susceptible to clogging than microdialysis probes due to the absence of membranes. Proteins and debris that enter the sampling channels may also interfere with the downstream analytical assays. Integration of nanoporous membranes into the miniaturized sampling probes can be performed to circumvent these potential issues.

A wide variety of techniques has been used to fabricate nanoporous membranes[118–120], e.g., ion-track etching[121,122], focused ion beam drilling[123], rapid annealing[124], anodization of silicon[125,126], and anodization of aluminum[127–130]. The widely used and appealing method is anodization of aluminum to form porous anodic aluminum oxide (AAO). In this method, the

formation of nanopores is a self-assembling process by anodizing an aluminum film in an acidic solution (e.g. oxalic acid, sulfuric acid, or phosphoric acid). Comparing to the other fabrication techniques, AAO process is relatively simple and inexpensive as it does not required sophisticated equipment. Further, the process can yield membrane with high density and straight pores (Figure **1.4**A). By altering electrolyte, electrolyte concentration, anodizing potential and temperature, the process can also be tuned to fabricate membranes with a wide range of porosity (10^8-10^{12} pores/cm^2 or 5 - 50%)[127,128], thicknesses (100 nm - 200 µm range)[131,132] and pore sizes (5 - 400 nm range)[127,133,134]. Due to these reasons, interests in AAO membranes have been renewed in the recent years[119,127,135–137]. Their applications are diverse, including patterning of functional nanostructures[138,139], filtering or size-based separation[134,140,141], and drug delivery[142].

Most of the previous work on membrane integration are designed for microfluidic devices rather than microprobe structures[124,126,143–152]. Embedding membranes in microfluidic neural probes is challenging because 1) the small support structures may lead to collapse of the membrane during fabrication, and 2) the limited surface area increases the difficulty of membrane attachment. Membranes should also contain sufficient porosity to allow suitable extraction efficiency/ recovery of analytes while having sufficient strength to avoid rupture as fluid infuses into the microchannels. Zahn et al has reported microfabrication of dialysis probes (Figure 1.4B)[143]. Preliminarily, a permeable polysilicon (100 nm thick with 5 – 20 nm pore defects) was fabricated on top of a 10 µm tall × ~150 µm wide channel. Although the membrane was successfully formed over the channel, according to the authors, the thin membrane was too fragile to be effectively used. An alternative approach was to employ a sacrificial oxide spacer layer in creating 30 nm diffusion passage (Figure **1.4**B, ii),

sandwiched between two layers of lithographically-patterned porous membranes (2 μm pores with a total thickness of 2-3 μm). Even though this probe proved its utility for in vitro sampling of a fluorescent dye, its capability for in vivo neurochemical sampling has not been tested. The membrane also had low porosity (i.e., 1.5%) which may limit recovery. The narrow flow passage may potentially lead to stiction issues[153]. Nevertheless, this pioneering work suggested possibility of miniaturization of dialysis sampling probe.

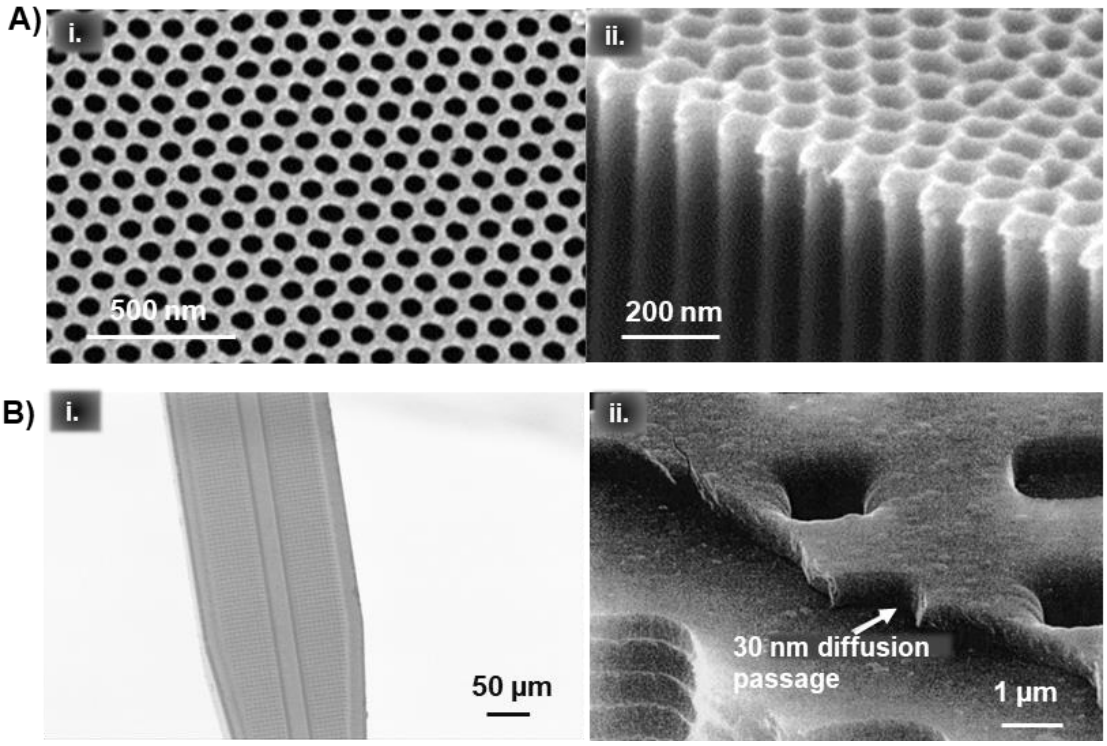

Figure 1.4 A) Example of highly-ordered AAO membrane. SEM images show top view (A, i) and cross-sectional view (A, ii) of a membrane with pore size of ~65 nm. B) SEM images of microfabricated dialysis needle. The array dots in (B, i) were 2 μm lithographically fabricated pores. Zoom-in image (B, ii) highlighted a 30 nm diffusion passage between two layers of microporous Si membrane. A, reproduced with permission from[129]; and B, reproduced with permission from[143].

Assays for Improved Temporal Resolution

In sampling techniques, temporal resolution is limited by mass sensitivity and throughput of analytical methods coupled to the sampling probe[28,71]. Particularly, the use of low flow rates (< 100 nL/min) in the microfabricated sampling probes can compromise temporal resolution as a long period is required to collect enough sample volume for the subsequent assay. Miniaturized analytical methods, such as microbore LC or CE, may be utilized for improved temporal resolution. However, as samples travel from probes to analytical system, the temporal resolution is also limited by broadening of concentration zones due to Taylor dispersion[154]. This reduction in temporal resolution depends inherently on flow rates and capillary dimensions. The band-broadening may be mitigated by using high sampling flow rate (> 1 μL/min) and short, small-bore connecting tubing. As a result, temporal resolution of 3 - 30 s could be achieved[41,155–157]. In spite of this improvement, this approach was limited to only anesthetized subjects. It is also not suitable for the miniaturized probes where low sampling flow rates are required.

Another effective approach for improved temporal resolution is to use segmented-flow or droplet microfluidics[158–160]. In this approach, a sample flow is segmented into a train of discrete aqueous droplets by an immiscible fluorinated oil (see Figure 1.5A, i). By flow segmentation, sample droplets do not mix by diffusion during transport, and the temporal resolution is hence preserved. In vitro studies have shown that chemical sampling with sub-second time resolutions could be attained by using segmented flow[73,117,159]. Furthermore, droplet technology facilitates handling and manipulation of small-volume samples collected at short intervals. Integration with other microfluidic devices was also made feasible for further analytical procedures[161,162].

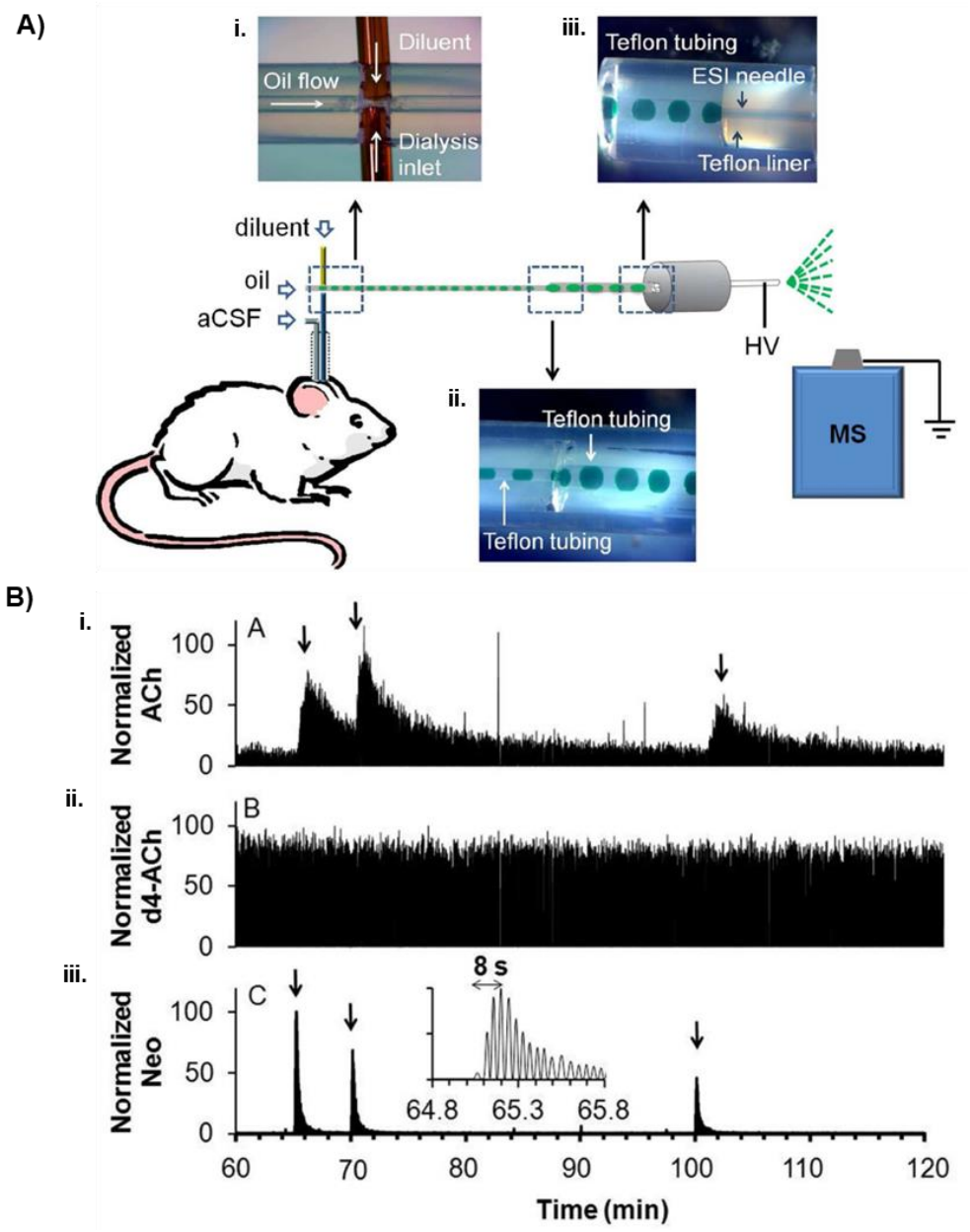

Figure 1.5 A) Illustration of segmented flow sampling coupled to direct infusion MS assay; A, i) Dialysate is perfused into a 4-way fluidic device (at bottom inlet) while fluorinated oil and internal standard solution are pumped into the device at separate inlets (left and top inlets). Resulting droplet train is moved to the right arm; A, ii) Sample droplets (~32 nL) were coalesced into bigger droplets (~160 nL) before pumping to the ESI source for online MS analysis (A, iii). HV denotes high voltage. B) in vivo neurochemical monitoring using the system in A; Figures show simultaneous recording of i) acetylcholine (ACh), ii) internal standard, d4-acetylcholine (d4-ACh), and iii) drug, neostigmine (Neo). Arrows indicated beginning of each drug microinjection. The inset shows a magnified view for detection of Neo during the first microinjection, highlighting fast response time possible. Reproduced with permission from[163]. © 2012 American Chemical Society

Analysis of droplets may be performed by a variety of high throughput analytical methods[164]. Particularly, suitable analytical techniques for neurochemical analysis of droplets included enzyme assay, microchip CE, and direct infusion electrospray ionization (ESI)-MS. Low-flow push-pull perfusion with segmented flow was coupled to an enzyme assay for analysis of glutamate, with 7 s resolution and a LOD of 300 nM[73]. Microchip CE with LIF detection was used for simultaneous measurement of amino acids in droplet dialysates with LODs of 80 - 100 nM[165,166]. By using an offline analysis, droplets could be generated at a high frequency (2 nL droplet at ~0.5 s interval) before pumping them into the chip at a slower rate. Each droplet was therefore analyzed without loss of temporal resolution although the separation time was 50 s. As a result, 9 s temporal resolution was achieved in vivo. Using ESI-MS assay, acetylcholine in dialysate droplets (160 nL at 5 s interval) was monitored with 5 s temporal resolution and a LOD of 5 nM (see Figure 1.5)[163]. In addition, choline and the acetylcholine esterase inhibitor were simultaneously detected. In principle, the MS assay offers the most versatile route to analyze droplet samples. This assay provides many advantages, such as high sensitivity and selectivity, label-free detection, and multi-analyte capability. In contrast to the CE assay, flow desegmentation prior to ESI-MS was also not necessary when using suitable oils and optimized flow rate and voltage[167]. Further, enhancement of MS sensitivity and reduction of matrix effects can be achieved by using nanospray ionization[168–170]. This approach has enabled compatibility of the assay with much smaller sample volume (i.e., analysis of < 5 nL droplets have been made possible), thus facilitating neurochemical sampling at low flow rates while providing high temporal resolution.

Dissertation Overview

The overall goal of this dissertation is to use microfabrication to miniaturize sampling probes for studying neurochemistry at high spatial resolution. Further, microfluidic interfaces are developed to enable integration of the microfabricated probes with droplet-based platforms before coupling to high-throughput assays for diminishing the temporal resolution disadvantage of the method. The resulting integrated systems offer spatial and temporal resolution approaching those of electrochemical sensors while preserving the capability of multiplexed chemical measurements. Even though the focus of this work is on monitoring brain chemistry, the technology developed herein could potentially be useful for a variety of bioanalytical applications.

In Chapter 2, a novel approach to microfabricate dialysis probes is described. Bulk micromachining was used to create a microfluidic Si probe for sampling. Additionally, anodic aluminum oxide processing was adapted to develop a method for direct formation of nanoporous membranes on microchannels. The final probe size was 160 μm wide × 45 μm thick × 11 mm long, containing a buried 30 μm deep × 60 μm wide U-shaped channel. The probe was monolithically embedded with a 4 mm long × 5 μm thick nanoporous membrane with pore sizes of 50 – 70 nm. Compared to standard dialysis probes, the microfabricated probe provided over 6-fold improved spatial resolution and has potentials for low-invasive measurement. The probe yielded 2 - 20% relative recovery at 100 nL/min perfusion rate for a variety of small molecules. Coupling the probe to LC-MS, 14 neurochemicals were reliably monitored in vivo, including acetylcholine and dopamine.

Chapters 3 and 4 focus on continued development of the microfabricated push-pull probes. An additional channel was integrated in the probe for chemical delivery without

increasing overall probe dimension. The sampling area of these probes was comparable to that of a single carbon fiber electrode. Several microfluidic devices were developed to perform further analytical procedures. Interfaces that enabled interconnections between different devices were also created. In Chapter 3, the probe was integrated with the device for simultaneous segmented flow and addition of internal standard solution prior to a direct infusion MS assay. Utility of the system was demonstrated by monitoring dynamics of 4 physiologically important neurochemicals, including glutamate and GABA. The integrated system yielded temporal resolutions of 6 s in vitro and 15 s in vivo at a sampling rate of 100 nL/min. In Chapter 4, a thinner probe was further made; the final probe size was 85 μm wide × 50 μm thick × 11 mm long. This chapter demonstrated versatility of the method by coupling the segmented flow sampling to another throughput assay, i.e. a CE-LIF assay. A novel Teflon-based droplet extraction device was developed to facilitate the assay. The CE chip with a miniaturized separation channel was employed in enabling rapid separation (< 3 s) of multiple amino acid neurochemicals.

Chapter 5 explores refinement in the microfabrication process of the dialysis probes to enhance recovery. This chapter also reports possible sources of currently limited recovery and suggest potential strategies to improve upon the present fabrication process. In Chapter 6, several future directions are proposed to further increase performance and utility of the microfabricated probes. The first project is to make the probes even tinier than the current probes and to internally integrate a segmented flow system with the probes. These approaches will yield the next generation probes with unprecedented spatial and temporal resolution. The second project is to scale up a number of channels and to integrate more functions into the probes. More channels will allow simultaneous drug delivery, flow

segmentation, and multi-site samplings. The sampling probes can potentially be built with other neural interfaces including optogenetics. Such development will result in innovative tools that empower researchers to precisely elucidate and control brain function.

Chapter 2
Microfabrication and in Vivo Performance of a Microdialysis Probe with Embedded Membrane

 Equal authorship was awarded to Lee and Ngernsutivorakul. Specific contributions to this work from Ngernsutivorakul included device fabrication, performing in vitro and in vivo characterizations, and assisting in Comsol modeling.

Introduction

Microdialysis is widely used for in vivo sampling. In this technique, a semi-permeable membrane probe is inserted into tissue or fluid and perfused with an isotonic solution. Chemicals in the tissue diffuse across the membrane according to their concentration gradient and are collected in fractions for analysis[27,171,172]. The popularity of microdialysis stems from its favorable properties. Samples are continuously removed from a well-defined space without net fluid loss from the tissue. The membrane prevents large molecules and debris from being collected that might interfere with downstream assays. Collection of a series of fractions allows changes in tissue chemistry to be monitored over time. The probe can also be used for local delivery of chemicals. Microdialysis is versatile because it can be used to sample from organs, tissues, tumors, and body fluids[20,25,173–175].

Despite the advantages, the size of microdialysis probes creates some limitations. Probes are generally made by coupling capillaries to preformed dialysis tubing resulting in a cylindrical shape with a diameter defined by the dialysis tubing, typically no smaller than 220 μm. The relatively large probe diameter prevents sampling from microenvironments such as small brain nuclei. This problem is especially acute in smaller subjects, like mice,

which are often preferred for research because of the extensive genetic tools and models available. Tissue damage with potentially confounding effects on measured chemicals is another issue that is likely worse with larger diameter probe[176]. Finally, in clinical applications, smaller probes are desirable to minimize discomfort and increase precision[143].

A route to miniaturizing microdialysis probes is by microfabrication. Microfabricated needles without membranes have been applied for drug delivery[177–180] and sampling[181–184]. We have reported a 70 μm wide by 85 μm thick microfabricated "push-pull" probe for in vivo sampling[115]. Sampling occurred by pulling fluid through one channel while pushing an equal volume out the other at 50 nL/min. A limitation of push-pull and needle-type sampling is that proteins and debris can enter the sampling channel potentially interfering with assays or clogging channels. Another issue is that pull-flow connections must be made at the probe. The pull connection complicates sample collection, especially at the low sampling rates used. This plumbing requirement is in contrast to microdialysis where fluids are pumped into the inlet leaving the outlet free for sample collection. Finally, the push and pull flows must be balanced to avoid net fluid loss or gain around the probe. Fluid balancing is challenging at such low flow rates but is not necessary in microdialysis.

A key challenge in microfabricating a microdialysis probe is forming a membrane over an open channel. A variety of semi-permeable membranes have been formed as part of microfluidic systems (see Table **2.1** for summary)[122,126,143,144,146–152]. Most of these membranes were designed for on-chip sample processing and only a few have been designed as implantable probes. In one example, a cellulose membrane was cast over a parylene channel; however, this probe was actually larger than a conventional dialysis probe and was not demonstrated for sampling[144]. Microdialysis probes have also been fabricated in Si with

permeable polysilicon or fabricated pores as the permeable layer[143,146,147]. The polysilicon membrane was too fragile to use with pressure-driven fluid flows in microchannels. Probes with fabricated pores showed excellent promise in vitro although low pore density may limit recovery. These pioneering designs suggest the potential for in vivo microscale sampling; however, microfabricated dialysis probes with high pore density and suitable recovery have yet to be demonstrated for in vivo sampling.

We have developed a procedure to microfabricate a microdialysis probe in Si. The membrane is formed by electrochemical etching of a porous anodic aluminum oxide (AAO) layer to yield a high density of straight pores with controllable size[127,185,186]. The porous AAO is used as a mask for deep reactive ion etching (DRIE) of a polysilicon layer that is underneath the AAO and over a microfluidic channel. Utility of the probes was demonstrated by monitoring neurotransmitters in the brain of live animals.

Table 2.1 Examples of materials and fabrication processes of semi-permeable membranes on a microfluidic devices.

Device type	***Device material***	***Membrane material***	***Membrane fabrication Process***	***Ref #***
Probe	Polyimide	Polyimide	Ion irradiation and chemical etching by sodium hypochlorite[152]	[122]
	Silicon	Silicon	Sacrificial oxide spacer layer[146] or permeable polysilicon	[143]
	Parylene	Cellulose acetate	Spin coating and drying	[144]
Biocapsule	Silicon	Silicon	Sacrificial oxide spacer layer	[146]
Microchip	Glass	Zwitterionic polymer	laser-patterning techniques[149]	[150]
	PDMS	Polycarbonate	Oxygen plasma	[151]
	PDMS	Silicon-silicon nitride	Thermal annealing	[148]
	Silicon	Silicon	Electrochemical etching	[126]

Experimental

Chemicals and materials

Unless specified otherwise, all chemicals were purchased from Sigma Aldrich (St. Louis, MO) or Fisher Scientific (Fairlawn, NJ) and were certified ACS grade or better. Solutions were prepared with HPLC-grade water or water purified by a Milli-Q system (Millipore, MA). Fused silica capillaries were purchased from Molex (Phoenix, AZ). Epoxy glues were purchased from ITW Devcon (Danvers, MA) and Loctite (Westlake, OH). Crystalbond Adhesive was purchased from Structure Probe (West Chester, PA). Artificial cerebrospinal fluid (aCSF) consisted of 145 mM NaCl, 2.68 mM KCl, 1.10 mM $MgSO_4$, 1.22 mM $CaCl_2$, 0.50 mM NaH_2PO_4, and 1.55 mM Na_2HPO_4, adjusted pH to 7.4 with 0.1 M NaOH. Unions for 360 μm outer diameter (o.d.) capillaries were purchased from Idex Health and Science (P-772, Oak Harbor, WA).

Microfabrication of microdialysis probe with embedded nanoporous membrane

Overview. The scheme for microdialysis probes was designed in L-EDIT software (Tanner EDA). All processing was performed at the Lurie Nanofabrication Facility (LNF) at the University of Michigan. The overall probe layout is shown in Figure **2.1**. Probes were 11 mm long × 45 μm thick with a shank that narrowed to 160 μm wide at the tip. A microchannel with semicircular cross-section (60 x 30 μm) ran the length of the probe to form an inlet and outlet was fabricated in the surface (Figure **2.1**A). A 4 mm length of the probe at the tip was made porous by DRIE though an electrochemically etched AAO membrane (Figure **2.1**B) that was overlaid the thin Si layer shown in Figure **2.1**A.

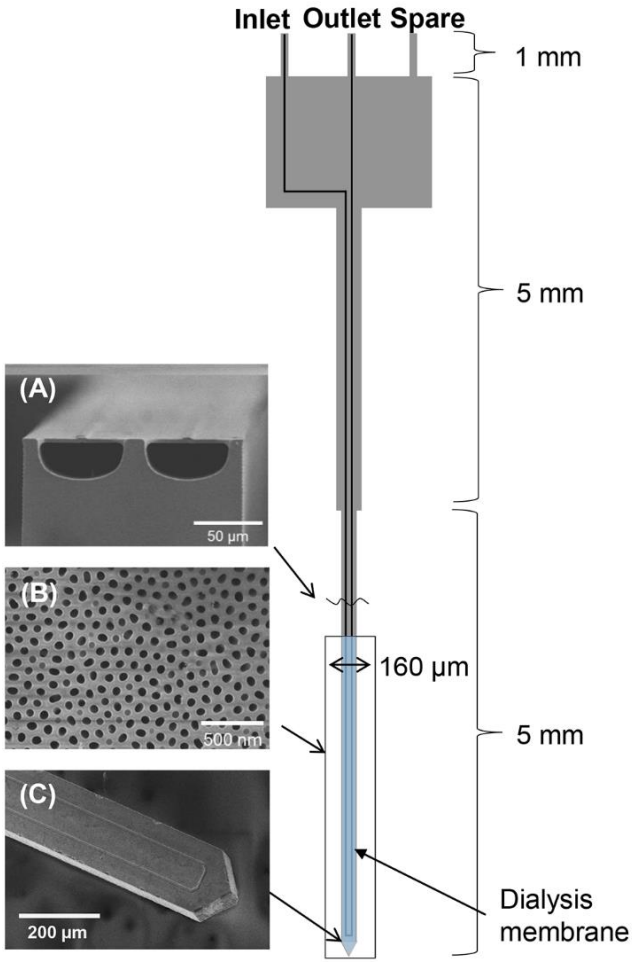

Figure 2.1 Layout of microfabricated microdialysis probe. A probe has 3 ports including inlet, outlet, and spare for other potential uses (it was not used at this probe). (A) SEM image of cross-section of channels showing semicircular shape and thin polysilicon top layer. (B) SEM image of AAO membrane over sampling area. (C) SEM image of sampling probe tip showing the channel pattern.

Channel formation. Probes were fabricated on 4 inch p-type wafers (Silicon Valley Microelectronics, Santa Clara, CA) using the process outlined in Figure **2.2**. A 2 µm SiO_2 layer was grown on a wafer by wet oxidation using a Tempress TS 6604 S3 tool. The initial line for channel etching was patterned by lithography in 3 µm of SPR220 photoresist (Dow, Marlborough, MA), see Figure **2.2**A. The exposed SiO_2 was removed with DRIE using the Bosch process (which uses C_4F_8 as a passivation material) with a STS Deep Silicon Etcher (Figure **2.2**A) and semicircular shaped channels (Figure **2.2**B) were formed using a SPTS

Xactix XeF_2 etcher (Allentown, PA). Channels were sealed by chemical vapor deposition (Tempress TS 6604 S3/T3) of 3 µm of polysilicon. The polysilicon layer on the wafer surface was etched by DRIE until the buried SiO_2 layer was exposed and then removed by treatment with buffered HF (Transene Co Inc, Danvers, MA) for 20 min. An additional 2 µm polysilicon layer was deposited followed by the deposition of a 1 µm SiO_2 layer for recovery of potential damage during the polysilicon removal process (Figure **2.2**C). The probe shape was patterned by a second lithography step and exposed SiO_2 was removed by DRIE. After photoresist removal in PRS 2000 (Avantor Performance Materials, Phillipsburgh, NJ), a sampling area at the probe tip was patterned by a third lithography step. The outline of the probe was etched by DRIE to 150 µm depth and the SiO_2 layer on the channel was removed by buffered HF (Figure **2.2**D). Finally, polysilicon thickness on the sampling area was reduced to 2 µm by DRIE (Figure **2.2**E).

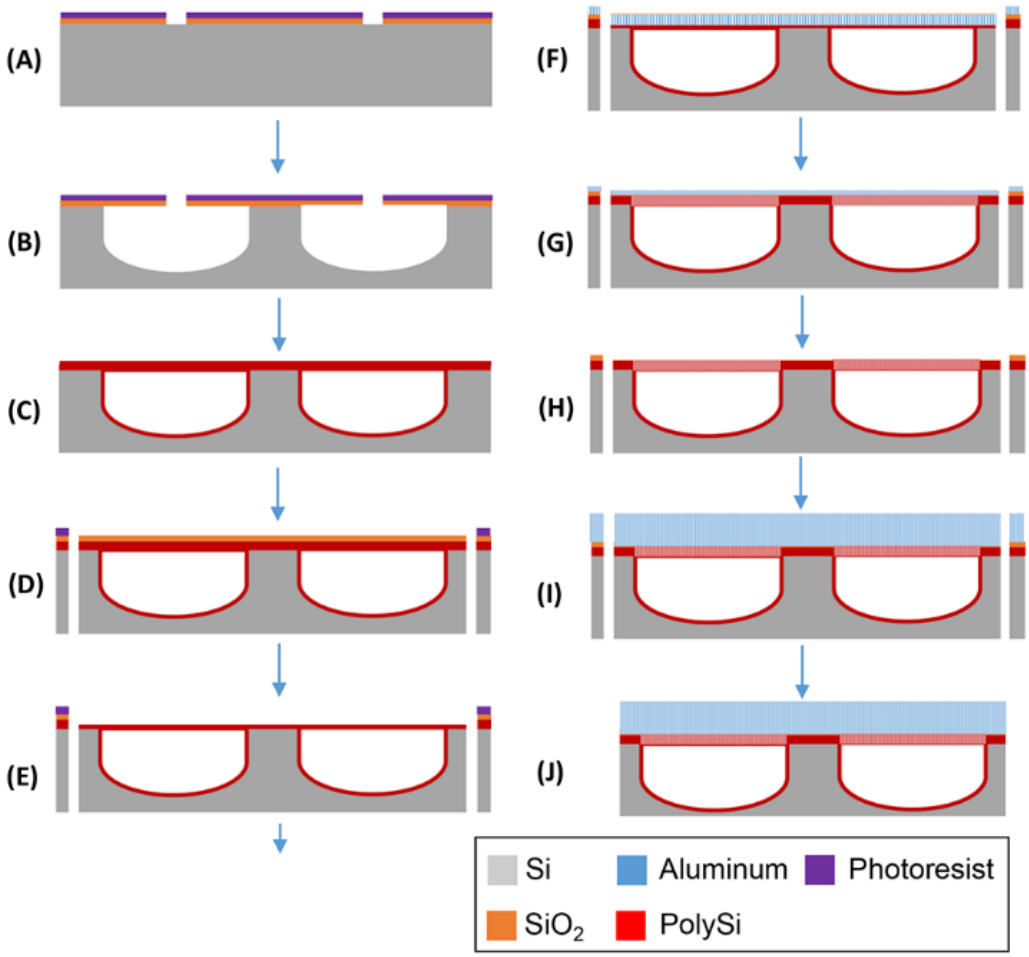

Figure 2.2 Illustration of microfabrication process for microdialysis probe. The channel line was patterned on 2 µm thick SiO_2 grown Si wafer (A). Semicircular shaped channels with 60 µm wide and 30 µm high were etched by XeF_2 (B) and sealed with polysilicon (C). After 1 µm thick SiO_2 was deposited, probe shape was patterned and etched by DRIE (D). Sampling area at the tip of the probe was opened and etched by DRIE to be 2 µm thick layer (E). 400 nm Al layer was deposited and anodized electrochemically forming nanoporous AAO membrane (F). Polysilicon layer was etched through AAO membrane by DRIE (G) and 400 nm AAO membrane was removed (H). For physical strength of sampling area, 3 µm AAO membrane was fabricated by the deposition and electrochemical anodization of Al layer (I). Finally, thinned probes were released in hot water after backside etching (J).

Membrane formation and probe release from wafer. A 400 nm Al layer was deposited over the wafer using an e-beam evaporator (Denton Vacuum, Moorestown, NJ), Figure **2.2**F. The Al coating was anodized at 60 V and 15 °C in 0.3 M oxalic acid solution for 15 min using Pt mesh (Alfa Aesar, Ward Hill, MA) as a counter electrode (see Figure **2.3**). The wafer was rinsed with DI water and then treated with 5% H_3PO_4 at room temperature for

50 min to widen the pores (Figure **2.2**F). The polysilicon layer overlying the microchannel was etched by DRIE at -15°C using the AAO layer as a mask (Figure **2.2**G). The AAO membrane was removed by treating with 5% H_3PO_4 at 65 °C for 1 h (Figure **2.2**H). A fresh 3 µm Al layer was deposited using the Enerjet evaporator. (For this step, the wafer was tilted to a 45° angle in order to prevent blocking of previous etched holes on polysilicon layer by Al metal vapor.) The Al layer was anodized at 60 V and 15 °C in 0.3 M oxalic acid solution for 45 min and pores widened by treating with 5% phosphoric acid at room temperature for 90 min (Figure **2.2**I). The results of each process were imaged by scanning electron microscopy (Hitachi SU8000 SEM). The wafer with embedded AAO membrane was bonded to a carrier wafer with Crystalbond 555 (Structure Probe, Inc., West Chester, PA) and backside etched by DRIE until the probe thickness reached 40 µm (Figure **2.2**J). Individual probes were released in hot water.

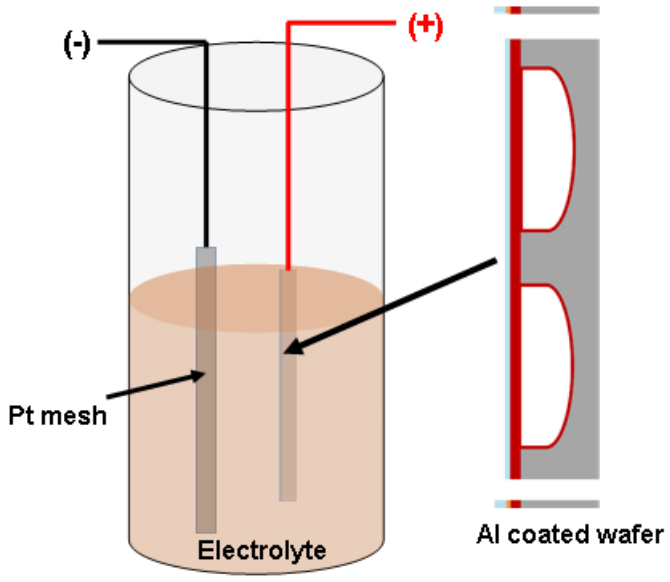

Figure 2.3 Overall setup of AAO process. After deposition of 400 nm Al layer over the wafer, the Al coating was anodized at 60 V in 0.3 M oxalic acid for 15 min at 15 °C. Platinum mesh was used as a counter electrode, which was aligned parallel to the Al coated wafer. The device wafer was facing toward and 1inch apart from the platinum mesh.

Probe holder fabrication and assembly. Resulting probes were too small and fragile to be conveniently handled and plumbed to connection tubing; therefore, a holder was microfabricated similar to that described previously for push-pull probes[115]. Full description of holder fabrication and assembly is given in Figure **2.4**. 12 cm lengths of 100 µm i.d./ 360 µm o.d. capillary were connected to the inlet and outlet. The outlet capillary was then joined to a 22 cm long, 50 µm i.d./ 360 µm o.d. fused-silica capillary for fraction collection. Flow through probes was driven using a Chemyx syringe pump (Stafford, TX).

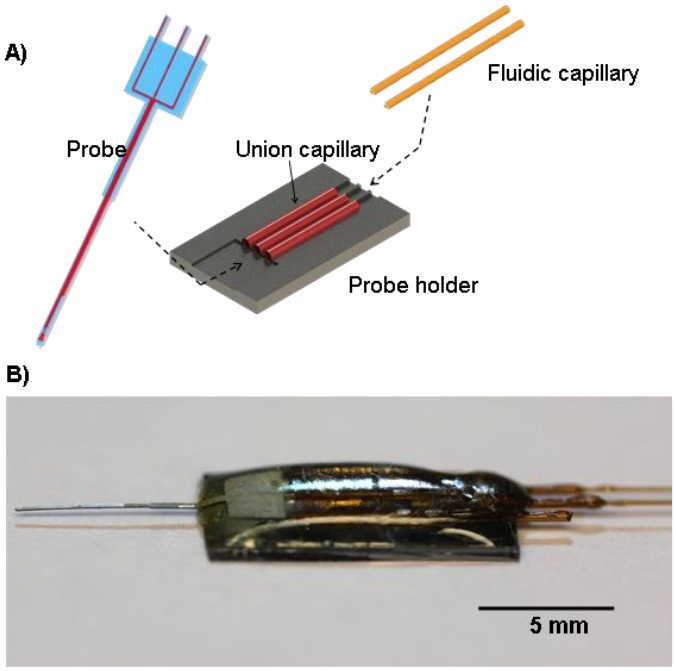

Figure 2.4 Fabrication of Probe Holder. The probe holder has guides to connect probe ports and capillaries. Probe holders were fabricated from a silicon wafer with growth of a 1 µm silicon dioxide layer. The 2 mm wide rectangle for a guide of probe connection ports was patterned by lithography and SiO_2 layer was removed by BHF. A second lithography step was performed to pattern 360 µm wide trenches for a guide of capillaries and DRIE etched 50 µm deep. Photoresist on the wafer was removed by positive resist stripper (PRS 2000; Avantor Performance Materials, PA) and 40 µm deep trenches and rectangles were additionally etched by DRIE. To connect fluidic capillaries to microchannels in a probe, a union capillary of 1 cm length with 180 µm i.d. and 360 µm o.d. was glued on the guiding trenches of a probe holder with epoxy gel resin. (A) Probe ports were inserted into union capillaries and 12 cm length of 100 µm i.d. and 150 µm o.d. fluidic capillaries were joined to inlet and outlet probe ports through the union capillary. Finally, all assembled devices were sealed with epoxy gel resin. The probe glued to the holder as shown in (B).

In vitro characterization

To determine the dynamic response during sampling, probes were perfused with water at a flow rate of 100 nL/min and placed into a stirred vial of water (see Figure **2.6**A). The flow rate and flow stability within a system was periodically validated using a microfluidic flow meter (SLG1430-025, Sensirion, Zurich, Switzerland). The solution was subsequently changed to a 50 µM fluorescein solution while recording fluorescence within the exit tubing using a fluorescence microscope.

For study of probe relative recovery, the microfabricated probe ("µFab") was compared to a concentric microdialysis probe ("MD") which was prepared as previously described[187]. The concentric probe had a regenerated cellulose membrane with 18 kDa molecular weight cut-off that was 4 mm long and 220 µm diameter (Spectrum Labs, Rancho Dominguez, CA). Probes were dipped into a well-stirred vial containing: 0.5 µM acetylcholine (ACh), dopamine (DA), 3-methoxytyramine (3-MT), and serotonin (5-HT); 1 µM 3,4-dihydroxyphenylalanine (DOPA) and histamine (Hist); 10 µM 3,4-dihydroxyphenylacetic acid (DOPAC), ɣ-aminobutyric acid (GABA), 5-hydroxyindoleacetic acid (5-HIAA), homovanillic acid (HVA), phenylalanine (Phe), and tyrosine (Tyr); 50 µM choline (Cho), serine (Ser), and taurine (Tau); and 1 mM glucose (Gluc) in aCSF at 37˚C. The aCSF was supplemented with 0.25 mM ascorbate to protect against oxidation of analytes. After an equilibration time of 30 min, dialysates were collected in 20 min fractions with a perfusion rate of 100 nL/min.

Dialysate samples were derivatized with benzoyl chloride and analyzed by LC-MS, as described previously[45]. Briefly, 1.5 µL of standards or fractions were mixed with 3 µL of 100 mM sodium carbonate buffer at pH 11 and 3 µL benzoyl chloride (2% in acetonitrile, v/v).

The samples were mixed with 3 µL of [^{13}C]-labeled or [d4]-labeled benzoylated internal standards, consisting of 5 nM [^{13}C]-DA, [^{13}C]-3-MT, [^{13}C]-5-HT, and [^{13}C]-DOPA; 10 nM [d4]-ACh and [d4]-Cho; 50 nM [^{13}C]-GABA and [^{13}C]-Hist; 125 nM [^{13}C]-DOPAC, [^{13}C]-5-HIAA, and [^{13}C]-Tyr; 0.5 µM [^{13}C]-Tau, Glu and Gln; 1.25 µM [^{13}C]-Phe and [^{13}C]-Ser; and 12.5 µM [^{13}C]-Gluc in 50% acetonitrile v/v containing 1% H_2SO_4. Samples were analyzed using an Accela UHPLC interfaced to a TSQ Quantum Ultra triple quadrupole mass spectrometer (Thermo Fisher Waltham, MA) operated in multiple reaction monitoring mode. 3 µL samples were injected onto a 2.1 mm x 100 mm Phenomenex biphenyl Kinetex HPLC column (Torrance, CA). Mobile phase A was 10 mM ammonium formate with 0.15% formic acid, and mobile phase B was acetonitrile. The mobile phase gradient was: initial, 0% B; 0.01 min, 19% B; 1 min, 26% B; 1.5 min, 75% B; 2.5 min, 100% B; 3 min, 100% B; 3.1 min, 5% B; and 3.5 min, 5% B at 0.45 mL/min.

In vivo sampling

All procedures were conducted according to a protocol approved by the University Committee for the Use and Care of Animals (UCUCA). Male Sprague-Dawley rats weighing between 250-300 g, (Harlan, Indianapolis, IN, USA) were used for all experiments. Rats were housed in a temperature and humidity controlled room with 12 h light/dark cycles with access to food and water *ad libitum*. Measures were taken to prevent animal pain and discomfort throughout the experiment. All animal experiments were within the guidelines of Animal Research Reporting *in vivo* Experiments (ARRIVE). Animals were anesthetized using 2-4% isoflurane and placed in a stereotaxic frame (David Kopf, Tujunga, CA). Two burr holes were drilled above the striatum +1.0 mm anterior-posterior and ± 3.0 mm lateral

from bregma. The MD probe and µFab probe were lowered into opposite hemispheres – 6.15 mm from the top of the skull. Rats were maintained under anesthesia for the duration of the experiment using isoflurane. Both probes were perfused with aCSF at 100 nL/min. After 1 h equilibration, two 20 min fractions were collected for basal concentrations (2 µL per fraction) and two more were collected after an amphetamine injection (5 mg/ kg, i.p). Following the experiment, the probes were withdrawn from the brain using the stereotaxic frame and the rat was euthanized. Brains were extracted to confirm probe placement.

Results and Discussion

Probes

A challenge in fabricating microdialysis probes is embedding nanoporous membranes over channels while balancing the need for sufficient physical strength and good recovery across the membrane. The process described in Figure **2.2** allowed formation of a nanoporous membrane covering a total of 8 mm length of channel (but only 4 mm length of probe because the channel has a 180^{o} turn at the tip). The resulting 5 µm thick membrane has straight pores that are 60 - 80 nm wide at a density of 8.4 ± 0.2 x $10^{13}/m^2$ (n = 3), as shown in Figure **2.5**. 50 - 70 probes (representing a 50% success rate) could be recovered from a single wafer. AAO membranes have been previously used as a photomask on a solid surface[188]; however, our approach is unique in using AAO as a DRIE mask directly over a microchannel.

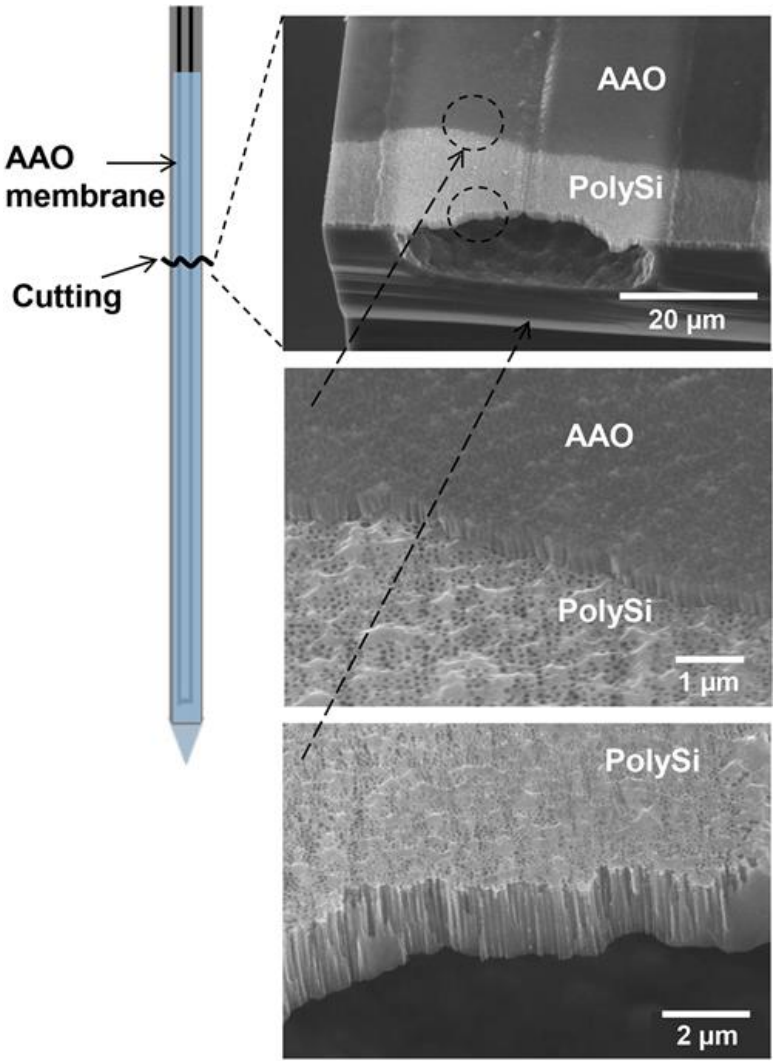

Figure 2.5 Scanning electron micrographs of fabricated microchannels with pores. Drawing at left indicates where the probe sampling tip was broken to expose channels. Images show AAO and polysilicon membranes overlaid. Lowest image shows that pores go through the polysilicon base layer over the open channel.

In preliminary experiments fabrication stopped at step G in Figure **2.2**; however, we found that the resulting membranes were fragile and ruptured when attempting to flow through the probe. The additional 3 µm AAO membrane (Figure **2.2** I - J) gave the probes sufficient mechanical strength. A drawback of this approach is that the final AAO pores do not necessarily line up with the polysilicon pores; however, the pore density was sufficient to give enough overlap and allow molecular exchange as described below.

In vitro characterization

The response of the μFab probe to a change in concentration was determined by switching the sampled solution from 0 μM to 50 μM fluorescein while monitoring fluorescence at the probe outlet (see Figure **2.6**). Fluorescence signals began to increase 14.5 min after switching. This delay is expected because the perfusion rate was 100 nL/min and the internal volume from sampling tip to detection point was ~ 1400 nL. The good agreement shows that leakage through the system was insignificant and allows accurate correlation of concentration changes in collected fractions and time of event in the sample. Once the fluorescence signal increased, it had a 10 - 90% rise time of 47 ± 2 s (n = 7). This rise time, which determines the best possible temporal resolution, is close to the estimated rise time of 44 s using the combined diffusion and Taylor dispersion equation[73]. The predicted rise time is 1 s for probe channel and 43 s for combined outlet and collection capillaries. Because most of the dispersion is in the connecting channel, it may be possible to improve temporal resolution by using segmented flow or smaller connection capillaries[73,163,166]. We also tested relative recovery as a function of flow rate and found the expected relationship of decreasing recovery with increasing flow rate, similar to larger dialysis probes (see Figure **2.6**C). For further experiments we used 100 nL/min as a practical choice. Operating at much higher flow rates results in greater chance of rupturing the membrane or causing leaks in the system. Operating at lower flow rates might increase recovery but yields smaller samples to manipulate.

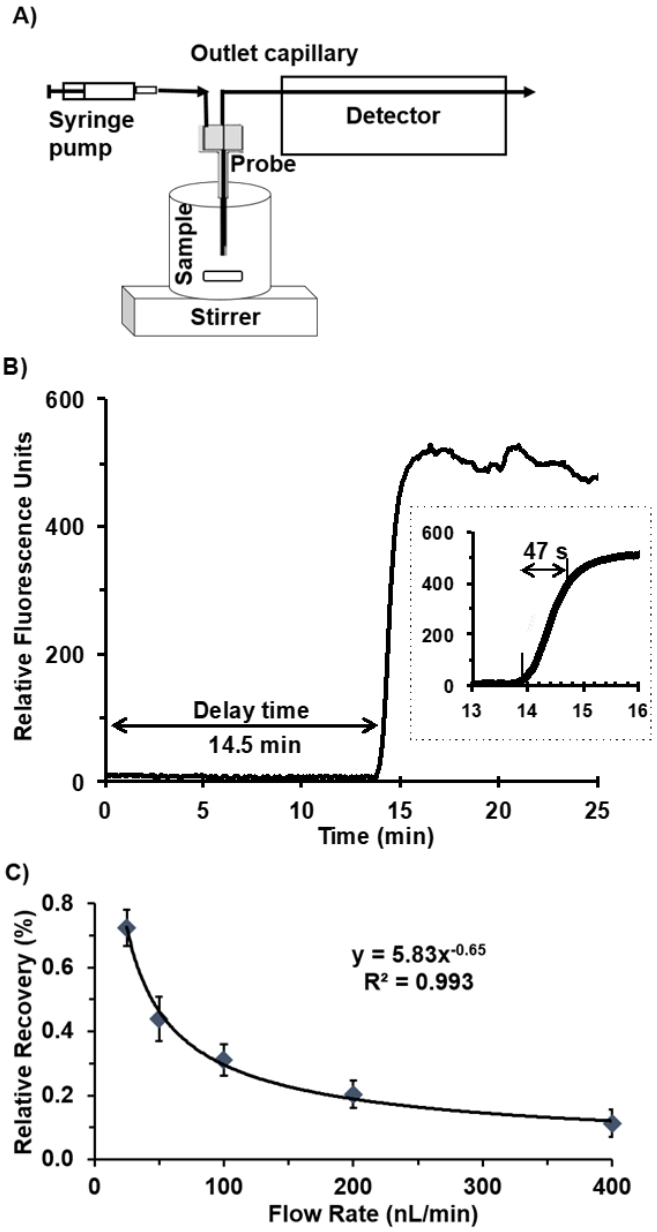

Figure 2.6 Determination of the dynamic response time of the microfabricated probe to step change in sampled concentration, and the relationship between perfusion flow rate and relative recovery. (A) Illustration of experimental setup. Probe was inserted into a solution of water and then switched to a solution of 50 µM fluorescein as the sample. Fluorescence was monitored downstream on the outlet capillary. (B) Trace shows representative example for detection fluorescent change with time beginning at switch. Delay time is 14.5 min, which corresponds to the internal volume of ~1400 nL at the perfusion rate of 100 nL/min. Inset shows the 10% to 90% response time. Average was 47 ± 2 s (n = 7). (C) Scatter plot shows an inverse relationship between flow rate and relative recovery from the microfabricated probe sampling.

In vitro relative recovery of neurochemicals was evaluated by comparing dialysate samples with samples taken directly from the stirred vial (Table **2.2**, Figure **2.7**A). For the µFab probe, the recovery was from 2 to 21% for selected neurochemicals. The variation in recovery may be caused by differences in molecular structure, charge effects, hydrophobicity, and membrane interactions. These results can be contrasted with the nearly 100% relative recovery obtained using the traditional probe at 100 nL/min. Compared to the MD probe, the µFab probe provides lower relative recovery values, at least in part, because of its 6-fold smaller surface area of sampling. Table **2.2** also shows that different µFab probes had greater variability in recovery from probe to probe than conventional probes. The reason for higher variation is not clear. Some variation in conventional probes may be masked by operating near 100% recovery. For µFab probes, variability could be due to variations in the fabrication process or variability induced by handling and analyzing the smaller samples. Continued refinement of the process will likely reduce this effect.

To gain more insight into the recovery, computational simulation of fluid flowing through the µFab probe was performed (see Figure **2.8**). Initial modeling indicated that flow rate and membrane porosity are the main variables that significantly affect recovery. Using the diffusion coefficient for dopamine[189], estimated porosity of 33% and flow rate of 100 nL/min (Figure **2.8**A), the simulated recovery was 98%, much larger than our observed value of 5 - 7% for dopamine. When porosity was lowered to 1%, the simulated and actual recovery matched (Figure **2.8**B). These results suggest that porosity is lower than expected. This discrepancy may be due to several factors. The final overlaid AAO pores do not line up with the polysilicon pores resulting in lower porosity than measured by observing the top of the membrane surface. The polysilicon membrane may also trap air in the pores giving

reduced porosity. Some pores may also be clogged with particulates or wax (used for wafer-mounting during back-side etching). Changes in probe processing or modifying surfaces may prove useful to improve recovery[190,191].

Table 2.2 In vitro recovery of selected neurochemicals at flow rate of 100 nL/min. The results from the microfabricated probes (μFab) are compared with the conventional dialysis probes (MD). Recovery values are given as mean ± 1 standard deviation for different probes (n = 4 probes).

Analyte (tested concentration)	μFab % Recovery	MD % Recovery
Acetylcholine (500 nM)	7 ± 1.2	105 ± 6
Choline (50 μM)	6 ± 1.1	99 ± 12
3,4-Dihydroxyphenylacetic acid (10 μM)	2 ± 0.6	92 ± 5
3,4-Dihydroxyphenylalanine (1 μM)	3 ± 0.5	94 ± 9
Dopamine (500 nM)	5 ± 0.9	100 ± 3
ɣ-Aminobutyric acid (10 μM)	3 ± 1.2	109 ± 3
Glucose (1 mM)	3 ± 0.6	95 ± 10
Glutamate (10 μM)	21 ± 7.7	106 ± 10
Glutamine (500 μM)	2 ± 0.5	105 ± 6
Histamine (1 μM)	5 ± 1.0	109 ± 8
5-Hydroxyindoleacetic acid (10 μM)	4 ± 0.5	99 ± 3
Homovanillic acid (10 μM)	3 ± 1.1	105 ± 4
3-Methoxytyramine (500 nM)	4 ± 0.8	95 ± 2
Phenylalanine (10 μM)	4 ± 2.1	115 ± 6
Serine (50 μM)	3 ± 0.9	111 ± 20
Serotonin (500 nM)	4 ± 0.6	103 ± 4
Taurine (50 μM)	4 ± 0.6	110 ± 4
Tyrosine (10 μM)	4 ± 1.3	105 ± 7

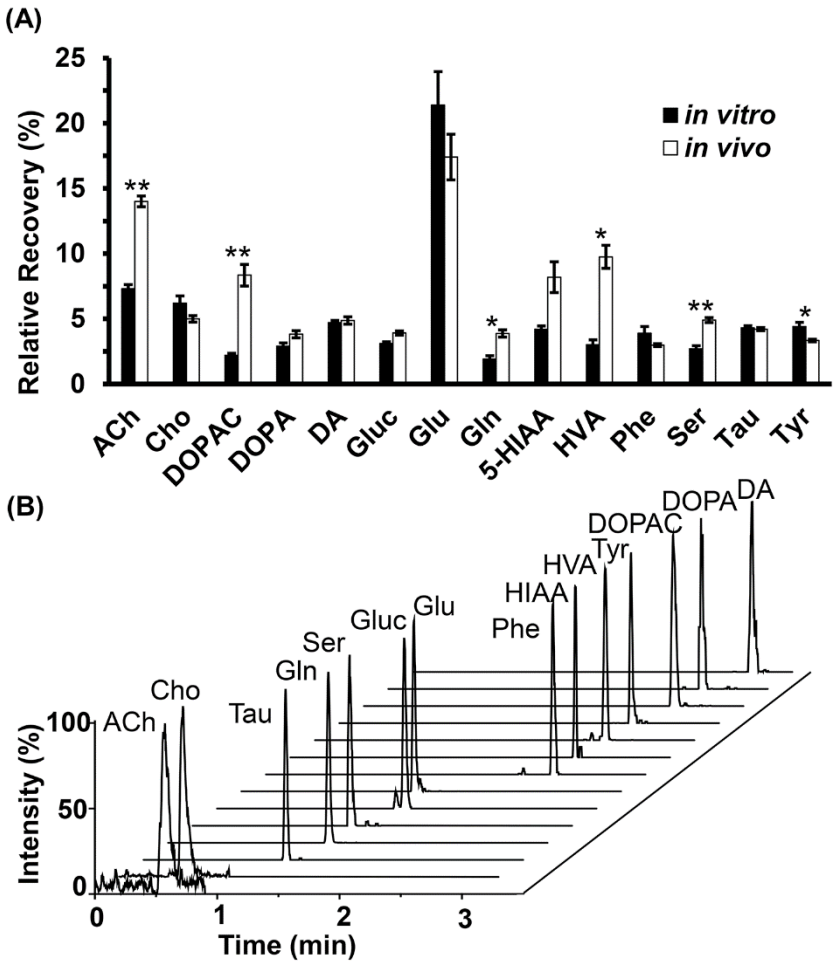

Figure 2.7 A) Comparison of relative recoveries of analytes between in vitro and in vivo experiments. The bar chart represents averaged relative recovery with SEM. * indicates different with $p < 0.05$, ** indicates $p < 0.001$ obtained by the two-tailed Student's t-test test. B) Multiple reaction monitoring mass chromatograms of a representative fraction (1.5 µL) collected from the striatum of an anesthetized rat through the microfabricated probe. The chromatogram shows the trace for 14 detectable neurochemicals. Abbreviations used are: acetylcholine (ACh), choline (Cho), taurine (Tau), glutamine (Gln), serine (Ser), glucose (Gluc), glutamate (Glu), phenylalanine (Phe), 5-hydroxyindoleacetic acid (5-HIAA), homovanillic acid (HVA), tyrosine (Tyr),

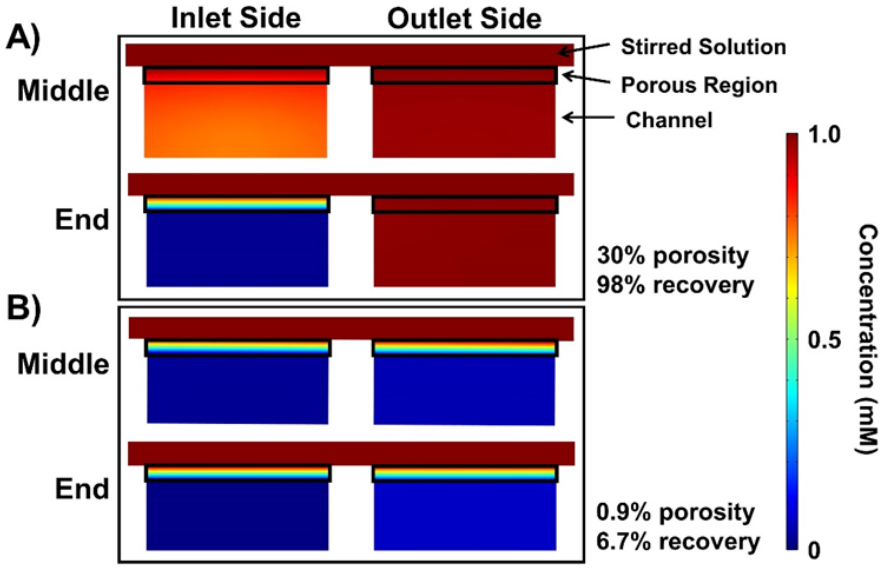

Figure 2.8 Comsol modeling and simulation of 1 mM dopamine diffusing through the membrane of microfabricated probe. The microfabricated probe was constructed in COMSOL Multiphysics 4.4 (Burlington, MA) to model its recovery. The fabricated probe has semi-circular fluidic channels; but for ease of modeling, the channels were designed as 60 µm x 24 µm rectangles which gave the same cross-sectional area as the actual probes. The total length of the channels was 8 mm in a 'U' shape like the actual probe. The porous membrane was designed as a polysilicon rectangle, 5 µm x 60 µm, overlaid the channels. A large box was connected to the external boundary of the membrane region for simulating the probe in a well-stirred solution. The 'Free and Porous Media Flow' and 'Species Transport in Porous Media' physics models were applied to the channel and membrane regions. Navier-Stokes equations modeled the fluid (water) in the open channel with a flow rate of 100 nL/min. Fluid movement in the porous region was defined by the Brinkman equation and a permeability of 50 nm^2 was used. The porosity variable was modified to match experimental data. For the transport of chemical species, the diffusion coefficient of dopamine, 6 $x10^{-10}$ m^2/s was used. The exterior probe volume used 'Laminar Flow' and 'Transport of Diluted Species' physics with a flow rate of 10 mL/min to simulate a well-stirred solution. Images below show cross section of probe at the middle and end of the probe color coded for DA concentration. A) Recovery for probe with 30% porosity and B) for 0.9% porosity.

In vivo sampling

To determine their suitability for in vivo experiments, µFab probes were used to sample from the striatum of anesthetized rats. 14 neurochemicals were consistently detected in 20 min fractions with good signal to noise ratio (Figure **2.7**). For comparison, we also sampled from the same animals with a MD probe operated at the same flow rate. Basal concentrations from both types of probes are reported in Table **2.3**. Concentrations were not corrected for recovery; however, the MD probes achieved nearly 100% recovery; therefore, these concentrations can be considered a good estimate of the in vivo concentration[192].

Comparison of these concentrations with other reports of calibrated in vivo MD experiments reveals reasonable agreement for most neurochemicals[163,192–198]. Acetylcholine and dopamine are generally found in low nanomolar concentrations. Glutamate, phenylalanine, 5-HIAA, and tyrosine are typically in low micromolar range (< 10 μM) while glutamine, serine and taurine are in high micromolar range (> 10 μM). We observed about 5 times higher concentration of glucose than prior reports; however, our experiment was performed with anesthetized rats which may account for this difference. GABA, histamine, 3-MT and 5-HT were not detectable in dialysates from μFab probe sampling due to their low concentration and insufficient recovery to reach the instrument detection limit.

Because the MD probe recovery approaches 100% at 100 nL/min, the in vivo recovery of μFab probe could be estimated by dividing dialysate concentrations from μFab probes by dialysate concentrations from MD probes. This calculation assumes that the in vivo concentration is the same on both sides of the brain and at both probes. As shown in Figure **2.7**, the in vitro recovery and estimated in vivo recovery of the μFab probe are comparable for 8 of the neurochemicals. For several compounds (Gln, HVA, Tyr, Ach, DOPAC, and Ser) the estimated in vivo recovery is significantly higher than in vitro recovery. The origin for this difference is not clear. It is possible that active processes and mass transport within the brain is sufficiently different from in vitro for these analytes to cause the in vitro recovery to differ from the in vivo recovery[199,200]. Another interpretation is that the actual basal concentrations from the sampling site of μFab probe are higher than the concentrations from MD probe sampling. Such discrepancies could be due to differences in local concentrations (different areas were sampled) or to artifacts that result from different tissue reactions due to membrane material and probe size.

Table 2.3 Comparison basal extracellular concentration by the microfabricated probes, conventional probes with previous reports. The in vivo recovery for the microfabricated probes is estimated by finding the ratio between [μFab] and [MD]. All measurements are from sampling of the striatum of rats. Values given as mean ± SEM (n = 5 animals). In vivo recovery of μFab probe estimated by dividing μFab concentration by MD concentration, where recovery was estimated at 100%. n.d. stands for not detected.

Analyte	Previously-reported concentration (Anesthesia, Quantification method, Ref #)	[MD]	[μfab]	Estimated in vivo recovery, %
ACh	10 ± 3.0 nM (Ketamine, 20% in vitro recovery, [163])	32 ± 4.5 nM	4.5 ± 0.46 nM	14 ± 0.4
Choline		11 ± 0.93 μM	0.54 ± 0.022 μM	5 ± 0.2
DOPAC	17.4 ± 2.6 μM (Awake, No-net-flux, [192])	8.9 ± 1.4 μM	0.74 ± 0.084 μM	8 ± 0.8
DOPA		150 ± 17 nM	5.6 ± 0.41 nM	4 ± 0.3
Dopamine	10 ± 1.7 nM (Awake, No-net-flux, [192])	6.7 ± 0.62 nM	0.32 ± 0.046 nM	5 ± 0.3
Glucose	350 ± 20 μM (Awake, No-net-flux, [195])	1431 ± 82 μM	56 ± 3.3 μM	4 ± 0.2
GABA	120 ± 50 nM (Urethane, 20% in vitro recovery, [193])	780 ± 340 nM	n.d.	-
Glutamate		7.5 ± 0.74 μM	1.5 ± 0.18 μM	21 ± 2
Glutamine	385 ± 16 μM (Awake, No-net-flux, [197])	472 ± 24 μM	18 ± 2.2 μM	4 ± 0.3
Histamine		39 ± 16 nM	n.d.	-
5-HIAA	3500 ± 100 nM (Awake, Low-flow-rate, [192])	1200 ± 130 nM	95 ± 16 nM	8 ± 1.2
HVA	17 ± 1.1 μM (Awake, Low-flow-rate, [192])	8.3 ± 1.1 μM	0.81 ± 0.097 μM	10 ± 0.9
3-MT		6.9 ± 0.46 nM	n.d.	-
Phe	2 ± 0.2 μM (Chloral Hydrate, Low-flow-rate, [194])	7.5 ± 0.49 μM	0.22 ± 0.012 μM	3 ± 0.1
Serine	7 ± 0.5 μM (Awake, Corrected for in vitro recovery, [196])	36 ± 2.3 μM	1.8 ± 0.12 μM	5 ± 0.2
5-HT		19 ± 4.2 nM	n.d.	-
Taurine	25 ± 5.1 μM (Halothane, No-net-flux, [198])	60 ± 4.9 μM	2.8 ± 0.21 μM	4 ± 0.1
Tyrosine	3300 ± 900 nM (Chloral Hydrate, Low-flow-rate, [194])	6700 ± 330 nM	220 ± 1.1 nM	3 ± 0.1

To assess the probe performance in response to dynamic in vivo chemical changes, the μFab and MD probes were simultaneously used to monitor concentration changes of DA and other neurochemicals after administration of AMPH. When expressing the changes as a percent of baseline, nearly identical changes are seen at both the MD and μFab probes as shown in Figure **2.9**. The large change of about 4300% for DA is in agreement with expected effect of AMPH which inhibits uptake and promotes secretion of DA[201]. Other measured neurochemicals that have significant changes ($p < 0.05$, Student's t-test) in their post drug levels were DOPAC, DOPA, HVA, 5-HIAA, and Tyr. The overall results show the μFab probe provides dynamic measurements nearly the same to a MD probe under the conditions of 100 nL/min flow rate and 20 min fractions.

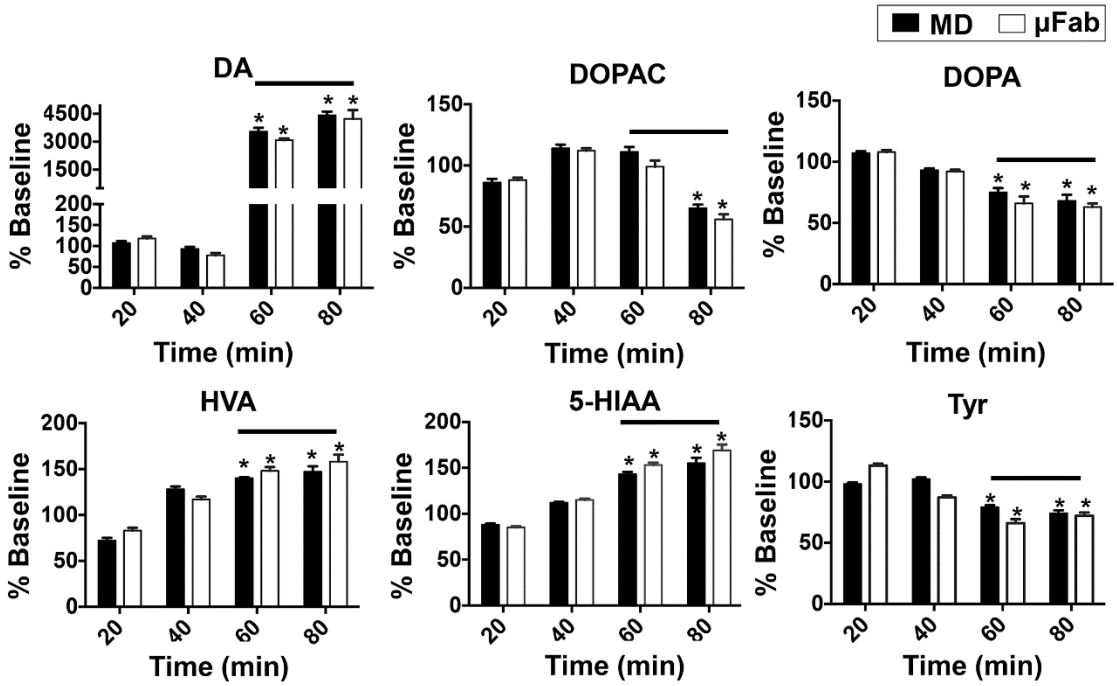

Figure 2.9 Dual probe microdialysis of rat striatum showing effects of AMPH (5 mg/kg, IP) on DA release and other neurochemicals sampled by a concentric microdialysis probe (MD) and microfabricated probe (μFab). Both probe types have similar performance on response to dynamic in vivo chemical changes. Lines indicates when AMPH was present (fractions at 60 and 80 min). Data were converted to percent of baseline measurement to normalize pre-drug levels to 100 percent. Student's t-test indicates a significant change (*$p < 0.05$) between basal and post drug levels. Results are the mean ± SEM, n = 3 animals. For other measured neurochemicals, their post drug levels did not significantly change.

Histological examination of the sampling sites from both types of probes were performed to visualize overall probe placement within the brain (see Figure **2.10**). The µFab probe generates a much smaller tract than the MD probe as expected. This difference presumably results in lower tissue damage.

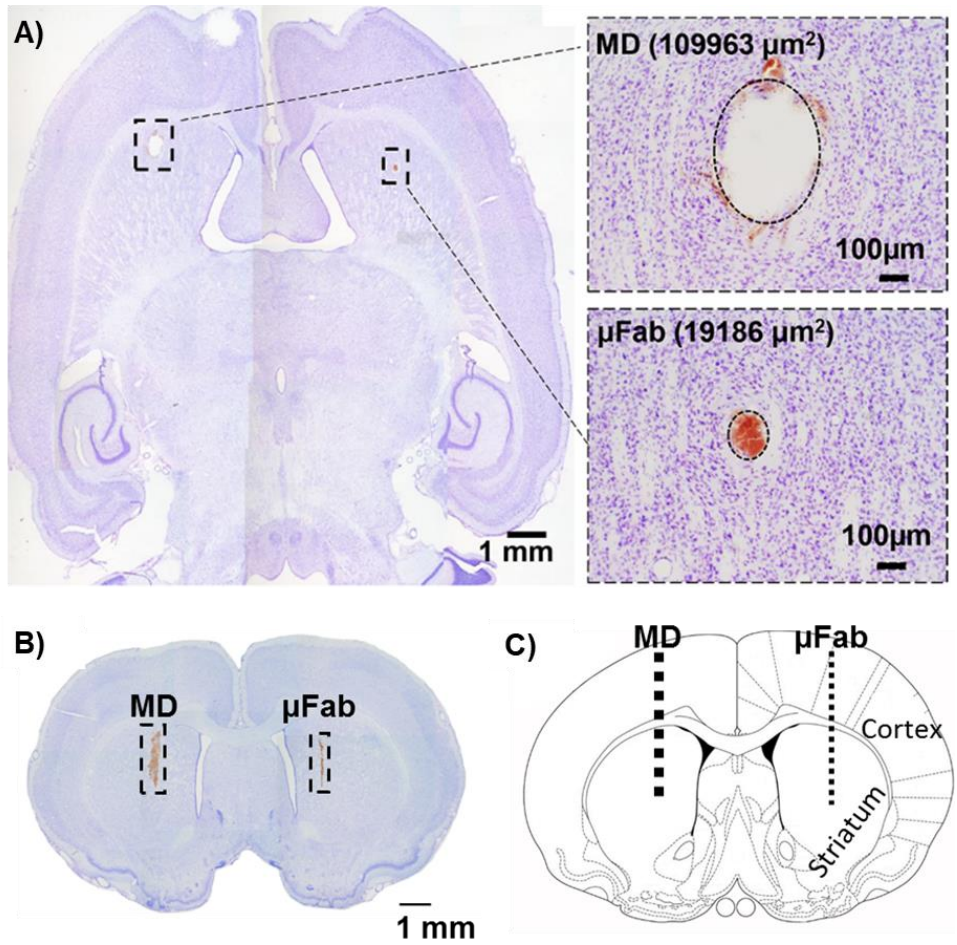

Figure 2.10 A) Horizontal histological section of the brain. The zoomed in images in the insets indicates the probe tract areas of both µFab and MD probes. As shown, the µFab probe tract is 83% smaller than the MD probe tract. B) The brain was cut into 40 µm coronal sections and Nissl stained to show overall brain structure with probe tracts (boxes with dashed line). C) Dotted lines indicates tracts overlaid on a rat brain atlas diagram, corresponding to (A).

Conclusion

The in vivo results show that the µFab probe can be reliably used for studying neurochemicals and monitoring dynamic chemical changes in live animal brain. The chief advantage of the probes is that they have 79% smaller cross-section than conventional MD probes and therefore can be used in smaller subjects and brain regions. Despite the small size, the probes are strong enough to penetrate tissue without flexing or breaking. The low recovery at 100 nL/min is a drawback of these probes; however, preliminary experiments suggest that small changes in membrane fabrication will mitigate this issue. Fortunately, the excellent sensitivity of LC-MS allows many neurochemicals to be detected even at this recovery. A likely route to improve temporal resolution and detect less abundant analytes is to use miniaturized analytical methods like capillary LC, capillary electrophoresis, or droplet enzyme assays[41,73,202–205]. The sensitivity of such methods would allow good temporal resolution while preserving the advantages of better spatial resolution and lower tissue damage. The use of microfabricated probes may allow integration of other functionality such as electrodes for chemical or potential sensing, microfluidics for sample preparation (e.g. derivatization), or droplet formation for fraction collection at nanoliter scale. The probe may also be utilized for other applications that require continuous chemical sampling or delivery from microenvironments.

Chapter 3
Microfabricated Push-Pull Probes Coupled to Droplet-Based Microfluidics and Mass Spectrometry for in Vivo Multiplexed Monitoring of Neurochemicals

Thitaphat Ngernsutivorakul, Alec C. Valenta, Daniel J. Steyer, and Robert T. Kennedy, *Manuscript in prep.*

Introduction

In vivo neurochemical monitoring provides valuable insights into chemical neurotransmission, which can be related to behaviors as well as brain functions and diseases[206–209]. One of the powerful approaches to perform such measurement is to couple sampling methods (i.e., microdialysis and push-pull perfusion) to suitable analytical techniques, such as liquid chromatography coupled to mass spectrometry (LC-MS), and capillary electrophoresis coupled to laser-induced fluorescence (CE-LIF)[27,45,71,210]. By this approach, chemical measurement can be conducted with excellent sensitivity and selectivity. Multiple compounds can also be measured simultaneously, allowing studies of drugs and interactions between neurotransmitter systems[45,211]. Although the method has proven extremely versatile and indispensable to neurochemical studies, it is limited in spatial and temporal resolution[212,213]. The aim of this study is to develop an analytical system that overcomes these limitations.

Spatial resolution is important because of small size and heterogeneity of the brain structures[25,214]. For in vivo neurochemical monitoring, spatial resolution is usually limited by probe size, which correlates with an active sampling area. In microdialysis, sampling occurs at the membrane tubing of the probe, which is typically 220-400 μm in diameter with a 1-4 mm length[24,26,215]. These large sizes preclude high spatial resolution and experiments in

smaller brain regions. A more radical approach to achieve high spatial resolution is to use low-flow push-pull perfusion[72,73,216]. In this approach, artificial cerebrospinal fluid (aCSF) is pushed from one capillary at ~50 nL/min while a sample is pulled from another capillary at the same rate. An active sampling area is therefore restricted to only the space between the two orifices at probe tip, resulting in better resolution comparing to microdialysis. The use of low-flow push-pull perfusion for in vivo sampling resulted in at least 80-fold spatial resolution improvement over microdialysis[73]. Furthermore, our group has developed microfabrication procedures to further reduce the size of push-pull sampling probe[115]. The microfabricated probes provide not only even better spatial resolution, but also potential for less tissue disruption. In addition, the microfabrication process offers the possibilities for mass production, flexibility in designs, and incorporating more functions into the probe.

Temporal resolution is important since neurochemical concentrations in the brain can alter rapidly during behavior or stimuli[41,43,44]. When coupling the probe to an analytical method, temporal resolution can be limited by different factors[28], including time to collect enough sample volume required for the assay, separation time, sample handling, and zone broadening due to flow and diffusion (i.e., Taylor dispersion). Nanoscale analytical techniques, such as microbore LC and CE, can be used to reduce the collection volume and separation time to a few seconds[41,156,194,217,218]. Furthermore, segmented-flow sampling has proven to prevent Taylor dispersion from occurring during transfer. Droplet-based microfluidic systems have also provided a more convenient way to manipulate nanoliter fractions that are collected[73,159,163,165,219,220]. With these methods, previous works have shown in vivo neurochemical monitoring with improvement of temporal resolution from 10 - 30 min to less than 10 s.

A versatile approach for droplet analysis is to use direct infusion MS. MS is a universal detector with high sensitivity, multi-analyte capability, and commercial availability. With multiple reaction monitoring (MRM) mode and addition of isotopically-labeled internal standards, quantitation of analytes in complex biological samples can be achieved with high selectivity. In addition, coupling nano-electrospray ionization (nESI) to MS provides enhancement in sensitivity. For droplet analysis, this method allowed direct introduction of the droplet stream without the need to remove an immiscible oil phase[163,167]. The method is also robust and salt-tolerant. Overall, the nESI-MS method is a versatile and attractive tool for analysis of sample droplets collected from push-pull perfusion in the brain.

A significant challenge in coupling the miniaturized probe to segmented flow is to develop compatible microfluidic interfaces that allow reliable sample transfer and droplet manipulation. In this work, we have successfully developed the interfaces and coupled microfabricated push-pull probes to droplet microfluidics. Arrays of nanoliter samples were transferred, segmented and simultaneously added with internal standards (I.S.) prior to an offline nESI-MS assay. The system was evaluated in vitro for multiplexed measurements of 4 neurochemicals including acetylcholine (ACh), glutamate (Glu), glutamine (Gln) and γ-aminobutyric acid (GABA), achieving ~6 s temporal resolution with a sampling rate of 100 nL/min. Furthermore, by microfabrication, an additional channel was integrated to the probe for microinjection of a neural stimulant. Utility of the integrated system was demonstrated by monitoring multiple neurochemical dynamics in vivo at high spatiotemporal resolution.

Experimental

Chemicals and materials

Unless otherwise specified, chemicals were purchased from Fisher Scientific (Fairlawn, NJ) or Sigma Aldrich (St. Louise, MO) and were certified ACS grade or better. Solutions were prepared with HPLC-grade water, filtered and degassed prior to use. Teflon tubing were purchased from IDEX Health & Science (Oak Harbor, WA). Polyimide-coated glass capillaries were purchased from Molex (Phoenix, AZ). Epoxy glues were purchased from ITW Devcon (Danvers, MA) and Loctite (Westlake, OH). A commercial tee (100 µm i.d.) was purchased from Valco Instruments (Houston, TX). Polydimethylsiloxane (PDMS) was purchased from Curbell Plastics (Momentive® RTV 615, Livonia, MI). Crystalbond 555 Adhesive was purchased from Structure Probe (West Chester, PA). Artificial cerebrospinal fluid (aCSF) consisted of 145 mM NaCl, 2.68 mM KCl, 1.01 mM $MgSO_4$, 1.40 mM $CaCl_2$, 0.45 mM NaH_2PO_4, and 1.55 mM Na_2HPO_4, adjusted to pH of 7.4 with 0.1 M NaOH. High-potassium (K^+)-aCSF consisted of 100 mM KCl and 47.7 mM NaCl; the other components were the same as regular aCSF.

Push-pull probe and holder

Fabrication of probe. Probes were microfabricated on a 525 µm thick 4 inch wafer (University Wafer, MA) as described elsewhere[115] with modification in probe design and additional step for removal of adhesive. Briefly, microfabrication of sampling probes was performed within a class 1000 cleanroom (Lurie Nanofabrication Facility at the University of Michigan). The probes were fabricated from 525 µm thick n-type 100 mm silicon wafers coated with SiO_2 mask. A series of microchannels were masked on a wafer by

photolithography before the wafer was etched by deep reactive ion etching (DRIE) and XeF_2 etching. The wafer was sealed with poly Si using low pressure chemical vapor deposition. Lithography and DRIE were again used to assign and etch probe shapes and sampling orifices with desired dimensions. The wafer was mounted to a carrier wafer with Crystalbond 555 adhesive and backside etched using DRIE prior to probe release in hot water. To ensure complete removal of the adhesive, probes were baked at 610 °C for 8 h in a laboratory kiln. Additional fabrication details are provided in Appendix A.

The final probe size was 11 mm long, 84 µm wide × 70 µm thick. In this work, microfabricated probes included 3 channels of 20 µm i.d. One channel was used for pull flow. Another channel was used for push flow. For the probe with 3 channels, the third channel was merged with the channel for push flow at 0.5 mm from the probe orifice. The additional channel was used for microinjection. Schematics of the probe and its operation are shown in Figure **3.1** & Figure **3.3**A.

Probe holder and fluidic capillaries. A holder was used to handle and plumb the probes to connection tubing. A design of probe holder was the same as described previously[115]. A 0.5 cm of 150 µm i.d. / 360 µm o.d. tubing was mounted to each trench of a probe holder and used as the "union". The holder was used as a guide for insertion of the probe into the union before gluing with epoxy gel resin. 5 cm of 50 µm i.d. / 150 µm o.d. fused-silica capillary was inserted into each union, joint to each probe post, and used as the "fluidic capillary" for delivery of fluid from/to the probe. To adapt these capillaries to 360 µm fittings for pushing, fluidic capillaries were sheathed with 2 cm of 180 µm i.d./ 360 µm o.d. capillary.

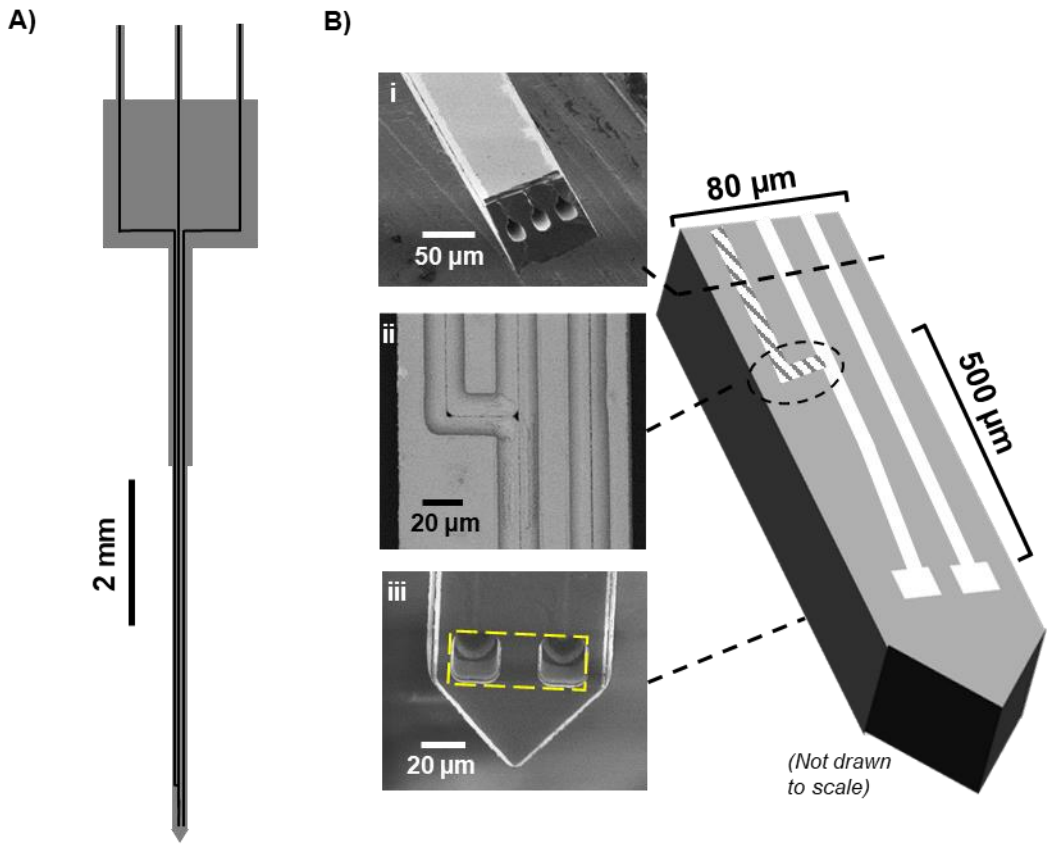

Figure 3.1 A) Overview of probe shape and channels. B) SEM images of microfabricated push pull probe with additional channel for microinjection. The images show cross section of the probe (i); top view of an integrated tee after backside etch to reveal the channels (ii); and tip of the probe (iii) with an estimated sampling area (yellow dashed) of 1200 µm^2.

Droplet-based microfluidic chips

PDMS microchips were designed to couple the microfabricated sampling probes to segmented-flow and reagent addition (see Figure **3.2**& Figure **3.3**B). The droplet-based PDMS chips were fabricated using a combination of a standard soft lithography technique and a pour over method[221]. In all procedures, PDMS had a 10:1 base:curing agent ratio and was cured at 75˚C for 45 min. Briefly, a PDMS chip, replicated from a SU-8 mold with 125 µm wide × 100 µm tall channels was first fabricated (Figure **3.2**A). The device contained a 4-way junction (manifold) for flow segmentation with simultaneous reagent addition. The

device channels were derivatized with 1H,1H,2H,2H-perfluorooctyltrochlorosilane (4% v/v in anhydrous hexadecane). The PDMS chip was cut under a microscope so that the end of each channel was ~ 0.5 mm long. A 100 µm o.d. capillary was then inserted through the PDMS channel and 230 µm o.d. capillaries were inserted into the other two channels (Figure **3.2**B). The PDMS chip with inserted capillaries were placed on a petri dish before pouring PDMS over and cure. After cure, all capillaries were removed and the chip was trimmed to size using a razor blade (Figure **3.2**C). The capillary-molded channels were necessary as they ensure proper microfluidic sealing (i.e., no air leaks during vacuum applied). 100 µm cylindrical PDMS channels accommodated tight sealing with 150 µm o.d. tubing connected to sampling probe and reagent reservoir while 230 µm cylindrical PDMS channels accommodated a proper sealing with 360 µm o.d. tubing connected to oil reservoir and Teflon storage tubing. To facilitate device connection or removal during experiments, an additional step of molding of 360 µm o.d. tubing was carried out to form guiding channels for ease of device connection or removal (Figure **3.2**D). The final design and configuration of the droplet-based PDMS device are shown in Figure **3.2**E & F. The same procedures described herein was also utilized to fabricate a 3-way junction (tee) for flow segmentation only.

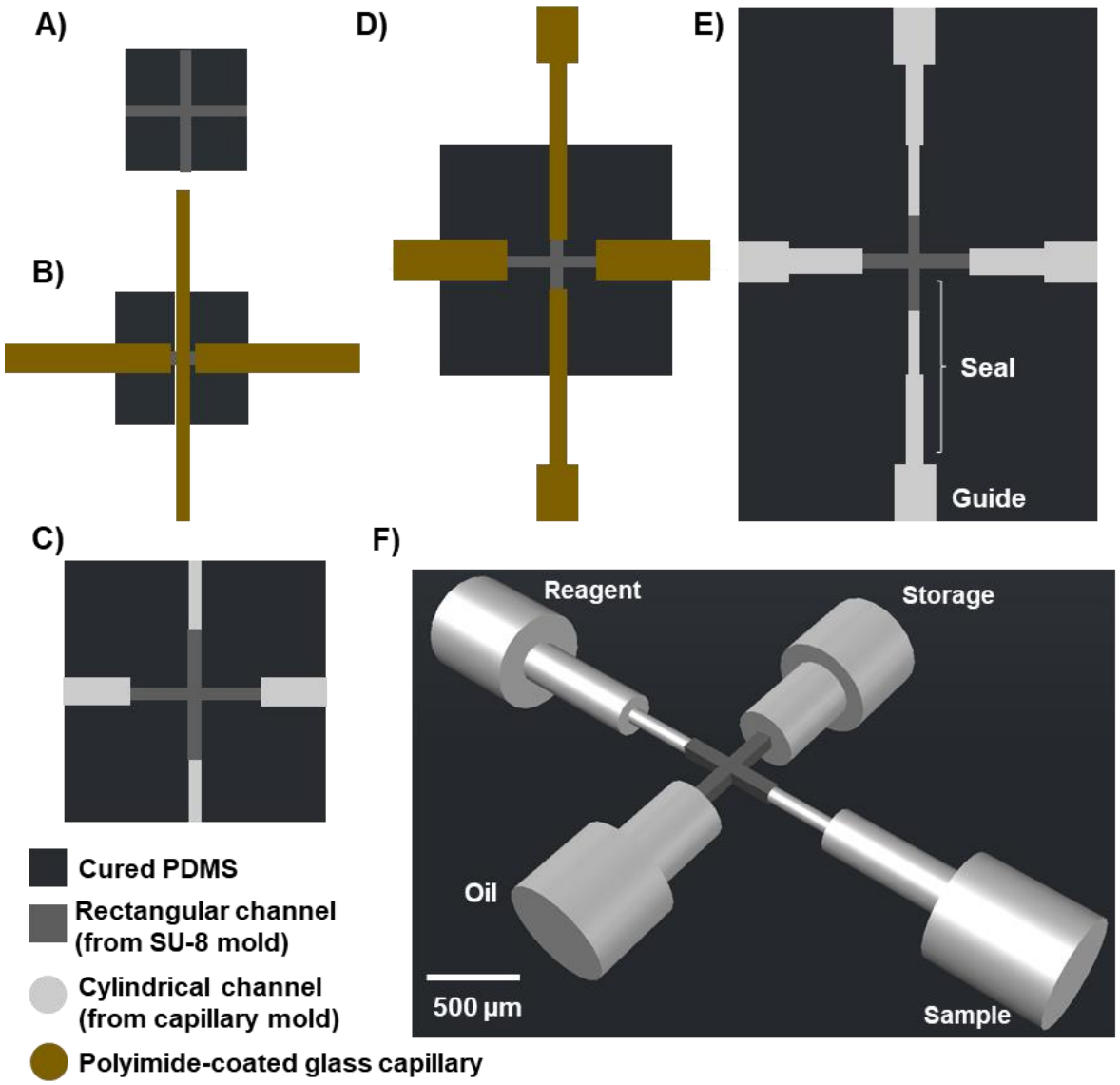

Figure 3.2 Illustration of fabrication and design of a PDMS manifold. The device was designed to minimize dead volume while allowing pre-alignment of fluidic capillaries and ensuring no leakage during vacuum applied. Fabrication was based on replication of PDMS from a microfabricated SU-8 mold (A) and a polyimide-coated glass capillaries (B), yielding a combination of microchannels with appropriate shapes and dimensions (C). Further molding step (D) was employed in forming guides for ease of capillary insertion. Top view of the device (E) and its 3D view (F) are also shown. An actual image of the complete device after tubing connection can be seen in the inset of Figure **3.3**B.

In vitro characterization

Device operation. An outline of the integrated system is illustrated in Figure **3.3**. Method for operation of the segmented-flow push-pull system[73] was adapted for use in this work. One fluidic capillary was coupled to a gastight 100 µL syringe (Hamilton, Reno, NV) using a 360 µm o.d. Teflon union. A syringe pump (Chemyx, Stafford, TX) was used to generate the push flow. Prior to experiments, a flow meter (SLG1430-025, Sensirion, Zurich, Switzerland) was utilized to validate flow rate and stability. Before starting pull flow, the first inlet of the manifold was connected to the fluidic capillary of probe outlet. The second inlet of the tee was attached to a 4 cm long 50 µm i.d. capillary/ 360 µm o.d. capillary which was placed in a vial of oil (50:1 v/v PFD:PFO, viscosity of 5.1 cps). The third inlet of the tee was connected to a 40 cm length of 150 µm i.d./ 360 µm o.d. Teflon tubing for storage of droplets. A 4-way manifold was employed in simultaneous reagent addition. The first three inlets were connected with appropriate tubing, as described above. The fourth inlet of the 4-way manifold was connected to a 1.8 cm of 20 µm i.d./ 150 µm o.d., which was place in a vial of a reagent containing fluorescein and a mixture of internal standards in water. For sampling, a microfabricated probe was placed in a stirred vial of an aCSF prior to addition of a mixture of standards. A set of standards included 0, 0.01, 0.05, 0.1, 0.2, and 0.4 µM ACh 0, 0.05, 0.2, 0.4, 0.8 and 1.6 µM GABA, 0, 0.1, 0.5, 1, 2 and 4 µM Glu, and 0, 10, 50, 100, 200 and 400 µM Gln. To generate pull flow, a vacuum was applied at the end of the Teflon storage tubing. Vacuum pressure was adjusted between – 100 mmHg to – 200 mmHg in order to achieve the pull flow of samples within the range of 50 nL/min to 100 nL/min, and ~1:1.5 aqueous:oil droplets. Flow rate was determined by monitoring plug size and frequency.

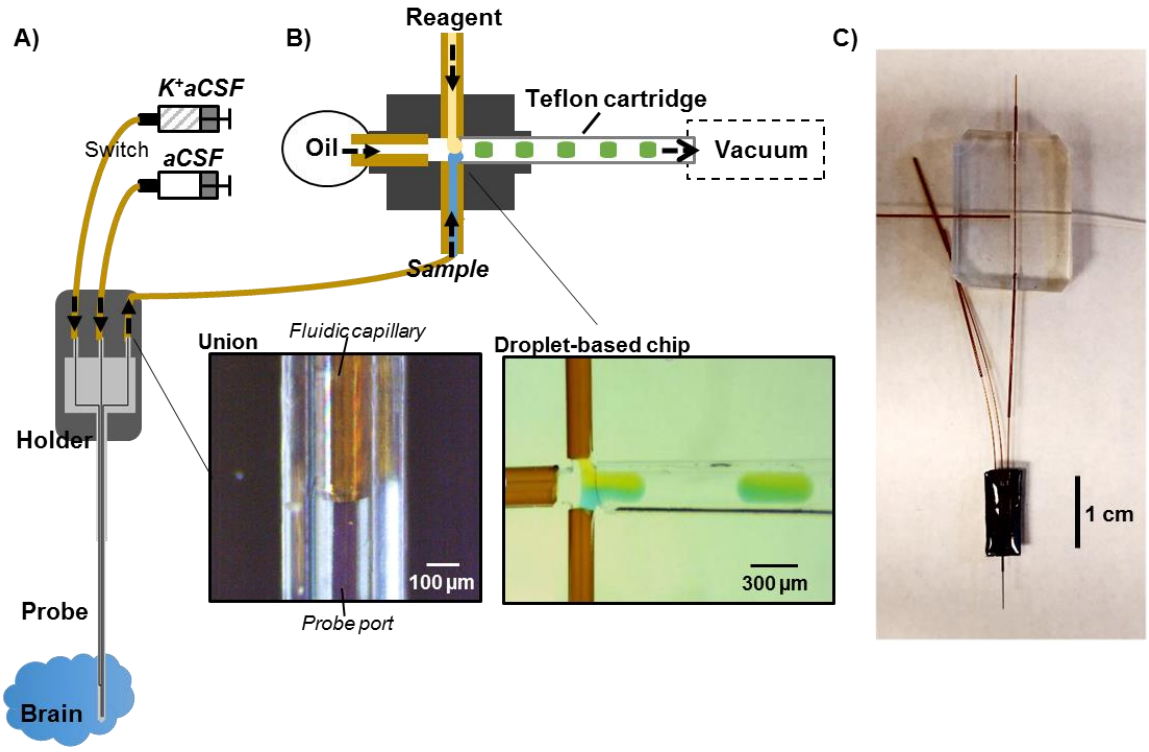

Figure 3.3 Overview of experimental setup for monitoring brain chemical dynamics with high spatiotemporal resolution. (A) Microfabricated push-pull probe with 3 channels. The first and second channels were used for pushing regular aCSF and microinjection of K^+-aCSF. The last channel was used for pulling sample. The inset showed microfluidic interface between the probe and a "fluidic" capillary. This capillary was used for sample transfer prior to connecting with a microfabricated manifold for simultaneous flow segmentation and reagent addition (B). Generated droplets were collected in a Teflon storage tubing prior to an offline analysis. The inset showed a microscopic photograph of the flow segmentation with reagent addition. Food dyes were added to sample and reagent for visualization. (C) Photograph of the probe connected to the droplet-based device.

Droplet analysis. Analysis of droplets was carried out offline using fluorescent microscopy for fluorescein detection and ESI-MS for neurochemical detection. After collection of droplets, the Teflon storage tubing was disconnected from the PDMS device before connecting with an oil-filled syringe in a syringe pump. Fluorescence of droplets were imaged by using an inverted fluorescence microscope (Olympus IX71) with a Xe arc lamp, appropriate filters, and a CCD camera (Hamamatsu ImageEM X2). When reagent addition was performed, a ratio of added reagents to samples was determined based on the fluorescein intensity in aqueous droplets.

For the ESI-MS assay, the other end of the Teflon storage tubing was connected to a nanospray tip using a commercial union. (PicoClear, New Objective, Woburn, MA) The spray tip is pulled to 15 µm i.d. with conductive coating on its exterior. Sample droplets were perfused at 50 nL/min through the nanospray tip. The ESI voltage was 1.25 kV. Samples were analyzed by using a Micromass (Waters, Milford, MA) Quattro Ultima triple-quadrupole mass spectrometry, operated in multiple reaction monitoring (MRM) mode using conditions listed in Table **3.1**. Data was recorded by Masslynx 4.1 (Waters, Milford, MA). Cutter[222] was used for peak detection and determination of peak intensities. Ratio of the peak intensity to I.S. was then calculated and used for calibration.

Table 3.1 MRM condition of analytes. Four analytes with their internal standards were simultaneously monitored in the droplets. Inter-channel delay time was 10 ms. Inter-scan delay time was 100 ms. Total MS cycle time was ~1.4 s.

Analyte	m/z transition	Dwell time (ms)	Cone voltage	Collision energy (eV)
GABA	104 → 87	150	35	10
13C-GABA	110 → 93	150	35	10
ACh	146 → 87	150	35	15
d4-ACh	150 → 91	150	35	15
Glu	148 → 130	150	35	10
13C-Glu	153 → 135	150	35	10
Gln	147 → 130	150	35	10
13C-Gln	152 → 135	150	35	10

Temporal resolution. To initially test temporal resolution of the sampling system, a probe was coupled to a microfabricated tee for testing flow segmentation only (Figure **3.4**A). The probe was placed in a stirred vial of an aCSF solution containing a sample. During sampling, the concentration of sample was rapidly changed to higher concentrations via

pipette pouring. Temporal resolution of the system was determined by measuring 10% to 90% dynamic response time during step changes in sampled concentrations.

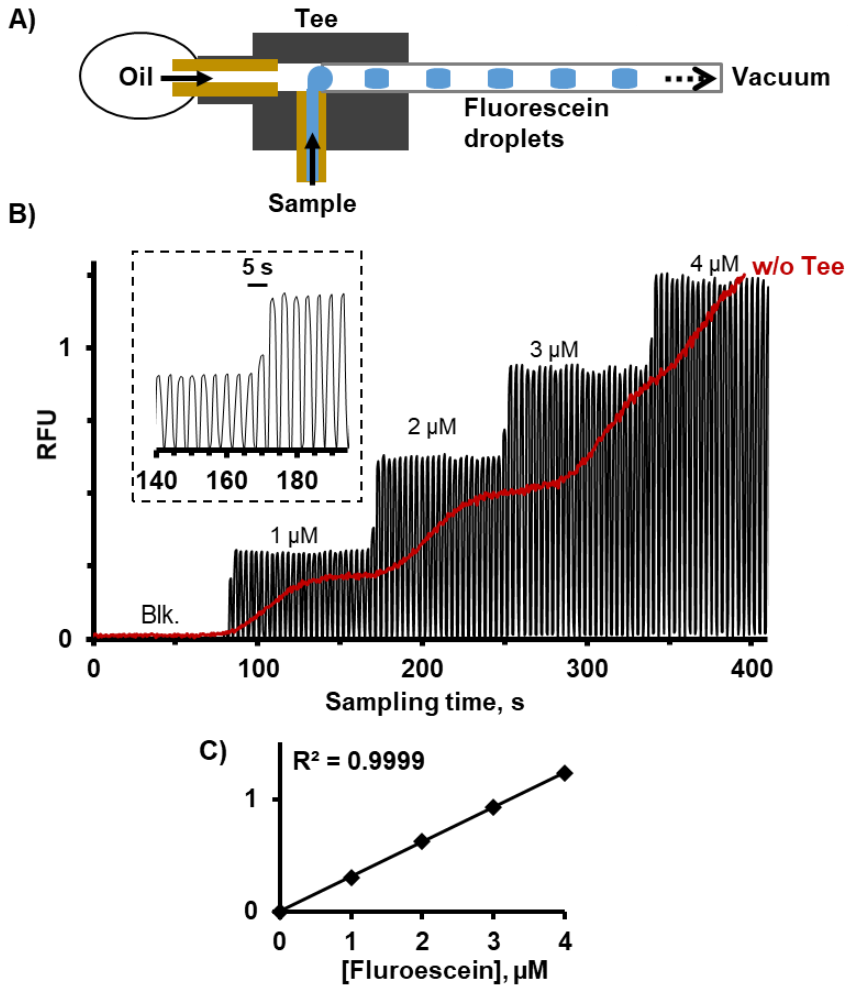

Figure 3.4 Test of temporal resolution. A) Schematic of a segmented flow sampling; B) step changes of fluorescein concentration revealing temporal resolution of ~6 s at a sampling rate of 100 nL/min; C) Resulting calibration from the above sampling experiment. Each point was the average of 25 standard droplets

In vivo experiments

Surgical procedures were similar to those described previously (see Chapter 2)[223]. Male Sprague-Dawley rats weighting between 250 - 350 g were anesthetized using 2 – 4% isoflurane, and placed in a stereotaxic frame (Koft Instrument, Tujunga, CA). Animals were

maintained under isoflurane over the entire experiment. Probes were stereotaxically inserted to the striatum at coordinates +1.5 mm anterior, ± 3.0 mm lateral to bregma, and a depth of 4.5 mm ventral from dura. Probes were lowered slowly over 1 min. During probe insertion, probe channels were back-flushed at 200 nL/min to prevent clogging before immediately reducing flow rates to be 100 nL/min at depth. After 5 min of flow stabilization, an outlet of the pull channel was then connected to the PDMS manifold. To generate pull flow at 100 nL/min, -200 mmHg of vacuum was applied at the end of the Teflon tubing previously filled with droplets. Pull flow rate was monitored by observation of plug frequency and measurement of volumetric flow rate. If necessary, optimization of flow rate was carried out by manually adjusting vacuum pressure. Push-pull flow was continued for at least 30 min following implantation for stabilization of baselines. At about an hour after probe implantation, K^+ stimulation was performed by switching a push flow from a regular aCSF to high K^+-aCSF through the integrated channel. High K^+-aCSF was perfused at 100 nL/min for 1 min before switching flow back to aCSF. After sample collection, the Teflon storage tubing was removed from the chip prior to droplet analysis.

Results and Discussion

Probe and microinjector

Micromachining of silicon based on buried channel technology was utilized to fabricate push-pull probes[115]. In this work, the method for microfabricating the probes was validated. Although the method was proven successful, it was still imperfect as ~30% of the final probes were either clogged or partially-clogged during the flow test. We found that this issue was due to the use of adhesive (i.e., Crystalbond mounting wax) during the backside

etching that may enter and clog probe channels (see Figure **3.5**). In our previous work, the wax removed by soaking the probe in hot water and perfusing hot water through each channel. However, we experienced that this approach was inconvenient and did not guarantee complete removal of the adhesive. To address this problem, we have added a batch process of baking probes at 610 °C for 8 h to decompose the wax. As a result, the wax was completely removed and a fabrication yield was improved from 60% to 90% (~10% of the probes were broken during probe release and manual transfer). Overall, the current fabrication process was reliable, yielding smooth channels with high replication fidelity (see Figure **3.1**). By processing a single 4 in. wafer, about 120 functional probes were obtained.

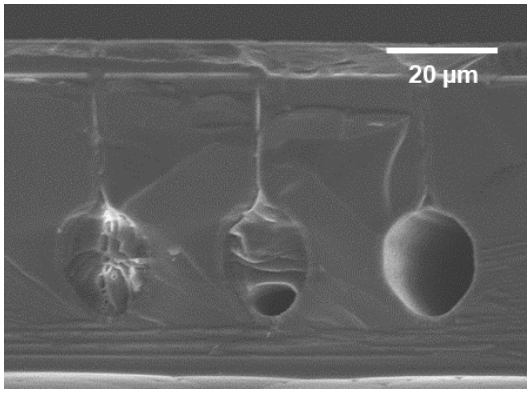

Figure 3.5 Clogged channel by adhesive used during the backside etching.

Design of the probe was adapted from our previous report[115]. In this work, we integrated an additional channel to the probe for microinjection of a stimulant. As illustrated in Figure **3.1**, the microfabricated probes were 80 µm wide × 75 µm thick, consisting of 3 buried round channels with 20 µm diameter. The two main channels were used for push and pull flow. The additional channel was merged with the push channel, creating a tee-junction

at 500 μm above the orifice. Switching the flow at the tee junction allowed microinjection of a stimulant. A solved equation for calculating a 10% to 90% rise time required for a concentration step change can be expressed as shown below, by substituting the equation for the effective diffusion coefficient for Taylor dispersion into the equation for diffusion from a finite concentration step[73].

$$Rise\ time = \frac{3.62}{V}\sqrt{\left(1 + \frac{r^2V^2}{48D^2}\right)Dt}$$

where r is a capillary radius, V is an average flow velocity, D is a diffusion coefficient, and t is a time to flush the capillary (i.e., capillary volume divided by volumetric flow rate). At a flow rate of 100 nL/min, a rise time during flow switching for microinjection was estimated to be 72 ms with the flush time of 94 ms. Therefore, a time delay during microinjection should be minimal due to use of the microfabricated tee. At the probe tip, the orifices for push-pull sampling were rectangles with 20 μm square. Microfabrication allowed limiting a space between the two orifices to be merely ~20 μm, as shown in Figure **3.1**. The active sampling area of the probe, defined as spatial resolution, was then approximately to be 20 μm × 60 μm or 0.0012 mm^2. This sampling area is about 10-fold smaller than that of miniaturized push-pull probe made by hand assembly. Comparing to a conventional microdialysis probe with 2 mm long × 220 μm diameter membrane, spatial resolution of the microfabricated push-pull probe is approximately 1000-fold better.

Probe connection

Probe holders were used for handling microfabricated probes and coupling the tiny probes to standard "fluidic" capillaries. A "union" capillary, pre-aligned on the probe holder,

was utilized to connect the probe port (1 mm long, 70 µm square with 20 µm buried channel) with a fluidic capillary prior to sealing (see Figure **3.3**A, inset). Selecting proper dimensions of a union capillary and a fluidic capillary was critical to achieve reliable sample flow without compromising on temporal resolution. In this work, optimized dimensions were 8 mm long, 150 µm i.d. / 360 µm o.d. for a union capillary and a 5 cm long, 50 µm i.d. / 150 µm o.d. for a fluidic capillary. Using the rise time equation and a diffusion coefficient of 5×10^{-10} m^2/s, temporal resolutions of the coupled system were calculated to be 4.9 s at a perfusion rate of 100 nL/min and 7.2 s at a perfusion rate of 50 nL/min.

In principal, a relatively small tubing diameter (such as, 10 or 20 µm i.d.) could be used as a fluidic capillary to further minimize the effect of Taylor dispersion. However, too small diameter of tubing could also lead to mismatch between the lumen of a fluidic capillary and the port channel, resulting in even more dead volume and dispersion. Our initial study found that temporal resolution was instead worse when 20 µm i.d. was used as a fluidic capillary (data not shown). This result was in agreement with the previous report[115]. When a 10 cm long, 20 µm i.d. / 90 µm o.d. capillary was used as a fluidic capillary, temporal resolution at a flow rate of 50 nL/min was found to be 26 s. In contrast, the theoretical rise time suggested that temporal resolution could be 1.9 s. Consequently, in practice, use of a 50 µm i.d. fluidic capillary is more effective as it allows reliable sample transfer while still yielding adequate temporal resolution (less than 10 s resolution).

PDMS device

In this work, we have developed PDMS microfluidic devices that were compatible with the microfabricated push-pull probe that allowed tubing connection for sample pulling,

flow segmentation, reagent addition, and droplet collection. Several requirements during the device development included ease of device removal and reconnection due to probe backflushing during in vivo experiments as well as proper sealing and tubing alignment. To achieve these requirements, we used a combination of soft lithography and pour-over methods to fabricate PDMS microchips containing suitable channel shapes and dimensions (see Figure **3.2**F). The cylindrical channel features made by a pour-over method were necessary in order to create tight sealing. We found that 100 µm diameter and 230 µm diameter channels facilitated proper sealing with 150 µm o.d. tubing and 360 µm o.d. tubing, respectively. The resulting chips allowed tubing connection with ease of insertion and without any leaks during vacuum applied (tested up to -500 mmHg), allowing device operation at a wide range of sampling rates. On the other hand, our initial tests indicated that without the use of cylindrical channels for sealing, air leakage and device failure started occurring when applied vacuum was at -100 inHg. This leakage occurred because rectangular channels made from an SU-8 mold do not fit perfectly with standard cylindrical capillaries.

In our initial studies, we also attempted to use commercially available tee or manifold (C360QTPK4 or C360QXPK4, Valco, Houston, TX) for droplet manipulation. However, these devices often generated irreproducible droplets due to errors during manual tightening of the fitting. We also found that the dead volume of the commercial devices normally led to ~3 s loss of temporal resolution, in agreement with a previous report[73]. On the other hand, loss of temporal resolution in the microfabricated devices were negligible (discussed in the next section). In addition, the smallest commercially available fitting permits connection of only 360 µm o.d. tubing, making it less flexible to change design of microfluidic interface. Hence, the devices developed in this work are more suitable for integrating with the

microfabricated push-pull probe as well as easily adapting to other miniaturized sampling probes[223,224].

In vitro characterization

Droplet generation. The microfluidic system for segmented-flow sampling, reagent addition, and droplet collection is illustrated in Figure **3.3**. Push flows for perfusion of aCSF/ K^+-aCSF were operated by using programmable syringe pumps. Pull flows were obtained by using a vacuum pump applied at the end of collection tubing. Regulation of pull flow rates was achieved based on flow resistance of each tubing, which can be estimated by using a Poiseuille's Equation. In other words, desired flows of sample, oil, and reagent could be achieved by selecting appropriate capillary geometries. In this work, a 4 cm long, 50 µm i.d. capillary was selected as an inlet for oil phase (viscosity of 5.1) and a 1.8 cm long, 20 µm i.d. capillary was selected as an inlet for aqueous reagent (viscosity of 0.89). As discussed above, a 5 cm long, 50 µm i.d. capillary was connected to a 1.1 cm long, 20 µm i.d. probe channel for aqueous-phase sampling. With all these parameters and a constant pressure applied, droplets with ~1: 1.5 aqueous:oil volume ratio were generated (see Figure **3.3**B, inset), where the reagent was added at ~1:1.5 reagent:sample volume ratio. As shown in Figure **3.6**A, robust and reliable sampling and reagent addition could be attained with an average of 3% RSD in peak height for serial sampling and reagent additions. By using a 150 µm i.d. Teflon tubing as a storage tubing, formation of regularly shaped aqueous droplets with fraction volume of ~5 nL were formed (3 s per droplet at 100 nL/min), collected and reliably transferred to the subsequent assay. This i.d. tubing also allowed sufficient storage time,

facilitated operation of pull flow within a practical range, and is readily compatible with our previously-developed assays[73,163,221].

Temporal resolution. To determine the temporal resolution of the system, the probe was coupled to a microfabricated tee for sampling of fluorescein (Figure **3.4**A). As seen in Figure **3.4**, step changes in concentrations of fluorescein were observed within 2 droplets at a sampling rate of 100 nL/min, corresponding to ~6 s temporal resolution. This resolution was nearly close to the theoretical temporal resolution (4.9 s) as determined above, indicating that the dead volumes at the union capillary and the droplet-based device were minimal.

Multiplexed chemical measurement. Direct infusion nESI-MS assay was utilized for analysis of multiple neurotransmitters in perfusate droplets with high sensitivity and selectivity. Analysis of droplets was performed in an offline fashion in order to accommodate the use of vacuum during sample collection and the MS speed. Using a MS flow rate of 50 nL/min, droplets were reliably transferred to the electrospray tip via a commercial union without coalescence. This flow rate was chosen to ensure stable signals while providing enough data points per each droplet peak. Using a microfluidic manifold, I.S. of each analyte was also included in a reagent solution for normalizing the effect of matrix and instrument drift on signals. In contrast to our previous work that used a mixture of 1:1 acetonitrile:water as a solvent, water only was used in this work because we found that acetonitrile could lead to irreproducible reagent addition as well as causing coalescence during droplet transfer.

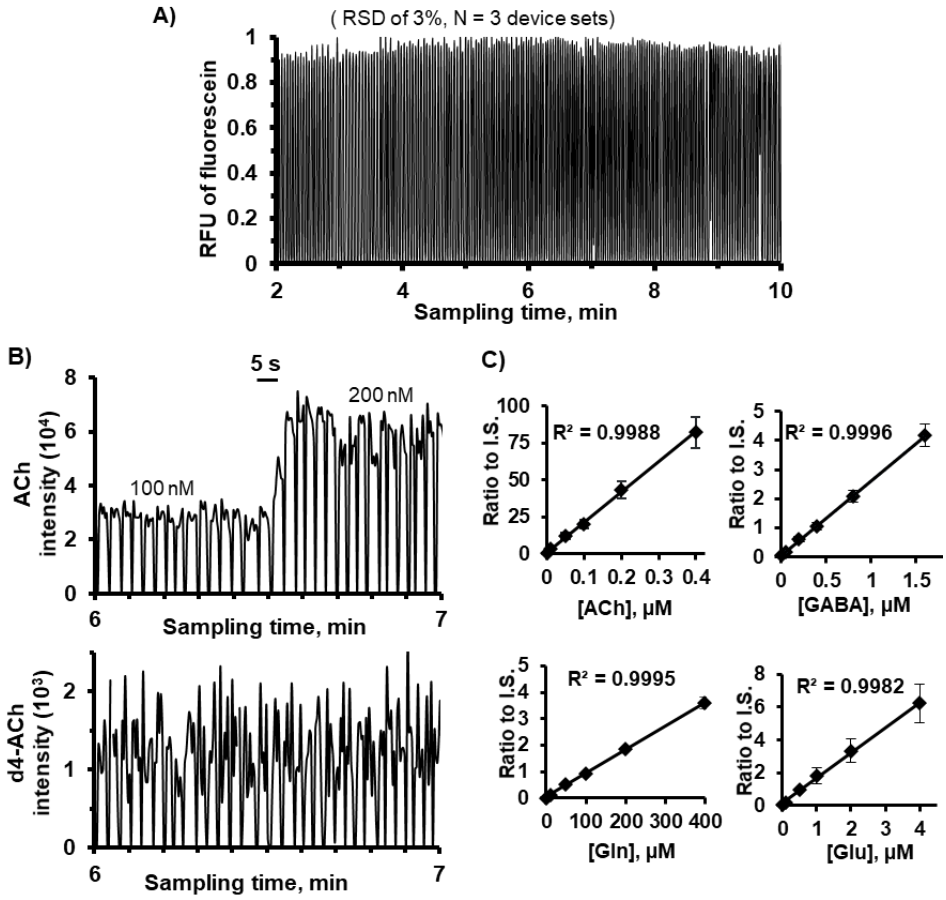

Figure 3.6 In vitro characterization of sampling coupled to segmented flow and reagent addition. Samples were a mixture of standards in aCSF and reagents contained fluorescein and a mixture of internal standards. A) Detection of for fluorescein in droplets yielded peak heights with RSD of 3% (n = 3 device sets). An example of a step change of ACh during switching concentration is shown in (B) along with related I.S. added at the same period. C) Calibration curves from ratio of signal traces of standards to internal standards. Linear calibration curves were achieved.

In this work, we selected to study 4 physiologically important neurochemicals: Gln, Glu, GABA and ACh. Temporal resolution and sensitivity of the method were characterized in vitro by sampling from a stirred vial of a mixture of the 4 analytes in aCSF. An example of droplet analysis for monitoring ACh is illustrated in Figure **3.6**B. As shown in the inset, a rise time during concentration change was observed within 2 droplets (~6 s resolution) at a perfusion rate of 100 nL/min. This rise time was in agreement with the above fluorescent result using the tee for flow segmentation only. Hence, the temporal resolution was not limited by the reagent addition as well as the MS assay. Using signal to noise ratio of 3, the

limit of detections (LODs) were found to be 140 nM for Gln, 95 nM for Glu, 35 nM for GABA, and 2.5 nM for ACh. The LOD of ACh was comparable to our previous report[163]. Nevertheless, in this work, nanospray ionization was used to enhance sensitivity, allowing analysis of much smaller sample volume (i.e., 5 nL droplets as compared to 160 nL droplets). Further, more analytes were measured in this study (i.e., 8 analytes as compared to 4 analytes). The MS assay used here also did not require desegmentation of aqueous fractions prior to analysis[163,167]. Overall, the coupled system provided sufficient sensitivity and was robust, simple, and suitable for in vivo studies.

In vivo monitoring of neurotransmitter dynamics

The integrated system (microfabricated push-pull probe with microinjection, droplet-based chip with addition of I.S., and direct infusion MS assay) was used for in vivo neurochemical monitoring. In these in vivo studies, sampling flow rates were performed at 100 nL/min as a means to better temporal resolution. Another purpose was to test feasibility of a relatively higher flow rate for in vivo low-flow push pull perfusion, which has not been previously reported[72,73]. At the perfusion rate of 100 nL/min, the in vitro recoveries of the probe were measured to be 83 ± 3%, 47 ± 10%, and 18 ± 7% (n = 5) by sampling fluorescein in a stirred vial, a non-stirred vial, and a 0.6% agarose gel[225], respectively. To demonstrate the capability of the system for detection of rapid chemical changes, switching of the push flow to a microinjection of high K^+-aCSF solution was performed to stimulate neurochemical releases in striatum. In this work, to minimize tissue damage[226], microinjection was achieved at a low flow rate (i.e., 100 nL/min) as opposed to a typical high flow rate stimulation (i.e., short puff at over 1.5 µL/min[73,165]). As shown in Figure **3.7**, microinjections of the high

potassium solution evoked release of all the four analytes. For the first injection, the changes at peak maximum from the baselines were 540 ± 140% for Gln, 860 ± 410% for Glu, 1800 ± 1200% for GABA, and 640 ± 320% for ACh (mean ± SEM, n = 4 animals). Neurochemical levels returned to their baselines after switching the flow back to a regular aCSF. For the subsequent injection, the average increases were 460 ± 160% for Gln, 340 ± 140% for Glu, 850 ± 440% for GABA, and 330 ± 110% for ACh. The percentages of increase in Glu were reasonably comparable to other previous work (see Table **3.2** for comparison[41,73,89,166,205,227–229]). In addition, substantial effect of potassium stimulation on GABA levels was also in agreement with the previous studies[166,202,205].

The rise time for potassium response was 15 - 20 s. This rise time is slower than the temporal resolution of the monitoring system. The delay in this rise time was due to the use of a syringe pump for microinjections, which typically required at least 5 – 10 s before reaching the desired perfusion rate. Rise times of below 10 s were reported in other work when using a gas pressure-pulse system "Picospritzer"[73,89,165]. Other factors that may also affect to differences in neurochemical response and rise time between this work and others included type of probe, type of anesthesia, position of microinjector, and dose of stimulant. The current work demonstrated utility of the integrated tee with a syringe pump for infusion of a stimulant. Although effective, variability in chemical responses between experiments was observed. We suspected that it was caused by interference between microinjection flow and pull flow. Development of a probe with a spaced shank for microinjection may allow chemical infusion that is more reliable. Our ongoing work is to engineer the probe with different microinjector designs that allow chemical delivery at high-spatially different locations as well as to explore the effect of infusion rates on neurochemical response.

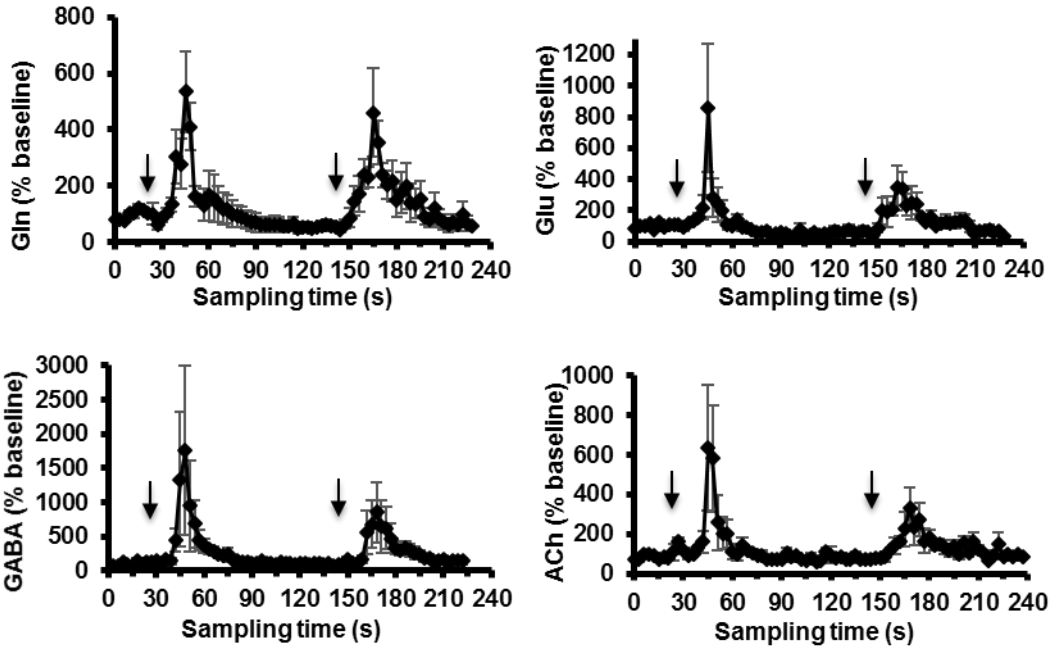

Figure 3.7 In vivo monitoring of response to microinjection of 100 mM K^+ aCSF (infused at 100 nL/min for 1 min) in the rat striatum. Arrows indicate beginning of microinjection. Data are expressed as percentage of baseline (mean ± SEM, n = 4 rats) upon switching to microinjection of high potassium. Responses of glutamine (A), glutamate (B), GABA (C) and acetylcholine (D). Rise times could be observed within 15 - 20 s.

Table 3.2 Comparison of in vivo recording of Glu response to high potassium stimulation.

Ref. #	Probe type	Sampling rate	$[K^+]$	Delivery method	Injection volume	Injector, positioning	Anesthesia	Brain region	Average of number-folds increase at max	Rise time	Assay
This work	µFab PP	0.1 µL/min	100 mM	Syringe pump + microinjection	100 nL	Push outlet, 20 µm spaced	Isoflurane	Striatum	8.6 (1st) 3.4 (2nd)	15 - 20 s	Droplet MS
227	PP	0.05 µL/min	75 mM	Syringe pump + microinjection	500 nL	Push outlet, 75 µm spaced	Chloral hydrate	Striatum	3.3	45 s	CE-LIF
73	PP	0.05 µL/min	70 mM	Syringe pump + microinjection	100 nL	Sharpened glass pipette, 10° to coronal plane, 100 µm spaced	Ketamine + Dexmedetomidine	Striatum	5.0	22 s	Droplet Enzyme-LIF
228	MD (4 mm long)	1 µL/min	100 mM	Syringe pump + reverse dialysis	Continuous	Dialysis membrane	Isoflurane	Cortex	~4	-	CE-ED
41	MD	1 µL/min	60 mM	Syringe pump + reverse dialysis	333 nL	Dialysis membrane	Urethane	Hippocampus	~5	12 - 18 s	CE-LIF
166	MD (2 mm long)	0.3 µL/min	145 mM	Picospritzer + microinjection	200 nL	Fused-silica tubing, glued w/ probe, 1 mm above probe tip, 150 µm spaced	Ketamine + Domitor	Striatum	4.3	9 - 12 s	Droplet CE-LIF
205	MD (0.5 mm long)	0.1 µL/min	75 mM	Picospritzer + microinjection	200 nL	Fused-silica capillary, glued w/ probe, ~0.5 mm above probe tip, 45 µm spaced	Ketamine + Dedetomidine	Striatum	16	10 s	Droplet CE-LIF
89	µFab ceramic electrode array	-	70 mM	Picospritzer + microinjection	133 nL	Sharpened glass pipette, glued w/ probe, 50-100 µm spaced	Urethane	Striatum	2.9	2 s	Amp
		-	″	″	″	″	″	Cortex	4.2	2 s	″
		-	120 mM	″	″	″	″	Striatum	6.7	3 s	″
		-	″	″	″	″	″	Cortex	8.0	2 s	″
229	Enzyme coated carbon fiber electrode	-	120 mM	Picospritzer + microinjection	500 nL	Sharpened glass pipette, ~100 µm spaced	Equitensine	Striatum	1.5	8 s	Amp
		-	″	″	1 µL	″	″	″	2.3	″	″
		-	″	″	2 - 3 µL	″	″	″	4.0	″	″

Abbreviation list: µFab = microfabricated; PP = push-pull; MD = microdialysis; MS = mass spectrometry; CE = capillary electrophoresis; LIF = laser-induced-fluorescence; ED = electrochemical detection; Amp = amperometry

The in vivo experiments illustrated capability of the miniaturized analytical method for high spatiotemporal resolution and multiplexed neurochemical monitoring. Based on these initial studies, a number of improvements are herein discussed for future development. In the course of in vivo experiments, we occasionally observed disturbance of segmented-sampling flow that led to flow blockage or eventual clogging. This flow disturbance may also led to imbalance of sampling flow rates (i.e. pull flow is slower than push flow) that could result in lower-than-expected relative recoveries of analytes. The origin of the cause of flow disturbance is still not clear. Nevertheless, we found that flow disruption was typically initiated at the probe orifices where they were in contact with living tissues. The cause of this disruption might be due to aggregations of cell particulates, blood clot, tissue debris, or glial cells[230]. Future work will involve modification of design of probe orifices in order to mitigate this issue. In addition, it is possible that variations in intracranial pressure (caused by several factors, such as surgery procedure and brain exposure to local room pressure[117]), flow rate of CSF[231,232], and viscosity of sampled fluid[233,234] can affect to flow disruption. Although these variations were not previously reported to be an issue in other push-pull studies[72,73,227], their negative effects on device operation might become significant in miniaturized sampling with segmented flow (i.e., when active sampling area and fraction volumes are extremely small). Further work is required in order to understand these effects. Development and use of integrated, automated pressure controller and flow meter will help to accordingly adjust microfluidic flows and overcome the above issue

Conclusion

In this work, we have demonstrated potential utility of the miniaturized analytical technology that is pertinent to multiplexed monitoring chemicals in living tissues at high spatial and temporal resolution. The spatial resolution of the microfabricated sampling probe is approaching that of a single carbon fiber microelectrode. The temporal resolution of the system is comparable to the state-of-the-art technology for in vivo neurochemical sampling. By microfabrication, an additional channel can also be integrated directly within a probe for microinjection of a stimulant. Besides chemical delivery, this additional channel can be further used for other purposes, such as reagent addition, or flow-segmentation that allows sub-second temporal resolution. Based on similar microfabrication technologies, it is also possible to integrate the probe with other features, such as electrodes for electrophysiological recording and optical waveguides[31,235] for optogenetics. Furthermore, the miniature sampling system or droplet-based microfluidic devices developed in this work are easily amendable to integrate with other microfluidic analytical systems, such as immunoassays[159], enzyme assays[73,236], electrochemistry[219,224], and capillary electrophoresis[166,221] (as also demonstrated in the next chapter). Nevertheless, the direct infusion MS assay provides an effective way to measure multiple neurochemicals in samples with nanoliter volumes. Advances in the assay and instrumentation will also yield better sensitivity as well as allowing simultaneous detection of many more chemicals. Besides in vivo neurochemical monitoring, the technology developed here may also be adaptable to other microenvironments (such as other organs and cultured cells) that require chemical monitoring and drug delivery at high spatiotemporal resolution.

Chapter 4
Microfabricated Sampling Probes Coupled to Droplet-Based Microchip Electrophoresis

Introduction

Sampling methods are versatile for studying neurochemistry since they can be coupled to a variety of appropriate analytical assays. The assays often require a separation to reduce selectivity demands on the detector. Neurochemicals in brain dialysates or perfusates have routinely been studied using high performance liquid chromatography (HPLC) coupled to detectors such as electrochemical, fluorescence, and mass spectrometric (MS)[37]. In one comprehensive assay, samples were derivatized with benzoyl chloride prior to analysis by HPLC-MS, allowing simultaneous measurement of multiple neurotransmitters and metabolites[45,237]. Although the HPLC-based method is powerful, it has poor temporal resolution as this method typically requires large sample volumes (microliters) and long separation time (minutes).

A more suitable separation method for high temporal resolution monitoring is capillary electrophoresis (CE) or microchip CE. Comparing to HPLC, the CE-based method requires much smaller sample volumes (less than a few hundred picoliters) and resolves neurotransmitters within seconds[71,165]. With the use of high speed CE separation coupled to laser-induced fluorescence (LIF) detection, analysis of a large number of samples collected within intervals of seconds was made possible. In this case, temporal resolution was limited only by broadening of sample zones due to Taylor dispersion[154]. Although using short

connecting tubing helped to mitigate the band-broadening issue[41,156,238,239], it was infeasible for experiments in awake animals or in clinical settings. A preferable approach to address the zone broadening issue is to use segmented flow or droplet microfluidics. As demonstrated in Chapter 3 and other previous reports[73,159,166], droplet microfluidics has proven to be an effective approach to preserve temporal resolution from sampling and to manipulate large numbers of small volume samples.

Our group has previously reported utility of microchip CE coupled to droplet-based sampling for monitoring neurochemical dynamics[165,166,240]. In these systems, sample droplets were extracted ("desegmented") before electrokinetic-gated injection, providing high separation efficiency (excess of 2×10^5 plates made possible) with good injection reproducibility (~5 - 6% RSD for serial injections). Although these systems were effective, there were still limitations. First, for flow desegmentation, the previously developed systems relied on modification of glass surface on the chip. This process involved surface chemistry patterning, which added more complexity to fabrication procedure. Second, the CE chips yielded long separation times (i.e., 20 – 50 s), which could limit temporal resolution. An offline format may be used to allow droplet analysis without loss of temporal resolution by pumping droplets into the CE chip at a low flow rate[166]. However, this approach had limitation in terms of throughput and flexibility in operational flow rates, restricting its potential use for online or real-time chemical monitoring. Lastly, the previously developed interfaces were primarily intended for use in microdialysis sampling, which inherently had poor spatial resolution. Our goal in this work is to overcome the above limitations.

Here we reported a combination of the microfabricated push-pull probe with compatible droplet-based microchip CE interface for monitoring amino acid neurochemicals

at high spatiotemporal resolution. Using a 5-way PDMS manifold, samples were collected from the microfabricated probe, segmented, and simultaneously derivatized with naphthalene-2,3-dicarboxaldehyde (NDA) and potassium cyanide (KCN). A novel extraction device was consequently developed to allow reliable and robust extraction and transfer of aqueous droplets into microchip CE. The microchip CE developed here enabled rapid separation (< 3 s) of multiple amino acid neurochemicals. The integrated system was proven to be suitable for multiplexed neurochemical measurement, providing ~11 s temporal resolution at a sampling rate of 50 nL/min.

Experimental

Chemicals and materials

Unless otherwise specified, all chemicals were purchased from Fisher Scientific (Fairlawn, NJ) or Sigma Aldrich (St. Louise, MO) and were certified ACS grade or better. Solutions were prepared with HPLC-grade water or water purified by a Milli-Q system (Millipore, MA). Teflon HPFA tubing were purchased from IDEX Health & Science (Oak Harbor, WA). Fused silica capillaries were purchased from Molex (Phoenix, AZ). Epoxy glues were purchased from Loctite (Westlake, OH) for regular 5-min Epoxy, and ITW Devcon (Danvers, MA) for 5-min Epoxy (gel-type) and 2-Ton Epoxy. Polydimethylsiloxane (PDMS) was purchased from Curbell Plastics (Momentive® RTV 615, Livonia, MI). Artificial cerebrospinal fluid (aCSF) contained 145 mM NaCl, 2.68 mM KCl, 1.01 mM $MgSO_4$, 1.40 mM $CaCl_2$, 0.45 mM NaH_2PO_4, and 1.55 mM Na_2HPO_4, adjusted to pH of 7.4 with 0.1 M NaOH. NDA was purchased from Life Technologies/ Invitrogen (Carlsbad, CA). Glass slides with chrome masks were purchased from Telic (Valencia, CA).

Microfabricated probe and holder

Microfabricated push-pull probes were fabricated using the same method, as previously described in Chapter 3. In this work, backside of the probes was further etched in order to yield thinner probes. The final probes had a dimension of 11 mm long, 83 µm wide, and ~50 µm thick (Figure **4.1**). The fluidic capillary connected to the probe port for pull flow was 2 cm long of 40 µm i.d. / 150 µm o.d.

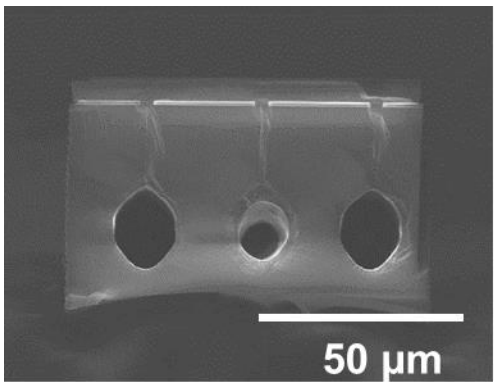

Figure 4.1 Thin microfabricated push-pull probe

A probe holder was used to handle and plumb the probes to connection tubing. A design and procedures to microfabricate the holder were similar to what described previously[115]. Alternatively, as a means to reduce time and cost of fabrication, probe holders were fabricated using a 3D printer, 3D System's Projet 3500 HD Max (Rock Hill, SC). The bio-compatible, acrylic-based resin ("M3 Crystal") was used for printing the devices. The printer provides the xyz resolution between 16 - 32 µm layers with the accuracy of 25 – 50 µm per inch of part dimension. For post-processing, the printed parts were soaked in soapy water at 60 °C overnight, rinsed with water while sonicating, and air-dried.

Sample derivatization

NDA in excess CN^- was used as a fluorescent tag for amino acid neurochemicals. Reagent and buffer solutions were prepared using procedures based on the previous reports[165,205], with slight modifications. Methanol was used as a solvent for NDA instead of acetonitrile in order to form more stable droplets. Buffer used for preparing the reagents was 20 mM sodium tetraborate, 0.9 mM hydroxyproply-β-cyclodextran, pH = 10. NDA solution (10 mM) was prepared in a 50:50 mixture (v:v) of methanol and the buffer. Excess CN^- was prepared using potassium cyanide (20 mM) with 0.5 M EDTA in the buffer.

Flow segmentation and reagent addition

A 5-way PDMS manifold was coupled to microfabricated probes for flow segmentation and simultaneous addition of two reagents. The PDMS chip was fabricated using the procedures described in Chapter 3, with slight modifications in device design and channel size. In this work, the 5-way junction was designed for 1) sampling, 2) flow segmentation, 3 & 4) addition of 2 reagents, and 5) droplet collection. At the junction for droplet generation, the channel size was 100 µm wide × 100 µm tall. The overall scheme of the system is illustrated in Figure **4.2**A.

The first inlet of the chip was attached to a fluidic capillary of the sampling probe. The second inlet was connected to a 3 cm length of 50 µm i.d. capillary which was placed in a vial containing 50:1 (v:v) solution PFD:PFO for flow segmentation. The third and fourth inlets were attached to 9 cm length of 20 µm i.d. capillaries placed in vials of reagents. The fifth inlet of the manifold was connected to a 3 cm length of 150 µm i.d. / 360 µm o.d. Teflon

tubing (fixed tubing). This fixed tubing was connected to another 30 cm length of 150 µm i.d. / 360 µm o.d. Teflon tubing (removable tubing) via a PDMS union. Pull flow was achieved by applying a -130 mmHg vacuum to the outlet of thee Teflon storage tubing, providing a sampling rate of 50 nL/min. For push-pull perfusion, push flow with desired flow rate was performed using a syringe pump. The push flow rate was validated using a flow meter while the pull flow rate was monitored by measuring droplet frequency and size. Using the described system, ~3 nL aqueous droplets were generated. Based on flow resistance of the inlet capillaries, mixed reagents were added at 30% of total aqueous droplet volume and volume ratio of aqueous to oil was ~1:3.

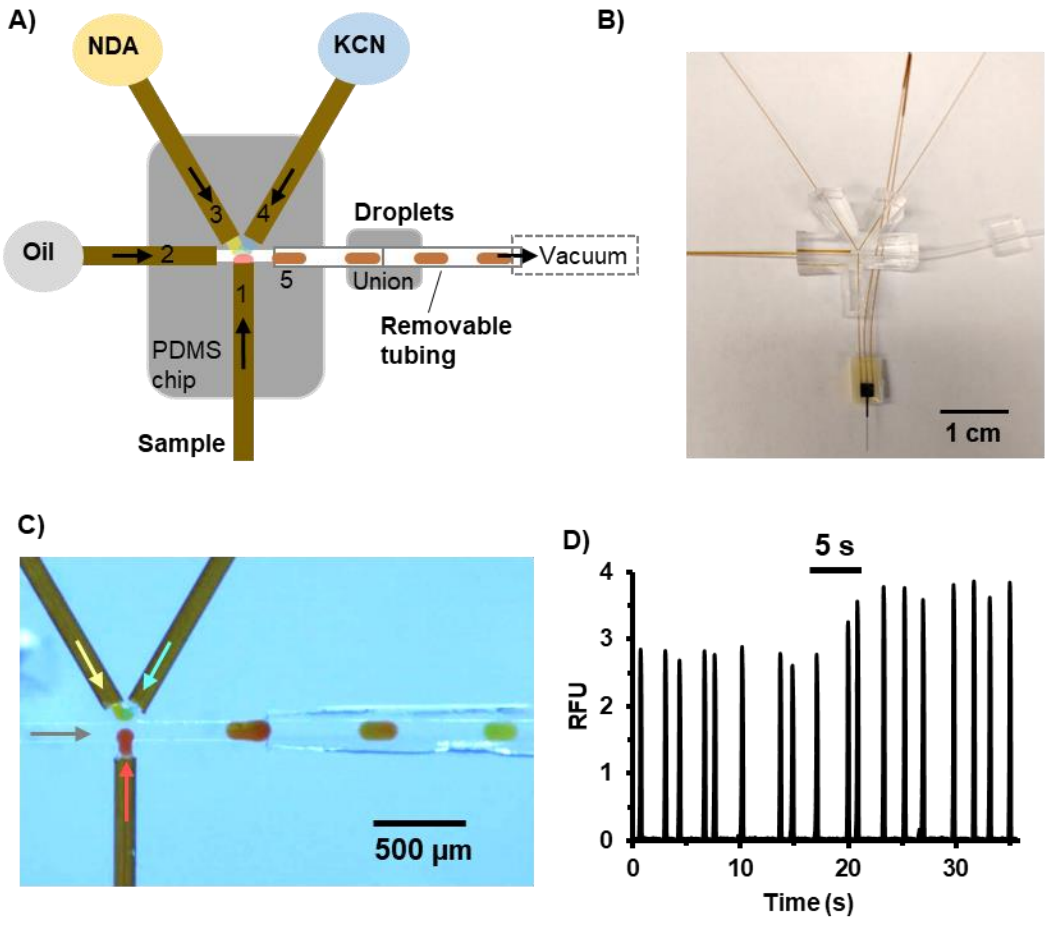

Figure 4.2 A) Illustration of the droplet generator with reagent additions, driven by a vacuum (the image was not drawn to scale). B) A photograph of the manifold connected to a microfabricated push-pull probe. The

holder was made by 3D-printing. C) An experiment with food dyes was performed to aid visualization. When sample was switched from a blank to red dye, color change was observed within 1 - 2 droplets (D) Switching of Glu concentration, resulting in a rise time of ~3-5 s at a sampling rate of 50 nL/min.

To initially test temporal resolution of the system, the microfabricated probe was coupled to the PDMS manifold for flow segmentation and addition of NDA and KCN This system was used for sampling of glutamate standard in aCSF solution in a stirred vial. The solution was then switched from 2 µM to 4 µM. Offline analysis of derivatized droplets were performed using the LIF detection system described below.

Fabrication of a Teflon -based device for droplet extraction

Passive droplet extraction was accomplished using a hybrid of Teflon and fused silica. A schematic of fabrication procedure for the Teflon device is shown in Figure **4.3**. The fabrication method was based on drilling Teflon PFA tubing and sealing with PDMS chip. A 100 µm wide × 100 µm tall PDMS tee, "Tee I", was fabricated using soft lithography techniques. As the Teflon tubing was small and extremely slippery, this tee was used to fasten and secure the Teflon tubing prior to drilling. A 4 cm long of 150 µm i.d./ 360 µm o.d. Teflon tubing was reinforced with 150 µm o.d. polyimide-coated fused silica capillary prior to insertion into the PDMS tee (Figure **4.3**A). The PDMS tee with inserted Teflon tubing was placed on a flat glass slide for support. A 150 µm diameter drill bit (Kyocera Tycom, Costa Mesa, CA) was used to extend a 150 µm hole through the wall of fixed Teflon tubing (Figure **4.3**B). After drilling, another 150 µm o.d. fused silica capillary was inserted into the extended hole to ensure straight and through drilling (Figure **4.3**C). The 150 µm capillaries were then slid back and forth through the drilled hole in order to remove debris. The Teflon tubing with drilled hole was removed from the Tee I and inserted into a new and clean PDMS tee, "Tee II" (Figure **4.3**D). To facilitate insertion of 360 µm o.d. Teflon tubing while accommodating

proper sealing with connection to 150 µm o.d. extraction capillary, the PDMS Tee II was designed to have cylindrical channels of 220 µm i.d. intersected with 100 µm i.d. (220 µm channel fitted with 360 µm o.d. tubing while 100 µm channel fitted with 150 o.d. capillary). This PDMS tee was fabricated using a pour over method previously described[221]. After insertion of the Teflon tubing into the 220 µm inlet of Tee II, the extended hole was aligned with the 100 µm inlet prior to removal of the reinforcing capillary. The final Teflon device is illustrated in Figure **4.3**E. For droplet extraction, the Teflon device was connected to a fused silica capillary attached to the CE chip.

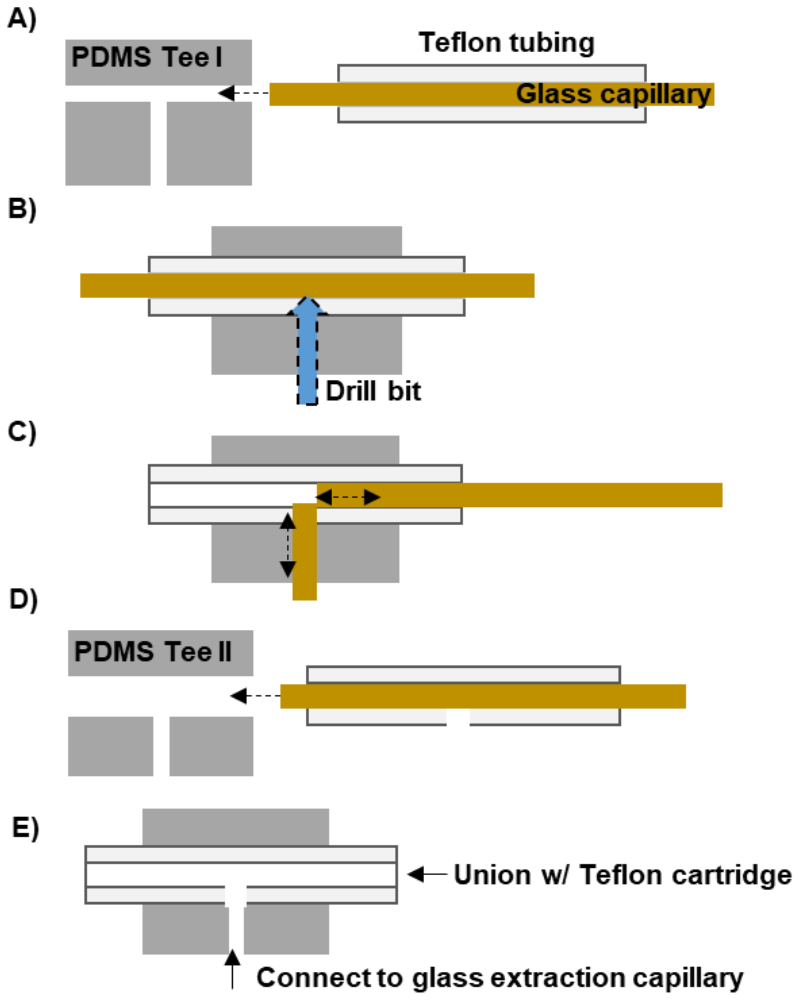

Figure 4.3 Fabrication of a Teflon-based device for droplet extraction. A) Insert Teflon tubing into "Tee1", B) Drill a 150 µm diameter hole on Teflon tubing, C) Clean debris, D) Insert the tubing into "Tee 2". All the procedures were carried out under a microscope. "Tee 1" was used to hold Teflon tubing in place and aid the

drilling process. Fused-silica capillary was used to reinforce Teflon tubing and protect the tubing wall from damage. “Tee 2” was used to seal the device and align drilled Teflon tubing with the fused-silica extraction capillary that was attached to the CE chip (Figure **4.4**A).

Microchip electrophoresis

A design of the CE chip is shown in Figure **4.4**. Glass CE chips were fabricated using lithographic patterning and HF wet etching. Fabrication of glass CE chips was described in detail elsewhere[221]. Briefly, one glass slide was etched to 100 μm for insertion of extraction glass capillary. A second glass slide was etched to 100 μm for extraction capillary insertion and 3 μm for all channels. Separation channel was 3 cm long, 36 μm wide × 3 μm deep. Access holes were then drilled with a 500 μm drill bit (Kyocera Tycom, Costa Mesa, CA) before sonicating the glass slides in water for 30 minutes for debris removal. Photoresists and chrome masks on the glass slides were then stripped off prior to piranha and RCA cleaning processes. Slides were then triple-rinsed with water. The two slides were sandwiched and their channels for insertion of extraction capillary were aligned under a microscope. The chips were baked at 80 °C for 3 hours, inspected for defects, and annealed at 610 °C for 8 hours. Reservoirs and ports (IDEX Health and Science, Oak Harbor, WA) were attached above the access holes using 2-Ton Epoxy. A side of the glass chip was polished so that the channel for inserting extraction capillary were 0.5 mm long. A 2 mm long of 30 μm i.d. / 150 μm o.d. glass extraction capillary was inserted into the insertion channel and waxed in place.

Prior to use, all reservoirs and channels were filled with electrophoresis buffer (10 mM sodium tetraborate buffer with 0.9 mM hydroxyproply-β-cyclodextran, pH = 10) and all air bubbles in the chip were removed. Voltages were applied using power supplies (Spellman, Hauppauge, NY) with a high-voltage relay (Kilovac, Santa Barbara, CA) for performing electrokinetic-gated injection[241] (+7 kV and -9 kV, with injection time between 30 to 50 ms). Detection of derivatized amino acids was done on-chip via confocal laser-induced

fluorescence at the end of separation channel. 440-nm line from a 10 mW solid-state laser (CrystaLaser, Reno, NV) directed through a 436 ± 10 nm band-pass filter was used for excitation. Emission was filtered through a 490 ± 10 nm band-pass filter and detected by a photon counting detector (Thermo Oriel, Stratford, CT). Voltage supply, high-voltage relay time, sample injection time, peak integration time, and data collection were controlled by an in-house LabVIEW program (National Instruments, Austin, TX). Data was analyzed using Cutter 7.0[222], Excel 2013 (Microsoft, Redmond, WA), and Matlab (R2016a, MathWorks, Natick, MA).

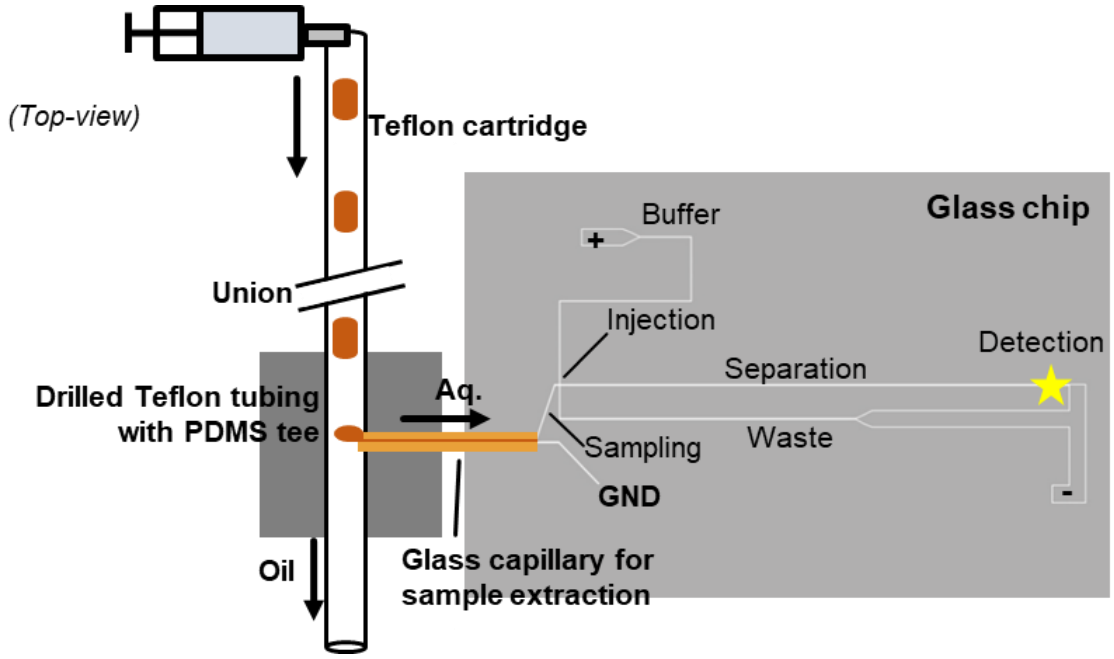

Figure 4.4 Schematic of droplet extraction device coupled to microchip CE

In vitro characterization

The probe coupled to the PDMS manifold was dipped into a vial of aCSF containing standard solution of amino acid mixtures, including γ-aminobutyric acid (GABA), arginine (Arg), aspartate (Asp), glutamate (Glu), glutamine (Gln), glycine (Gly), serine (Ser), and

Taurine (Tau). In this study, fluorescein was also added into a reagent vial of KCN (the final concentration of fluorescein in the vial was 10 µM) for quantification of the percentage of reagents in droplets. Step changes of standard solutions were made via pipetting while the solution was rapidly stirred. After collection of derivatized droplets, offline analysis of droplets was performed by connecting the Teflon storage tubing to the hybrid device for droplet extraction-CE using a PDMS union. The other end of the Teflon tubing was connected to a syringe pump. Droplets were pumped into the analysis chip at 170 nL/min, yielding 1 electropherogram per ~1 droplet.

Results and Discussion

Thinner probe

Microfabricated push-pull probes has allowed chemical monitoring at high spatial resolution and have potential for minimizing tissue damage[115]. In this work, we further explored applicability of thinner probes to sampling. As shown in Figure **4.1**, the thickness of these probes was smaller than that of previously reported microfabricated push-pull probes[115] (i.e. 50 µm versus 70 µm). The probe contained three 11 mm long buried channels of ~15 - 17 diameter, which encompassed with 25 µm thick top wall and 5 µm thick bottom wall. Side-walls were 10 µm thick for the first and second channel, and 4 µm thick for the third channel. Connecting the probe inlets with fluidic capillaries to a syringe pump, water perfusion was achieved up to 2 µL/min (higher flow rates were not attempted) with no failures or wall ruptures (n = 4). This result indicated that 4 - 5 µm wall thicknesses were sufficiently strong for device operation at high flow rates. It also suggested possibility for future development of smaller probe designs. Based on the above results and estimation of

microchannel back-pressure (i.e., ~30 psi), 5 µm wall thickness should be suitable for aqueous perfusion through a 5 mm long channel of 10 µm diameter at a flow rate of 500 nL/min. With these dimensions of channels and walls, sampling probes containing two channels can be made as small as 35 µm wide × 20 µm thick. The potential to develop such tiny probes will lead to accessibility of chemical monitoring in small brain regions and reduce tissue damage during probe insertion that may confound measurements[74].

Sample derivatization and on chip reaction with flow segmentation

NDA reaction was used for derivatization of amino acids in samples because this reaction yields stable fluorescent adducts with high quantum efficiency and reasonably fast reactions (i.e., less than 6 min.)[242,243]. In this work, methanol was selected to be used as a solvent for NDA instead of acetonitrile[166,205]. This was because our initial tests using a tee for reagent addition indicated that use of methanol yielded a more stable droplet formation (see Figure **4.5**). On the other hand, acetonitrile-contained droplets tended to drag along the surface of PDMS chip during droplet breakoff, leading to improper reagent addition as well as droplet coalescence. We then tested the amino acid-NDA reaction using a microplate fluorimeter and found no difference in terms of fluorescent signals and reaction kinetics when methanol was used as a solvent, as compared to acetonitrile results (n = 3; data not shown). We also confirmed that the reaction was completed within 6 min, which was in agreement with our previous report[165]. Therefore, methanol was a suitable solvent for use in this study.

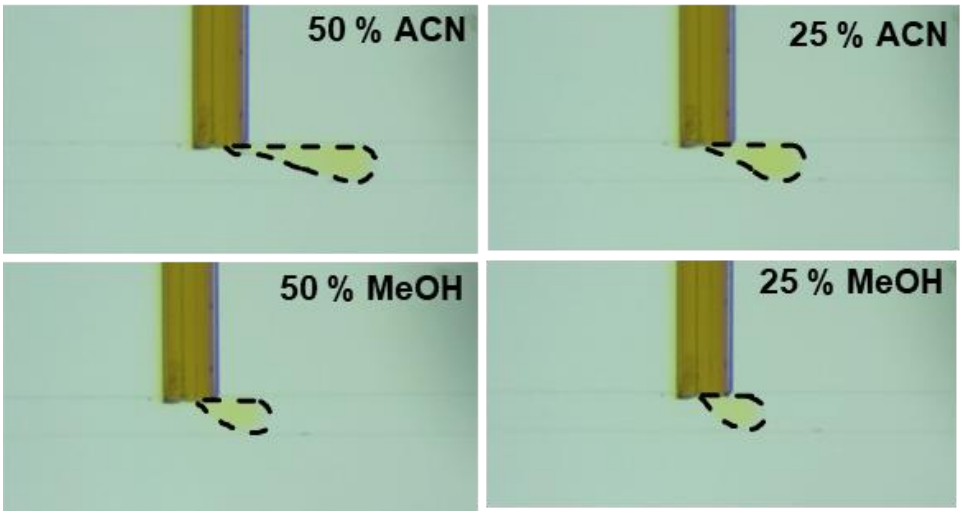

Figure 4.5 Effects of organic solvent contents on droplet formation

As illustrated in Figure **4.2**, a 5-way PDMS manifold was utilized for simultaneous flow-segmented sampling and reagent addition of NDA and CN^-. Fused silica capillaries, which inserted into the manifold, were utilized as channels for reagent delivery. Use of the fused silica capillaries for reagent additions was necessary as their hydrophilic surface accommodated droplet formation with uniform composition[166]. As discussed in Chapter 3, flow rates of each solution were regulated based on flow resistance of each capillary while a constant vacuum was applied at the end of the Teflon storage tubing. The system used in this study was designed to add a mixture of reagents to samples at 30% of total volume. Droplets were generated at ~1:3 aqueous: oil volume ratio. The 100 µm PDMS junction produced a train of aqueous droplets with fraction volume of ~3 nL prior to collection in a removable 30 cm long, 150 µm i.d. Teflon storage tubing. Based on the above parameters, at a sampling rate of 50 nL/min, a mixture of reagents was added at 22 nL/min while oil flow rate was 231 nL/min. With the total flow rate of 303 nL/min, a 30 cm long of 150 µm i.d. Teflon storage tubing (total volume of ~5 µL) allowed ~17 min of droplet collection time. Since this transit

time was longer than the 6-min reaction kinetics, completion of the NDA reaction with amino acids was ensured prior to the subsequent assay. The relatively large oil spacers (as compared to what used in Chapter 3) were used to accommodate speeds of droplet extraction and CE separation.

Precipitation with the NDA reaction is often a problem[165,242]. Our initial tests in a vial or a microplate indicated that precipitates started forming at about 10 min after mixing the NDA with CN^- reagents. To prevent this problem, the on-chip system was designed to mix NDA and CN^- solutions just immediately before their addition to amino acid samples. Next, we found that having sufficient amount of amino acids in samples was necessary to avoid precipitates because the amino acid adducts helped to stabilize the reaction mixture. Finally, we also observed that use of the droplet system mitigated the precipitation issue, as opposed to the reaction with continuous phases. We believed that this was due to 1) oil carrier phase protected the walls of the device from reagent adsorption and eventual accumulation of precipitates, and 2) steady recirculating flow within droplets facilitated fast and consistent mixing during droplet moving[244]. With all these considerations (mix reagents freshly, add sufficient amounts of amino acids into samples, and use on-chip segmented flow), derivatized droplets were consistently generated with no precipitates over a long period (stable for at least 2 h).

Test of temporal resolution

In this work, we used a relatively small dimensions of fluidic capillary (2 cm long, 40 μm i.d. versus 5 cm long, 50 μm o.d. used in the previous chapter) to demonstrate potential for improved temporal resolution at low flow rate (i.e., 50 nL/min). Tests of temporal

resolution were performed by using the probe-manifold system for segmented flow sampling of Glu and addition of the derivatizing agents. As shown in Figure **4.2**D, a step change in Glu concentration was observed within 1 - 2 droplets at a sampling rate of 50 nL/min, corresponding to 3 - 5 s temporal resolution.

Droplet extraction

Prior to droplet analysis by microchip CE, flow desegmentation was required in order to remove the carrier phase (i.e., fluorinated oil) from the droplet stream because the oil phase was non-conductive and interfere with the assay. This process could be achieved in a passive approach, which relied on surface chemistry and pressure balance of channels for extraction. To elucidate working conditions, a channel with hydrophilic surface was used for extraction of aqueous phase while a hydrophobic channel was used for extraction of oil phase. Proper design and selection of channel dimensions were also critical to balance capillary force and backpressure for favoring reliable extractions. In our previous reports[165,166,205], droplets were extracted across a shallow "extraction bridge" connected to the CE chip. This extraction bridge was fabricated by silanization of a microfabricated glass channel. However, this surface-patterning step was laborious and the hydrophobicity of the surface diminished over time. An alternative and simpler approach was to use a hybrid device containing channels with different native properties, e.g., glass (hydrophilic) for aqueous extraction and PDMS (hydrophobic) for oil extraction[221].

We initially explored several designs and configurations of a hybrid interface made of a network of PDMS channel and a fused silica capillary, similar to that described previously[221]. However, we often experienced an issue with surface fouling of PDMS,

resulting in unreliable droplet extraction. Especially for extraction of aqueous mixtures that contained an organic solvent, we found that the device stopped functioning only after a few minutes of use. Consequently, we developed a droplet extraction device based on a 150 µm i.d. Teflon tubing, as shown in Figure **4.3**. In this device, a drilled hole on the Teflon tubing was aligned with a fused silica capillary that was attached to the glass CE chip using a PDMS tee (Figure **4.3**E & Figure **4.4**A). Through experimentation, proper dimensions of the device interface were found to be 2 – 2.5 mm long of 30 µm i.d. fused silica capillary for aqueous extraction, and 5 - 7 mm long at the end of 150 µm i.d. Teflon tubing for oil extraction. With these ranges of dimensions, pressure resistance in each tubing was balanced so that reliable droplet extraction were attained (i.e. entire aqueous droplet enter glass capillary only while entire oil droplet enter Teflon tubing only). Figure **4.6** shows an illustration and an example of droplet extraction. Furthermore, due to stability and non-adhering property of the Teflon surface, droplet extraction was stable over 3 - 4 h without interruption. Longer times may be possible; but, were not attempted.

The extraction system developed in this work provided a convenient way to reliably separate aqueous phase from oil phase prior to CE injection. Due to superiority of the Teflon PFA surface, the Teflon device could also be reused for many experiments. With optimized tubing dimensions discussed above, this extraction system facilitated use of a wide range of droplet flow rates (tested from 90 to 3000 nL/min). Therefore, this system might be suitable for incorporating into different types of microfluidic analytical systems that require phase separation (e.g., droplet-based CE for neurochemical monitoring[162,165] or high-throughput analysis[221,245,246], and droplet-based (MALDI)-MS for complex protein analysis[247]).

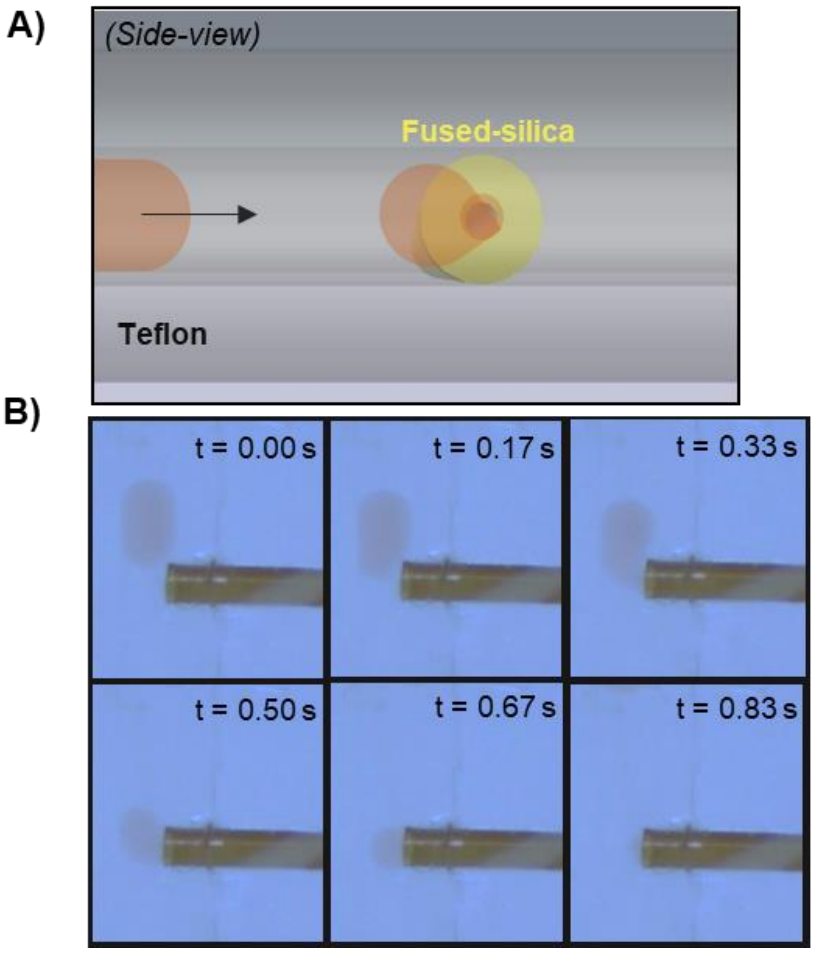

Figure 4.6 A) Illustration of a side-view of the Teflon-fused-silica interface for droplet extraction. B) An example of droplet extraction, series of images showed extraction of aqueous droplets when it contacted the fused-silica surface.

Microchip CE

After droplet extraction, aqueous samples filled the glass extraction channel before directing towards the sampling channel and the injection cross of the CE chip by electroosmotic flow (EOF) using applied electric field, as illustrated in Figure **4.4**. A cross buffer flow connected to high positive voltage through a relay was used to gate the sample stream towards a waste reservoir and to provide fresh separation buffer. The gaiting flow was then momentarily shut off by switching the relay, allowing a small volume of sample to be

injected into the separation channel. In this approach, the extraction channel served as a reservoir for supplying samples to the CE inlet. The small volume of the extraction channel (i.e., < 2 nL) allowed each droplet to completely fill it and wash the previous plug prior to serial injections.

In this work, we attempted to further push the limit of separation time by using a microchip CE with small (36 μm wide × 3 μm deep) and short (3 cm long) separation channel. This shallow channel efficiently dissipated the heat, accommodating application of remarkably high electric field at 2652 V/cm. By using 10 mM sodium tetraborate buffer at pH 10, a separation of less than 3 s with adequate separation efficiency and reproducible injections (peak height RSD of below 6 % for 50 serial injections) was routinely achieved for separation of 8 amino acids and fluorescein dissolved in aCSF. An example of the rapid separation is shown in Figure **4.7**A. With optimization of the injection and integration times, LODs were typically 100 – 200 nM for amino acids. Comparing to our previously-reported microchip CE for monitoring amino acid neurochemicals[165,166,205], the microchip system developed here provides significant improvement in separation time. This improvement will allow droplet analysis at higher throughput, and open more possibilities for multiplexed neurochemical monitoring at high temporal resolution. Future improvement in efficiency may be performed by using a higher electric field, which is currently limited by the effect of Joule heating in the CE channel and arcing at electrodes occurred when high voltage applied. Development of an on-chip cooling system and better insulator for electrode would mitigate the mentioned limitation.

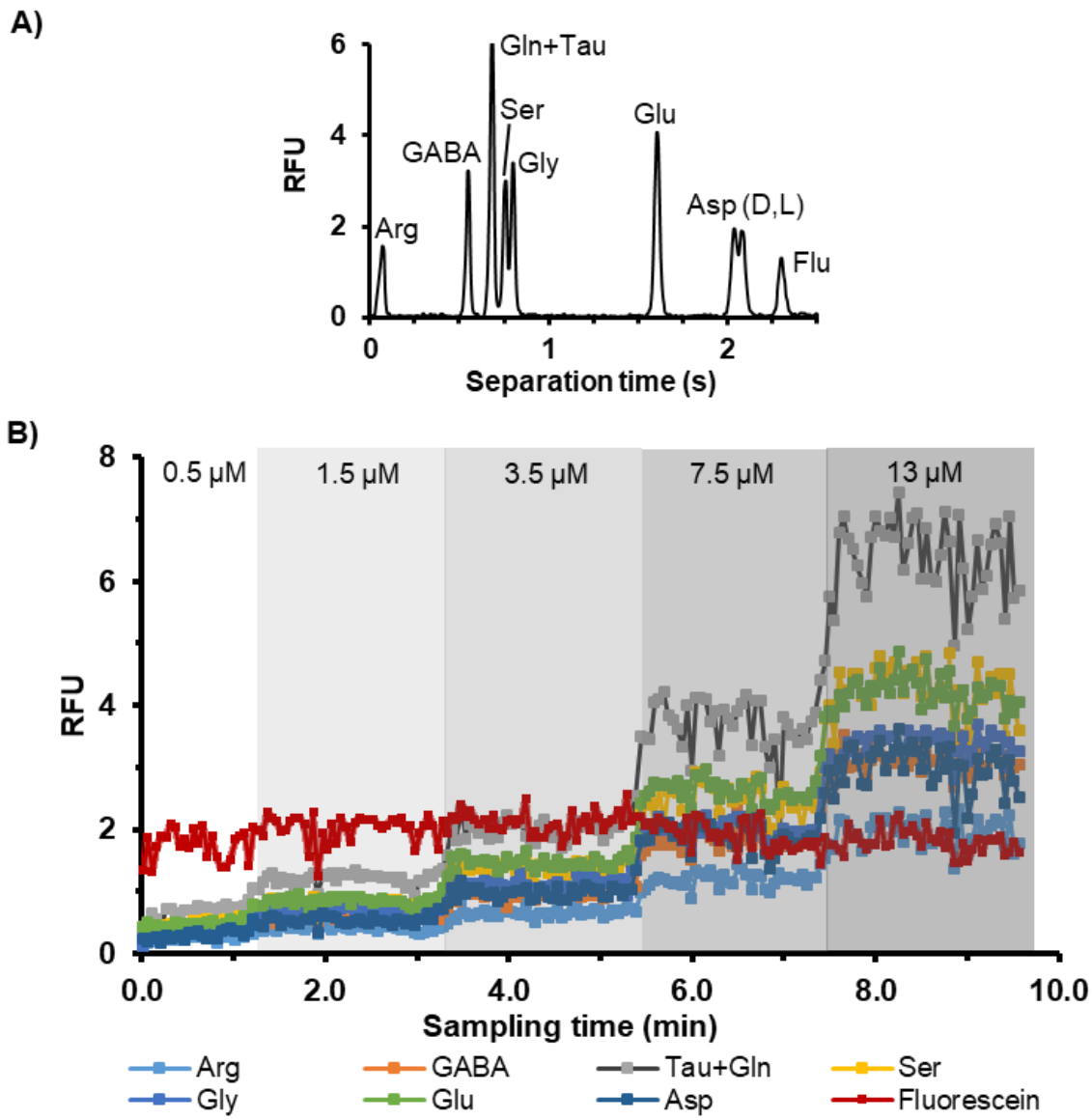

Figure 4.7 A) an example of electropherogram for separation of fluorescence-labelled amino acids and fluorescein. B) In vitro monitoring of neurochemical dynamics. The integrated system was used for sampling, flow segmentation, reagent addition, droplet extraction, and microchip CE analysis.

In vitro characterization

To demonstrate suitability of the integrated system, we monitored rapid changes of a mixture of amino acid neurochemicals in vitro. In this study, fluorescein was added with a reagent for quantification of the percentage of reagents in aqueous droplets. In an offline format, a collected droplet train was pumped into the extraction-CE device at a flow rate of

170 nL/min, allowing one aqueous droplet to be extracted at ~4 s (3.2 nL aqueous droplet with 9.6 nL oil spacer). Consequently, approximately one electropherogram could be observed per an extracted droplet using 4 s interval time between CE injections. Figure **4.7**B showed peak heights of each separated compound from serial injections. Based on the average of peak height values of fluorescein, the reagents were added at 34% of the total volume. These values fell within the expected range as the device was designed to add reagents at 30% of the total volume. Using the integrated system, over 200 sample droplets could be successively analyzed. Peak height RSDs ranged from 6 – 10 % (e.g., 6.1 ± 1.4 % for Glu, 7.5 ± 1.5 % for GABA, and 8.7 ± 1.6 % for Arg, n = 3 device sets; at least 30 samples each). The variation in peak RSD might be caused by differences in dissociation constants and NDA interactions.

As compared to the previous reports[165,240], the slightly higher RSD in this study was likely due to the use of lower flow rate in each step (i.e., 72 nL/min versus > 600 nL/min for sampling with reagent addition; and 170 nL/min versus > 2000 nL/min for droplet extraction). The lower flow rate used during sampling could lead to less stability in droplet formation as droplets had greater chance of dragging along the PDMS chip's surface. For droplet extraction, the lower flow rate used, the smaller sample volume filling the gap between extraction capillary and separation channel during sample accumulation time. This factor might generate a less uniform concentration zone of sample at the inlet of separation channel, leading to less reproducible injections[248]. In spite of that, the resulting RSD values were reasonable, considering every analytical steps involved from sampling to detection. Linear calibration curves corresponding to the experiments were achieved for all compounds (Figure

4.8), demonstrating that the integrated system could potentially be adapted for in vivo neurochemical monitoring.

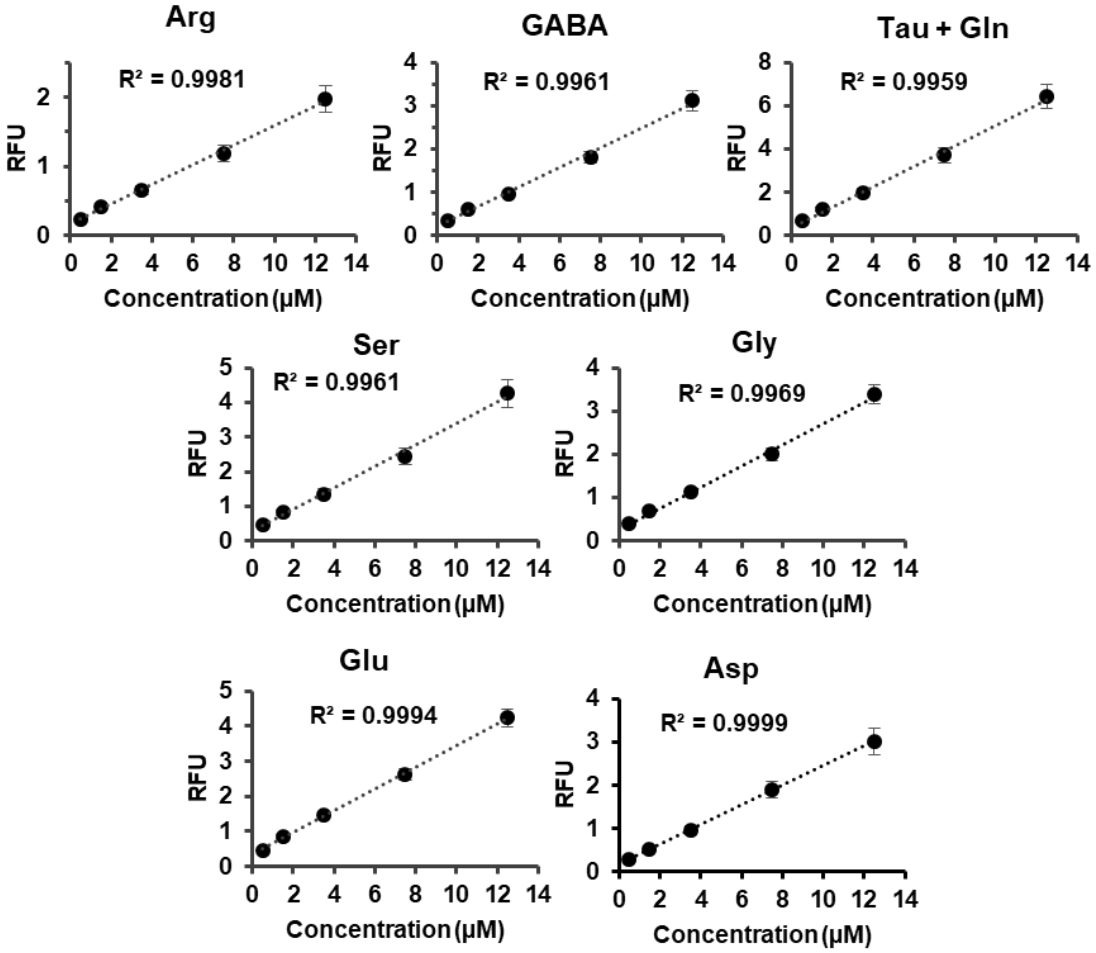

Figure 4.8 Calibration curves resulting from Figure **4.7**B. Each point was an average of ~30 samples with a standard deviation as the error bar.

During switching concentrations of amino acids, 10% to 90% step changes were observed within 4 - 5 electropherograms, corresponding to 11 - 13 s rise time at a sampling rate of 50 nL/min with reagent addition rate of 22 nL/min. This resulting rise time was slower than what expected (i.e., < 5 s resolution when test the system without droplet extraction-CE device). This meant that the further loss in temporal resolution occurred after

sample extraction. We suspected that the delay in rise time was due to a dead volume at the CE inlet (see Figure **4.9**). This dead volume could lead to further diffusion and mixing during sample transfer prior to CE injections. Modification of the chip design to minimize the dead volume will mitigate this issue. Nevertheless, the integrated system overall worked reliably, and still yielded adequate temporal resolution.

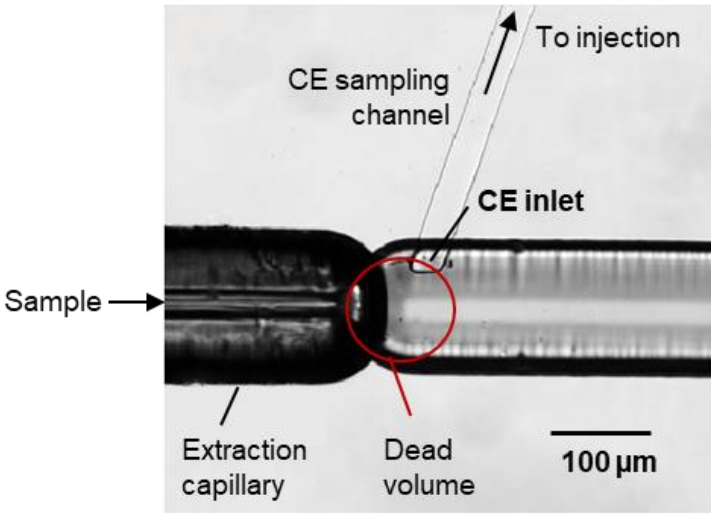

Figure 4.9 Dead volume at the CE inlet caused diffusion and mixing prior to CE injection. This dead volume led to further loss of ~8 s.

Based on these initial results, several improvements are discussed for future development. In the course of these experiments, we experienced some difficulties that should be addressed. The microchip CE-based method had low tolerance of air bubbles. The CE chip can stop functioning when air bubbles entered the separation channel. Large air bubbles (e.g., > 5 nL) can also adversely alter balanced pressure at the extraction tee, leading to improper droplet extraction. Although careful considerations of the procedures to avoid or remove trapped bubbles were performed during preparation of any reagents and solutions, connection tubing, and chips, we still occasionally observed the presence of air bubbles

within the system. Future implementation of the integrated device for bubble removal would be helpful to solve this problem[249,250]. As the CE chip contained an extremely small channel (i.e., 36 μm wide × 3 μm deep), it was susceptible to clogging. Integration of an inline filter within the storage tubing or use of the dialysis sampling probe[223] may reduce chances of clogging due to dust, debris, and protein. Future work will also investigate whether a CE chip with slightly deeper channel (e.g., 4 - 5 μm deep) is less prone to clogging, while still allowing adequately fast separation. Additionally, the CE method required the procedures for conditioning the chip prior to analysis. Our current procedures involved several manual steps of removing air traps from the chip before rinsing and refilling the channel with solutions for multiple times. This process can be burdensome because of the manual process. The small channel also necessitated high pressure for perfusion of solutions. Future development of an automated perfusion system and use of a high pressure driven pump will be useful for the process of chip preparation.

Conclusion

In this chapter, we have developed the droplet-based CE interface that was compatible with the microfabricated sampling probe. The integrated system allows fast and multiplexed measurement of amino acid neurochemicals at high spatiotemporal resolution. We have initially explored the possibility to fabricate smaller probes. Coupled the probe to the PDMS manifold with optimized channel and tubing, numerous samples and multiple reagents at nanoliter scale could feasibly be manipulated by using only one driving vacuum. The hybrid Teflon-fused silica interface provides a simple, reliable, and robust way to couple segmented-flow sampling to a CE-based system. The microchip CE system with reduced separation channel size is particularly effective for rapid separation of multiple analytes. The

improvement in speed of separation demonstrated here will accommodate online or real-time chemical monitoring without compromising temporal resolution. Future development in software and instrumentation will further yield improved separation efficiency and detection sensitivity. In the microchip CE-based approach, it is also possible to miniaturize optical detection system (see Appendix D); ultimately creating a compact and portable platform that enables on-site chemical monitoring as well as parallel analysis. Moreover, the microfluidic analytical platform developed in this work has flexibility in its range of operating flow rates. It is therefore applicable to be coupled to various types of miniature sampling systems[159,223] as well as other droplet microfluidic analytical devices[160,161].

Chapter 5
Strategies for Improving Recovery of Microfabricated Dialysis Probe

Introduction

Microdialysis is an essential tool for in vivo chemical monitoring[25,26,28,71]. This technique has been widely used because of its ease of operation and feasibility for coupling to various analytical methods that allow studies covering a wide range of substances[37,71]. Despite advantages of the technique, conventional dialysis probes are typically made by assembly leading to several limitations: 1) large size (probe diameters are over 220 μm), resulting in inevitable tissue damage and poor spatial resolution; 2) limited flexibility in their designs; and 3) tedious to make by hand. To overcome these limitations, our lab has used a microfabrication approach to develop miniaturized dialysis probes[223], as demonstrated in Chapter 2.

The use of microfabrication in Si allowed construction of the dialysis probe that was 6-fold smaller in size and sampling area. Coupling the probe to an LC-MS assay[45,237], its utility was demonstrated in vivo by monitoring 14 neurochemical at basal concentrations. The probe yielded 2 – 7% relative recovery at a perfusion rate of 100 nL/min. Although effective for detection of many neurochemicals, the low recovery was a main drawback of the microfabricated probe. In contrast to the experimental results, computational fluid dynamics simulation (COMSOL modeling) of the membranes indicated recovery of 98% based on high-density straight pores (i.e., 30%) and use of a low flow rate. Hence, the model

suggested that the actual porosity of the fabricated membrane was lower than expected. Causes of this discrepancy were unclear. Nevertheless, we suspected that the lower-than-expected porosity was due to the factors described below.

In our fabrication process, nanoporous anodic aluminum oxide[138,127,128,139] was adapted to directly integrate semipermeable membranes onto microchannels (see Figure **5.1** for summary). The process relied on using a 400-nm thick layer of AAO mask with 50 – 70 diameter pores for etching through a 2-μm thick layer of poly Si underneath (Figure **5.1**A – C). As the pores in the AAO mask were not always perfectly uniform, the etch rates could be inconsistent across the substrate. As a result, incomplete pore formation in the poly Si layer may be obtained. Next, in our previous study, we found that the 2.4-μm thick membrane (combined AAO and poly Si layers) was insufficiently strong to withstand backpressure during flow. We consequently increased a physical strength of the membrane by replacing the 400-nm thick AAO layer with a 3-μm thick layer of AAO (Figure **5.1**D – F). Although this thick layer strengthened the membrane, it can reduce porosity because its formed pores may not necessarily align with the earlier formed pores in the poly Si layer. Finally, during the backside etching step (Figure **5.1**G), the front side of the device wafer must be mounted on another substrate ("carrier wafer") using a wax that was soluble in hot water. As a surface of the porous membrane was directly exposed to the melted wax during mounting, the pores could be clogged. Even though this wax was removed by hot water during the latter step, some pores may remain clogged due to the wax residues. Our aim in this study is to mitigate these possible issues.

In this chapter, we initially examined possible causes of eventual low recovery by characterization with scanning electron microscopy of the probes fabricated by the original

method. We accordingly modified probe processing to mitigate those causes. Using the modified procedure, our preliminary results suggested potential for improvement in recovery of neurochemicals by over 6 folds. Herein possible directions for continued refinement in the fabrication process are also suggested.

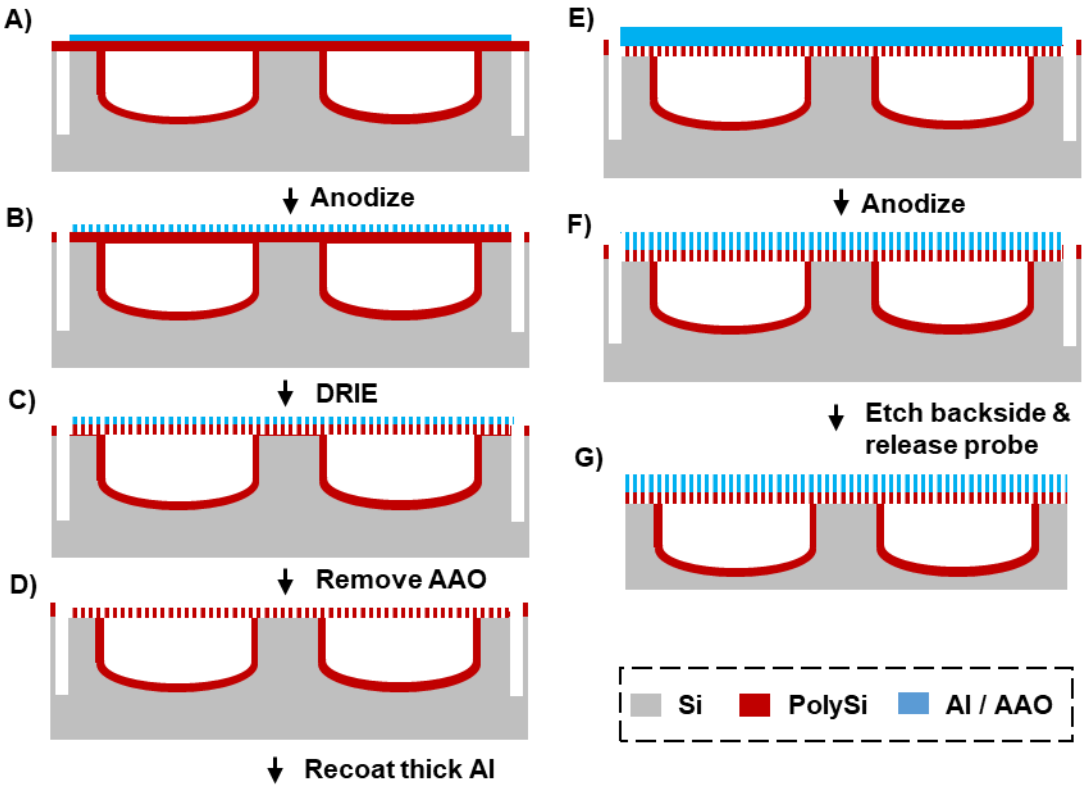

Figure 5.1 Summary of the original process for membrane fabrication. A & B) 400 nm thick of Al was deposited onto Si microchannels prior to anodization to form AAO mask. C) DRIE was used for etching the poly Si layer to form poly Si membrane. D - F) To provide sufficient strength, 400 nm thick layer of AAO was remove and instead coated with a 3 µm thick layer of Al prior to another anodization. G) Backside etching with DRIE was used to define probe thickness prior to probe release.

Experimental

Chemicals and materials

Unless otherwise specified, all chemicals were purchased from Fisher Scientific (Fairlawn, NJ) or Sigma Aldrich (St. Louise, MO) and were certified ACS grade or better.

Solutions were prepared with HPLC-grade water or water purified by a Milli-Q system (Millipore, MA). Fused silica capillaries were purchased from Molex (Phoenix, AZ). Epoxy glues were purchased from Loctite (Westlake, OH) for regular 5-min Epoxy, and ITW Devcon (Danvers, MA) for 5-min Epoxy (gel-type). Crystalbond Adhesive, (Crystalbond 555, soluble in water at 55°C), was purchased from Structure Probe (West Chester, PA). Artificial cerebrospinal fluid (aCSF) consisted of 145 mM NaCl, 2.68 mM KCl, 1.10 mM $MgSO_4$, 1.22 mM $CaCl_2$, 0.50 mM NaH_2PO_4, and 1.55 mM Na_2HPO_4, adjusted pH to 7.4 with 0.1 M NaOH.

Device fabrication and preparation

The overall procedures included 1) channel formation, 2) membrane formation, and 3) probe release and assembly to a holder. Detailed microfabrication and design of a microdialysis probe were previously described[223]. Device fabrication was performed at the LNF at the University of Michigan. Probes were imaged after each fabrication step by using scanning electron microscope (SU8000 SEM, Hitachi, Tokyo, Japan). The anodizing process, probe release, and assembly to the holder were conducted in our laboratory.

Membrane formation. Illustration of an overview of the modified process for preparation of membrane is shown in Figure **5.2**. Steps for formation of the 400-nm thick AAO mask (Figure **5.2**A – C) were the same as the original process. Instead of coating the membrane with a 3-μm thick AAO (Figure **5.1**D – F), a 2-μm thick layer of Ag was used to protect the membrane without removal of the 400 nm thick AAO (Figure **5.2**D).

Through the AAO mask, the polysilicon layer was etched by DRIE at – 15 °C (STS Pegasus 4, SPTS, Newport, UK). Ag was deposited using an e-beam evaporator (Cooke

Evaporator, Cooke Vacuum Products, South Norwalk, CT). For the Ag deposition step, the wafer was tilted at a 30° angle during deposition to prevent a blockage of membrane pores. Prior to using the probe for sampling, the Ag protective layer on the membrane was removed by wet etch with 0.1 M $Fe(NO_3)_3$ for 45 min (Figure **5.2**F).

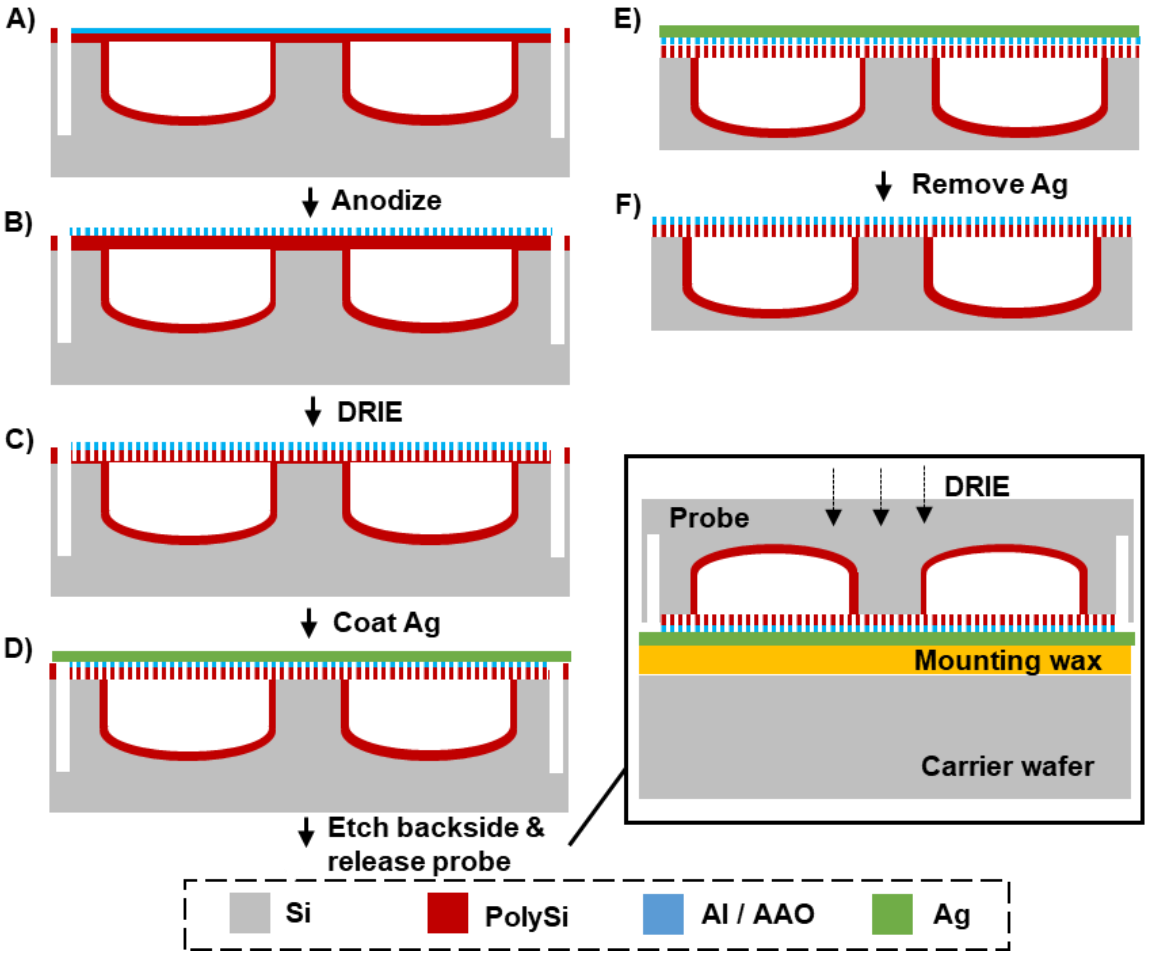

Figure 5.2 Summary of the modified fabrication process. A - C) 400 nm thick Al layer was deposited over the formed channels prior to anodization. The 400 nm thick AAO layer was used as a mask for DRIE of the poly Si layer. D) To protect the membranes from damage and wax clog, a 2 µm thick layer of Ag was coated. The wafer with embedded membranes was attached to a carrier wafer using a mounting wax prior to DRIE for probe thinning (D, inset). E & F) Individual probes were released in hot water. Ag layer was removed later by wet etch.

Probe assembly to a holder and connection tubing. A holder was used to connect the probe to standard fused silica capillaries for fluid transfer. Full description of holder

fabrication and assembly was previously provided[115,223]. In this study, the procedure for probe assembly was modified to facilitate wax removal at the probe inlet/ outlet. An illustration of the procedure is shown in Figure **5.3**. The probe was trimmed with a razor blade at ~1 mm from the end of probe ports to remove wax that had entered the opening (Figure **5.3**A). Capillaries of 2.5 cm length with 180 µm i.d. / 360 µm o.d. were attached to the holder using a regular epoxy resin. Probe ports were inserted into the capillaries and sealed with a gel-type epoxy resin (ITW Devcon, Danvers, MA). At this step, epoxy seal was covered only at the jointed region between the probe ports and capillaries (see Figure **5.3**B, red area). This seal was sufficient for temporary fluid transfer while allowing surface areas of the probe in contact with hot water. In this way, proper heat transfer was ensured for dissolving any remaining wax in the latter step.

According to the manufacturers, the epoxy resin can withstand temperatures up to ~90 °C while the wax is soluble in water at 55 °C. To remove wax residues from the probe, the assembled device including capillaries was submerged in hot water (at 75 °C) while perfusing hot water through the probe at 200 nL/min for 30 min (Figure **5.3**C). The assembled device was then dried overnight before complete sealing with an epoxy resin (Figure **5.3**D). Flow through the probe was driven by a Chemyx syringe pump (Stafford, TX). For fluid transfer and sample collection, 20 - 30 cm of 100 µm i.d. / 360 µm o.d. fused-silica capillaries were directly connected to the inlet/outlet capillary of the probe via a 360 µm-diameter Teflon union.

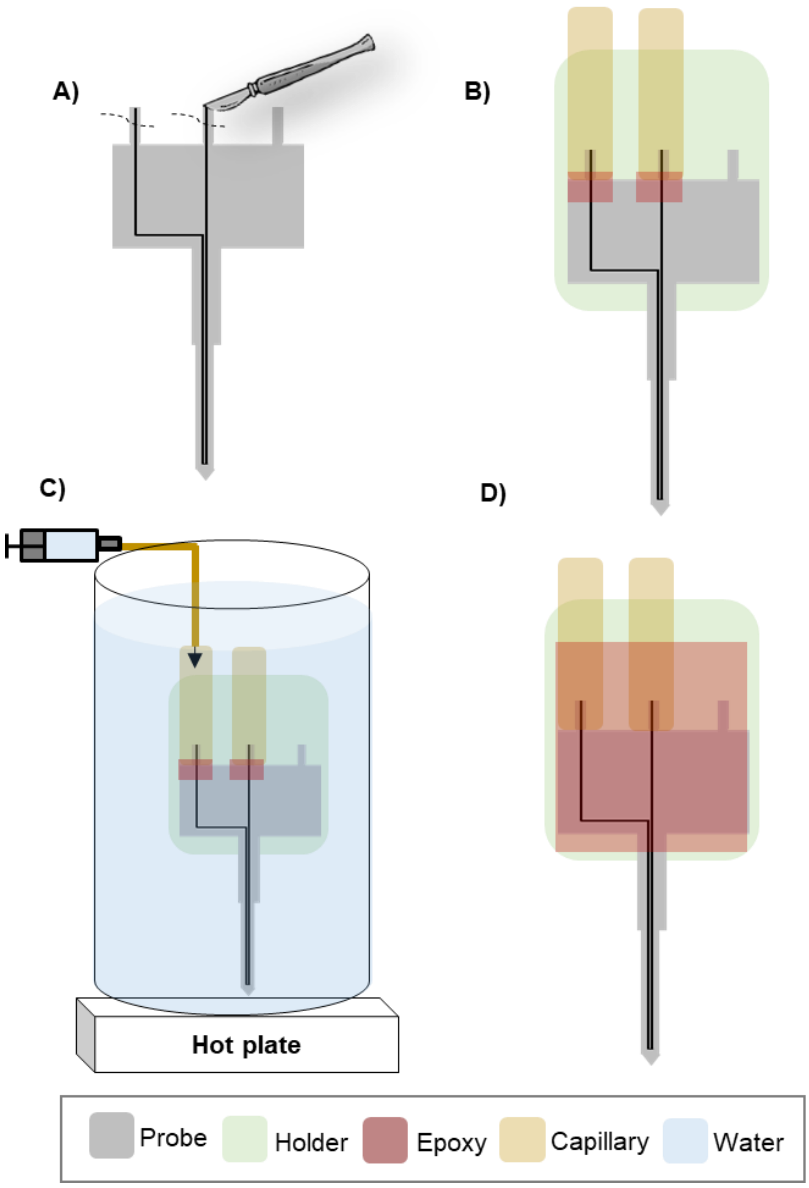

Figure 5.3 Overall procedures for wax removal. A) The inlet and outlet of the probe were trimmed to minimize wax clog. B) Probe ports were inserted into standards capillaries prior to partially sealing with an epoxy resin. C) Hot water was used to remove wax residues. D) After wax removal, the packaged device was dried overnight prior to complete sealing with an epoxy resin.

Recovery test

For study of probe relative recovery, probes fabricated by the modified process were compared to the probe fabricated by the original process. Initial recovery tests were performed by using the probes for sampling a 100 µM fluorescein solution at different

perfusion rates (i.e., 400, 200, 100, and 50 nL/min) in a stirred vial at room temperature. Fluorescence was recorded downstream using a conventional fluorescent microscope system with an arc-lamp source and CCD camera. The probes were then dipped into a well-stirred vial containing: 0.5 μM dopamine (DA), 3-methoxytyramine (3-MT); and 1 μM serotonin (5-HT) 3,4-dihydroxyphenylacetic acid (DOPAC), ɣ-aminobutyric acid (GABA), and 50 μM taurine (Tau) in aCSF at 37˚C. The aCSF was supplemented with 0.25 mM ascorbate to protect against oxidation of analytes. After an equilibration time of 30 min, dialysates were collected in 20 min fractions with a perfusion rate of 100 nL/min. Dialysate samples were derivatized with benzoyl chloride and analyzed by LC-MS, as described previously in Chapter 2.

Results and Discussion

Even though the original fabrication method was successful, it was still imperfect as the probe yielded low recovery. By characterization with SEM images of previously developed probes, we found several possible sources of reduced porosity and eventual low recovery (see Figure **5.4**). Further discussion of these causes and refinement of the procedures were described below.

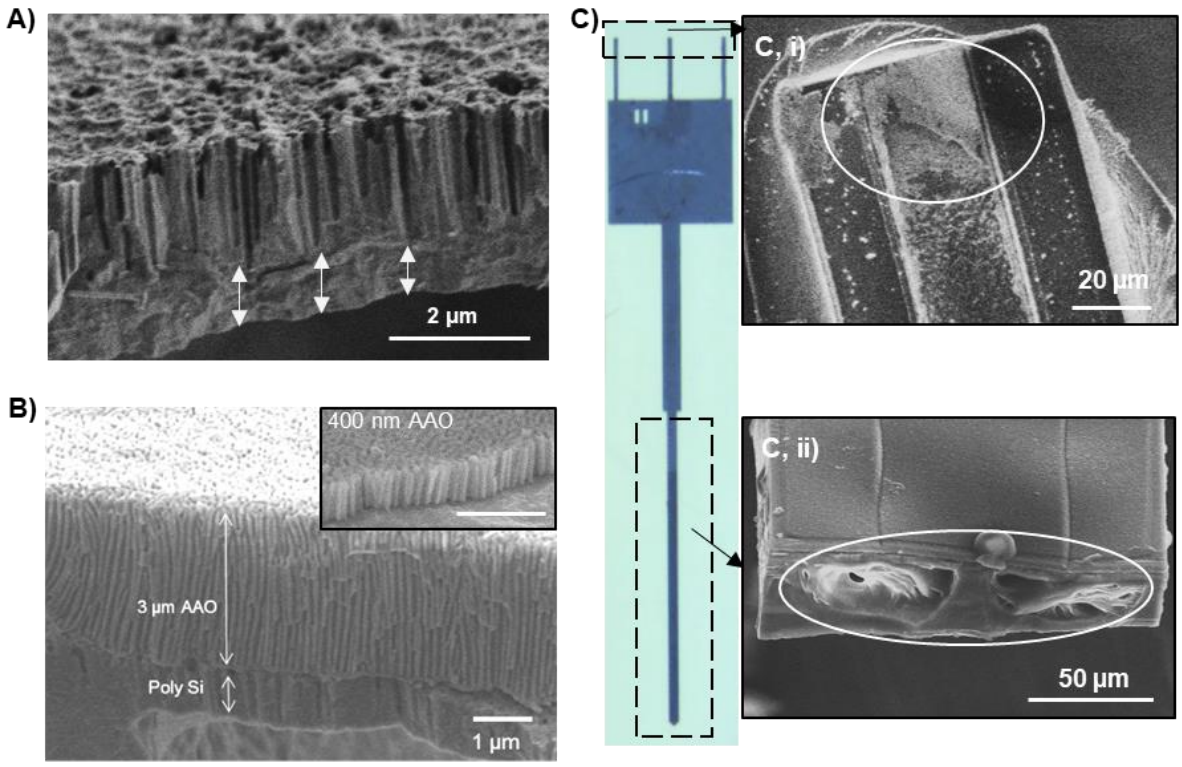

Figure 5.4 Exampled SEM images of probes fabricated by the original process. The images revealed several possible causes of low recovery, including A) incomplete pore formation (the arrows indicated unetched depth of 500 - 700 nm); B) non-aligned pores between the poly Si and thick AAO layers; C) wax clog reduced membrane porosity and necessitated high pressure required for flow (prohibiting use of high porous membrane). SEM images in B&C were courtesy of W.H. Lee.

Incomplete pore formation and etch longer

We observed incomplete pore formation in some parts of the underneath poly Si layer (for example, see Figure **5.4**A). This incomplete formation was likely due to variations in morphology of the etched poly Si substrate and the AAO mask. The variation in thickness of the poly Si layer occurred due to equipment variabilities during multiple deposition and etching steps. Although our previous target thickness of the poly Si layer was 2.2 µm, we found that the final thickness could vary from 2.2 to 2.7 µm (suggesting a range of ~20% deviation above the target thickness). Furthermore, it has been shown that the poly Si film inherently has large grain size and rough surface[251,252]. As deposition of the following Al

layer was based on the poly Si layer, the variations in thickness and surface roughness of the poly Si layer can lead to formation of an uneven AAO mask (Figure 5.5A). Furthermore, pore sizes of the AAO mask were not always uniform. With our current anodization process, pore sizes could vary from 50 – 70 nm (Figure 5.5B). A combination of the variations in the substrate and mask can lead to differences in the etch rate across the wafer. For example, in plasma etching, the etch rate through narrower and thicker pores can be slower than that of wider and thinner pores[99,253–255]. Thus, the time required for thorough etch in some parts of the poly Si layer can be longer than expected.

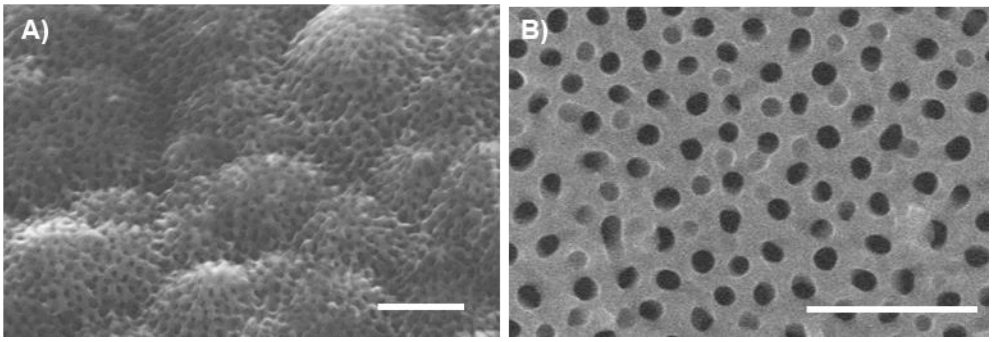

Figure 5.5 Non-uniformity in AAO mask. A) Uneven surface; and B) Variations in pore size and shape. Scale bars were 500 nm.

A straightforward approach to mitigate the issue of incomplete pore formation was to etch through the AAO mask with an extended time while using a slightly thinner poly Si layer. In this study, a target thickness of poly Si layer was 1.8 µm instead of 2.2 µm. The final thickness of the fabricated layer then ranged between 1.8 – 2.2 µm. Through several characterization runs (based on 10-min etching tests), we found that a typical range of etch rate through the poly Si layer with the 400 nm AAO mask was 0.12 to 0.14 µm/min. The etch time was consequently selected to be 22 min (representing 20% longer than the expected

time for complete formation). An example of the poly Si membrane with thorough etched pores was illustrated in Figure **5.6**A.

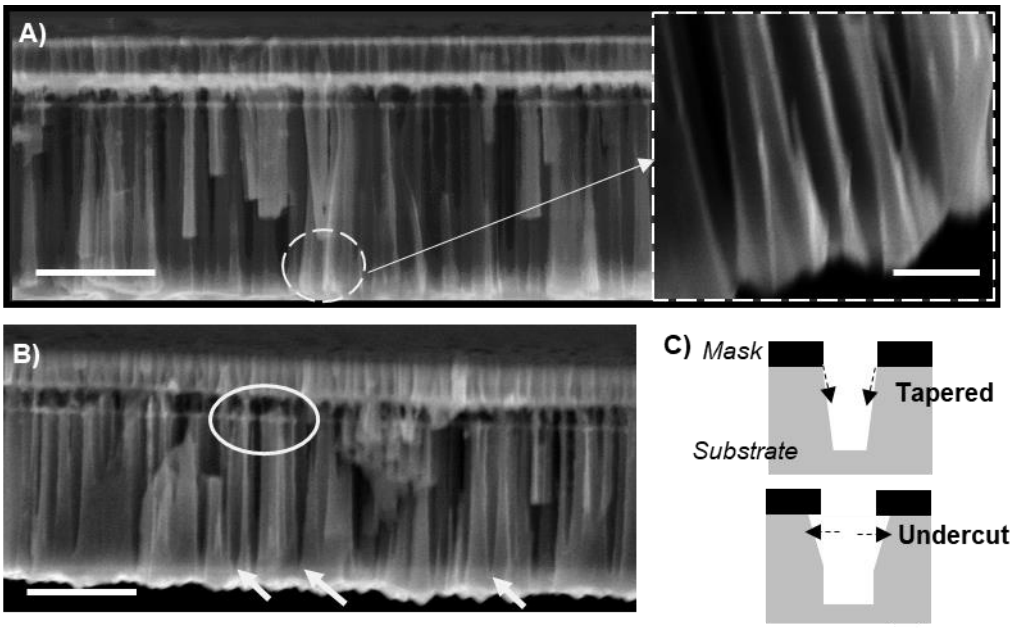

Figure 5.6 Representative SEM images of the membrane with overetch time. (A) shows complete pore formation; (B) shows incomplete pore formation. Circle indicated merging pores due to the undercut profiles. Arrows indicated tapered profiles with unetched depths; (C) illustrates imperfection profiles. Scale bars were 1 μm for A & B, and 250 nm for A, inset.

However, even with use of the extended etch time; incomplete pore formation was still found in some areas of inspected samples (Figure **5.6**B). This result suggested that the etch rate in these areas was lower than expected. This discrepancy was likely due to variations in thickness and pore sizes of the mask, as discussed above. The etch rate can also decrease as the etching goes deeper because of depletion of the gas phase etchant by reaction with the substrate[256–258]. Additionally, angled pores on rough poly Si surface may lead to distorted etch profiles[251]. For example, tapered features of poly Si pores were observed during etching. Sidewalls of the pores also started to merge over time because of

undercutting profiles (see Figure **5.6**B & C). These factors limited the maximal etching depth as too large merging pores can yield a fragile membrane. As a result, further etching of the poly Si layer was not attempted despite the existence of some incomplete pore formations.

Nevertheless, as compared to the membrane from the previous work (Figure **5.4**A), we observed fewer non-opened poly Si pores in the membrane fabricated with the extended etch time. Overall, the unetched depths were less than that of the previous batch fabricated, i.e., 183 ± 65 nm versus 862 ± 210 nm (n = 8 samples). Therefore, we anticipated that the membrane in this study had porosity more than the previous membrane. Even though the membrane contained merged pores, we found no membrane collapse during the etching process. To minimize the risk of membrane damage during latter steps, we accordingly protected the membrane with non-porous Ag and reduced sources of high pressure required for flow as described in the next section.

Despite the fact that DRIE is nominally an anisotropic etch process, imperfections are common due to 1) artifacts induced by surface phenomena, and 2) distortions generated by reflection of reactive species at surfaces of the etched features[251,259]. As mentioned previously, we found that the AAO mask did not necessarily contain uniform and perfectly straight pores. The reactive species may reflect off the angled edges and distort the etched profiles. Besides this effect, it is also possible that ion charging can accumulate overtime at the silicon-insulator interface (i.e., poly Si-AAO in this case), resulting in undesired lateral etching[260]. Further work is required to understand mechanisms of these effects. Future optimization of DRIE parameters and mask alteration may prove useful to solve the problem[261–263]. Our ongoing work is to improve quality of the AAO mask by using a two-step anodization process[127,136,264]. This subject is further discussed in the later section.

Replacing thick AAO with Ag protective layer

Another source of reduced porosity was the 3 μm thick AAO layer. Although this layer strengthened the membrane, the pores in this layer did not necessarily align with the pores in the poly Si layer that was formed earlier through the 400 nm AAO mask (Figure **5.4**B). This thicker AAO layer also had less straight pores as compared to a 400 nm thick AAO (Figure **5.4**B, inset). Furthermore, during the step of backside etching, the porous AAO was directly exposed to the mounting wax, leading to clogged pores. As a result, porosity and eventual recovery could be diminished due to the use of thick AAO.

To overcome the above issues, we protected the membrane by using a 2 μm thick layer of nonporous Ag instead of using a 3 μm thick AAO (Figure **5.2**C & D versus Figure **5.1**C - F). Ag was a chosen material due to its mechanical property, ease of fabrication and removal, and availability in our cleanroom facility. During the deposition process (i.e., physical vapor deposition), the wafer was tilted at ~30° angle to prevent the metal vapor from entering pores of the underneath membrane. The tilting approach was effective as we found that the deposited Ag layer completely laid on top of the membrane and did not block the pores (Figure **5.7**). This Ag layer served to protect the pores from wax clogs as well as damage that may occur during late fabrication steps. Compared to the original process, the modified process has fewer overall steps, which was desirable to lessen chances of damage and contamination to the device, and to reduce the cost of fabrication. Additionally, the Ag layer provided the membrane with sufficient strength during the latter step of flow test. As a result, probes can be used without the addition of the thick AAO.

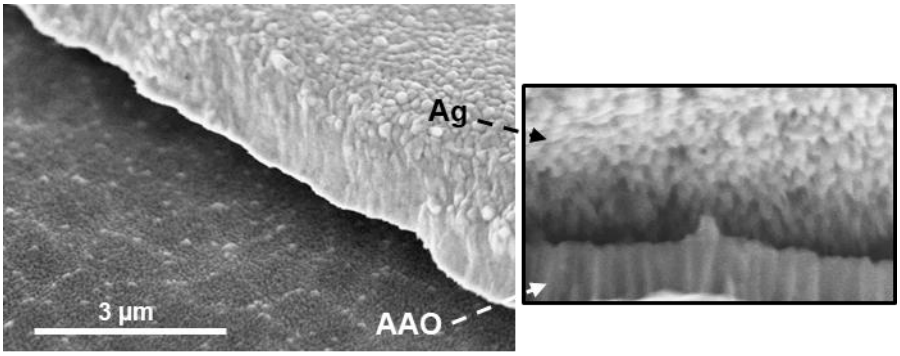

Figure 5.7 Ag protective layer on membrane. The inset showed a cross-sectional view

Wax clog and modified removal process

The wax used during backside etching of the device could enter and block the channels through the inlet/outlet at the probe ports (Figure **5.4**C, i) and the opening pores of the membrane (Figure **5.4**C, ii). Wax clogs inside the pores reduced porosity, resulting in low recovery. Moreover, wax blockage within the system increased backpressure and necessitated high pressure required for flow. We observed that several probes ruptured during the process of wax removal. These probes might have contained high porous membranes, but they were too fragile to withstand the high operating pressure due to wax blockage.

As described in the previous section, the issue with wax that entered the system through the opening pores of the membrane was resolved by using the non-porous Ag protective layer. However, the wax could also enter system through the probe inlet/outlet, thus the process for wax removal was still required. Wax removal can be achieved by immersing the probe in hot water while perfusing water through the probe inlet. In our original process[115,223], the procedures for wax removal were performed after the probe outlet was already connected with a long capillary (12 cm length) of 100 µm i.d. The packaged

device was also entirely sealed with an epoxy resin. We found that this approach made it difficult to remove wax completely from the system because 1) the wax can still enter and block the long connection tubing, and 2) the sealed epoxy created thermal insulation between the probe ports and hot water while heat was required to flow wax. Consequently, backpressure was unexpectedly high and the membrane often ruptured during flow. Indeed, ~80% of the tested probes were broken during wax removal.

To mitigate the above problem, we modified the procedures in order to aid wax removal process. We first trimmed the probe at the end of its ports to minimize the amount of wax clog (Figure **5.3**A). Next, we used a shorter and larger connection tubing to facilitate wax to flow out of the system (Figure **5.3**B). The shorter length allowed the complete length of capillary to be submerged in hot water (Figure **5.3**C). The larger capillary dimension also reduced the backpressure occurred during wax flow. Additionally, the partial epoxy sealing (red regions in Figure **5.3**B & C) allowed exposure of the probe surface to hot water. Due to these reasons, efficient heat transfer from hot water was better achieved to dissolve wax residues in the system. Viscosity of the dissolved wax was also reduced due to increase in its temperature, thus lowering pressure required for the flow. As a result, as compared to the original process, we observed 3 - 4 times more probes that survived this wax removal process (6 out of 8 probes).

Recovery test

In vitro relative recovery was evaluated by comparing dialysate samples with samples taken directly from a stirred vial. Probes made by the original procedure (“old”) were used for comparison with the probes made by the modified procedure (“new”). Initial studies were

performed by sampling a fluorophore and testing relative recovery as a function of flow rate. As seen in Figure **5.8**A, both types of probes had similar inverse relationship between flow rate and relative recovery, which was within our expectation. Nevertheless, the new probes yielded better recovery. For testing recovery of neurochemicals, we used a flow rate of 100 nL/min as a practical choice to obtain sufficient sample volume and recovery. As shown in Figure **5.8**B, recovery was improved 6 - 9 fold when sampling by the new probes. For example, recovery was increased from 5% to 28% for DA, 3% to 21% for GABA, and 4% to 37% for 5-HT.

The above results suggested the possibility of improving recovery by refining the fabrication procedures. However, the improved recovery reported here was still a few folds lower than the 98% recovery suggested by the model. Based on the previous discussions, the main reason for this discrepancy was due to incomplete pore formation of the membrane. In addition, the lower-than-expected recovery was indirectly caused by an unexpectedly high pressure during flow due to channel blockage. In other words, probes containing membranes with high porosity might be existed within the fabricated batch; but, they fractured before the recovery test because of the abruptly high pressure. Prior to the sampling procedure, ~25% of the probes were broken during wax removal, and ~30% of the remaining probes were broken after connecting to a long tubing for sample collection. These results indicated that variations in thickness and porosity of the fabricated membranes have remained. To improve upon these imperfections, future directions for continued refinement of the process are discussed below.

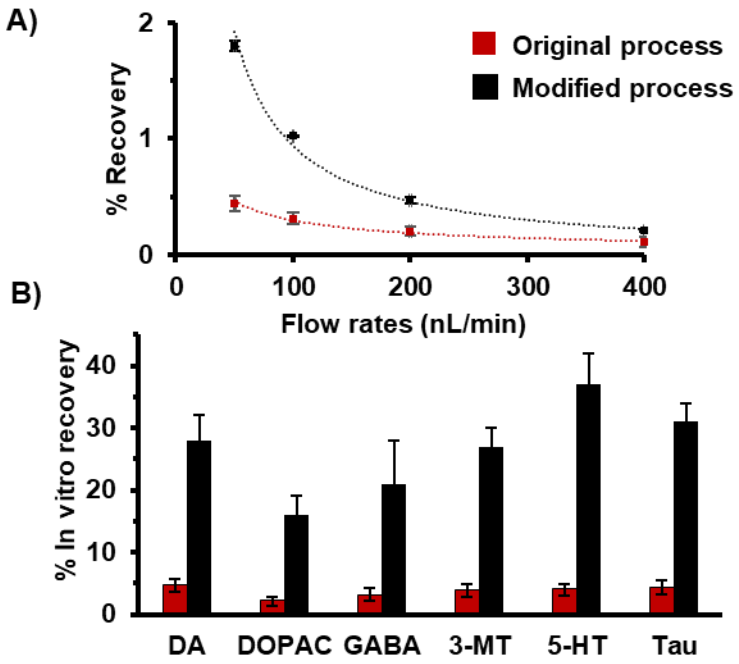

Figure 5.8 Comparison of recovery by probes made by the modified process and the original process. A) Relative recovery of fluorescein, sampling at different flow rates at room temperature B) Relative recovery of selected neurochemicals, sampling at 100 nL/min at 37˚C. Values were given as mean ± 1 standard deviation (n = 3 probes for both A & B).

Future directions and potential

Based on these initial studies, a number of improvements are suggested for future development. As discussed above, uniformity of the AAO mask and poly Si substrate were critical to etch rate and depth, which relate to porosity and performance of the membrane. As it is difficult to control uniformity of the poly Si substrate (due to equipment limitation and its inherent property), a more favorable direction is to focus on improving uniformity of the AAO mask. To achieve this, future work will use two-step anodization process to form a mask that has a smoother surface and more ordered and straight pores[127,264,136]. Use of The two-step AAO mask may provide more consistent etch rates across the wafer, leading to more opening pores in the poly Si layer.

Although longer etch time allowed increase in porosity, the maximal etching depth was still limited by the profile imperfections that caused pore merging overtime. Future work will focus on mask alteration to overcome this problem. Our preliminary results has revealed possibility of increasing the maximal etching depth by using a thinner, better quality mask (e.g., 150 nm thick AAO made by two-step anodization, see Appendix C). By this approach, it is possible to etch 3-μm thick poly Si layer thoroughly without merged pores while the etching depth has been limited to be < 2 μm. In addition, future work will investigate whether alteration of DRIE process parameters (e.g., RIE power, temperature, cycle times, pressures, and gas flows) can be performed to further push the limit of aspect ratio.

Furthermore, the integrated microfluidic system should have minimized backpressure to accommodate use of the enhanced-porous membrane without rupturing. As discussed previously, one major source of the high pressure needed for flow was the wax that entered the channels through the probe inlet and outlet. Although the cleaning method demonstrated in this work proved to mitigate the issue, the process was laborious involving manually trimming the probe and perfusing hot water through the channel. Hot water might also not necessarily dissolve all the wax residues. Some residues can be very difficult to remove as they might undergo cross-linking during the dry etching process. Future work will investigate whether different methods, such as decomposition at high temperature (as demonstrated in Chapter 3) and/or oxygen plasma ashing[265,266], are more suitable for probe cleaning.

In parallel, we will focus on modification in probe design to prevent the inlet and outlet of the probe from clogging. For example, a different design of probe outline (i.e., longer ports) can be used to close the inlet and outlet during the fabrication process. Trimming or wet etch will be performed to open the inlet and outlet just prior to assembly to

a holder. Additionally, channel designs will be modified to minimize backpressure (i.e., eliminate sharp turns/corners). Use of alternative backside etching methods (e.g., processes based on wet etch[30,143]) may also be explored to totally avoid usage of the mounting wax.

With the above suggestions, complete pore formation and straight pores could potentially be achieved, allowing fabrication of the membrane with truly high porosity and uniformity. We anticipate that these improvements will allow recovery approaching the 98% of the model. This recovery will enable detection of many more molecules with potentially reducing sampling areas. The membrane will also be stronger due to vertical etch profiles. Future development will facilitate fabrication of a thicker poly Si layer to increase a physical strength of the membrane. The AAO layer can eventually be removed to provide the final device with an improved integrity. Increase in the membrane strength will also accommodate reduction in channel sizes as the membrane can withstand more backpressure. With these improvements, the microfabricated probe can be made even smaller and a faster flow rate can be used to improve temporal resolution.

Conclusion

In this chapter, we described three possible sources of low recovery from the microfabricated dialysis probes, including incomplete pore formation, non-aligned pores, and wax clog. We illustrated potential for improving recovery by modification of probe processing. Despite this improvement, the issue of incomplete pore formation has remained due to the limited maximum attainable etch depth caused by non-uniformity in the mask and substrate. Strategies for continued refinement in the process were accordingly suggested to overcome all the causes of low recovery and to further improve the probe performance. The

improvement in probe performance will open the door to development of next generation probes that enable new studies in neuroscience.

Chapter 6
Summary and Future Directions

Summary

This dissertation describes the development and utility of microfabricated sampling probes for multiplexed neurochemical monitoring with high spatial and temporal resolution. Two types of the sampling probes included microdialysis probe and push-pull perfusion probe. The probes made by microfabrication are at least 6 times smaller than standard probes made by assembly, thus allowing monitoring at substantially improved spatial resolution. Other advantages included scalability, design flexibility, mass production, and potential for monolithic integration with other neural interfaces. The microdialysis probe particularly has benefits of sample cleanup and ease of device operation. Even though the push-pull probe is more prone to clogging, it provides unprecedented spatial resolution, approaching to that of the smallest electrochemical sensors (see Table **6.1** for summary). The advantage of the sampling methods over other in vivo monitoring techniques stems from their capability of measuring a larger number of neurochemicals as well as feasibility of multiplexing. Furthermore, based on the concept of segmented flow for improving temporal resolution, external integration of a droplet microfluidic device enables temporal resolution as good as ~5 s at a low sampling rate. This improved temporal resolution further utility of the method for recording rapid neurochemical changes that are typically required for behavioral or pharmacological studies (see Figure **6.1**). Below is a brief summary of development and enhancement of the microfabricated probes described in this dissertation.

Microfabricated Microdialysis Probe

Microfabrication approach was used to create a monolithic, miniaturized microdialysis probe. An essential part of this work was adapting anodic aluminum oxide processing to develop an innovative method for direct formation of nanoporous membranes on microchannels. The microfabricated sampling probes was coupled to LC-MS for reliable monitoring of multiple neurochemicals in living rat brain at basal concentrations. The probe yielded 2 – 7% relative recoveries at a perfusion rate of 100 nL/min. Continued refinement of the fabrication process suggested potential for improving recovery by ~10 folds. The microfabricated probe has at least 3-fold better spatial resolution than a regular dialysis probe made by assembly of a smallest available membrane tubing. Moreover, the 6-fold smaller probe size will open the door to monitoring of small brain regions that are previously inaccessible by conventional dialysis probes.

Table 6.1 Improvement in spatial resolution due to the use of microfabricated sampling probes. Spatial resolution is defined by an active surface area of chemical monitoring. The active surface area of sampling methods are compared to that of electrochemical sensors. The area of conventional dialysis probe is based on 2 mm long, 220 µm diameter membrane tubing. The conventional push-pull probe is based on the probe made by Slaney et al[73]. The carbon fiber electrode is 50 µm long, 7 µm diameter. Enzyme coating layer for detection of non-electroactive molecules typically adds ~5 µm thickness. The microfabricated sensor is based on work by the Gerhardt group[90]. For sampling probes in particular, microfabrication has allowed reduction of sizes of the probe size, hence providing considerably improved spatial resolution.

Probe type	Active surface area (μm^2)
Conventional dialysis	1400000
Microfabricated dialysis	440000
Conventional push-pull	16000
Microfabricated push-pull	1200
Carbon fiber sensor	1100
Carbon fiber sensor w/ enzyme coat	1900
Microfabricated sensor	7500

Microfabricated Push-Pull Probe with Droplet-Based Microfluidic System

Since initial development of the microfabricated push-pull probe, device capability has been enhanced by incorporation of additional microfluidic functions. An extra channel was internally integrated into the probe for chemical delivery at high spatial resolution. Furthermore, other microfluidic devices were developed to perform further analytical procedures, including sample derivatization, flow segmentation and extraction, and separation. Probe-compatible interfaces were also created to enable interconnections between different microfluidic devices. These interfaces consequently allowed integration of the microfabricated push-pull probes with droplet microfluidic system before analysis of nanoliter droplets by microchip CE or direct infusion nano-ESI MS. Compared to conventional analytical methods, such integrated system offered 100-fold improvement in temporal resolution. The integrated miniaturized system ultimately enables multiplexed monitoring of rapid brain chemistry dynamics. Although this part of dissertation focuses on the push-pull probe, the same concepts and designs of the droplet-based system should be pertinent to the microfabricated dialysis probe as well.

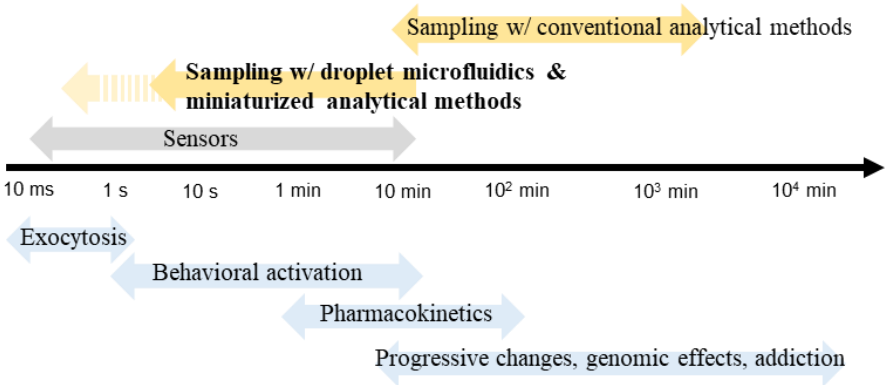

Figure 6.1 Improvement in temporal resolution by implementation of droplet-based microfluidic system. The diagram shows temporal resolution of neurochemical events and analytical methods at different time scales. Incorporation of droplet microfluidic system and miniaturized analytical techniques with sampling probe allowed improvement in temporal resolution of the method. Future direct integration of flow segmentation within a microfabricated sampling probe will further push the temporal resolution, as described below. This diagram was adapted from[36].

Future Directions

Building on the current generation probes, the next generation probes can be made even smaller to further push the limit of spatial resolution. Future monolithic integration of a tee within the probe will offer a possibility for chemical monitoring at sub-second resolution. Another intriguing aspect of the microfabricated probes is that the number of channels can be scaled up. Further, the multi-channel probes can be feasibly integrated with other neural sensing and control tools, such as electrophysiology and optogenetics. Such development will lead to innovative probes that open opportunities for new discoveries in brain research.

Next Generation Sampling Probes

Smaller. Further miniaturization is advantageous to improve spatial resolution and minimize tissue damage. In our current designs, push-pull probes are 80 μm wide, 70 μm thick, containing 20 μm spaced push-pull orifices (20 × 20 μm square) on buried channels of 20 μm diameter. Dialysis probes are 160 μm wide × 50 μm thick, consisting of 4 mm long, 2.4 μm thick membrane embedded on a 60 μm wide × 30 μm tall U-type channel. As discussed in Chapter 4, use of 5 μm wall thicknesses was suitable for push-pull probes with 15 μm channel diameter. Thus, push-pull probes can readily be made as 45 μm wide × 25 μm thick, with 5 μm spaced orifices of 15 μm × 15 μm square. For dialysis probes, the equation below[123,267] suggests that a theoretical maximum load (i.e., pressure that the membrane can withstand before collapse, ΔP_{max}) could be 2.8 MPa or ~400 psi for a 2 μm thick × 30 μm wide poly Si membrane with 30% porosity.

$$\Delta P_{max} = 0.29 \cdot K \cdot \left(\frac{t}{r}\right) \cdot \sigma_{yield} \cdot \sqrt{\frac{\sigma_{yield}}{E}}$$

K is a non-perforated fraction of membrane, t is membrane thickness, r is half of membrane width, σ_{yield} is yield strength (1.2 GPa for poly Si[268]), and E is young's modulus (160 GPa for poly Si[269]). Within a useful range of 0.1 – 2 µL/min flow rate, backpressure in a probe consisting of 2.2 cm long × 30 µm wide × 15 µm tall channel is estimated to be 20 – 400 psi. According to the above maximum load and the range of useful driving pressures, we anticipated that sizes of the channel and membrane could be reduced by half, after improvement in membrane morphology and prevention of unexpectedly high backpressure/ clogging. This size reduction will consequently allow fabrication of dialysis probes with a total size of 75 µm wide × 25 µm thick.

If needed, lower flow rates can be used to compensate for recovery loss due to further miniaturization of sampling area. For push-pull perfusion, 10 – 30 nL/min may be used instead of 50 nL/min. The lower flow rate not only improves recovery but also may cause less tissue disruption[270]. For dialysis, 50 nL/min may be used instead of 100 nL/min. Our preliminary data indicated that recovery of the microfabricated dialysis probe was improved by ~2-fold when using a flow rate of 50 nL/min versus 100 nL/min.

A layout of the system with further miniaturization is illustrated in Figure **6.2**, dashed insets. Based on the dimensions described above, the next generation probes will be 6-fold smaller than the first generation microfabricated probes and at least 30-fold smaller than conventional probes. As compared to a standard dialysis probe containing a 2 mm long, 220 µm diameter membrane, the next generation probes will offer improvement in spatial resolution by 1500-fold for push-pull and 10-fold for dialysis.

Faster and more compact. Use of low flow rates is favorable to the miniaturized probes for recovery; however, lower flow rates lead to the poorer temporal resolution. To

mitigate this problem, temporal resolution can be preserved by using an external tee for flow segmentation (as demonstrated in Chapters 3 & 4). Although the external device has proven effective, it requires extra capillary length for connection, which can limit temporal resolution (i.e., best possible resolution is ~5 s at 50 nL/min). The integrated system can also be bulky, which is not ideal for small animals. To improve on this system, a tee for segmenting the sample stream will be monolithically integrated in the probe (see Figure **6.2**).

Using microfabrication, this internal tee can be placed close to the sampling area (e.g., 100 µm above the pull orifice; or 2 mm at the end of dialysis membrane). Such system will allow flow segmentation immediately after sampling, ultimately enabling a sub-second temporal resolution. Using the rise time equation[73], temporal resolution could be 30 ms for push-pull (15 pL when sampling at 30 nL/min) and 890 ms for dialysis (740 pL when sampling at 50 nL/min). We estimated that the small channels will form droplets within a size of 6 pL – 10 pL (by calculating volume of droplets with 15 µm diameter, 15 - 60 µm long). To collect these small droplets, a 50-µm i.d. HPFA tubing (smallest size commercially available) can be used for coalescing the small droplets into bigger droplets (70 – 400 pL) in case the subsequent assay requires relatively large sample volumes. Otherwise, a 20-µm i.d. fused-silica capillary can be silanized and used for collection of sub-10 pL droplets. Another possible approach for collecting and manipulating small droplets is to use a PDMS or Teflon microfluidic chip[271] with a channel in the size of 20 µm.

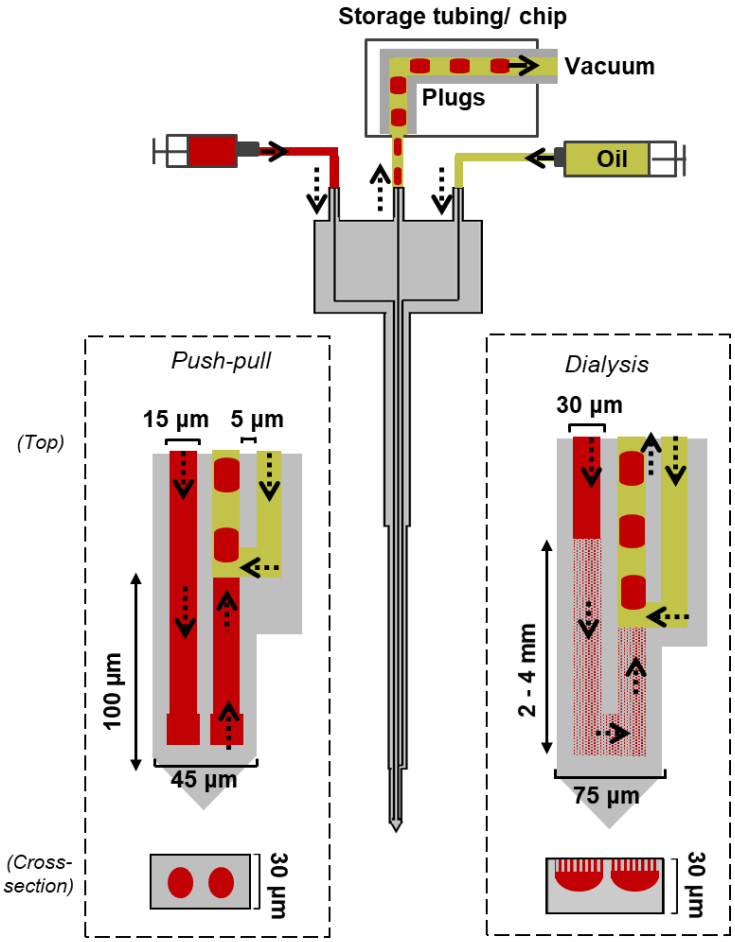

Figure 6.2 Layout of small sampling probes with integrated flow segmentation. Center is an overview of the integrated system. Left dashed inset shows push-pull probe. Right dashed inset shows dialysis probe (hatched red is membrane).

Advanced Neural Probes

Multi-channels. By microfabrication, more components can be combined to a sampling probe with high integrity and scalability. As demonstrated in Chapter 3, an extra channel can be embedded into a sampling probe for drug delivery (microinjection) to stimulate release of neurochemicals. Besides microinjection, the inclusion of multiple channels indicates other purposes, such as reagent addition or flow segmentation via an integrated tee. An additional channel can be used as a back-up channel for sampling in case the main channel defects or occludes during experiments. It is also possible to add more channels for monitoring chemicals at high spatially different locations.

Multifunctional probe. An exciting aspect of the microfabricated probes is that they are constructed by the same microfabrication technologies as other Si neural sensing and stimulating platforms, including electrophysiology[272] and optogenetics[31,273,274]. Hence, it is feasible to develop multifunctional/ modal neural probes with combined microfluidic, electrical and optical functions.

Optogenetics has emerged as an important tool for neuroscience due to its ability to manipulate neurons precisely[275–277]. In most studies, experiments have relied on using optical fibers for stimulation, which is consequently detected by behavioral observation or electrophysiological recording. Simultaneous monitoring neurochemical release can provide better insights into the neuronal effects[278]. However, only a few reports have demonstrated neurochemical monitoring during optical stimulation[279–281]. In these reports, measurements were achieved by using conventional dialysis probes, which were bulky and had poor spatial resolution. Microfabrication technologies will allow development of miniaturized sampling probes with integrated optical elements.

Several efforts have attempted to miniaturize optogenetic neural probes (see [282–284] for reviews of different designs and interfaces). Two main approaches to integrate an optical function onto a Si neural probe include using 1) an optical waveguide connected to an external light source, and 2) μLEDs. Comparing between the two approaches, the optical waveguide approach offers more flexibility in selection of materials and wavelengths, and control of power output levels. However, this approach inherently has limitation in term of scalability. The minimum possible size of microfabricated waveguides has been at least a few tens of microns wide and ~10 μm thick[285,286]. This relatively large size restricted probe design and a number of recording and stimulation sites that can be integrated in a small probe.

For example, considering a probe size of 45 µm wide × 25 µm thick described above, integration of a microfabricated waveguide in this probe would require more than half of the space on the probe surface. The final probe thickness will also be increased remarkably (by ~40%). On the other hand, the µLED approach is highly effective in terms of reducing the probe size and integrating multiple optical elements at high spatially different locations. Therefore, the µLED approach seems appealing, as our ultimate goal is to develop a miniaturized, highly integrated neural probe.

The Yoon Group at the University of Michigan has reported integration of µLED onto a Si neural probe[31]. As compared to other µLED-integrated neural implants[287,288], this work is more attractive due to its overall small probe size, monolithic integration, and the possibility for implementing on process flow of Si micromachining. In this report, 3 µLEDs at ~50 µm vertically apart could be integrated onto a shank along with 8 recording electrodes while maintaining a total dimension of 5 mm long × 70 µm wide × 30 µm thick. The thickness of each µLED was less than 0.5 µm thick and had an emission area of 150 μm^2 (10 µm × 15 µm). Four-shank probes were fabricated and tested in the hippocampal region CA1 of both anesthetized and freely-moving mice. The probes has also proven suitable for uses in both acute and chronic studies. We believed that the key design and fabrication process of these probes can be adapted to combine with those of the microfabricated push-pull probes described above.

An example of a possible design for the combined microfluidic and optogenetic neural probe is illustrated in Figure **6.3**. The probe thickness is 30 µm thick to accommodate fabrication of 15-µm diameter channels with ~5-µm wall thickness. Within a width of 85 µm, it is feasible to incorporate 4 microfluidic channels for segmented flow sampling and drug

delivery, 2 μLEDs for optical stimulation, and at least 4 electrodes for physiological recording into a single probe shank. The microchannels are embedded in a shank while the diodes and electrodes are constructed on a shank. The modified bevel design will allow opening of the microinjection channel at different axis/ angle to prevent interference between microinjection and sampling flows.

For the fabrication process, channel formation can be completed before deposition and etching steps for constructing μLED, electrodes and interconnection lines, and insulators. Sampling orifices, and probe shapes and thicknesses are subsequently defined by using plasma etching. Since the original procedures for microfabricating both probe types (i.e., sampling and optoelectronic neural probes) were previously conducted at the Lurie Nanofabrication Laboratory (LNF) at the University of Michigan, it is expected that all necessary microfabrication tools and resources are readily available.

The above-proposed neural probe will offer multifunctional capabilities to study the brain at high spatial control and at an unprecedented size-scale. The microfluidic channels allow multiplexed monitoring of neurochemicals as well as delivery of drugs and larger substances (e.g., viruses). The μLEDs enable light delivery for optogenetics to manipulate neuronal activities at subcellular levels. The microelectrodes can be used for electrophysiological recording and/or stimulation. By microfabrication, size of the electrodes can also be adjusted to facilitate electrochemical measurements. The multi-functionality of this advanced probe will open the door to new studies on dissecting both chemical and electrophysiological basis of neuronal functions and disorders.

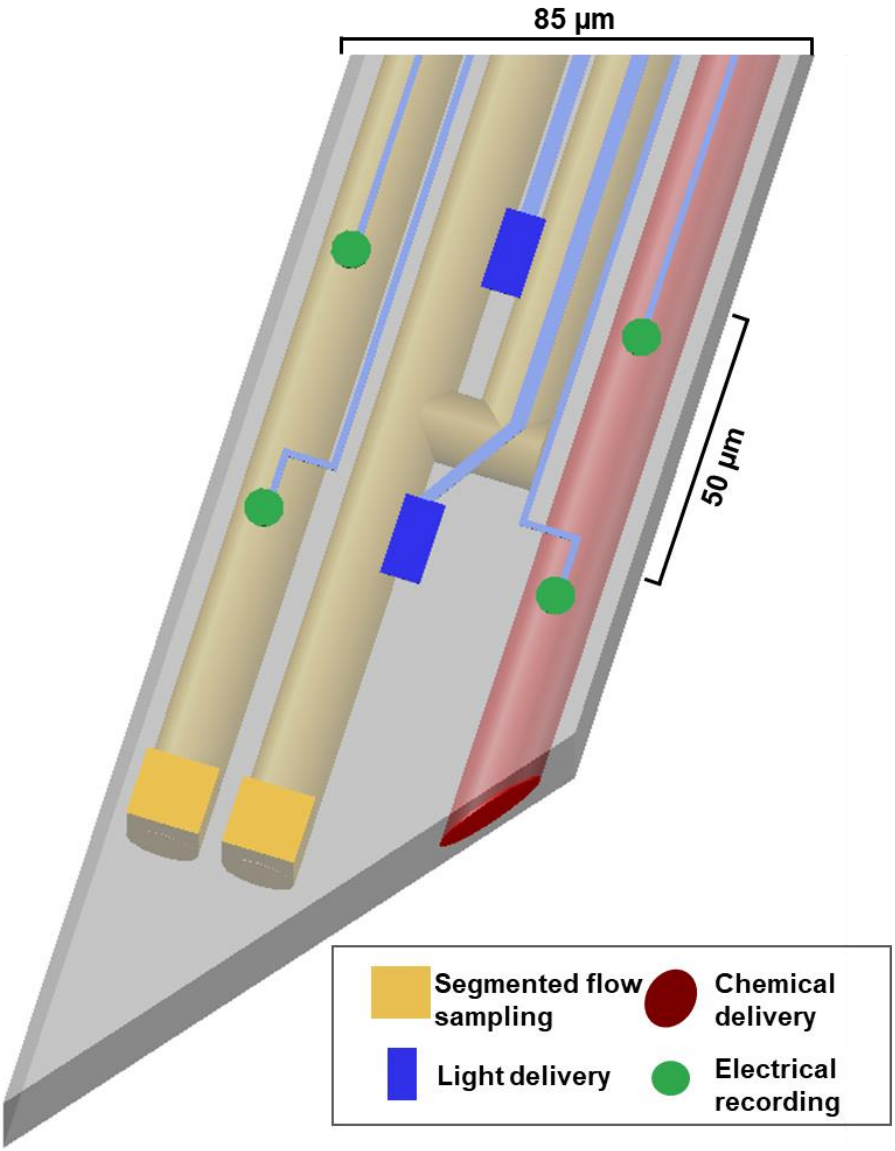

Figure 6.3 3D schematic of the proposed design for multimodal/ functional Si neural probe, consisting of 4 microfluidic channels with 2 micro-LED and 5 microelectrodes. 3 channels (yellow) are for push-pull sampling with flow segmentation. New bevel design facilitates placement of sampling orifices further down while allowing opening of another channel (dark red) for microinjection at different axis/ angle. Such positioning will allow sampling and chemical delivery without interference. LEDs (blue) and electrodes (green) are monolithically embedded on the microfluidic probe. Electrical and optical elements are less than 500 nm thick. Microchannels are 15 – 20 µm tall with 5 µm thick walls. Total size of the probe is 85 µm wide × ~30 µm thick.

Appendix A
Step-by-Step Procedures for Microfabrication of Push-Pull Probes

Fabrication of push-pull probes were performed within a class 1000 cleanroom (LNF at the University of Michigan). The probes were fabricated from 525 µm thick N-type 100 mm silicon wafers (Silicon Valley Microelectronics, Santa Clara, CA) using the procedures described below. Schematics of probe processing are shown in Figure A.**1** - Figure A.**4**.

Channel formation

1. Clean surface of wafers using RCA clean process
2. Deposit 1 µm oxide layer using thermal oxidation
3. Pattern channels using lithography
4. Remove oxide layer on channel patterns using RIE
5. Etch 30 µm deep trenches with coated C_4F_8 wall using DRIE
6. Etch 20 µm i.d. buried channels using XeF_2 etch
7. Removal C_4F_8 wall using RIE
8. Remove photoresist using Nanostrip etch
9. Clean surface of wafers using RCA clean process
10. Deposit 3-4 µm poly Si for channel seal using LPCVD
11. Deposit 500 nm oxide layer using LPCVD

Probe shape and orifices

12. Pattern probe shapes using lithography (photoresist = 3 µm SPR 220)

13. Remove 500 nm oxide layer on probe shape patterns using RIE or BHF wet etch

14. Remove poly silicon layer on probe shape using DRIE

15. Remove 1 µm oxide layer on probe shape using RIE

16. Remove photoresist using Nanostrip etch

17. Pattern probe shapes and orifices using lithography (photoresist = 10 µm AZ9260)

18. Etch probe shapes for 100 µm depth using DRIE

19. Remove 500 nm oxide layer on orifices using RIE

20. Remove poly silicon layer on orifices using DRIE

21. Remove 1 µm oxide layer on orifices using RIE

22. Etch orifices to 25 µm depth using DRIE

23. Remove photoresist using Nanostrip etch

24. Mount the wafer on a carrier wafer using Crystalbond 555 adhesive

25. Etch backside of the wafer until achieving desire thickness of 50 – 70 µm using DRIE

26. Release probes in hot water

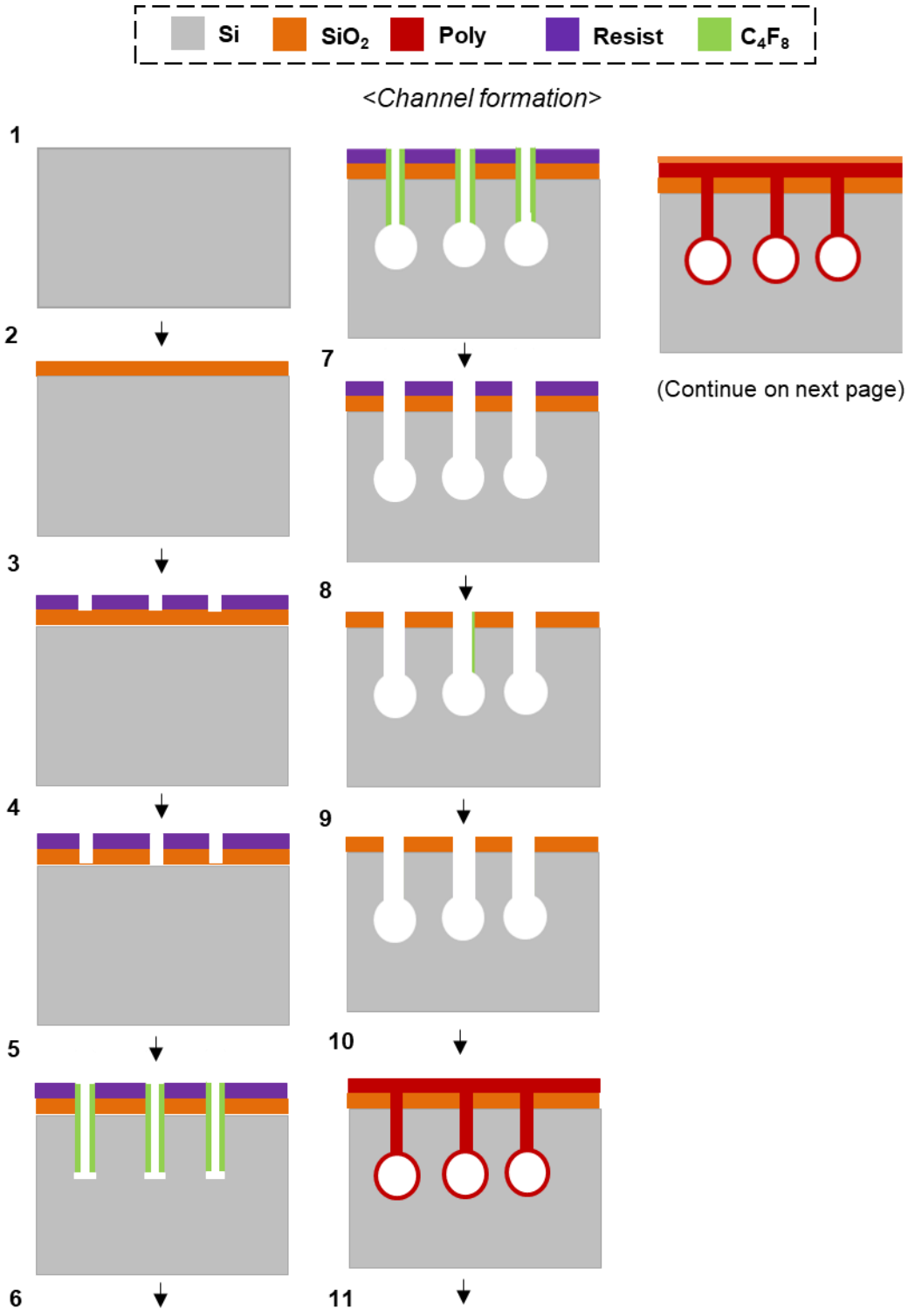

Figure A.1 Channel formation (Steps 1 – 11)

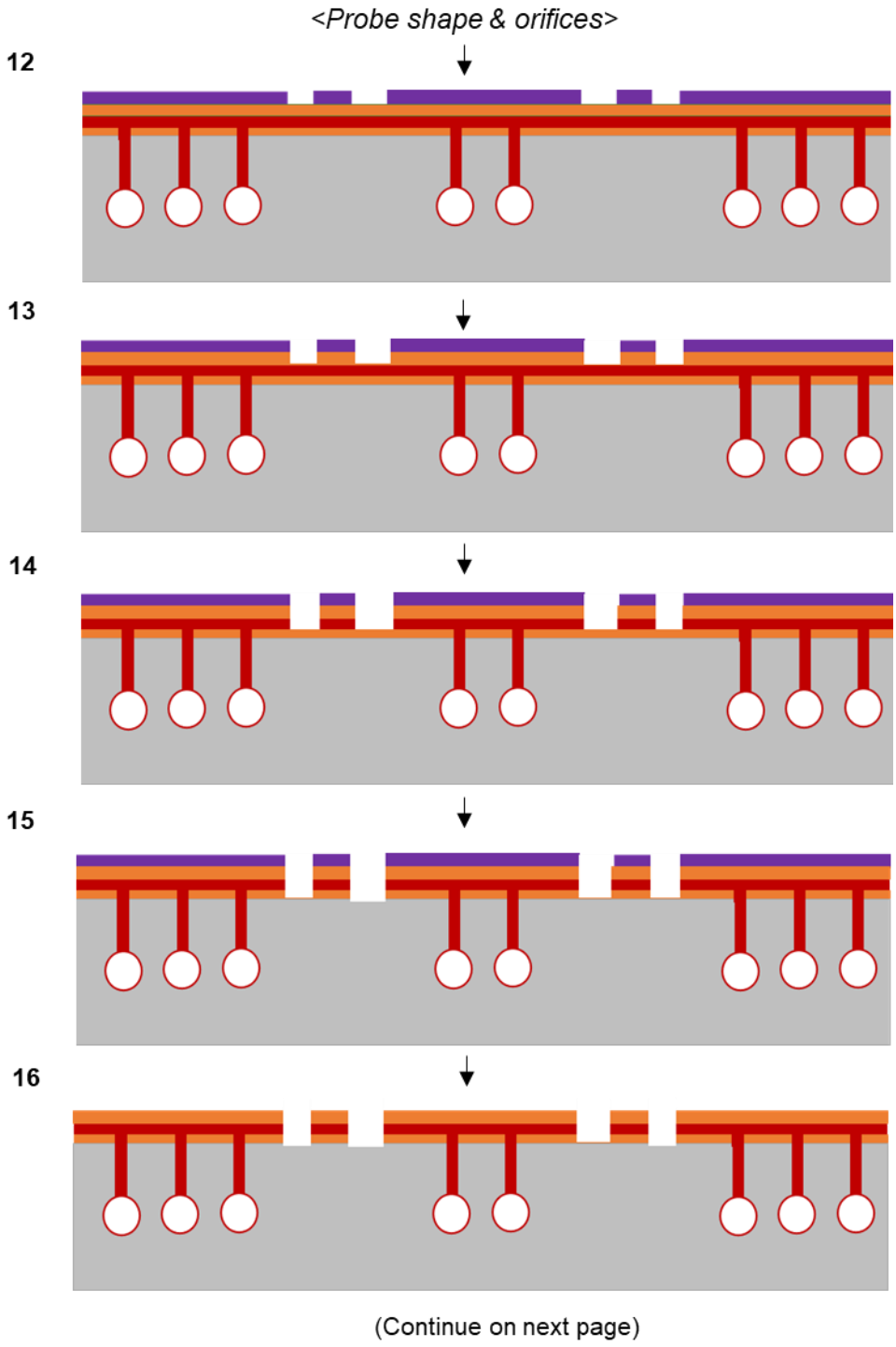

Figure A.2 Patterning and etching of probe shapes and orifices (Steps 12 – 16).

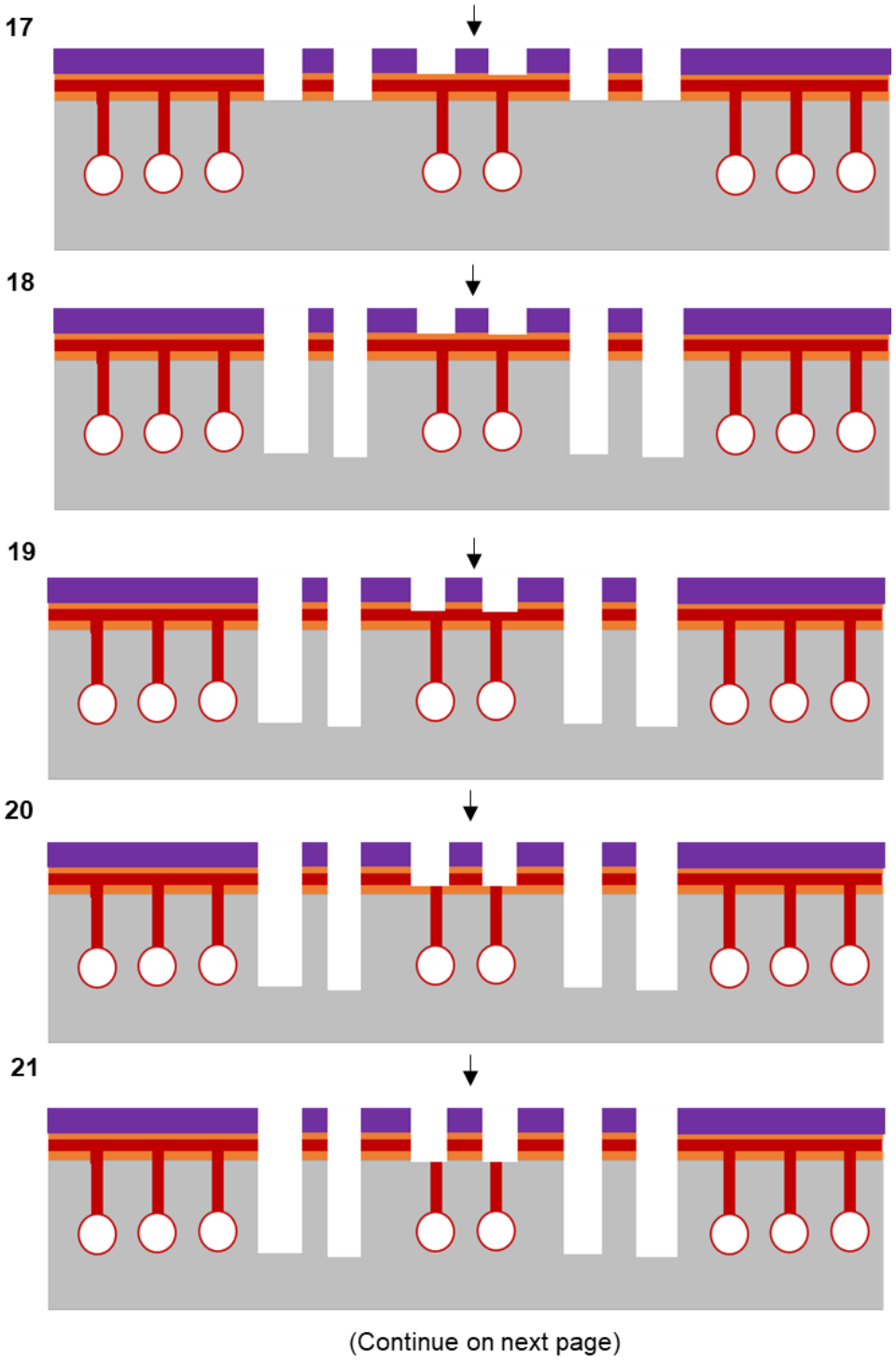

Figure A.3 Continued patterning and etching of probe shapes and orifices (Steps 17 – 21).

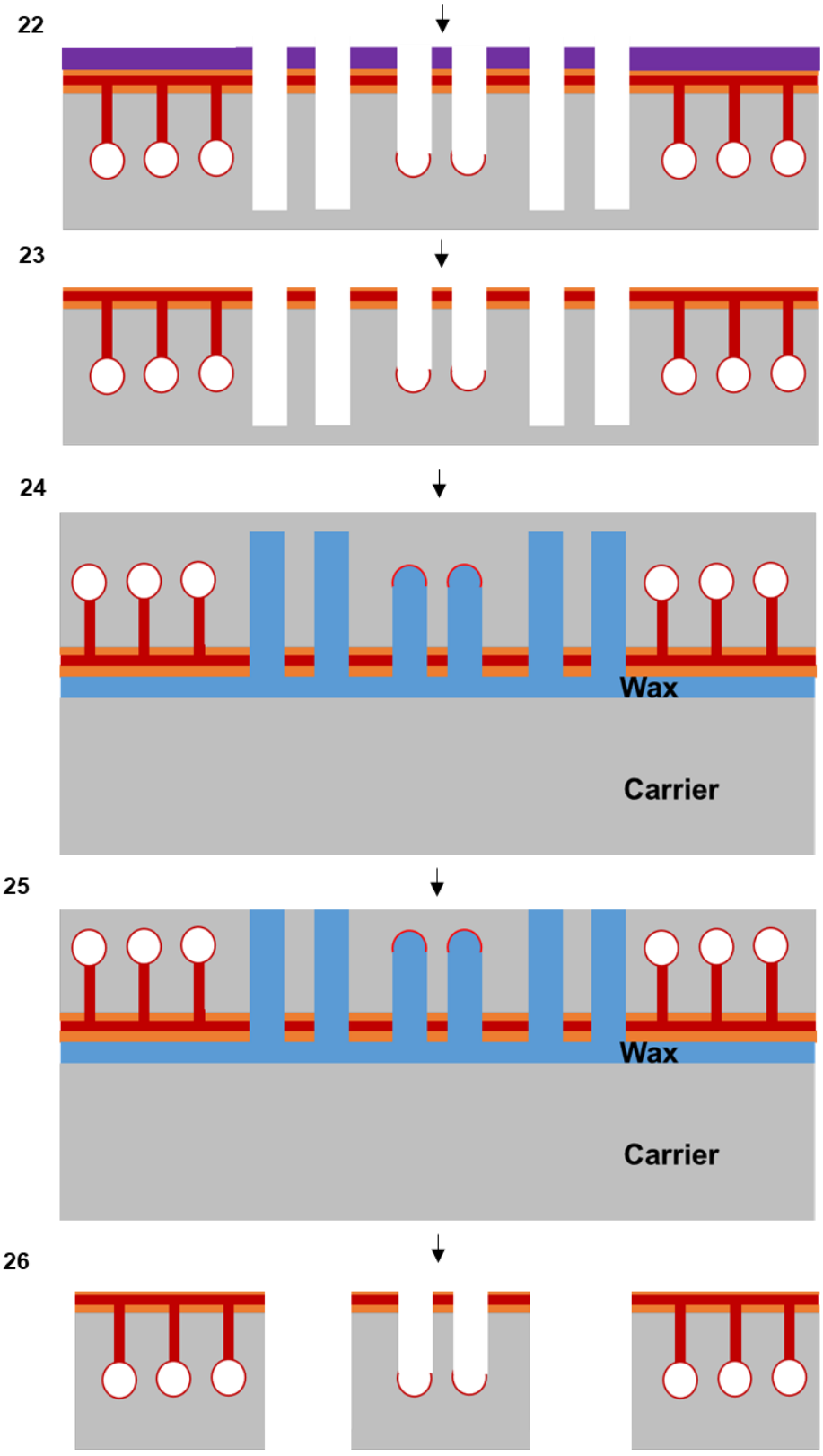

Figure A.4 Continued patterning and etching of probe shapes and orifices, following by backside etching and probe release (Steps 22 – 26)

Appendix B
Step-by-Step Procedures for Microfabrication of Microdialysis Probes

Fabrication of push-pull probes were performed within a class 1000 cleanroom (LNF at the University of Michigan). The probes were fabricated from 525 µm thick N-type 100 mm silicon wafers (Silicon Valley Microelectronics, Santa Clara, CA) using the procedures described below. Schematics of probe processing are shown in Figure B.**1** - Figure B.**5**.

Channel formation

1. Clean surface of wafers using RCA clean process
2. Deposit 2 µm oxide layer using thermal oxidation
3. Pattern channels using lithography
4. Remove oxide layer on channel patterns using RIE
5. Etch channel isotropically to 60 µm wide × 30 µm tall using XeF_2 etch
6. Remove photoresist using PRS2000 or Nanostrip etch
7. Clean surface of wafers using acetone and IPA, and deposit 3 µm poly Si for channel seal using LPCVD
8. Remove poly Si surface until the oxide layer expose using DRIE
9. Remove 2 µm oxide layer using RIE or wet etch in BHF
10. Clean surface of wafers using acetone and IPA, and deposit 2 µm poly Si for channel reseal using LPCVD
11. Deposit 500 nm oxide layer using LPCVD

Probe shape and sampling areas

12. Pattern probe shapes using lithography
13. Remove 500 nm oxide layer on probe shape patterns using RIE or wet etch in BHF
14. Remove photoresist using PRS2000 or Nanostrip etch
15. Pattern probe shapes and sampling areas using lithography
16. Etch probe shapes for 100 µm depth using DRIE
17. Remove 500 nm oxide layer on probe shape patterns using RIE or wet etch in BHF
18. Remove photoresist using PRS2000 or Nanostrip etch
19. Etch poly Si sampling areas to 2 µm thick using DRIE
20. Deposit 400 nm thick of Al using e-beam evaporator
21. Form nanoporous AAO using anodization process
22. Etch poly Si sampling areas through AAO mask using DRIE
23. Remove 400 nm thick AAO mask using wet etch in Al etchant
24. Deposit 3 µm thick of Al using e-beam evaporator
25. Form nanoporous AAO using anodization process
26. Mount the wafer on a carrier wafer using Crystalbond 555 adhesive
27. Etch backside of the wafer to desire thickness of 40 - 50 µm using DRIE
28. Release probes in hot water

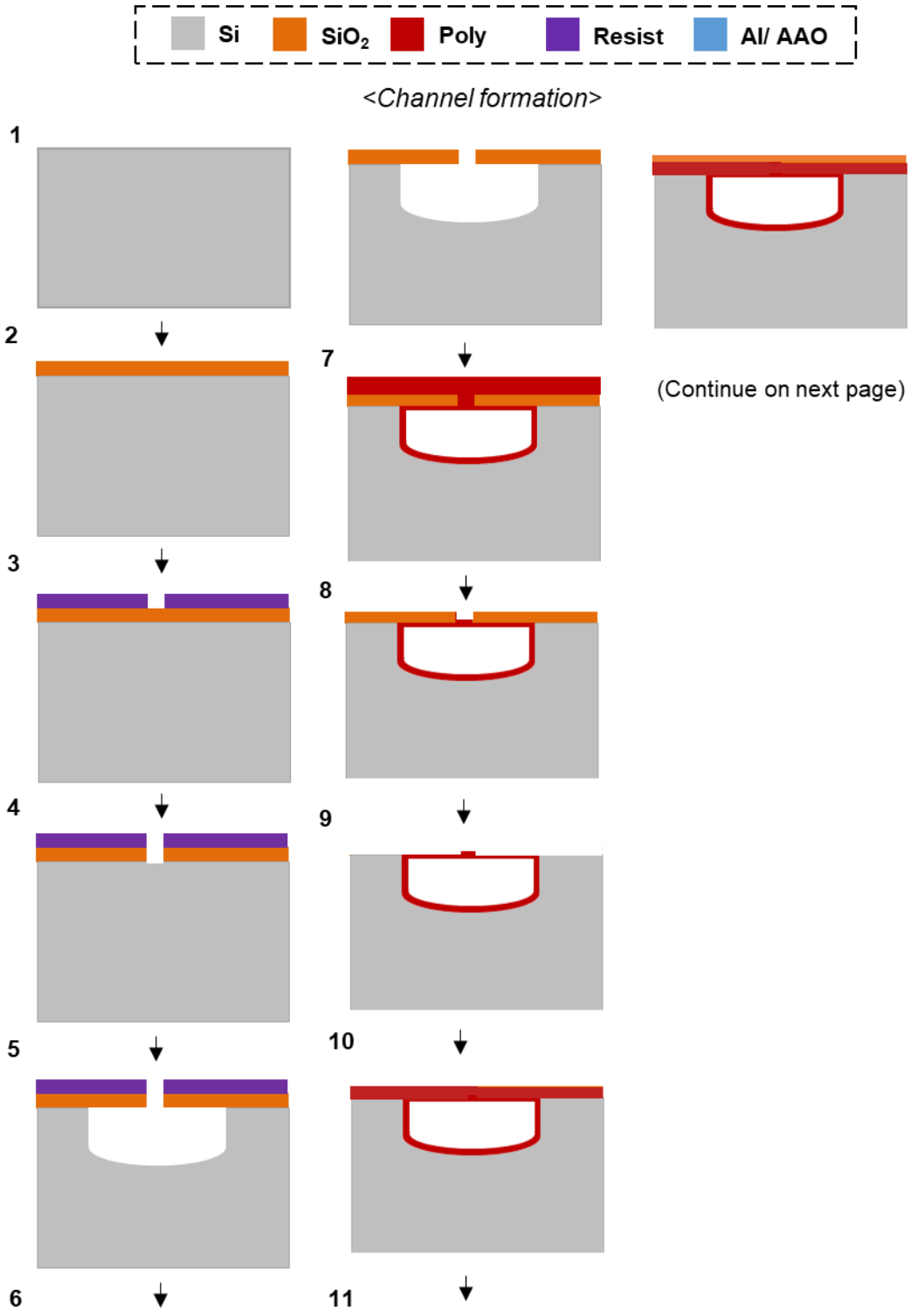

Figure B.1 Channel formation (Steps 1 – 11).

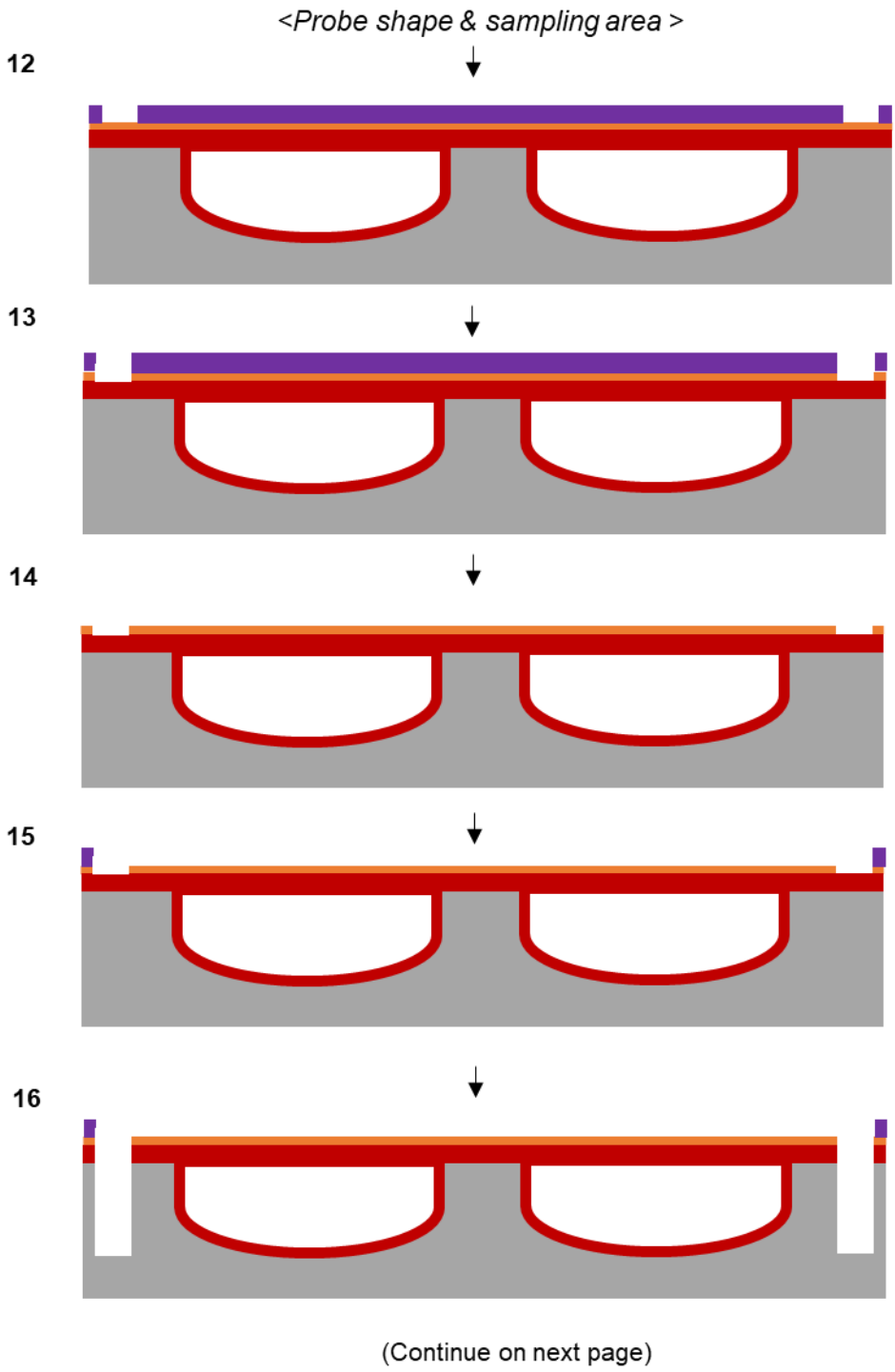

Figure B.2 Patterning and etching of probe shape and sampling area (Steps 12 – 16)

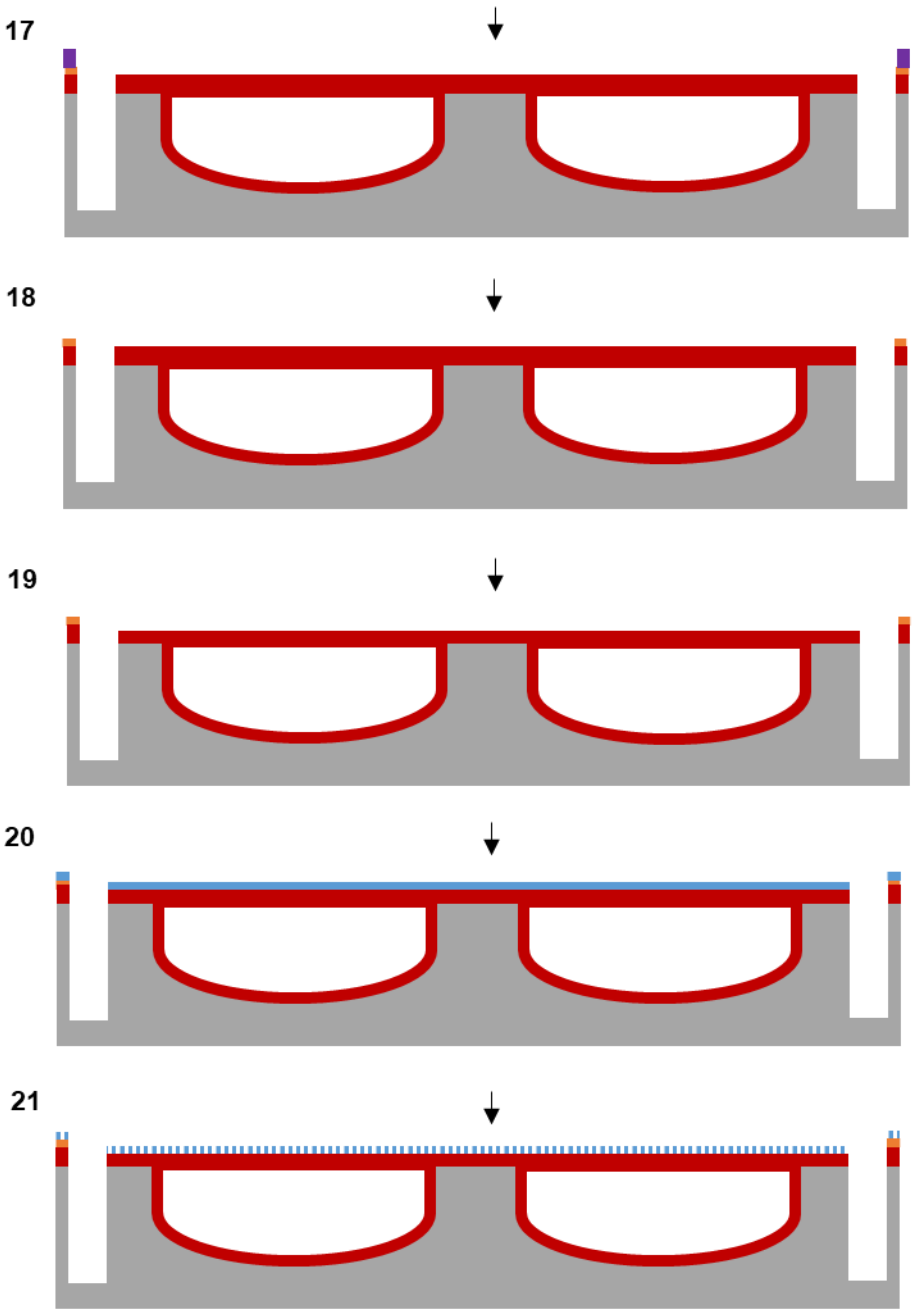

(Continue on next page)

Figure B.3 Continued patterning and etching of probe shape and sampling area

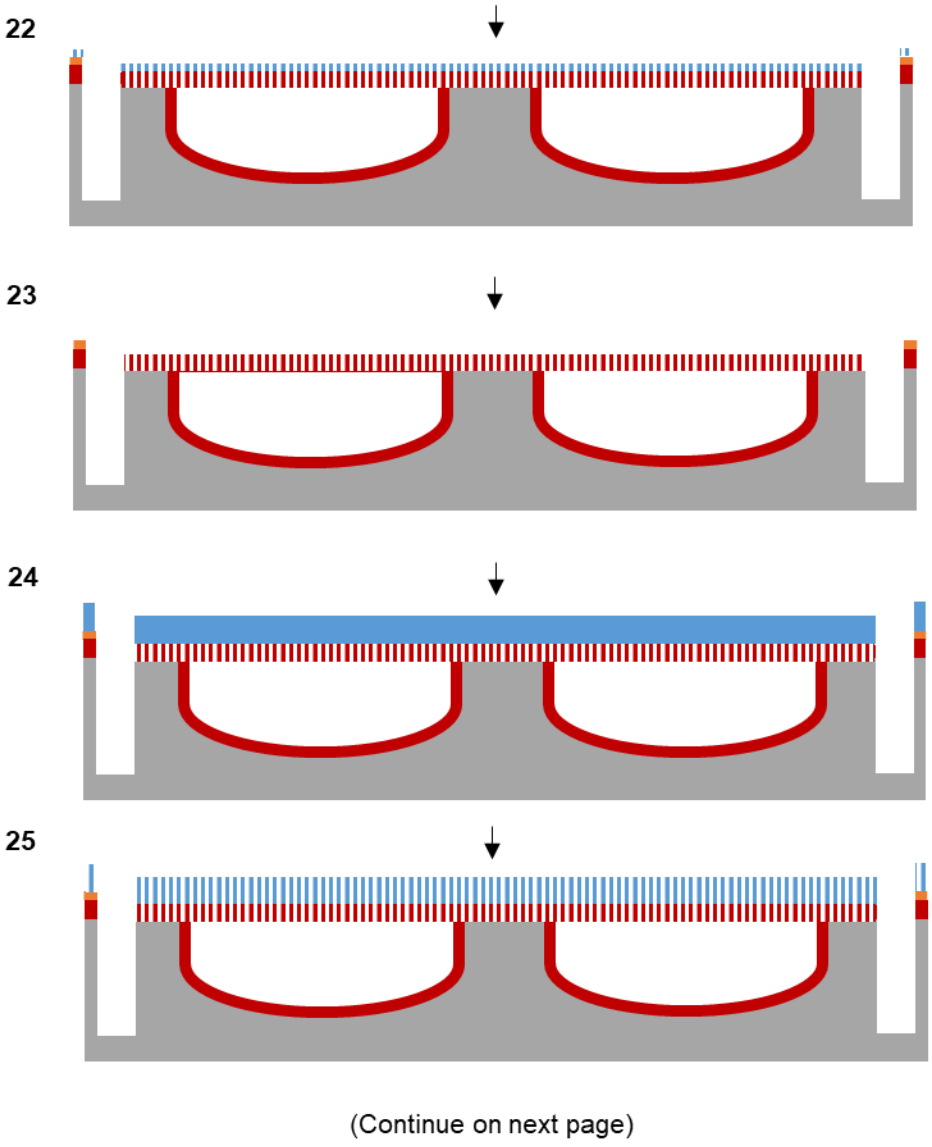

(Continue on next page)

Figure B.4 Continued patterning and etching of probe shape and sampling area (Steps 22 – 25)

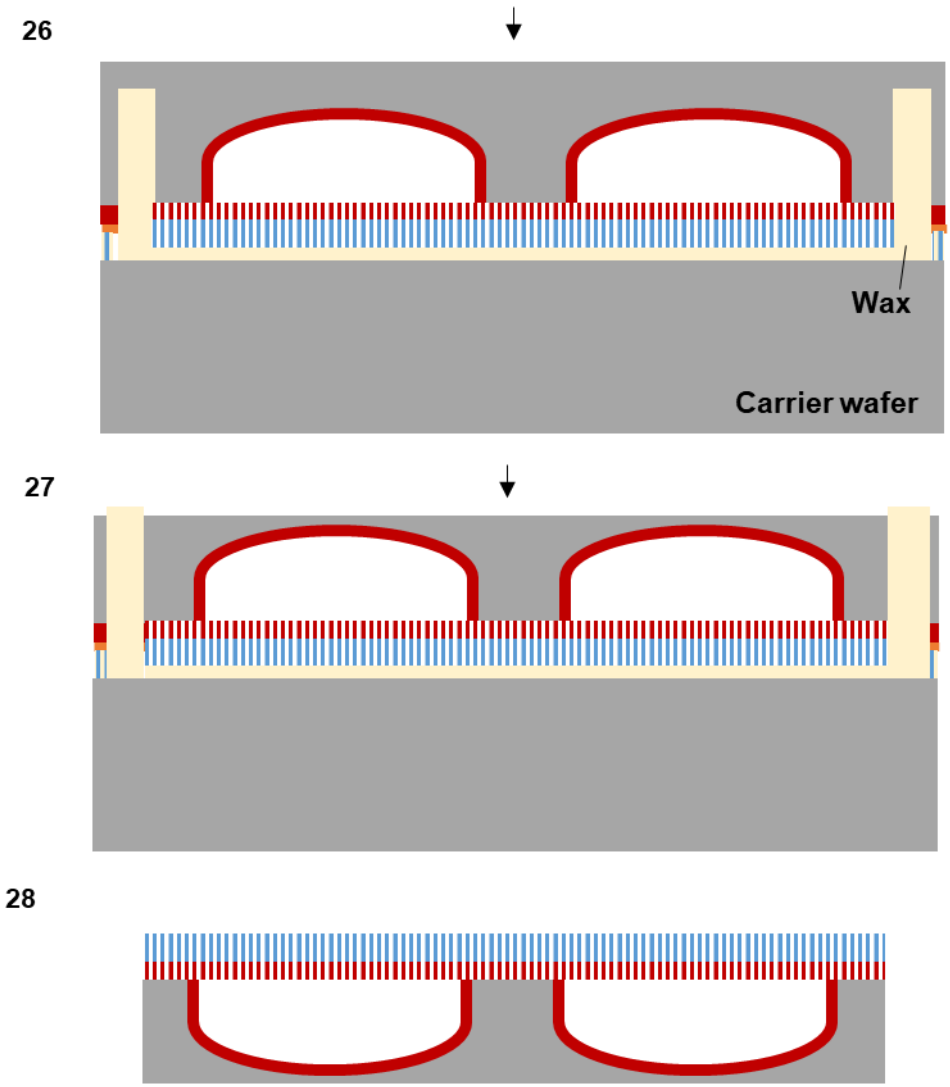

Figure B.5 Backside etching and probe release

Appendix C
Two-Step Anodization Process for Membrane Fabrication

Our AAO mask for fabrication of the dialysis membrane has been made by one-step anodization process[223]. This process had limitation in quality of its formed structures, as demonstrated in Chapter 5. Consequently, variations in feature proximity and aspect ratio of the mask were often observed, especially when it was formed on rough poly Si surface. These factors ultimately led to inconsistent etch rate across the substrate and distorted etch profiles. In this work, we have adapted the two-step AAO process with the aim of improving quality of the membrane fabrication. Two-step anodization process has been reported to improve overall quality of the AAO[127,136]. The two-step AAO is based on a typical AAO processing with replication of anodization process. After first anodization, the first-step AAO is removed to expose highly periodic and indented surface. These sites allow formation of highly ordered and uniform pores in the second anodization.

This study was performed using a standard silicon substrate covered with a ~3 μm thick layer of poly Si using LPCVD. A schematic of the procedure for fabricating the two-step AAO mask, in comparison with the one-step AAO mask, is shown in Figure C.**1**. Since the two-step process required removal of the initiated AAO, a thicker layer of Al (i.e., 1000 nm) was coated on the substrate instead of a 400 nm thick Al. Anodization conditions were 0.3 M oxalic acid at 60 V and 15 °C. For the first anodization in the two-step processing, optimization of the time must be performed as the final thickness was based on the thickness of this first step AAO (i.e., final thickness equals to the thickness of deposited Al subtracted

by the thickness of first step AAO). Removal of the first step AAO was carried out by wet etch using a mixture of 0.2 M chromic acid and 0.4 M phosphoric acid, at 60 °C for 30 min. After rinsing, the second anodization was performed as usual (i.e., in 0.3 M oxalic acid at 60 V and 15 °C for 15 min; the longer time was generally used to ensure complete pore growth and ordering). Finally, for pore widening and barrier removal, the AAO was immersed in 0.86 M phosphoric acid at room temperature for 55 min.

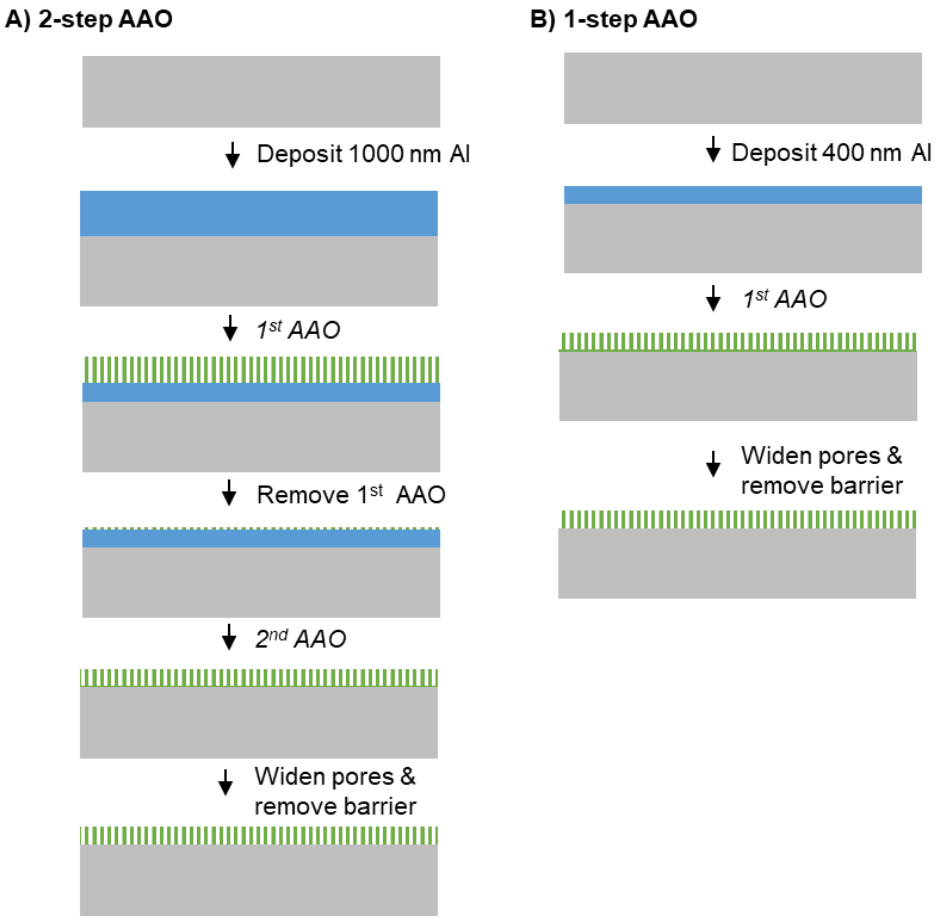

Figure C.1 Fabrication procedures for A) two-step AAO mask and B) previously reported one-step AAO mask

With the above anodization conditions, we found that the first-step AAO layer was formed at ~5 nm/s. Anodization time of 120 s was used to create the first AAO layer with

600 nm thick. Hence, the final thickness of the AAO mask was 400 nm. This process allowed flexibility in controlling and modifying thicknesses of the final mask based on adjusting the anodization time (versus using several runs of PVD to deposit Al at different thicknesses). For example, in addition to the 400 nm thick mask, the anodization time in the first step can feasibly be adjusted to 150 s to fabricate a 150 nm thick AAO mask. Thus, this approach proved to be useful when one would like to alter the mask thickness during optimization of etching process, as demonstrated below.

An example of the SEM images for comparison between one-step AAO mask and two-step AAO mask fabricated on the rough poly Si substrate is shown in Figure C.**2**, A&B. As expected, the two-step AAO process produced more ordered and straight pores. Furthermore, due to the process of removal of the first-step AAO, the top surface of the two-step AAO mask was more even and cleaner as compared to that of the one-step AAO. To investigate the effect of mask qualities on etching profiles, DRIE was used to etch the poly Si layer through the different AAO masks. As seen in Figure C.**2**, use of the two-step AAO mask yielded poly Si pores with more ordered and more vertical features. As a result, almost no merging pores at the upper sidewalls were observed when using the two-step AAO mask.

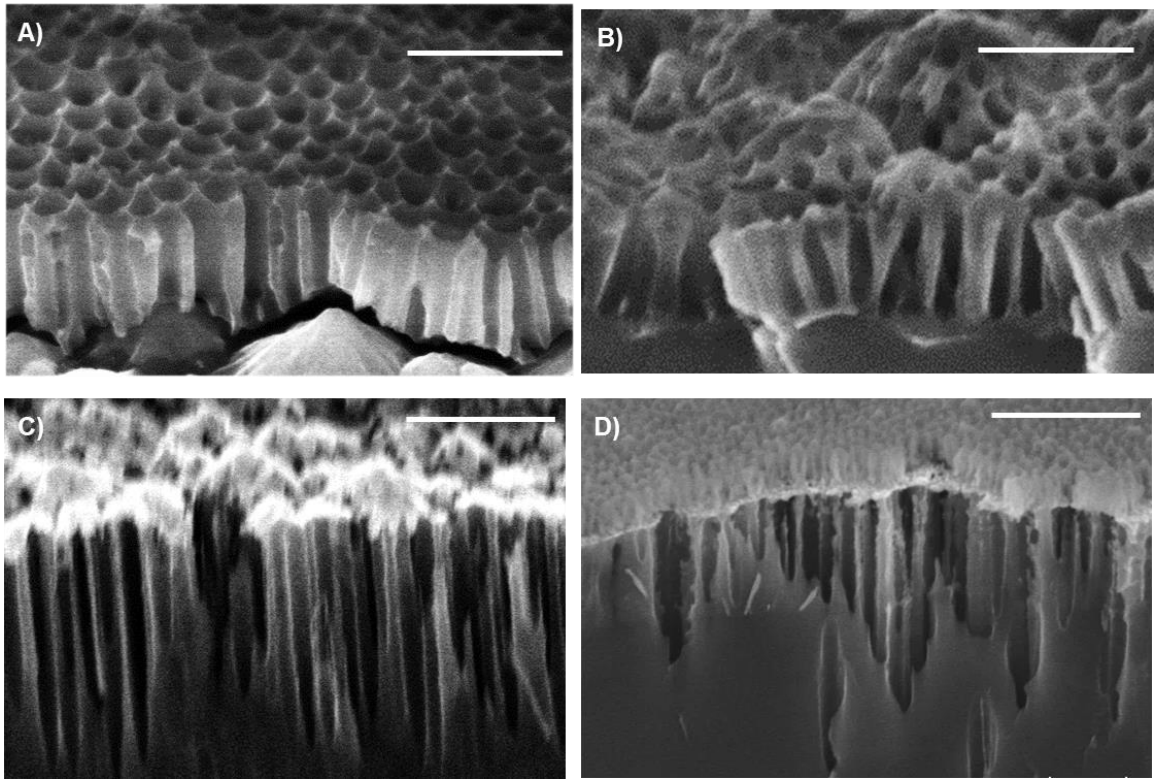

Figure C.2 Representative SEM images of AAO masks made by A) two-step processing and B) one-step processing. The mask A and B were used for DRIE of the underneath poly Si layer, resulting in C) and D), respectively. DRIE time was 15 min. Scale bars were 500 nm for A&B and 1 μm for C&D.

Although the quality of etched features was improved, tapered profiles still occurred in some etched pores (starting at the etching depth of 1.5 - 2 μm). This factor may eventually limit the maximal etching depth. In plasma etching, a thin mask is generally favorable to a thick mask because the thin mask has less propensity for etch stop and distortion of sidewall's etched features[251]. Additionally, because of depletion of etching species as they go deeper, the etching is slower as the depth increases[255]. Thus far the AAO mask was selected to be used at a target of 400 nm thick. We accordingly further investigated whether a thinner mask can be used to improve upon the above limit of etching depth. A two-step AAO mask with a thickness of 150 nm was fabricated and used in DRIE through the poly Si substrate. An example of the etched poly Si pores is shown in Figure C.**3**. As seen, the thinner mask

facilitated formation of pores with vertical features, which was desirable. Furthermore, with the same etching time used above (i.e., 15 min), over 3 μm of the poly Si layer was etched thorough, indicating a faster etch rate when using a thinner mask. A combination of these features (more vertical profiles and faster etch rate) facilitated fabrication of a poly Si membrane with high aspect ratio nanopores, i.e., an aspect ratio of > 50 was made possible while it was limited to < 30 in the previously fabricated membrane.

These initial findings illustrated potential utility of the 2-step AAO mask in formation of a high quality poly Si membrane. The process with a 400 nm thick mask should be suitable to fabricate 2 μm thick poly Si membrane with complete pore formation. Using a thinner mask, the process ensures desirable etched features and further allows fabrication of a thicker poly Si membrane, which can be advantageous to improve its physical strength. With these improvements, we anticipate that the poly Si membrane will be functional even without the AAO layer. The AAO layer can eventually be removed from the probe, resulting in the final membrane with improved integrity. While the procedure describe here is intended to be implemented in microfabrication of a dialysis probe, it is readily adaptable to fabrication of other analysis microsystems in need of nanoporous membranes[118,289].

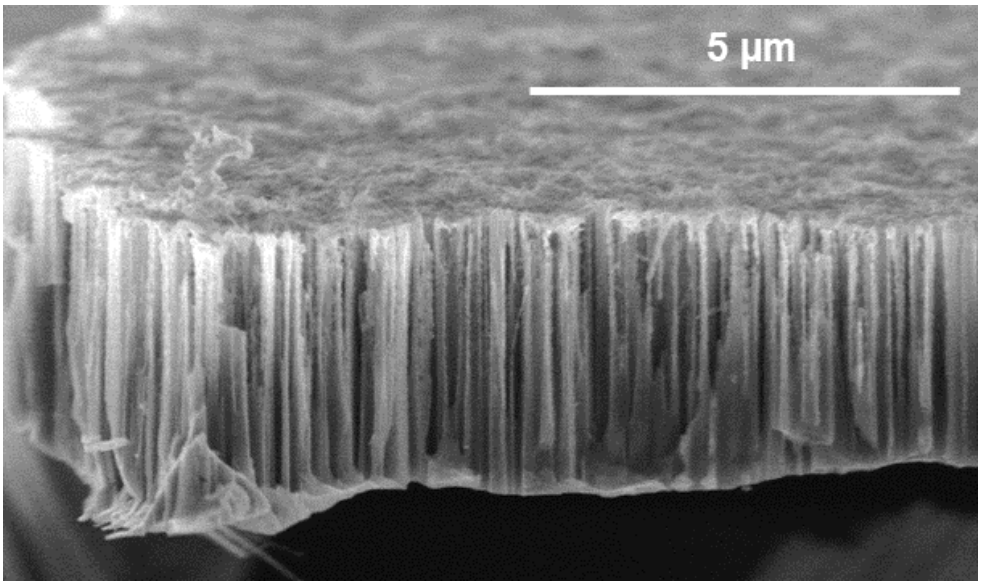

Figure C.3 High aspect to ratio nanoporous poly Si membrane, fabricated by using a thin AAO mask.

Appendix D
Design and Microfabrication of a Miniature Fiber Optic Probe with Integrated Lenses and Mirrors for Raman and Fluorescence Measurements

Introduction

Raman and fluorescence spectroscopies, are powerful analytical tools due to their high sensitivity, fast response, and information content. One format for these techniques is based on fiber optic probes that incorporate lenses and mirrors on the probe tip for guiding light between sample and optical fibers. Probes can be placed directly on or into a sample providing convenient, sensor-like operation. Such probes have been used for pharmaceutical process monitoring[290], on-site environmental analysis[291,292], study of animal tissues in vivo[293,294] and diagnosis during clinical endoscopy[295,296]. Although popular, the bulk of such systems can limit their application where miniaturization is needed. One area where miniaturized probes may be used is in biomedical Raman because the small size is useful in reducing invasiveness of clinical procedures and allowing measurements on smaller structures. Miniaturized probes could also enable measurements in other small environments, e.g. in microfluidic analytical systems.

Miniaturized Raman probes have been made by assembly of compact optical components (e.g., lenses and filters) and fiber optics[297,298]. Such probes are commercially

available, but they are typically expensive because of costs associated with material handling and precise optical alignment at small scale. These approaches also limit the extent of miniaturization. Commercially-available Raman probes are typically 10 mm diameter or larger. Several miniaturized fiber optic probes with lenses have been reported that are 2 mm diameter[299–301]. The smallest lensed probes reported are 0.75 mm diameter but require a complex and tedious fabrication process including assembly and alignment of a bundle of 125 μm diameter optical fibers, use of adhesives for bonding, and procedures for handling, grinding, and polishing micro-optical components[302]. For biomedical applications, sterilization protocols add mechanical requirements and manufacturing complexity. Routes to simpler fabrication and further miniaturization are of interest.

Microfabrication has emerged as a useful approach for miniaturizing optical systems[303–308]. Microfabricated optics for chemical analysis have primarily been used in microfluidic chips. Through microfabrication, optics can be integrated into a microfluidic chip with precise alignment and produced en masse. The integrated devices have been used for a variety of applications including protein separation, DNA analysis, and flow cytometry[309–311]. Many designs utilize rapid prototyping in polydimethylsiloxane (PDMS) due to advantages such as low-cost and ease of fabrication[312,313]. Optical elements such as lenses and other waveguides can be fabricated using air-PDMS[314–319] or liquid-liquid interfaces[308,320–326]. Typical designs use fiber optics to deliver light from the source and to collect signal from microfluidic channels[327–332]. These systems are usually developed with extensive integration in mind and their sophisticated designs allow specific performance to be achieved; however, they also require fixed optics and therefore are not flexible in their use. In addition, the optics and the microfluidic systems must be manufactured simultaneously,

leading to more potential points of failure and complication in fabrication processes[333]. Although extensive precedence exists for microfabricated optical systems, little work has been reported on microfabricated free-standing probes. Such an approach may allow miniaturization of probes to enable Raman or fluorescence measurements in small spaces while also reducing the cost.

We report microfabrication of miniaturized, freestanding optical probes that can be coupled to fiber optics for Raman or fluorescence measurements. The probes are over 100-fold smaller than conventional Raman probes and are the thinnest lensed probes reported[299,300,302]. The miniaturized probes allow measurements in small spaces, e.g. on microfluidic devices. Finally, the potentially low cost of fabrication suggests the possibility of disposable probes that would facilitate at patient or in vivo diagnostics and other applications.

Experimental

Refractive Index (RI) Characterization and Optical Design

The RI of PDMS (Sylgard 184, Dow Corning, Midland, MI) from 200 to 800 nm was measured on a flat surface of the polymer using an ellipsometer (Sopra GESP-5, Semilab, North Billerica, MA). For these measurements, a 1/4" thick slab of PDMS was cast against a glass plate and cured between 90 °C and 100 °C for 45 min according to the manufacturer directions (1:10 ratio of parts A:B).

Zemax (Zemax LLC, Kirkland, WA) was used in non-sequential mode to model multimode glass optical fibers and air-gap optical elements in a PDMS device. The measured RI values of the PDMS were used to design lensed probes for collecting light from a liquid

sample outside the PDMS probe through 0.22 numerical aperture (NA) low-OH multimode optical fibers. Mirror elements were created using total internal reflection by designing the angle of incidence on the mirror elements to be greater than the critical angle. Molds forming the optics were designed to avoid high aspect ratio elements that would resist demolding of the final device. Lens and mirror properties (position, angle, height, thickness and curvature) were adjusted to maximize fluence arriving at the focal region of the probe. For simplicity, both the excitation and collection fibers were treated as fiber optic light sources in the model. An example of Zemax simulation is shown in Figure D.**1**A.

Mask Design

AutoCAD was used to design lithographic masks based on the optimized Zemax models. Additional features were incorporated such as skid-and-post structures for holding the fiber optics, a bounding box to act as the outer edge of the probe mold, and registration patterns for allowing spatial alignment of multiple feature layers. Three separate layers were designed and printed onto emulsion film masks with a 7 μm minimum feature size (Fineline Imaging, Colorado Spring, CO). These masks (Figure D.**2**) were used to sequentially expose each physical layer in the lithography process. An illustration of the fiber encapsulation features are shown in Figure D.**1**B, which shows skids made in the first lithographic layer, posts in the second lithographic layer, and the bounding box formed in the third lithographic layer, along with a fiber snapped into place after development of the unexposed SU8.

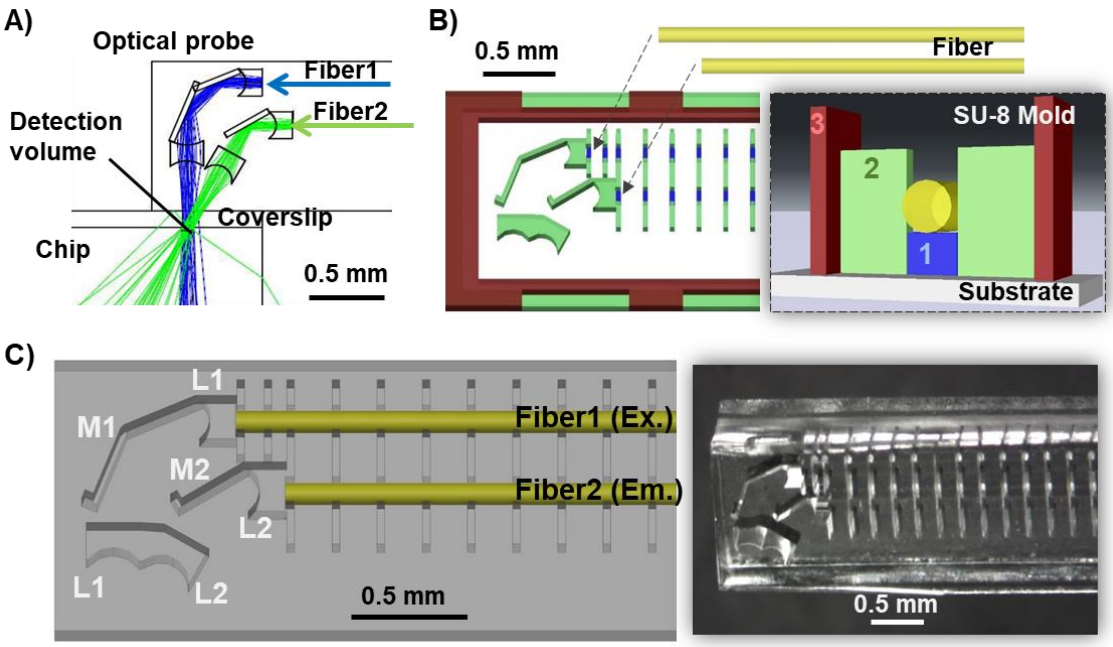

Figure D.1 Design of a microfabricated probe. A) Zemax simulation of the optical pathway of the probe coupled to a microfluidic system. The optics include mirrors (M) and lenses (L), which are designed to focus 100 μm below the coverslip. Fiber 1 is used for guiding excitation light from a light source, which corresponds to 90° incidence, and Fiber 2 is used for guiding emitted light to a detector, which corresponds to 65° incidence (° incidence= angle at which the light ray strike the sample surface. L1 and M1 reflect and focus excitation light from Fiber1 onto a sample in a microfluidic chip. L2 and M2 gather and focus the emitted light to Fiber2. B) Drawing of a mold used to fabricate the PDMS probes. Mold is made from SU-8 photoresist on a Si substrate. The inset shows a cross-sectional view of the mold with fiber optic inserted. The mold is fabricated from 3-layers of SU-8. The drawings are color-coded by layer thickness. The blue layer (#1) is the thinnest and serves to hold the fibers at the proper height like "skids". The green layer (#2) consists of the posts for guiding and holding the fiber in place. The green layer also creates the optics on the probe tip. The red layer (#3) creates the outer boundary of the mold and therefore defines the overall probe size. The fiber optic is inserted to act as part of the mold and create a defined space for the probes. The fiber optics are butted to the optical lenses. C) Drawing (left) and microphotograph (right) of PDMS probe created using mold in Figure 1B. The probe includes 2 fiber optics which are inserted through the guide created by the molding process. Optical components formed by air gaps (white-text label) created from the mold. The final overall probe dimensions are 1.1 mm wide x 0.52 mm thick.

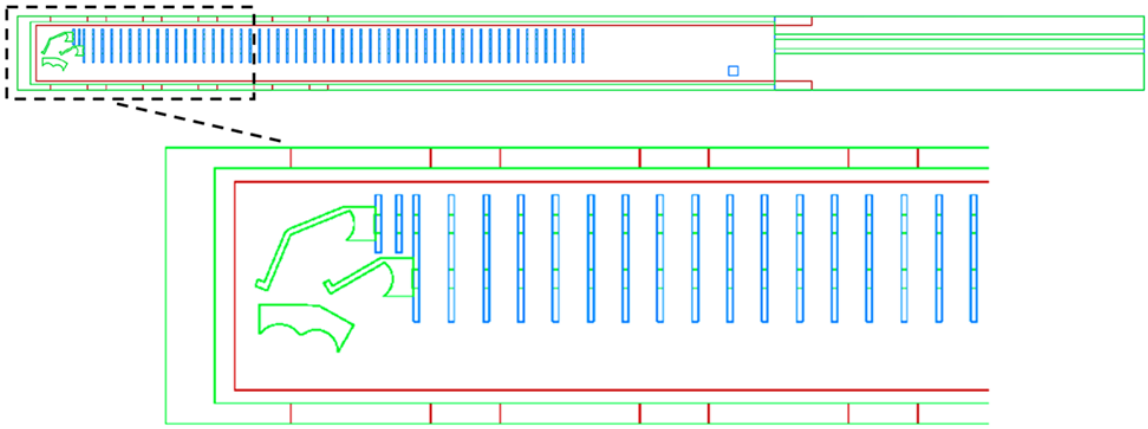

Figure D.2 AutoCAD design of a representative probe (side-firing), showing layouts of 3 lithographic masks. The first lithographic layer (blue) includes the skids for lifting optical fibers from the mold. The second layer (green) consists of the posts for holding optical fibers, and optical components at fiber tips. The third layer (red) includes a bounding box, used as the outer edge of the probe.

SU-8 master mold fabrication

The master mold was microfabricated using SU-8 2075 photoresist (MicroChem, Newton, MA) on a 4-inch Si wafer (ID: 1116, University Wafer , Boston, MA). This mold consisted of 3 layers (see Figure D.**1**B). The first layer was created by spin-coating a 110 µm thick layer of photoresist onto the wafer, followed by a soft-bake process. The wafer was aligned to the photomask and UV exposed for 18 s at 17 mW/cm^2. The photoresist layer was then post-exposure baked to polymerize the exposed pattern. The second and third layers of the device were created via a similar process. The second layer was 300 µm thick using an exposure time of 28 s, while the third layer was 110 µm thick with 34 s exposure time. Each subsequent exposure during the UV lithography process crosslinks all polymer in the lower layers, creating solid structures down to the silicon wafer substrate. After the final post-exposure bake, SU-8 developer solution (MicroChem) with sonication was used to dissolve unexposed photoresist. The SU-8 mold surfaces were exposed to trichloro(methyl)silane (Sigma-Aldrich, St. Louis, MO) vapor to later aid the release of PDMS from the mold. All times and temperatures used for soft-bake and post-exposure bake were according to the

MicroChem SU-8 2000 processing guidelines for the cumulative thickness (see Table D-1 for specific used temperatures and times).

Table D.1 Summary of specific conditions for soft-bake, exposure, and post-exposure bake processes. The baking processes were two-step processes, with 65 °C followed by 95 °C. The exposure energy was 17 mW/cm^2.

		Soft bake			Post-exposure bake	
	Thickness	**65°C**	**95°C**	**Exposure**	**65°C**	**95°C**
1	110 μm	5 min	20 min	18 s	5 min	10 min
2*	2 × 150 μm	2 × 5 min	2 × 30 min	28 s	5 min	23 min
3	110 μm	5 min	20 min	34 s	5 min	29 min

*Layer 2 is 300 μm thick, created by spin-coating twice of 150 μm thick photoresist layer. The 300 μm thick layer was then exposed at once.

Probe Fabrication

A schematic summarizing the fabrication process of probe can be seen in Figure D.**3**. A pair of 2 m long segments of 105 μm core/125 μm clad/ 250 μm polyimide coated low-OH optical fiber (FG105LCA, Thorlabs, Newton, NJ) were used. A 4 cm segment at the end of each fiber was stripped to remove the polyimide, and then flat-cleaved using a wide-blade fiber scribe (F-CL1, Newport, Irvine, CA). The flat-cleaved optical fiber segments were manually positioned in the SU-8 skid-and-post mold structures so that the cleaved end of the fiber was in contact with a physical stop designed at the entrance of the optical system, as illustrated in Figure D.**1**B. A small volume of PDMS prepolymer (~1 mL Sylgard 184, Dow Corning, Midland, MI) was prepared in a 1:10 w/w ratio, mixed, and poured into the SU-8 molds after insertion of the optical fibers. The wafer assembly was placed in a vacuum chamber to degas the PDMS. A glass microscope slide was pressed firmly into contact with the upper surface of the SU-8 mold to control the probe thickness. The silicon

wafer/SU-8 mold/PDMS/glass assembly was placed in an oven at 95 °C and allowed to cure for 45 min. The lensed fiber optic probes were removed from the mold by carefully separating the glass slide and SU-8 mold. An image of the final probe is shown in Figure D.**1**C. The free ends of the optical fibers were terminated with standard FC-PC connectors (F12073, Fiber Instrument Sales, Inc., Oriskany, NY) using low-fluorescence epoxy (EPO-TEK 301, Epoxy Technology, Billerica, MA).

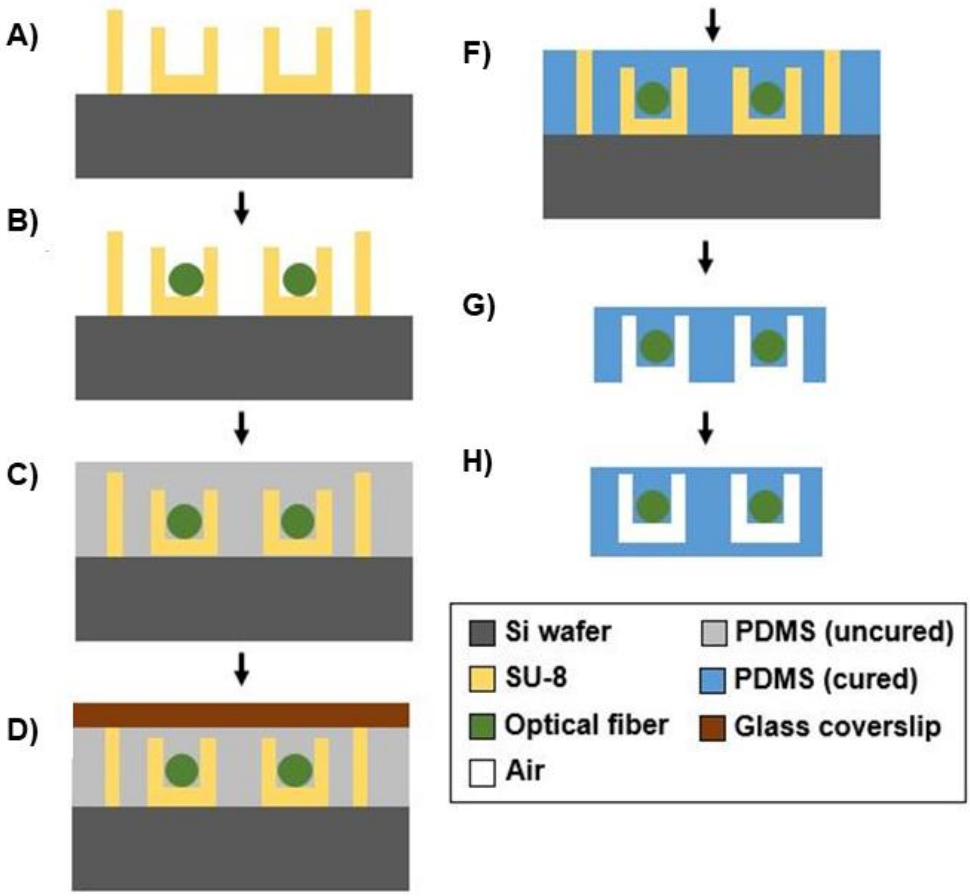

Figure D.3 Illustration of microfabrication process for optical detection probe. The SU-8 mold was created on a silicon wafer by lithographic process and its surface was silanized for ease of PDMS release (A). A pair of optical fibers were inserted into the SU-8 skid-and-post mold structures (B) and a small volume of PDMS prepolymer was poured into the mold (C). A glass coverslip was pressed firmly into the contact with the upper surface of the SU-8 mold; hence, the thickness of the probe was defined by the height of the mold (D). The silicon wafer/SU-8 mold/PDMS/glass assembly was placed in an oven at 95 °C for 45 min to cure PDMS. A glass coverslip was then removed (E) and the probe was released by peeling of PDMS from the SU-8 mold (F). The probe was bonded with a cover layer of ~ 100 μm thick PDMS to prevent dusts and/or solvents from entering air gaps (G).

Probe optical characterization

The transmission efficiency and spectral throughput characteristics of the microprobe were measured and compared against a probe consisting of two bare cleaved fibers. Light transmission through both probes was measured using an optical power meter (PM100, Thorlabs, Newton, NJ) and a 543 nm 1.5 mW He-Ne laser (25-LGR-193-249, Melles Griot, Carlsbad, CA). The transmittance of a NIST calibrated white light source (Hololab Calibration Accessory, HCA, Kaiser Optical Systems, Inc., Ann Arbor, MI) was measured using a spectrometer (USB2000, Ocean Optics, Dunedin, FL) to determine the spectral throughput characteristics of each probe from 200 to 800 nm with an integration time of 1 s. Reflectance spectra using one fiber as a source and the other as a collector were conducted using a fiber optic illuminator (Fiber-Lite 3100, Dolan-Jenner Industries, Woburn, MA) as the source and the same spectrometer, using Teflon as a high reflectance standard.

Fluorescence measurement

Characterization of the fluorescence performance of the probes was preliminarily conducted using a 543 nm He-Ne laser source and USB2000 spectrometer with integration times of 0.1 s to 0.5 s. The probe was placed in contact with a droplet of 10 μM resorufin on a silver-coated glass coverslip (EMF, Ithaca, NY) to determine the response of a bulk solution. To evaluate probe performance on a microfluidic chip, the probes were aligned to a PDMS microfluidic chip consisting of 60 μm deep × 100 μm wide channels, with a 100 μm thick cover layer of PDMS.

For other microfluidic fluorescence assays, the 543 nm He-Ne green laser or the 473 nm blue laser source (473-ST DPSS laser, Sintec Optronics, The Spire, Singapore) were used with a photomultiplier tube detector (Model R1547, Hamamatsu, Japan), coupled to a 580 nm (XF3022, Omega Optical, Brattleboro, VT) or a 535 nm emission filter (HQ535/50M, Chroma Technology Corp, Rockingham, VT). The voltage and amplifier gain of the PMT were set at 0.75 kV and 10^7 V/A, respectively. Initial data were collected with resorufin standards pumped through a fused silica capillary with 150 μm inner diameter × 360 μm outer diameter (Polymicro Technologies, Phoenix, AZ) and a 60 μm deep x 100 μm wide PDMS microfluidic chip. These data were used to determine the detection limit using a 249 point (~1 s) boxcar smoothing.

Figure 6.4 illustrates the arrangement of the probe for on chip fluorescence detection. The PDMS microfluidic chip was fabricated by soft lithography with a channel network design used for enzyme assay and similar to a previously published device[334]. Glycerol standard solutions (Sigma-Aldrich, St. Louis, MO) were diluted to concentrations of 14, 28, 56, and 112 μM with Hank's Balanced Salt Solution (Life Technologies, Carlsbad, CA) before on-chip mixing with free glycerol reagent (Sigma-Aldrich, St. Louis, MO) and 1 mM Amplex UltraRed (Life Technologies, Carlsbad, CA) in 35% DMSO. The solutions were pumped at 1 μL/min using a syringe pump (Chemyx, Stafford, TX). The channel was designed with serpentine mixing and incubation regions. The proprietary fluorescent product (similar to resorufin) was detected at the outlet by a microfabricated probe positioned on the chip.

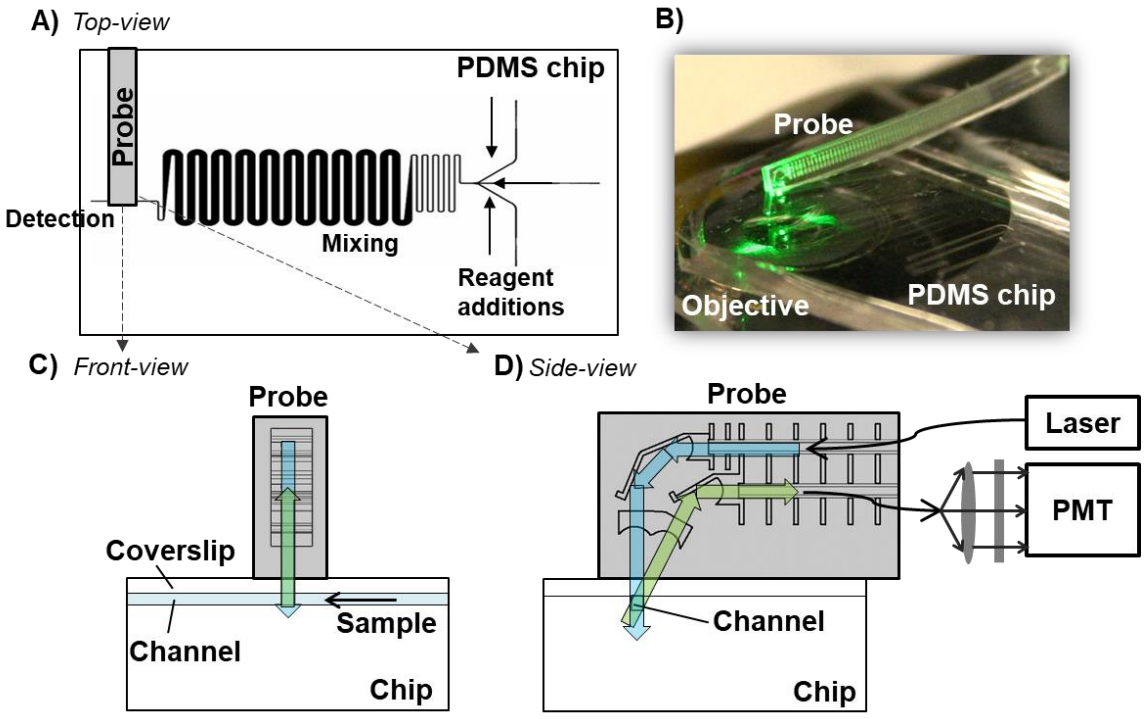

Figure D.4 Position of probe for measuring fluorescence in microfluidic channels. A) Top-view layout of probe positioning on a PDMS-based glycerol assay chip; and B) image of the probe on the PDMS chip with comparison of probe size with a conventional microscope objective underneath the chip. C) Schematic of front-view of the probe on a chip; and D) side-view of the probe on a chip and its experimental set-up for fluorescence detection. At probe tip, the arrows indicate the light pathways into the channel (blue) and from the channel (green).

The same probe was used for on-chip fluorescence detection in glass-based microfluidic devices. Borofloat glass microfluidic devices were fabricated and conditioned as previously described[335–337]. An initial experiment was conducted by passing fluorescein standards through a 25 μm deep × 80 μm wide channel. For an electrophoresis experiment, the channels were filled with sieving media (an entangled polymer solution of proprietary composition, Ab Sciex, part 390953, Framingham, MA). FITC protein ladder (LC5928, Invitrogen, Carlsbad, CA) was diluted 1:10 in the sieving media to a final concentration of ~0.1 mg/mL for each protein. The pinched injection method was used to introduce the sample in separation channel[337]. Size-based separation (separation field of 400 V/cm) was

recorded 4 cm downstream from the injection cross using the probe detection system. At detection, the channel size was 15 μm deep × 50 μm wide.

For on-chip detection using the microfabricated probe, a stereotaxic frame (Model 900, KOPF, Tujunga, CA) was employed to manipulate the probe and align it to the detection zone. An analog-to-digital converter (NI USB-6008, National Instruments, Austin, TX) was used for data acquisition and collection at 250 samples/s under control of LabVIEW (Version 10.0.1, National Instruments). Data was processed in MATLAB (R2012b, MathWorks, Natick, MA).

Raman measurement

The efficacy of the probe for Raman experiments was demonstrated by collecting Raman spectra from water, DMSO, and a commercial aspirin tablet. A fiber-optic coupled Raman spectroscopy system (RamanRxn-1, Kaiser Optical Systems, Inc.) with a back-thinned deep-depletion imaging detector (Newton DU920P-BR-DD, ANDOR Technology, Belfast, Ireland) was operated in full-vertical-binning mode to collect Raman spectra. A 100 mW, 785 nm excitation laser was connected to the 65° incidence fiber, while the Raman signal was collected through the 90° incidence fiber channel. Raman spectra were collected with 5 s acquisition times.

Results and Discussion

Design and Fabrication of the Probes

Our goal was to design a free-standing probe with integrated optics that could focus and collect light from outside the probe, be easily coupled to fiber optics, and have separate

input (e.g. excitation) and output (e.g. emission) paths. Figure D.**1** illustrates the side-firing design that was fabricated and tested. The probe contains guides for inserting optical fibers precisely and optics at the probe tip for guiding light in and out of the probe.

One consideration for precise design of optical elements is the RI of the PDMS, which can vary significantly depending on selected wavelengths, curing times, and temperatures. The measured RI values at 200 to 800 nm wavelengths ranged from 1.42 to 1.58 for PDMS (Figure D.**5**). The RI change is particularly small between 400 and 800 nm. This small RI dispersion suggests the possibility of microfabricating PDMS lenses with low chromatic aberration at the wavelengths of visible light. On the other hand, the RI increases rapidly at the wavelengths of UV light (200 to 400 nm).

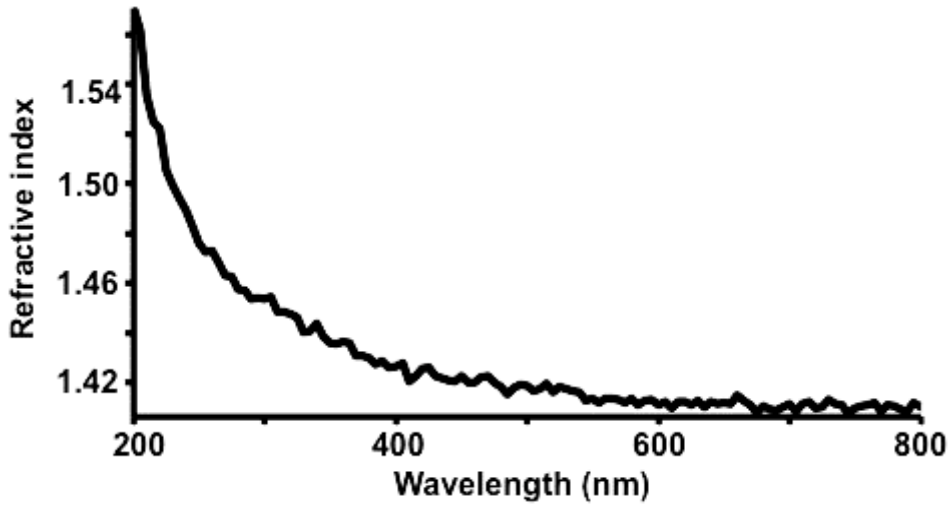

Figure D.5 Refractive index of PDMS, Sylgard 184, from 200 to 800 nm. The PDMS was cured at 95 °C for 45 min.

The measured RI values were used with Zemax to design optical elements that were optimized for light in the range of 200 to 800 nm (Figure D.**1**A). The cylindrical optics (e.g. lens and mirrors) in the fabricated probe were designed to generate a line-shaped focus100 μm below a coverslip. In the design, one fiber optic is used for excitation while the other is

for collection of emitted light. The probe generates focused light at 90° incidence for the first fiber and 65° incidence for the second fiber. Folding mirrors are incorporated so that the source and collection regions overlap as necessary for Raman or fluorescence measurements. The probe design has the benefit of maintaining the source and collection optical fibers along a common axis on a single side of the sample which facilitates having a small but robust probe. The side-firing design also avoids probe deformation during alignment to the sample.

To accommodate two 125 μm diameter optical fibers, the width of these probes must be at least 400 μm, including the protective layers. In practice, a 90° side-firing probe incorporating two 30º incidence total-internal-reflectance based mirrors requires a minimum width of approximately 1.1 mm based on the optimized Zemax model. These probes have a total thickness of approximately 500-600 μm, including an externally bonded 100 μm PDMS cover layer.

We fabricated devices using inexpensive emulsion masks with a surface roughness of approximately 2 μm. The layer thicknesses are within 2% of the design values, and the optical features are within 2% of the target size. The aspect ratio has not been well optimized; instead, feature sizes are deliberately kept large to avoid issues with mold fabrication and demolding of the PDMS structures. Resulting probes were too small and flexible to be handled conveniently; thus, a holder was required for further experiments. In this study, we selected a commercially-available stereotaxic alignment system for use as a holder and a micro-positioner. The stereotaxic system allowed us to precisely manipulate probe position and to secure probe placement on/in sample substrates.

Optical Characterization of Probes

To evaluate optical performance of the microprobe, a series of comparisons were made to a probe consisting of two cleaved bare fibers assembled side by side with identical FC connections. The optical throughput of the microfabricated probe was determined by injecting laser light at the FC fiber interface and measuring the optical power transmitted through the probe face. The bare fiber probe has 84% throughput while the probe with fabricated optics has 70% throughput. These results suggest that the majority of the 16% loss in the bare fiber is due to losses in injecting light through the FC connector, and in the microprobe an additional 14% loss is due to the probe optical elements. Reflection losses could potentially be further reduced by the use of coupling gels or index-matching fluids, which were not used in this case. To determine if any spectral artifacts are caused by the microfabricated optics, we compared white light throughput of the microfabricated probes to the throughput of a bare fiber using a spectrometer. The spectra are identical for both probe types, as illustrated in Figure D.**6**A, indicating no spectral artifacts are generated by the microoptical system.

To compare the background scattering arising from the probe optics, a white light reflectance spectrum was collected with the probes pointing into free space in a dark room, as shown in Figure D.**6**B. The scattered white light background generated from the microfabricated probe is significant, while the bare fiber probe has no discernible background because the bare fiber probe has no interfaces which can scatter light from the excitation channel back into the collection channel. The 2 μm roughness causes elastic light scattering from the optical surfaces of the microfabricated probe. Next, the collection efficiency from a highly scattering material (Teflon) was measured. Both probe types have

approximately the same collection efficiency, with slightly different spectral collection efficiency due to wavelength-dependent light scattering effects. However, when collection efficiency is tested against a transparent PDMS slab, the bare fiber probe collects 3.3 times more signal than the microprobe. This difference occurs because the surface reflections from the PDMS slab are collected very efficiently by the two parallel fibers. The spatial offset between the excitation and collection paths in the microprobe allow little reflectance to be collected, with half of this reflectance arising within the microprobe as shown by the reflectance in air.

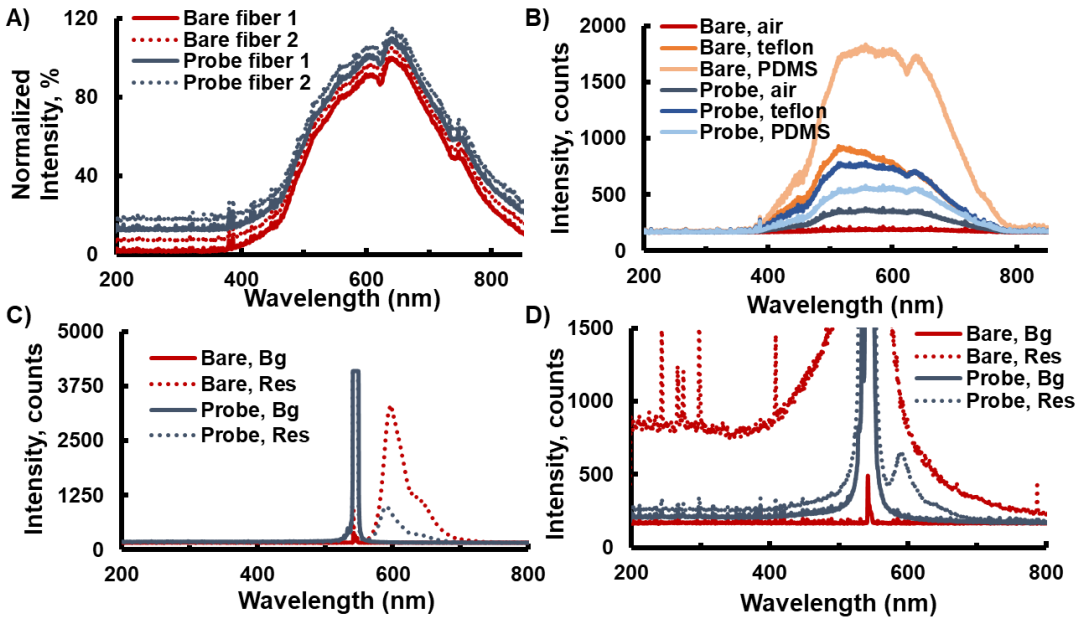

Figure D.6 Spectroscopic performance of probe in comparison to bare fibers. A) Detection of white light through bare fibers (red) and through each lensed fiber (blue), showing identical spectral shapes. Data were offset for comparison. B) White light reflectance spectrum from varied materials. C and D) Laser excitation of 10 µM resorufin with lensed and unlensed fibers immersed in the bulk solution (C) and in microfluidic channels through a 100 µm PDMS coverslip (D). The microfabricated optics' focusing capability offset the reduced light transmission and resulted in stronger fluorescence on chip.

When measuring fluorescence of resorufin in bulk solution, the bare fiber probe collects 2.2 fold more fluorescence than the microfabricated probe because of a higher overall collection solid angle (Figure D.**6**C). However, when measuring resorufin in a

channel buried 100 µm below the surface of the PDMS microfluidic device, the microfabricated probes detect fluorescence comparable to that of bulk solution, whereas the bare fiber probe returned no discernible fluorescence. This result is because the lensed microprobe focuses the light below the surface and into the channel. The bare fiber probe collects the excitation laser light reflected from the PDMS microchip so that the laser signal overwhelms any fluorescence (Figure D.**6**D). The much higher reflectance from the PDMS surface when using the bare probe is in agreement with the results shown in Figure D.**6**B, where the surface reflectance of the bare fiber probe is several fold greater than for the microprobe. The overall results indicate the utility of incorporating optics on a microprobe for collecting light from within a microfluidic sample.

Numerical aperture (NA) is used to characterize the angles accepted through an optical system. In this case, the NA of the probe was defined as a certain angular range over which the probe can deliver light to and collect light from a sample. The NA of the probes made for this study were limited by the NA of the fiber, which was 0.22.

Fluorescence Detection in Microfluidic Systems

Fluorescence in microfluidics or capillaries (e.g., for capillary electrophoresis detection) is usually measured using microscopes or other external assembled optics. Alternatively, microfabricated optics can be built into a chip[314,315]. Here we evaluated the microfabricated probe to measure fluorescence within capillaries or microfluidic chips. For these experiments, the probe was positioned over a capillary (e.g., Figure D.**7**) or microfluidic chip (e.g., Figure D.**4**) with a laser coupled to the inlet and detector to the outlet of the probe.

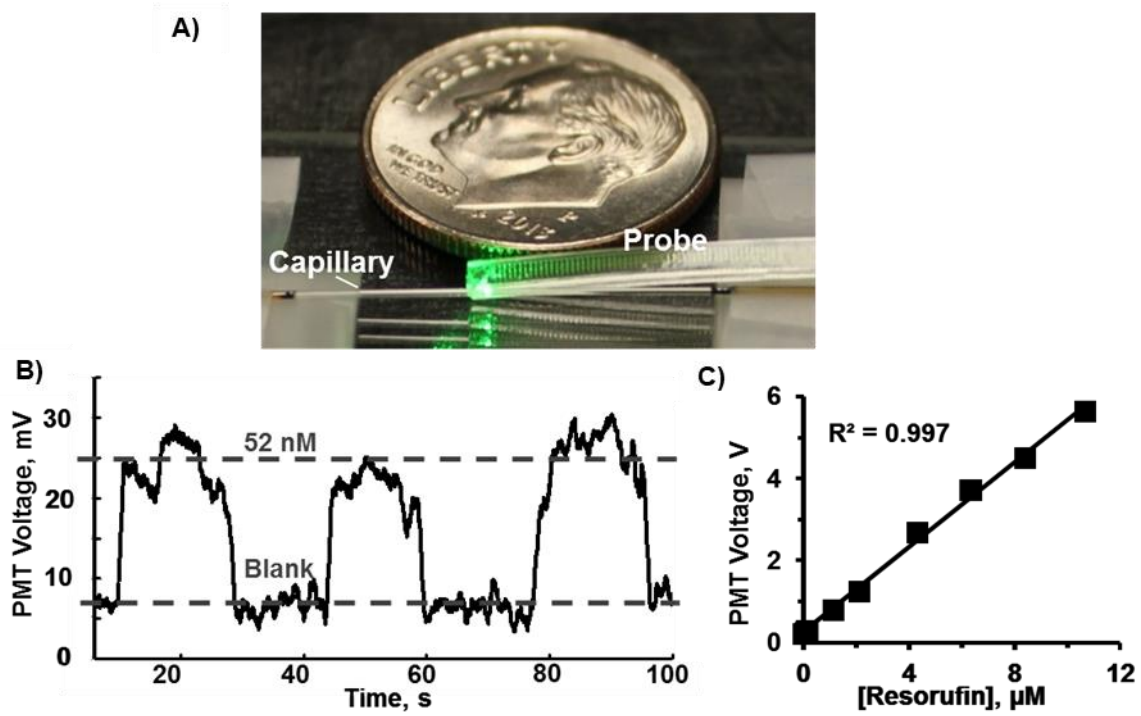

Figure D.7 Probe detection on a glass capillary. a) Image of the probe on the 150 µm inner diameter x 360 µm outer diameter capillary. b) Trace of 52 nM resorufin switching with a blank. C) Calibration curve of 0.05 to 10 µM resorufin, resulting in detection limit of 6 nM after 249 point boxcar smooth, acquisition rate of 250 samples/sec.

We initially tested the probe by detecting resorufin standards in a 150 µm inner diameter × 360 µm outer diameter fused-silica capillary. Figure D.**7** illustrates the trace detected using the probe while passing plugs of 52 nM resorufin through the capillary. Responses to a series of concentrations from 0.05 to 10 µM were linear with R^2 of 0.997. The limit of detection (LOD), determined as the concentration to give a signal 3 times the standard deviation of the blank, was 6 nM. These results demonstrate that the probe is suitable for fluorescence measurements within a capillary.

The probe was then placed on a 60 µm deep × 100 µm wide PDMS chip for on-chip measurement of 0 to 75 µM resorufin standards. This range of standard concentrations was selected to match with the concentrations of proprietary fluorescent products in the following

enzyme assay. Fluorescence detection of different resorufin concentrations is shown in Figure D.**8**A. As shown in Figure D.**8**B, the fluorescence changes were linear with concentration with R^2 of 0.990. The LOD was determined to be 100 nM. Next, we evaluated the performance of the probe to act as a detector for a microfluidic chip used for fluorescence enzyme assay. The probe was positioned over a PDMS chip used for continuous flow enzyme assay of glycerol. The signals of the fluorescent products from different glycerol concentrations pumped through the chip are shown in Figure D.**8**C. Each trace represents the signals upon switching between low and high glycerol concentrations. The fluorescence assay, using the probe as an optical probe, resulted in a linear response with R^2 of 0.988, as shown in Figure D.**8**D. The calculated LOD was 700 nM for glycerol. With probe detection, analytical performance of the on-chip assay is comparable to our previously reported on-line enzyme assay using a fluorescence microscope for detection[338] and other commercial glycerol assay kits[339]. Thus, in this case where the LOD is determined by the enzyme assay, the probe provides comparable LODs but in a compact and low-cost probe.

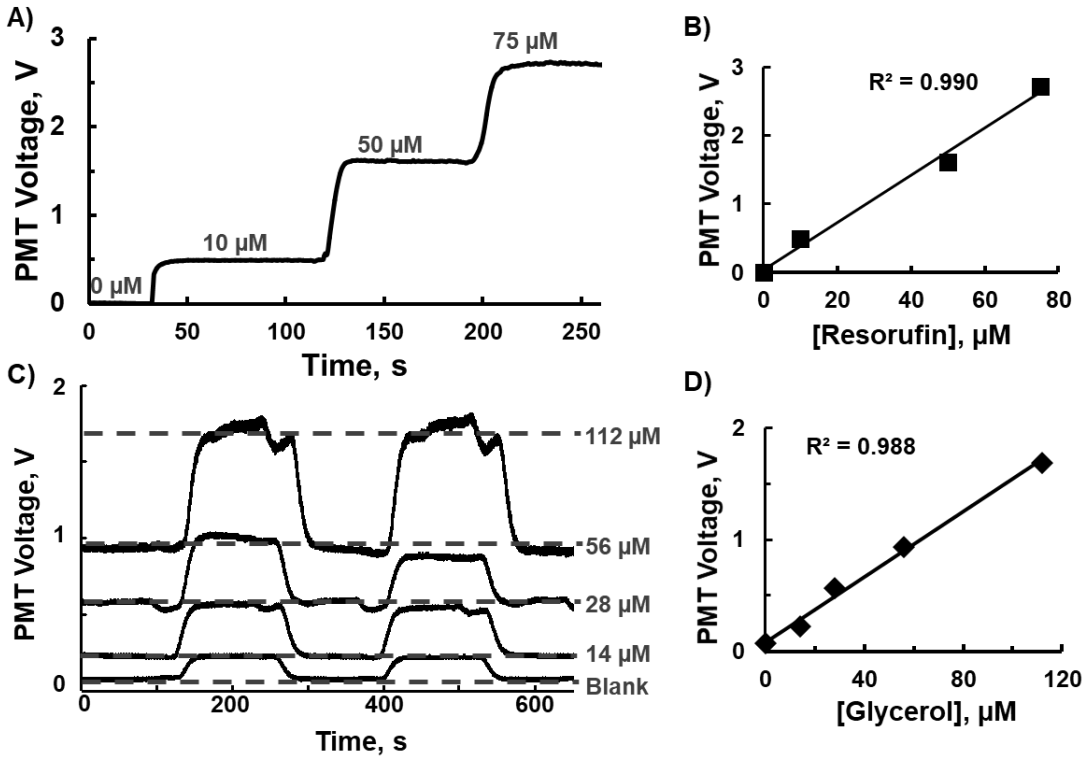

Figure D.8 Probe performance in 60 µm deep x 100 µm wide PDMS microfluidic chips. a) Trace shows detection of fluorescence changes from 0 to 75 µM resorufin. b) Calibration curve of resorufin concentrations corresponding to (a), resulting in detection limit of 100 nM (S/N =3). c) Probe detection of on-chip glycerol assay. Individual traces show alternating between low and high glycerol concentrations (0, 14, 28, 56, 112 µM, respectively). The features at the end of each peak (prominently in 112 µM) were due to pressure switching during syringe changes. d) Linear range of glycerol assay corresponding to (c). Deviation from the line at 14 µM is inherent to the assay.

The same probe was tested for fluorescence detection in glass microfluidic devices. The probe was positioned over a 25 µm deep × 80 µm wide glass microfluidic chip while pumping 0 to 100 nM fluorescein through the device. The trace in Figure D.**9**A illustrates the detection of fluorescent changes at different fluorescein concentrations. The resulting calibration curve was linear with R^2 of 0.999, as shown in Figure D.**9**B. The LOD was determined to be 11 nM. The probe was then used for detection of microchip electrophoresis separation of a fluorescent protein ladder (Figure D.**9**C). The probe was placed on a glass-based electrophoresis chip near the end of a 15 µm deep × 50 µm wide separation channel. The probe was able to detect the 7 separated proteins, as illustrated in Figure D.**9**D. Signal to

noise ratio was reasonably comparable to our previously reported assay using a conventional microscope system that used an arc-lamp source and CCD camera for detection[340]. The individual proteins are present at ~0.014 mg/mL in this example. While the sensitivity is not excellent, this measurement is in a challenging environment of a narrow channel with brief signals. The sensitivity is counter-balanced by the ease of the measurement; the probe is merely placed over the channel. This result demonstrates the suitability of the probe for measurement of non-discrete samples within shallow and narrow detection zones.

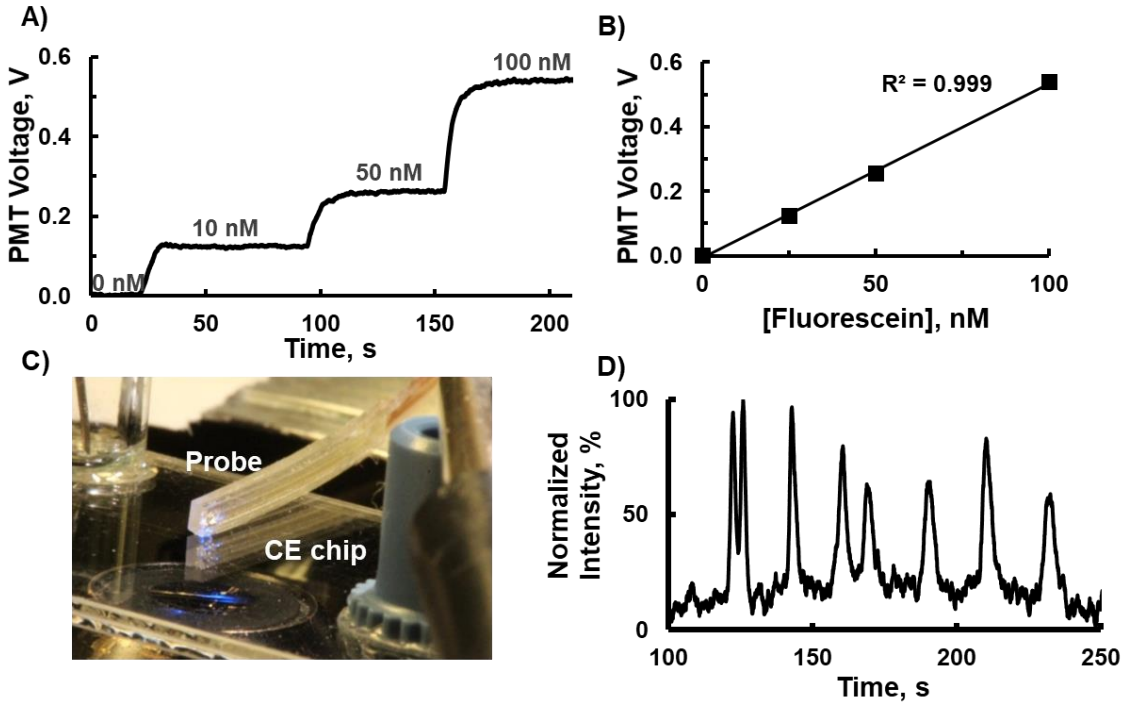

Figure D.9 Probe performance in glass microfluidic devices. A) Trace shows detection of changes from 0 to 100 nM fluorescein in a 25 μm deep x 80 μm wide glass microfluidic channel. B) Calibration curve of fluorescein concentrations corresponding to (A), resulting in detection limit of 11 nM (S/N =3). C) Image of the probe on a glass-based electrophoresis chip, demonstrating the feasibility of using probe as a plug and play device. D) Probe detection on the electrophoresis chip of a 0.1 mg/mL protein ladder with 15 μm deep x 50 μm wide detection channel, showing electropherograms of 7 separated proteins. Doublet feature of the first protein was due to degradation of sample and/or gel, or separation conditions. These discrepancies do not influence detection.

These applications of the probe illustrate a simple way to couple fluorescence detection to a chip. Although it is difficult to compare to different experiments, the LODs are comparable to other microfabricated devices with integrated optics and optical fibers (see Table 6.2)[314,326–328,341–343]. A significant limitation of the current design is lack of optical filters in the probe tip. The LODs reported here could be improved by integrating optical filters directly onto the tips of the fibers, thus reducing fluorescence background due to light scattering that occurs along the fiber length[344–346]. Nevertheless, our probes have the advantage of focusing into small channels (down to 15 μm deep × 50 μm wide), enabling their use for a variety of applications, such as electrophoresis. Furthermore, the probes incorporate both excitation and emission fibers in parallel on the same side of the microfluidic device, which allows for simplified fabrication and requires less space for integration. Because the probes are standalone devices, they can be used for different applications on different chips by moving the probe from one device to another as a "plug-and-play" detector. As the major microfluidic design characteristic is the coverslip material and thickness, a given design is reusable. Indeed the same probes could be used for all the experiments described above. Individual probes are easy to clean (using Scotch® Magic™ Tape), autoclavable, and reusable due to properties of the materials used.

Table D.2 Comparison of microfluidic optical detection systems. A detection system typically includes light source, optical fibers/waveguides, and detector. Discrepancy of limits of detection (LOD) could be due to several variables, such as excitation and emission wavelengths, quality of light source and detector, types of filters, alignment and efficiency of waveguides, light pathways, and detection volume.

Ref#	LOD	Analyte[a]	Chip material	Lens	Mirror	Light source	Fiber 1[b] arrangement[‡]	Channel dimension	Fiber 2[c] arrangement[‡]	Detector
*	6 nM	Resorufin	Glass capillary	✓	✓	Laser, 543 nm	Top, 0° - 360° xy	(150 µm i.d. × 360 µm o.d.)	Same as Fiber 1	Filter w/ PMT
	100 nM	Resorufin	PDMS	✓	✓	Laser, 543 nm	*same as above*	(100 µm × 60 µm)	*same as above*	*same as above*
	11 nM	Fluorescein	Glass	✓	✓	Laser, 473 nm	*same as above*	(80 µm × 25 µm)	*same as above*	*same as above*
327	25 nM	Fluorescein	PDMS	×	×	LED, 494 nm w/ Filter	Inside, 90° or 270° xy	(50 µm × 50 µm)	No Fiber 2	Filter w/ µAvalanche-photodiode
328	44 pM[†]	Near-IR dye (NN382)	PMMA	×	×	Laser, 750 nm	Inside, 60° xy	(150 µm × 75 µm)	Inside, 240° xy	Avalanche-photodiode
314	17 µM	FITC-labelled albumin	PDMS	✓	×	White lamp w/ Filter	Inside, 90° xy	(50 µm × 130 µm)	Inside, 270° xy	Spectrophotometer
347	21 nM	Rhodamine 6G	PDMS	✓	×	Laser, 532 nm	No Fiber 1	(50 µm × 125 µm)	Top, 90° xz	Filter w/ Spectrometer
348	120 nM	Fluorescein	PDMS	×	×	LED, 475 nm w/ Filter	No Fiber 1	(110 µm × 40 µm)	Inside, 90° or 270° xy	Filter w/ PMT
349	50 nM	Fluorescein	Glass	×	×	Laser, 473 nm	Inside, 90° or 270° xy	(100 µm × 25 µm)	No Fiber 2	Filter w/ PMT
350	200 nM	Fluorescein	PDMS	×	×	LED, 470 nm w/ Filter	Inside, 180° xz	(1 cm × 500 µm)[≠]	Same as Fiber 1	Filter w/ Photodiode

a. Excitation and emission wavelength of the analytes listed in the above table:
- *Resorufin (570 nm/ 585 nm)*
- *FITC/Fluorescein (490 nm/ 520 nm)*
- *NN 382 (780 nm/ 800 nm)*
- *Rhodamine 6G (526 nm/ 555 nm)*

b. Fiber 1 = waveguide from light source to sample

c. Fiber 2 = waveguide from sample to detector

** The microfabricated|probe reported herein*

† The LOD was determined using S/N = 2. The low LOD was achieved using direct contact of the optical fiber with a sample

≠ Not drawn to scale

‡ Arrangement of optical fibers for on-chip detection

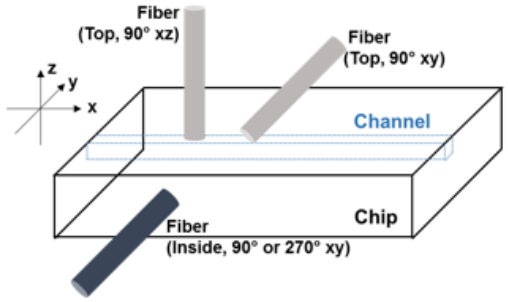

Raman measurement

To demonstrate another application, the same microfabricated probe was used to acquire Raman spectra. Figure D.**10**A illustrates Raman spectra of bulk solvents (water and DMSO). These solvents have been reported to not swell PDMS[351]; hence, we do not observe any carryover or interference with measurement. The probe allows detection of several major bands of DMSO over the much weaker scatter of water, for example C-S symmetric stretch at 668 cm^{-1}, C-S antisymmetric stretch at 700 cm^{-1}, S=O stretch at 1042 cm^{-1}, and CH_3 degenerate deformation at 1420 cm^{-1}. Placing the probe directly on an aspirin tablet allowed detection of the characteristic Raman bands of acetylsalicylic acid including the symmetric aromatic ring C-C stretching vibration at 1606 cm^{-1} and C=O stretching vibration of the carboxyl group at the shoulder peak of 1622 cm^{-1} as well as several other observed bands below 1500 cm^{-1}, such as O-H bending vibration at 1296 cm^{-1} and C-H bending vibration at 1045 cm^{-1} and near 1200 cm^{-1} (Figure D.**10**B). The Raman fingerprints are consistent with previous reports[352–355]. High background at < 600 cm^{-1} is caused by the silica of the optical fibers. Addition of optical filters to fiber optic tips would reduce this background.

These results show that the microfabricated probes can be successfully employed as Raman probes. The overall size of microfabricated probes is comparable to the smallest reported lensed Raman probes[302]; however, the use of microfabrication simplifies the making of the probes and enables low cost, mass production, flexible probes, and disposability.

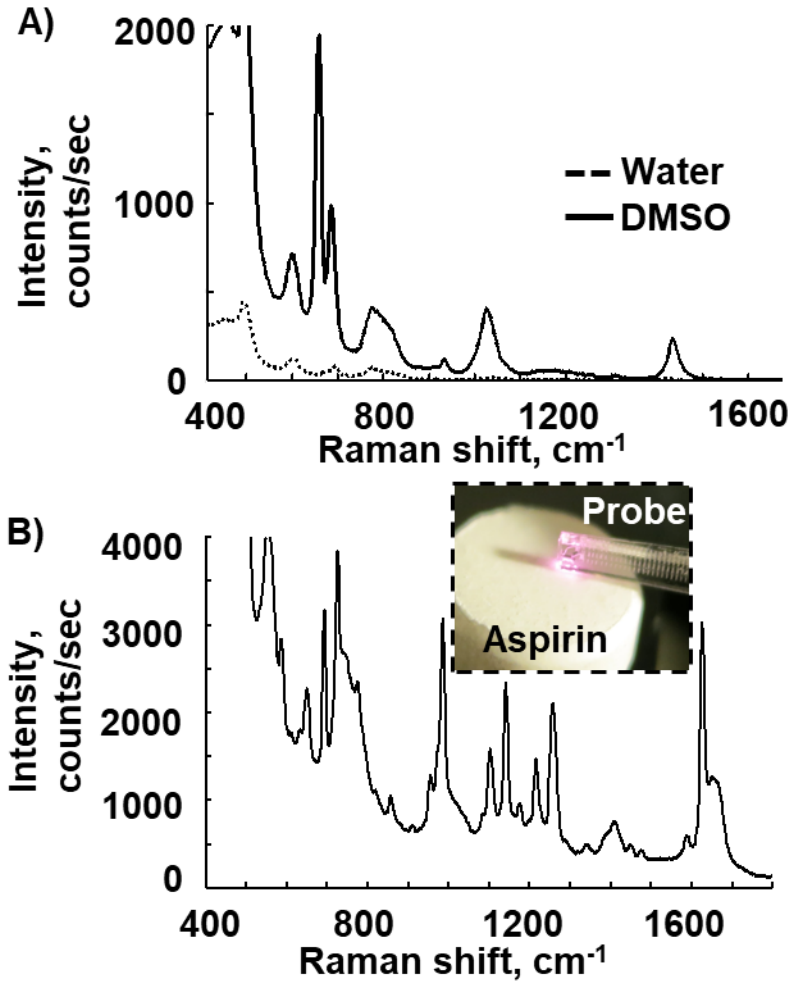

Figure D.10 Raman spectra collected using the microfabricated probe of: A) water and DMSO as bulk solvents, and B) an aspirin tablet, as shown in the inset.

Conclusions and Future Directions

Microfabrication using soft lithography is a viable and cost-effective way to miniaturize spectroscopic probes. The microprobes described here are only slightly larger than the optical fibers on which they are molded. The microfabricated probes are thus smaller than commercial optical probes, enabling chemical measurements in tight spaces. As demonstrated, the probes are versatile as the same probe can easily be transferred between samples. Some modifications can further improve performance of the system and its ease of use. The probes can feasibly be coupled with thinner optical filters[327,344–346], more compact light sources[356,357] and detectors[358], and other miniature optics[316,345], resulting in more integrated, smaller, portable, low-cost analytical and diagnostic devices. Incorporation of filters in the tip would lower background and improve sensitivity. Better lithographic masks may be used as previously described to yield subwavelength optical quality surfaces[314]. Additional designs are possible. In principle other geometries could be fabricated such as reflectance on a single point, diffuse reflectance including a spatial offset, collimated transmission, diffuse transmission, and multiple-input multiple-output tomographic configurations.

With further development, a variety of further applications can be envisioned due to the size, cost, materials, and configuration of the probes. The probes may have excellent potential for biomedical endoscopy. The small probe size suggests potential for less-invasive endoscopy[359,360]. Compared to traditional endoscope probes, the devices are low cost to fabricate. The materials are compatible with autoclaving, offering a unique potential compatibility with biomedical applications requiring sterilization as compared to traditional assembled microprobes that require the use of adhesives and have materials with dissimilar

thermal expansion coefficients. The probes also have more potential for pairing with microfluidic devices. Pairing a microfluidic device with the probes illustrates a simple approach for coupling fluorescence to a chip. Because the probe is mounted to the device, optics do not need to be incorporated into a chip allowing flexibility of design. The low cost and facile mounting of the probes may facilitate multipoint detection on a chip, a possibility that was previously restricted because of microscope dimensions[361,362]. On-chip alignment markers and probe holders for interfacing the probes to microfluidic devices can be customarily made using microfabrication or 3D printing could be used to facilitate positioning on microfluidics.

Bibliography

(1) Purves, D.; Augustine, G.; Fitzpatrick, D.; Hall, W.; LaMantia, A. S.; White, L. *Neuroscience*; Sinauer Associates: Sunderland, MA, 2012.
(2) Webster, R. *Neurotransmitters, Drugs and Brain Function*; John Wiley & Sons, 2001.
(3) Myhrer, T. *Brain Res. Rev.* **2003**, *41* (2), 268–287.
(4) Schultz, W. *Trends Neurosci.* **2007**, *30* (5), 203–210.
(5) Cools, R.; Roberts, A. C.; Robbins, T. W. *Trends Cogn. Sci.* **2008**, *12* (1), 31–40.
(6) Kása, P.; Rakonczay, Z.; Gulya, K. *Prog. Neurobiol.* **1997**, *52* (6), 511–535.
(7) Francis, P. T. *Int. J. Geriatr. Psychiatry* **2003**, *18* (S1), S15–S21.
(8) Francis, P. T.; Perry, E. K. *Mov. Disord.* **2007**, *22* (S17), S351–S357.
(9) Barone, P. *Eur. J. Neurol.* **2010**, *17* (3), 364–376.
(10) Fox, S. H.; Chuang, R.; Brotchie, J. M. *Mov. Disord.* **2009**, *24* (9), 1255–1266.
(11) Blesa, J.; Przedborski, S. *Front. Neuroanat.* **2014**, *8*.
(12) Barros, L. F.; Deitmer, J. W. *Brain Res. Rev.* **2010**, *63* (1), 149–159.
(13) Glenn, T. C.; Kelly, D. F.; Boscardin, W. J.; McArthur, D. L.; Vespa, P.; Oertel, M.; Hovda, D. A.; Bergsneider, M.; Hillered, L.; Martin, N. A. *J. Cereb. Blood Flow Metab.* **2003**, *23* (10), 1239–1250.
(14) Meierhans, R.; Béchir, M.; Ludwig, S.; Sommerfeld, J.; Brandi, G.; Haberthür, C.; Stocker, R.; Stover, J. F. *Crit. Care* **2010**, *14*, R13.
(15) Carpenter, K. L. H.; Jalloh, I.; Hutchinson, P. J. *Front. Neurosci.* **2015**, *9*.
(16) Volkow, N. D.; Morales, M. *Cell* **2015**, *162* (4), 712–725.
(17) Wise, R. A. *Neuron* **2002**, *36* (2), 229–240.
(18) Venton, B. J.; Wightman, R. M. *Anal. Chem.* **2003**, *75* (19), 414 A-421 A.
(19) Day, J. J.; Roitman, M. F.; Wightman, R. M.; Carelli, R. M. *Nat. Neurosci.* **2007**, *10* (8), 1020–1028.
(20) Darvesh, A. S.; Carroll, R. T.; Geldenhuys, W. J.; Gudelsky, G. A.; Klein, J.; Meshul, C. K.; Van der Schyf, C. J. *Exp Op Drug Disc* **2011**, *6* (2), 109–127.
(21) Adams, R. N. *Anal. Chem.* **1976**, *48* (14), 1126A–1138A.
(22) Robinson, D. L.; Venton, B. J.; Heien, M. L.; Wightman, R. M. *Clin. Chem.* **2003**, *49* (10), 1763–1773.
(23) Bucher, E. S.; Wightman, R. M. *Annu. Rev. Anal. Chem.* **2015**, *8* (1), 239–261.
(24) Ungerstedt, U. In *Measurement of neurotransmitter release in vivo*; Wiley New York, 1984; Vol. 6, pp 81–107.
(25) Watson, C. J.; Venton, B. J.; Kennedy, R. T. *Anal. Chem.* **2006**, *78* (5), 1391–1399.
(26) Westerink, B. H. C.; Cremers, T. I. F. H. *Handbook of microdialysis: methods, applications and perspectives*, 1st ed.; Academic Press, 2007; Vol. 16.
(27) Nandi, P.; Lunte, S. M. *Anal. Chim. Acta* **2009**, *651* (1), 1–14.
(28) Kennedy, R. T. *Curr. Opin. Chem. Biol.* **2013**, *17* (5), 860–867.
(29) Madou, M. J. *Fundamentals of Microfabrication: The Science of Miniaturization, Second Edition*; CRC Press, 2002.

(30) Chen, J.; Wise, K. D.; Hetke, J. F.; Bledsoe, S. C. *Biomed. Eng. IEEE Trans. On* **1997**, *44* (8), 760–769.
(31) Wu, F.; Stark, E.; Ku, P. C.; Wise, K. D.; Buzsáki, G.; Yoon, E. *Neuron* **2015**, *88* (6), 1136–1148.
(32) Fekete, Z. *Sens. Actuators B Chem.* **2015**, *215*, 300–315.
(33) Seymour, J. P.; Wu, F.; Wise, K. D.; Yoon, E. *Microsyst. Nanoeng.* **2017**, *3*, 16066.
(34) Sim, J. Y.; Haney, M. P.; Park, S. I.; McCall, J. G.; Jeong, J.-W. *Lab Chip* **2017**, *17* (8), 1406–1435.
(35) Fillenz, M. *Neurosci. Biobehav. Rev.* **2005**, *29* (6), 949–962.
(36) Schultz, K. N.; Kennedy, R. T. *Annu. Rev. Anal. Chem.* **2008**, *1* (1), 627–661.
(37) Perry, M.; Li, Q.; Kennedy, R. T. *Anal. Chim. Acta* **2009**, *653* (1), 1–22.
(38) Zhang, M.; Yu, P.; Mao, L. *Acc. Chem. Res.* **2012**, *45* (4), 533–543.
(39) Zhang, B.; Adams, K. L.; Luber, S. J.; Eves, D. J.; Heien, M. L.; Ewing, A. G. *Anal. Chem.* **2008**, *80* (5), 1394–1400.
(40) Trouillon, R.; Ewing, A. G. *ACS Chem. Biol.* **2014**, *9* (3), 812–820.
(41) Tucci, S.; Rada, P.; Sepúlveda, M. J.; Hernandez, L. *J. Chromatogr. B. Biomed. Sci. App.* **1997**, *694* (2), 343–349.
(42) Heien, M. L.; Khan, A. S.; Ariansen, J. L.; Cheer, J. F.; Phillips, P. E.; Wassum, K. M.; Wightman, R. M. *Proc. Natl. Acad. Sci. U. S. A.* **2005**, *102* (29), 10023–10028.
(43) Venton, B. J.; Wightman, R. M. *Synapse* **2007**, *61* (1), 37–39.
(44) Bruno, J. P.; Gash, C.; Martin, B.; Zmarowski, A.; Pomerleau, F.; Burmeister, J.; Huettl, P.; Gerhardt, G. A. *Eur. J. Neurosci.* **2006**, *24* (10), 2749–2757.
(45) Song, P.; Mabrouk, O. S.; Hershey, N. D.; Kennedy, R. T. *Anal. Chem.* **2012**, *84* (1), 412–419.
(46) Ametamey, S. M.; Honer, M.; Schubiger, P. A. *Chem. Rev.* **2008**, *108* (5), 1501–1516.
(47) Nasrallah, I.; Dubroff, J. *Semin. Nucl. Med.* **2013**, *43* (6), 449–461.
(48) Zimmer, L.; Luxen, A. *NeuroImage* **2012**, *61* (2), 363–370.
(49) Schulz, D.; Southekal, S.; Junnarkar, S. S.; Pratte, J.-F.; Purschke, M. L.; Stoll, S. P.; Ravindranath, B.; Maramraju, S. H.; Krishnamoorthy, S.; Henn, F. A.; O'Connor, P.; Woody, C. L.; Schlyer, D. J.; Vaska, P. *Nat. Methods* **2011**, *8* (4), 347–352.
(50) Yao, R.; Lecomte, R.; Crawford, E. S. *J. Nucl. Med. Technol.* **2012**, *40* (3), 157–165.
(51) Wong, D. F.; Brašić, J. R.; Singer, H. S.; Schretlen, D. J.; Kuwabara, H.; Zhou, Y.; Nandi, A.; Maris, M. A.; Alexander, M.; Ye, W.; Rousset, O.; Kumar, A.; Szabo, Z.; Gjedde, A.; Grace, A. A. *Neuropsychopharmacology* **2008**, *33* (6), 1239–1251.
(52) Tuominen, L.; Nummenmaa, L.; Keltikangas-Järvinen, L.; Raitakari, O.; Hietala, J. *Hum. Brain Mapp.* **2014**, *35* (5), 1875–1884.
(53) Sander, C. Y.; Hooker, J. M.; Catana, C.; Normandin, M. D.; Alpert, N. M.; Knudsen, G. M.; Vanduffel, W.; Rosen, B. R.; Mandeville, J. B. *Proc. Natl. Acad. Sci.* **2013**, *110* (27), 11169–11174.
(54) Zhu, H.; Barker, P. B. In *Magnetic Resonance Neuroimaging*; Modo, M., Bulte, J. W. M., Eds.; Humana Press: Totowa, NJ, 2011; Vol. 711, pp 203–226.
(55) Duarte, J. M. N.; Lei, H.; Mlynárik, V.; Gruetter, R. *NeuroImage* **2012**, *61* (2), 342–362.
(56) Gussew, A.; Rzanny, R.; Erdtel, M.; Scholle, H. C.; Kaiser, W. A.; Mentzel, H. J.; Reichenbach, J. R. *NeuroImage* **2010**, *49* (2), 1895–1902.
(57) Puts, N. A. J.; Edden, R. A. E. *Prog. Nucl. Magn. Reson. Spectrosc.* **2012**, *60*, 29–41.

(58) Betina Ip, I.; Berrington, A.; Hess, A. T.; Parker, A. J.; Emir, U. E.; Bridge, H. *Neuroimage* **2017**, *155*, 113–119.
(59) Marvin, J. S.; Borghuis, B. G.; Tian, L.; Cichon, J.; Harnett, M. T.; Akerboom, J.; Gordus, A.; Renninger, S. L.; Chen, T.-W.; Bargmann, C. I.; Orger, M. B.; Schreiter, E. R.; Demb, J. B.; Gan, W.-B.; Hires, S. A.; Looger, L. L. *Nat. Methods* **2013**, *10* (2), 162–170.
(60) Liang, R.; Broussard, G. J.; Tian, L. *ACS Chem. Neurosci.* **2015**, *6* (1), 84–93.
(61) Lin, M. Z.; Schnitzer, M. J. *Nat. Neurosci.* **2016**, *19* (9), 1142–1153.
(62) Robinson, D. L.; Hermans, A.; Seipel, A. T.; Wightman, R. M. *Chem. Rev.* **2008**, *108* (7), 2554–2584.
(63) Wang, J. *Chem. Rev.* **2008**, *108* (2), 814–825.
(64) Wilson, G. S.; Johnson, M. A. *Chem. Rev.* **2008**, *108* (7), 2462–2481.
(65) Weltin, A.; Kieninger, J.; Urban, G. A. *Anal. Bioanal. Chem.* **2016**, *408* (17), 4503–4521.
(66) Robinson, D. L.; Wightman, R. M. In *Electrochemical Methods for Neuroscience*; Michael, A. C., Borland, L. M., Eds.; CRC Press/Taylor & Francis: Boca Raton (FL), 2007.
(67) Jackowska, K.; Krysinski, P. *Anal. Bioanal. Chem.* **2013**, *405* (11), 3753–3771.
(68) Wightman, R. M.; Heien, M. L. A. V.; Wassum, K. M.; Sombers, L. A.; Aragona, B. J.; Khan, A. S.; Ariansen, J. L.; Cheer, J. F.; Phillips, P. E. M.; Carelli, R. M. *Eur. J. Neurosci.* **2007**, *26* (7), 2046–2054.
(69) Clark, J. J.; Sandberg, S. G.; Wanat, M. J.; Gan, J. O.; Horne, E. A.; Hart, A. S.; Akers, C. A.; Parker, J. G.; Willuhn, I.; Martinez, V.; Evans, S. B.; Stella, N.; Phillips, P. E. M. *Nat. Methods* **2010**, *7* (2), 126–129.
(70) Dressman, S. F.; Peters, J. L.; Michael, A. C. *J. Neurosci. Methods* **2002**, *119* (1), 75–81.
(71) Saylor, R. A.; Lunte, S. M. *J. Chromatogr. A* **2015**, *1382*, 48–64.
(72) Kottegoda, S.; Shaik, I.; Shippy, S. A. *J. Neurosci. Methods* **2002**, *121* (1), 93–101.
(73) Slaney, T. R.; Nie, J.; Hershey, N. D.; Thwar, P. K.; Linderman, J.; Burns, M. A.; Kennedy, R. T. *Anal. Chem.* **2011**, *83* (13), 5207–5213.
(74) Mitala, C. M.; Wang, Y.; Borland, L. M.; Jung, M.; Shand, S.; Watkins, S.; Weber, S. G.; Michael, A. C. *J. Neurosci. Methods* **2008**, *174* (2), 177–185.
(75) Wise, K. D. *IEEE Eng. Med. Biol. Mag.* **2005**, *24* (5), 22–29.
(76) HajjHassan, M.; Chodavarapu, V.; Musallam, S. *Sensors* **2008**, *8* (10), 6704–6726.
(77) Wise, K. D.; Sodagar, A. M.; Yao, Y.; Gulari, M. N.; Perlin, G. E.; Najafi, K. *Proc. IEEE* **2008**, *96* (7), 1184–1202.
(78) Grieshaber, D.; MacKenzie, R.; Voeroes, J.; Reimhult, E. *Sensors* **2008**, *8* (3), 1400–1458.
(79) Zachek, M. K.; Park, J.; Takmakov, P.; Wightman, R. M.; McCarty, G. S. *The Analyst* **2010**, *135* (7), 1556.
(80) Zachek, M. K.; Takmakov, P.; Moody, B.; Wightman, R. M.; McCarty, G. S. *Anal. Chem.* **2009**, *81* (15), 6258–6265.
(81) Johnson, M. D.; Franklin, R. K.; Gibson, M. D.; Brown, R. B.; Kipke, D. R. *J. Neurosci. Methods* **2008**, *174* (1), 62–70.
(82) Wassum, K. M.; Tolosa, V. M.; Wang, J.; Walker, E.; Monbouquette, H. G.; Maidment, N. T. *Sensors* **2008**, *8* (8), 5023–5036.

(83) Tolosa, V. M.; Wassum, K. M.; Maidment, N. T.; Monbouquette, H. G. *Biosens. Bioelectron.* **2013**, *42*, 256–260.
(84) Frey, O.; Holtzman, T.; McNamara, R. M.; Theobald, D. E. H.; van der Wal, P. D.; de Rooij, N. F.; Dalley, J. W.; Koudelka-Hep, M. *Biosens. Bioelectron.* **2010**, *26* (2), 477–484.
(85) Frey, O.; Holtzman, T.; McNamara, R. M.; Theobald, D. E. H.; van der Wal, P. D.; de Rooij, N. F.; Dalley, J. W.; Koudelka-Hep, M. *Sens. Actuators B Chem.* **2011**, *154* (2), 96–105.
(86) Vasylieva, N.; Marinesco, S.; Barbier, D.; Sabac, A. *Biosens. Bioelectron.* **2015**, *72*, 148–155.
(87) Wei, W.; Song, Y.; Wang, L.; Zhang, S.; Luo, J.; Xu, S.; Cai, X. *Microsyst. Nanoeng.* **2015**, *1*, 15002.
(88) Burmeister, J. J.; Pomerleau, F.; Palmer, M.; Day, B. K.; Huettl, P.; Gerhardt, G. A. *J. Neurosci. Methods* **2002**, *119* (2), 163–171.
(89) Day, B. K.; Pomerleau, F.; Burmeister, J. J.; Huettl, P.; Gerhardt, G. A. *J. Neurochem.* **2006**, *96* (6), 1626–1635.
(90) Burmeister, J. J.; Palmer, M.; Gerhardt, G. A. *Biosens. Bioelectron.* **2005**, *20* (9), 1772–1779.
(91) Burmeister, J. J.; Pomerleau, F.; Huettl, P.; Gash, C. R.; Werner, C. E.; Bruno, J. P.; Gerhardt, G. A. *Biosens. Bioelectron.* **2008**, *23* (9), 1382–1389.
(92) Lourenço, C. F.; Ledo, A.; Laranjinha, J.; Gerhardt, G. A.; Barbosa, R. M. *Sens. Actuators B Chem.* **2016**, *237*, 298–307.
(93) Li, C.; Limnuson, K.; Wu, Z.; Amin, A.; Narayan, A.; Golanov, E. V.; Ahn, C. H.; Hartings, J. A.; Narayan, R. K. *Biosens. Bioelectron.* **2016**, *77*, 62–68.
(94) Weltin, A.; Kieninger, J.; Enderle, B.; Gellner, A.-K.; Fritsch, B.; Urban, G. A. *Biosens. Bioelectron.* **2014**, *61*, 192–199.
(95) Wilson, G. S.; Hu, Y. *Chem. Rev.* **2000**, *100* (7), 2693–2704.
(96) Suzuki, M.; Akaguma, H. *Sens. Actuators B Chem.* **2000**, *64* (1), 136–141.
(97) Talauliker, P. M.; Price, D. A.; Burmeister, J. J.; Nagari, S.; Quintero, J. E.; Pomerleau, F.; Huettl, P.; Hastings, J. T.; Gerhardt, G. A. *J. Neurosci. Methods* **2011**, *198* (2), 222–229.
(98) Laermer, F.; Schilp, A. Method of anisotropically etching silicon. 5501893, March 26, 1996.
(99) Wu, B.; Kumar, A.; Pamarthy, S. *J. Appl. Phys.* **2010**, *108* (5), 051101.
(100) Burmeister, J. J.; Moxon, K.; Gerhardt, G. A. *Anal. Chem.* **2000**, *72* (1), 187–192.
(101) Burmeister, J. J.; Gerhardt, G. A. *Anal. Chem.* **2001**, *73* (5), 1037–1042.
(102) Rutherford, E. C.; Pomerleau, F.; Huettl, P.; Strömberg, I.; Gerhardt, G. A. *J. Neurochem.* **2007**, *102* (3), 712–722.
(103) Lacour, S. P.; Benmerah, S.; Tarte, E.; FitzGerald, J.; Serra, J.; McMahon, S.; Fawcett, J.; Graudejus, O.; Yu, Z.; Morrison, B. *Med. Biol. Eng. Comput.* **2010**, *48* (10), 945–954.
(104) Jeong, J.-W.; Shin, G.; Park, S. I.; Yu, K. J.; Xu, L.; Rogers, J. A. *Neuron* **2015**, *86* (1), 175–186.
(105) Kim, B. J.; Meng, E. *J. Micromechanics Microengineering* **2016**, *26* (1), 013001.
(106) Fekete, Z.; Pongrácz, A. *Sens. Actuators B Chem.* **2017**, *243*, 1214–1223.

(107) Suzuki, T.; Mabuchi, K.; Takeuchi, S. In *Neural Engineering, 2003. Conference Proceedings. First International IEEE EMBS Conference on*; IEEE, 2003; pp 154–156.
(108) Kim, B. J.; Kuo, J. T. W.; Hara, S. A.; Lee, C. D.; Yu, L.; Gutierrez, C. A.; Hoang, T. Q.; Pikov, V.; Meng, E. *J. Neural Eng.* **2013**, *10* (4), 045002.
(109) Tien, L. W.; Wu, F.; Tang-Schomer, M. D.; Yoon, E.; Omenetto, F. G.; Kaplan, D. L. *Adv. Funct. Mater.* **2013**, *23* (25), 3185–3193.
(110) Lecomte, A.; Castagnola, V.; Descamps, E.; Dahan, L.; Blatché, M. C.; Dinis, T. M.; Leclerc, E.; Egles, C.; Bergaud, C. *J. Micromechanics Microengineering* **2015**, *25* (12), 125003.
(111) Shin, H.; Lee, H. J.; Chae, U.; Kim, H.; Kim, J.; Choi, N.; Woo, J.; Cho, Y.; Lee, C. J.; Yoon, E.-S.; Cho, I.-J. *Lab Chip* **2015**, *15* (18), 3730–3737.
(112) Altuna, A.; Berganzo, J.; Fernández, L. J. *Front. Mater.* **2015**, *2*.
(113) de Boer, M. J.; Tjerkstra, R. W.; Berenschot, J. W.; Jansen, H. V.; Burger, G. J.; Gardeniers, J. G. E.; Elwenspoek, M.; van den Berg, A. *Microelectromechanical Syst. J. Of* **2000**, *9* (1), 94–103.
(114) Fekete, Z.; Pongrácz, A.; Fürjes, P.; Battistig, G. *Microsyst. Technol.* **2012**, *18* (3), 353–358.
(115) Lee, W. H.; Slaney, T. R.; Hower, R. W.; Kennedy, R. T. *Anal. Chem.* **2013**, *85* (8), 3828–3831.
(116) Chae, U.; Shin, H.; Lee, H.; Lee, J.; Choi, N.; Lee, Y. J.; Lee, S. H.; Woo, J.; Cho, Y.; Yoon, E.-S.; Yu, H.-Y.; Cho, I.-J. In *IEEE MEMS*; Shanghai, China, 2016; pp 329–332.
(117) Petit-Pierre, G.; Bertsch, A.; Renaud, P. *Lab Chip* **2016**, *16* (5), 917–924.
(118) Adiga, S. P.; Jin, C.; Curtiss, L. A.; Monteiro-Riviere, N. A.; Narayan, R. J. *Wiley Interdiscip. Rev. Nanomed. Nanobiotechnol.* **2009**, *1* (5), 568–581.
(119) Warkiani, M. E.; Bhagat, A. A. S.; Khoo, B. L.; Han, J.; Lim, C. T.; Gong, H. Q.; Fane, A. G. *ACS Nano* **2013**, *7* (3), 1882–1904.
(120) Rijn, C. van. *Nano and Micro Engineered Membrane Technology*; Elsevier, 2004.
(121) Apel, P. *Radiat. Meas.* **2001**, *34* (1), 559–566.
(122) Metz, S.; Trautmann, C.; Bertsch, A.; Renaud, P. In *Micro Electro Mechanical Systems, 2002. The Fifteenth IEEE International Conference on*; IEEE, 2002; pp 81–84.
(123) Tong, H. D.; Jansen, H. V.; Gadgil, V. J.; Bostan, C. G.; Berenschot, E.; van Rijn, C. J. M.; Elwenspoek, M. *Nano Lett.* **2004**, *4* (2), 283–287.
(124) Striemer, C. C.; Gaborski, T. R.; McGrath, J. L.; Fauchet, P. M. *Nature* **2007**, *445* (7129), 749–753.
(125) Lammel, G.; Renaud, P. *Sens. Actuators Phys.* **2000**, *85* (1), 356–360.
(126) Leïchlé, T.; Bourrier, D. *Lab Chip* **2015**, *15* (3), 833–838.
(127) Poinern, G. E. J.; Ali, N.; Fawcett, D. *Materials* **2011**, *4* (12), 487–526.
(128) Santos, A.; Kumeria, T.; Losic, D. *TrAC Trends Anal. Chem.* **2013**, *44*, 25–38.
(129) Lei, Y.; Cai, W.; Wilde, G. *Prog. Mater. Sci.* **2007**, *52* (4), 465–539.
(130) Yang, K. S.; Kim, H. J.; Ahn, J. K.; Kim, D. H. *Curr. Appl. Phys.* **2009**, *9* (2, Supplement), e60–e65.
(131) Ding, G. Q.; Zheng, M. J.; Xu, W. L.; Shen, W. Z. *Nanotechnology* **2005**, *16* (8), 1285.

(132) Belwalkar, A.; Grasing, E.; Van Geertruyden, W.; Huang, Z.; Misiolek, W. Z. *J. Membr. Sci.* **2008**, *319* (1–2), 192–198.
(133) Li, A. P.; Müller, F.; Birner, A.; Nielsch, K.; Gösele, U. *J. Appl. Phys.* **1998**, *84* (11), 6023–6026.
(134) Zhang, S.; Wang, Y.; Tan, Y.; Zhu, J.; Liu, K.; Zhu, J. *Mater. Res. Express* **2016**, *3* (7), 074004.
(135) Furneaux, R. C.; Rigby, W. R.; Davidson, A. P. *Nature* **1989**, *337* (6203), 337147a0.
(136) Masuda, H.; Fukuda, K. *Sci. Wash.* **1995**, *268* (5216), 1466.
(137) Ali, H. O. *Trans. IMF* **2017**, *95* (6), 290–296.
(138) Liang, J.; Chik, H.; Yin, A.; Xu, J. *J. Appl. Phys.* **2002**, *91* (4), 2544–2546.
(139) Lee, W.; Park, S.-J. *Chem. Rev.* **2014**, *114* (15), 7487–7556.
(140) Yamaguchi, A.; Uejo, F.; Yoda, T.; Uchida, T.; Tanamura, Y.; Yamashita, T.; Teramae, N. *Nat. Mater.* **2004**, *3* (5), nmat1107.
(141) Penumetcha, S. S.; Kona, R.; Hardin, J. L.; Molder, A. L.; Steinle, E. D. *Sensors* **2007**, *7* (11), 2942–2952.
(142) Gong, D.; Yadavalli, V.; Paulose, M.; Pishko, M.; Grimes, C. A. *Biomed. Microdevices* **2003**, *5* (1), 75–80.
(143) Zahn, J. D.; Trebotich, D.; Liepmann, D. *Biomed. Microdevices* **2005**, *7* (1), 59–69.
(144) Kotake, N.; Suzuki, T.; Mabuchi, K.; Takeuchi, S. *Int Conf Miniaturized Syst Chem Life Sci 12th* **2008**, 1687–1689.
(145) Metz, S.; Trautmann, C.; Bertsch, A.; Renaud, P. IEEE, 2002; pp 81–84.
(146) Desai, T. A.; Hansford, D.; Ferrari, M. *J. Membr. Sci.* **1999**, *159* (1), 221–231.
(147) Lebouitz, K. S.; Mazaheri, A.; Howe, R. T.; Pisano, A. P. In *Micro Electro Mechanical Systems, 1999. MEMS'99. Twelfth IEEE International Conference on*; IEEE, 1999; pp 470–475.
(148) Chung, H. H.; Chan, C. K.; Khire, T. S.; Marsh, G. A.; Clark, A.; Waugh, R. E.; McGrath, J. L. *Lab Chip* **2014**, *14* (14), 2456–2468.
(149) Song, S.; Singh, A. K.; Shepodd, T. J.; Kirby, B. J. *Anal. Chem.* **2004**, *76* (8), 2367–2373.
(150) Song, S.; Singh, A. K.; Kirby, B. J. *Anal. Chem.* **2004**, *76* (15), 4589–4592.
(151) Hsieh, Y.-C.; Zahn, J. D. *J Diabetes Sci Technol* **2007**, *1* (3), 375–383.
(152) Trautmann, C.; Brüchle, W.; Spohr, R.; Vetter, J.; Angert, N. *Nucl Instrum Methods Phys Res Sect B* **1996**, *111* (1), 70–74.
(153) Tas, N.; Sonnerberg, T.; Jansen, H.; Legtenberg, R.; Elwenspoek, M. *J Micromech Microeng* **1996**, *6*, 385–397.
(154) Taylor, S. G.; S, F. R. *Proc R Soc Lond A* **1953**, *219* (1137), 186–203.
(155) Boyd, B. W.; Witowski, S. R.; Kennedy, R. T. *Anal. Chem.* **2000**, *72* (4), 865–871.
(156) Parrot, S.; Sauvinet, V.; Riban, V.; Depaulis, A.; Renaud, B.; Denoroy, L. *J. Neurosci. Methods* **2004**, *140* (1–2), 29–38.
(157) Huynh, B. H.; Fogarty, B. A.; Martin, R. S.; Lunte, S. M. *Anal. Chem.* **2004**, *76* (21), 6440–6447.
(158) Thorsen, T.; Roberts, R. W.; Arnold, F. H.; Quake, S. R. *Phys. Rev. Lett.* **2001**, *86* (18), 4163–4166.
(159) Chen, D.; Du, W.; Liu, Y.; Liu, W.; Kuznetsov, A.; Mendez, F. E.; Philipson, L. H.; Ismagilov, R. F. *Proc. Natl. Acad. Sci.* **2008**, *105* (44), 16843–16848.
(160) Shang, L.; Cheng, Y.; Zhao, Y. *Chem. Rev.* **2017**, *117* (12), 7964–8040.

(161) Basova, E. Y.; Foret, F. *The Analyst* **2015**, *140* (1), 22–38.
(162) Croushore, C. A.; Sweedler, J. V. *Lab. Chip* **2013**, *13* (9), 1666.
(163) Song, P.; Hershey, N. D.; Mabrouk, O. S.; Slaney, T. R.; Kennedy, R. T. *Anal. Chem.* **2012**, *84* (11), 4659–4664.
(164) Zhu, Y.; Fang, Q. *Anal. Chim. Acta* **2013**, *787* (Supplement C), 24–35.
(165) Wang, M.; Roman, G. T.; Perry, M. L.; Kennedy, R. T. *Anal. Chem.* **2009**, *81* (21), 9072–9078.
(166) Wang, M.; Slaney, T.; Mabrouk, O.; Kennedy, R. T. *J. Neurosci. Methods* **2010**, *190* (1), 39–48.
(167) Li, Q.; Pei, J.; Song, P.; Kennedy, R. T. *Anal. Chem.* **2010**, *82* (12), 5260–5267.
(168) Gale, D. C.; Smith, R. D. *Rapid Commun. Mass Spectrom.* **1993**, *7* (11), 1017–1021.
(169) Wilm, M.; Mann, M. *Anal. Chem.* **1996**, *68*, 1–8.
(170) Gibson, G. T. T.; Mugo, S. M.; Oleschuk, R. D. *Mass Spectrom. Rev.* **2009**, *28* (6), 918–936.
(171) Tossman, U.; Ungerstedt, U. *Acta Physiol. Scand.* **1986**, *128* (1), 9–14.
(172) Kehr, J. *J. Neurosci. Methods* **1993**, *48* (3), 251–261.
(173) Yang, C.-S.; Tsai, P.-J.; Chen, W.-Y.; Liu, L.; Kuo, J.-S. *J Chromatogr B* **1995**, *667* (1), 41–48.
(174) Jansson, P. A.; Fowelin, J.; Smith, U.; Lönnroth, P. *Am. J. Physiol.* **1988**, *255* (2 Pt 1), E218-220.
(175) Fray, A. E.; Forsyth, R. J.; Boutelle, M. G.; Fillenz, M. *J. Physiol.* **1996**, *496* (1), 49–57.
(176) Bungay, P. M.; Newton-Vinson, P.; Isele, W.; Garris, P. A.; Justice, J. B. *J. Neurochem.* **2003**, *86* (4), 932–946.
(177) Chen, X.; Prow, T. W.; Crichton, M. L.; Jenkins, D. W.; Roberts, M. S.; Frazer, I. H.; Fernando, G. J.; Kendall, M. A. *J. Controlled Release* **2009**, *139* (3), 212–220.
(178) Lee, H. J.; Son, Y.; Kim, D.; Kim, Y. K.; Choi, N.; Yoon, E.-S.; Cho, I.-J. *Sens. Actuators B Chem.* **2015**, *209*, 413–422.
(179) Chandrasekaran, S.; Brazzle, J. D.; Frazier, A. B. *J Microelectromech Syst* **2003**, *12* (3), 281–288.
(180) Lee, J. W.; Park, J.-H.; Prausnitz, M. R. *Biomaterials* **2008**, *29* (13), 2113–2124.
(181) Verhoeven, M.; Bystrova, S.; Winnubst, L.; Qureshi, H.; De Gruijl, T. D.; Scheper, R. J.; Luttge, R. *Microelectron Eng* **2012**, *98*, 659–662.
(182) Jina, A.; Tierney, M. J.; Tamada, J. A.; McGill, S.; Desai, S.; Chua, B.; Chang, A.; Christiansen, M. *J Diabetes Sci Technol* **2014**, *8* (3), 483–487.
(183) Ainla, A.; Jeffries, G. D.; Brune, R.; Orwar, O.; Jesorka, A. *Lab Chip* **2012**, *12* (7), 1255–1261.
(184) Li, C. G.; Lee, C. Y.; Lee, K.; Jung, H. *Biomed Microdevices* **2013**, *15* (1), 17–25.
(185) Suh, J. S.; Lee, J. S. *Appl Phys Lett* **1999**, *75* (14), 2047–2049.
(186) Diggle, J. W.; Downie, T. C.; Goulding, C. *Chem. Rev.* **1969**, *69* (3), 365–405.
(187) Church, W. H.; Justice Jr, J. B. *Anal. Chem.* **1987**, *59* (5), 712–716.
(188) Wu, S.; Bammatter, M. O.; Tang, W.; Auzelyte, V.; Zhang, H.; Brugger, J. In *The 8th Annual IEEE International Conference on Nano/Micro Engineered and Molecular Systems*; 2013; pp 986–989.
(189) Gerhardt, G.; Adams, R. N. *Anal. Chem.* **1982**, *54* (14), 2618–2620.

(190) Popat, K. C.; Mor, G.; Grimes, C. A.; Desai, T. A. *Langmuir* **2004**, *20* (19), 8035–8041.
(191) Feichtner, F.; Schaupp, L.; Koehler, H. *Devices for and methods of monitoring a parameter of a fluidic sample by microdialysis*; US Patent 8,535,537, 2013.
(192) Smith, A. D.; Olson, R. J.; Justice, Jr., J. B. *J. Neurosci. Methods* **1992**, *44*, 33–41.
(193) Herrera-Marschitz, M.; You, Z.-B.; Goiny, M.; Meana, J. J.; Silveira, R.; Godukhin, O. V.; Chen, Y.; Espinoza, S.; Pettersson, E.; Loidl, C. F.; others. *J. Neurochem.* **1996**, *66* (4), 1726–1735.
(194) Lada, M. W.; Kennedy, R. T. *Anal. Chem.* **1996**, *68* (17), 2790–2797.
(195) Fray, A. E.; Boutelle, M.; Fillenz, M. *J. Physiol.* **1997**, *504* (3), 721–726.
(196) Hashimoto, A.; Kanda, J.; Oka, T. *Brain Res. Bull.* **2000**, *53* (3), 347–351.
(197) Kanamori, K.; Ross, B. D. *J. Neurochem.* **2004**, *90* (1), 203–210.
(198) Molchanova, S.; Oja, S. S.; Saransaari, P. *Amino Acids* **2004**, *27* (3–4), 261–268.
(199) Benveniste, H.; Huttemeier, P. C. *Prog. Neurobiol.* **1990**, *35*, 195–215.
(200) Menacherry, S.; Hubert, W.; Justice Jr, J. B. *Anal. Chem.* **1992**, *64* (6), 577–583.
(201) Butcher, S. P.; Fairbrother, I. S.; Kelly, J. S.; Arbuthnott, G. W. *J. Neurochem.* **1988**, *50* (2), 346–355.
(202) Boyd, B. W.; Witowski, S. R.; Kennedy, R. T. *Anal. Chem.* **2000**, *72* (4), 865–871.
(203) Song, H.; Chen, D. L.; Ismagilov, R. F. *Angew. Chem. Int. Ed.* **2006**, *45* (44), 7336–7356.
(204) Shackman, H. M.; Shou, M.; Cellar, N. A.; Watson, C. J.; Kennedy, R. T. *J. Neurosci. Methods* **2007**, *159* (1), 86–92.
(205) Wang, M.; Hershey, N. D.; Mabrouk, O. S.; Kennedy, R. T. *Anal. Bioanal. Chem.* **2011**, *400* (7), 2013–2023.
(206) Ungerstedt, U. *J. Intern. Med.* **1991**, *230* (4), 365–373.
(207) Westerink, B. H. C. *Behav. Brain Res.* **1995**, *70*, 103–124.
(208) Weiss, D. J.; Lunte, C. E.; Lunte, S. M. *Trends Anal. Chem.* **2000**, *19* (10), 606–616.
(209) Torregrossa, M. M.; Kalivas, P. W. *Pharmacol. Biochem. Behav.* **2008**, *90* (2), 261–272.
(210) Kennedy, R. T.; Watson, C. J.; Haskins, W. E.; Powell, D. H.; Strecker, R. E. *Curr. Opin. Chem. Biol.* **2002**, *6* (5), 659–665.
(211) Davies, M. I. *Anal. Chim. Acta* **1999**, *379*, 227–249.
(212) Davies, M. I.; Cooper, J. D.; Desmond, S. S.; Lunte, C. E.; Lunte, S. M. *Adv. Drug Deliv. Rev.* **2000**, *45* (2), 169–188.
(213) Chefer, V. I.; Thompson, A. C.; Zapata, A.; Shippenberg, T. S. In *Current Protocols in Neuroscience*; Crawley, J. N., Gerfen, C. R., Rogawski, M. A., Sibley, D. R., Skolnick, P., Wray, S., Eds.; John Wiley & Sons, Inc.: Hoboken, NJ, USA, 2009.
(214) Alivisatos, A. P.; Andrews, A. M.; Boyden, E. S.; Chun, M.; Church, G. M.; Deisseroth, K.; Donoghue, J. P.; Fraser, S. E.; Lippincott-Schwartz, J.; Looger, L. L.; others. *ACS Nano* **2013**, *7* (3), 1850–1866.
(215) Córcoles, E. P.; Boutelle, M. G. In *Biosensors and Invasive Monitoring in Clinical Applications*; Springer International Publishing: Heidelberg, 2013; pp 49–58.
(216) Kennedy, R. T.; Thompson, J. E.; Vickroy, T. W. *J. Neurosci. Methods* **2002**, *114*, 39–49.
(217) Chen, A.; Lunte, C. E. *J. Chromatogr. A* **1995**, *691* (1), 29–35.

(218) Shou, M.; Ferrario, C. R.; Schultz, K. N.; Robinson, T. E.; Kennedy, R. T. *Anal. Chem.* **2006**, *78* (19), 6717–6725.
(219) Rogers, M.; Leong, C.; Niu, X.; de Mello, A.; Parker, K. H.; Boutelle, M. G. *Phys. Chem. Chem. Phys.* **2011**, *13* (12), 5298.
(220) Niu, X.; deMello, A. J. *Biochem. Soc. Trans.* **2012**, *40* (4), 615–623.
(221) Guetschow, E. D.; Steyer, D. J.; Kennedy, R. T. *Anal. Chem.* **2014**, *86* (20), 10373–10379.
(222) Shackman, J. G.; Watson, C. J.; Kennedy, R. T. *J. Chromatogr. A* **2004**, *1040* (2), 273–282.
(223) Lee, W. H.; Ngernsutivorakul, T.; Mabrouk, O. S.; Wong, J.-M. T.; Dugan, C. E.; Pappas, S. S.; Yoon, H. J.; Kennedy, R. T. *Anal. Chem.* **2016**, *88* (2), 1230–1237.
(224) Rogers, M. L.; Feuerstein, D.; Leong, C. L.; Takagaki, M.; Niu, X.; Graf, R.; Boutelle, M. G. *ACS Chem. Neurosci.* **2013**, *4* (5), 799–807.
(225) Chen, Z.-J.; Gillies, G. T.; Broaddus, W. C.; Prabhu, S. S.; Fillmore, H.; Mitchell, R. M.; Corwin, F. D.; Fatouros, P. P. *J. Neurosurg.* **2004**, *101* (2), 314–322.
(226) Flanagan, T. R. *Providing Pharmacological Access to the Brain: Alternate Approaches*; Academic Press, 2013.
(227) Cellar, N. A.; Burns, S. T.; Meiners, J.-C.; Chen, H.; Kennedy, R. T. *Anal. Chem.* **2005**, *77* (21), 7067–7073.
(228) O'Shea, T. J.; Weber, P. L.; Bammel, B. P.; Lunte, C. E.; Lunte, S. M.; Smyth, M. R. *J. Chromatogr. A* **1992**, *608* (1), 189–195.
(229) Oldenziel, W. H.; Dijkstra, G.; Cremers, T. I. F. H.; Westerink, B. H. C. *Brain Res.* **2006**, *1118* (1), 34–42.
(230) Peterson, S. L.; McDonald, A.; Gourley, P. L.; Sasaki, D. Y. *J. Biomed. Mater. Res. A* **2005**, *72A* (1), 10–18.
(231) Reiber, H. *J. Neurol. Sci.* **1994**, *122* (2), 189–203.
(232) Reiber, H. *Restor. Neurol. Neurosci.* **2003**, *21* (3,4), 79–96.
(233) Brydon, H. L.; Hayward, R.; Harkness, W.; Bayston, R. *Br. J. Neurosurg.* **1995**, *9* (5), 639–644.
(234) Brydon, H. L.; Keir, G.; Thompson, E. J.; Bayston, R.; Hayward, R.; Harkness, W. *J. Neurol. Neurosurg. Psychiatry* **1998**, *64* (5), 643–647.
(235) Wu, F.; Stark, E.; Im, M.; Cho, I. J.; Yoon, E. S.; Buzsáki, G.; Wise, K. D.; Yoon, E. *J. Neural Eng.* **2013**, *10* (5), 056012.
(236) Wang, M.; Roman, G. T.; Schultz, K.; Jennings, C.; Kennedy, R. T. *Anal. Chem.* **2008**, *80* (14), 5607–5615.
(237) Wong, J.-M. T.; Malec, P. A.; Mabrouk, O. S.; Ro, J.; Dus, M.; Kennedy, R. T. *J. Chromatogr. A* **2016**, *1446*, 78–90.
(238) Bert, L.; Robert, F.; Denoroy, L.; Stoppini, L.; Renaud, B. *J. Chromatogr. A* **1996**, *755* (1), 99–111.
(239) Hogan, B. L.; Lunte, S. M.; Stobaugh, J. F.; Lunte, C. E. *Anal. Chem.* **1994**, *66* (5), 596–602.
(240) Roman, G. T.; Wang, M.; Shultz, K. N.; Jennings, C.; Kennedy, R. T. *Anal. Chem.* **2008**, *80* (21), 8231–8238.
(241) Jacobson, S. C.; Ermakov, S. V.; Ramsey, J. M. *Anal. Chem.* **1999**, *71* (15), 3273–3276.

(242) Shou, M.; Smith, A. D.; Shackman, J. G.; Peris, J.; Kennedy, R. T. *J. Neurosci. Methods* **2004**, *138* (1–2), 189–197.
(243) De Montigny, P.; Stobaugh, J. F.; Givens, R. S.; Carlson, R. G.; Srinivasachar, K.; Sternson, L. A.; Higuchi, T. *Anal. Chem.* **1987**, *59* (8), 1096–1101.
(244) Tice, J. D.; Song, H.; Lyon, A. D.; Ismagilov, R. F. *Langmuir* **2003**, *19* (22), 9127–9133.
(245) Niu, X.; Pereira, F.; Edel, J. B.; de Mello, A. J. *Anal. Chem.* **2013**, *85* (18), 8654–8660.
(246) Guetschow, E. D.; Kumar, S.; Lombard, D. B.; Kennedy, R. T. *Anal. Bioanal. Chem.* **2016**, *408* (3), 721–731.
(247) Pereira, F.; Niu, X.; deMello, A. J. *PLoS ONE* **2013**, *8* (5), e63087.
(248) Wang, M. In vivo neurochemical monitoring with high temporal and spatial resolution using segmented flow microfluidics, University of Michigan, 2011.
(249) Tsai, J.-H.; Lin, L. *Sens. Actuators Phys.* **2002**, *97–98* (Supplement C), 665–671.
(250) Xu, J.; Vaillant, R.; Attinger, D. *Microfluid. Nanofluidics* **2010**, *9* (4–5), 765–772.
(251) Nishi, Y.; Doering, R. *Handbook of Semiconductor Manufacturing Technology*; CRC Press, 2000.
(252) Voutsas, A. T.; Hatalis, M. K. *J. Electrochem. Soc.* **1993**, *140* (1), 282–288.
(253) Gottscho, R. A. *J. Vac. Sci. Technol. B Microelectron. Nanometer Struct.* **1992**, *10* (5), 2133.
(254) Taylor, H. K.; Sun, H.; Hill, T. F.; Farahanchi, A.; Boning, D. S. *J. Electrochem. Soc.* **2006**, *153* (8), C575–C585.
(255) Lang, J. *Multi-Wafer Rotating MEMS Machines: Turbines, Generators, and Engines*; Springer Science & Business Media, 2009.
(256) Mogab, C. J. *J. Electrochem. Soc.* **1977**, *124* (8), 1262–1268.
(257) Jansen, H.; de Boer, M.; Burger, J.; Legtenberg, R.; Elwenspoek, M. *Microelectron. Eng.* **1995**, *27* (1–4), 475–480.
(258) Hedlund, C.; Blom, H. -O.; Berg, S. *J. Vac. Sci. Technol. Vac. Surf. Films* **1994**, *12* (4), 1962–1965.
(259) Laermer, F.; Urban, A. *Microelectron. Eng.* **2003**, *67*, 349–355.
(260) Kiihamäki, J. *Fabrication of SOI micromechanical devices*; VTT publications; VTT: Espoo, 2005.
(261) Chekurov, N.; Grigoras, K.; Peltonen, A.; Franssila, S.; Tittonen, I. *Nanotechnology* **2009**, *20* (6), 065307.
(262) Owen, K. J.; VanDerElzen, B.; Peterson, R. L.; Najafi, K. In *Micro Electro Mechanical Systems (MEMS), 2012 IEEE 25th International Conference on*; IEEE, 2012; pp 251–254.
(263) Boufnichel, M.; Lefaucheux, P.; Aachboun, S.; Dussart, R.; Ranson, P. *Microelectron. Eng.* **2005**, *77* (3–4), 327–336.
(264) Hwang, S.-K.; Jeong, S.-H.; Hwang, H.-Y.; Lee, O.-J.; Lee, K.-H. *Korean J. Chem. Eng.* **2002**, *19* (3), 467–473.
(265) Taylor, G. N.; Wolf, T. M. *Polym. Eng. Sci.* **1980**, *20* (16), 1087–1092.
(266) Sahbari, J. J. Plasma Etching residue removal. EP1128221 A2, August 29, 2001.
(267) Rijn, C. van; Wekken, M. van der; Nijdam, W.; Elwenspoek, M. *J. Microelectromechanical Syst.* **1997**, *6* (1), 48–54.

(268) Sharpe, W. N.; Jackson, K. M.; Hemker, K. J.; Xie, Z. *J. Microelectromechanical Syst.* **2001**, *10* (3), 317–326.
(269) Materials, A. S. for T. and. *Mechanical Properties of Structural Films*; ASTM International, 2001.
(270) Cepeda, D. E.; Hains, L.; Li, D.; Bull, J.; Lentz, S. I.; Kennedy, R. T. *J. Neurosci. Methods* **2015**, *242*, 97–105.
(271) Ren, K.; Dai, W.; Zhou, J.; Su, J.; Wu, H. *Proc. Natl. Acad. Sci.* **2011**, *108* (20), 8162–8166.
(272) Wise, K. D.; Sodagar, A. M.; Yao, Y.; Gulari, M. N.; Perlin, G. E.; Najafi, K. *Proc. IEEE* **2008**, *96* (7), 1184–1202.
(273) Buzsáki, G.; Stark, E.; Berényi, A.; Khodagholy, D.; Kipke, D. R.; Yoon, E.; Wise, K. D. *Neuron* **2015**, *86* (1), 92–105.
(274) Kampasi, K.; Stark, E.; Seymour, J.; Na, K.; Winful, H. G.; Buzsáki, G.; Wise, K. D.; Yoon, E. *Sci. Rep.* **2016**, *6* (1).
(275) Boyden, E. S.; Zhang, F.; Bamberg, E.; Nagel, G.; Deisseroth, K. *Nat. Neurosci.* **2005**, *8* (9), nn1525.
(276) Fenno, L.; Yizhar, O.; Deisseroth, K. *Annu. Rev. Neurosci.* **2011**, *34* (1), 389–412.
(277) Deisseroth, K. *Nat. Methods* **2011**, *8* (1), 26–29.
(278) Parrot, S.; Denoroy, L.; Renaud, B.; Benetollo, C. *ACS Chem. Neurosci.* **2015**, *6* (7), 948–950.
(279) Carter, M. E.; Yizhar, O.; Chikahisa, S.; Nguyen, H.; Adamantidis, A.; Nishino, S.; Deisseroth, K.; de Lecea, L. *Nat. Neurosci.* **2010**, *13* (12), 1526–1533.
(280) Miyazaki, K. W.; Miyazaki, K.; Tanaka, K. F.; Yamanaka, A.; Takahashi, A.; Tabuchi, S.; Doya, K. *Curr. Biol.* **2014**, *24* (17), 2033–2040.
(281) Quiroz, C.; Orrú, M.; Rea, W.; Ciudad-Roberts, A.; Yepes, G.; Britt, J. P.; Ferré, S. *J. Neurosci. Off. J. Soc. Neurosci.* **2016**, *36* (3), 851–859.
(282) Fan, B.; Li, W. *Lab Chip* **2015**, *15* (19), 3838–3855.
(283) Zhao, H. *Int. J. Mol. Sci.* **2017**, *18* (8), 1751.
(284) Goncalves, S. B.; Ribeiro, J. F.; Silva, A. F.; Costa, R. M.; Correia, J. H. *J. Neural Eng.* **2017**, *14* (4), 041001.
(285) Zorzos, A. N.; Boyden, E. S.; Fonstad, C. G. *Opt. Lett.* **2010**, *35* (24), 4133–4135.
(286) Wu, F.; Stark, E.; Im, M.; Cho, I.-J.; Yoon, E.-S.; Buzsáki, G.; Wise, K. D.; Yoon, E. *J. Neural Eng.* **2013**, *10* (5), 056012.
(287) Kim, T. I.; McCall, J. G.; Jung, Y. H.; Huang, X.; Siuda, E. R.; Li, Y.; Song, J.; Song, Y. M.; Pao, H. A.; Kim, R. H.; Lu, C.; Lee, S. D.; Song, I.-S.; Shin, G.; Al-Hasani, R.; Kim, S.; Tan, M. P.; Huang, Y.; Omenetto, F. G.; Rogers, J. A.; Bruchas, M. R. *Science* **2013**, *340* (6129), 211–216.
(288) Jeong, J. W.; McCall, J. G.; Shin, G.; Zhang, Y.; Al-Hasani, R.; Kim, M.; Li, S.; Sim, J. Y.; Jang, K. I.; Shi, Y.; Hong, D. Y.; Liu, Y.; Schmitz, G. P.; Xia, L.; He, Z.; Gamble, P.; Ray, W. Z.; Huang, Y.; Bruchas, M. R.; Rogers, J. A. *Cell* **2015**, *162* (3), 662–674.
(289) Piruska, A.; Gong, M.; Sweedler, J. V.; Bohn, P. W. *Chem Soc Rev* **2010**, *39* (3), 1060–1072.
(290) De Beer, T.; Burggraeve, A.; Fonteyne, M.; Saerens, L.; Remon, J. P.; Vervaet, C. *Int. J. Pharm.* **2011**, *417* (1–2), 32–47.
(291) Blanco, M.; Villarroya, I. *TrAC Trends Anal. Chem.* **2002**, *21* (4), 240–250.

(292) Wolfbeis, O. S. *Anal. Chem.* **2008**, *80* (12), 4269–4283.
(293) Wang, J.; Bergholt, M. S.; Zheng, W.; Huang, Z. *Opt. Lett.* **2013**, *38* (13), 2321.
(294) Schwarz, R. A.; Arifler, D.; Chang, S. K.; Pavlova, I.; Hussain, I. A.; Mack, V.; Knight, B.; Richards-Kortum, R.; Gillenwater, A. M. *Opt. Lett.* **2005**, *30* (10), 1159–1161.
(295) Shim, M. G.; Song, L.-M. W. K.; Marcon, N. E.; Wilson, B. C. *Photochem. Photobiol.* **2000**, *72* (1), 146–150.
(296) Bergholt, M. S.; Zheng, W.; Ho, K. Y.; Teh, M.; Yeoh, K. G.; So, J. B. Y.; Shabbir, A.; Huang, Z. *J. Biophotonics* **2013**, *6* (1), 49–59.
(297) Krogmeier, J. R.; Schaefer, I.; Seward, G.; Yantz, G. R.; Larson, J. W. *Lab. Chip* **2007**, *7* (12), 1767.
(298) Kaigala, G. V.; Bercovici, M.; Behnam, M.; Elliott, D.; Santiago, J. G.; Backhouse, C. J. *Lab. Chip* **2010**, *10* (17), 2242.
(299) Day, J. C. C.; Bennett, R.; Smith, B.; Kendall, C.; Hutchings, J.; Meaden, G. M.; Born, C.; Yu, S.; Stone, N. *Phys. Med. Biol.* **2009**, *54* (23), 7077–7087.
(300) Grimbergen, M. C. M.; van Swol, C. F. P.; Draga, R. O. P.; van Diest, P.; Verdaasdonk, R. M.; Stone, N.; Bosch, J. H. L. R. SPIE, 2009; pp 716114-716114–716116.
(301) Latka, I.; Dochow, S.; Krafft, C.; Dietzek, B.; Bartelt, H.; Popp, J. In *Clinical and Biomedical Spectroscopy and Imaging II*; Ramanujam, N. and P., Ed.; Proceedings of SPIE-OSA Biomedical Optics; Optical Society of America, 2011; Vol. 8087, p 80872D.
(302) Komachi, Y.; Katagiri, T.; Sato, H.; Tashiro, H. *Appl. Opt.* **2009**, *48* (9), 1683–1696.
(303) Burns, M. A.; Johnson, B. N.; Brahmasandra, S. N.; Handique, K.; Webster, J. R.; Krishnan, M.; Sammarco, T. S.; Man, P. M.; Jones, D.; Heldsinger, D. *Science* **1998**, *282* (5388), 484–487.
(304) Roulet, J.-C.; Völkel, R.; Herzig, H. P.; Verpoorte, E.; de Rooij, N. F.; Dändliker, R. *Anal. Chem.* **2002**, *74* (14), 3400–3407.
(305) Verpoorte, E. *Lab. Chip* **2003**, *3* (3), 42N.
(306) Roman, G. T.; Kennedy, R. T. *J. Chromatogr. A* **2007**, *1168* (1), 170–188.
(307) Mogensen, K. B.; Kutter, J. P. *Electrophoresis* **2009**, *30* (S1), S92–S100.
(308) Zeng, X.; Jiang, H. *J. Phys. Appl. Phys.* **2013**, *46* (32), 323001.
(309) Vieillard, J.; Mazurczyk, R.; Morin, C.; Hannes, B.; Chevolot, Y.; Desbene, P.; Krawczyk, S. *J. Chromatogr. B* **2007**, *845* (2), 218–225.
(310) Bliss, C. L.; McMullin, J. N.; Backhouse, C. J. *Lab. Chip* **2007**, *7* (10), 1280.
(311) Godin, J.; Chen, C.-H.; Cho, S. H.; Qiao, W.; Tsai, F.; Lo, Y.-H. *J. Biophotonics* **2008**, *1* (5), 355–376.
(312) Becker, H.; Gärtner, C. *Anal. Bioanal. Chem.* **2007**, *390* (1), 89–111.
(313) Nge, P. N.; Rogers, C. I.; Woolley, A. T. *Chem. Rev.* **2013**, *113* (4), 2550–2583.
(314) Camou, S.; Fujita, H.; Fujii, T. *Lab. Chip* **2003**, *3* (1), 40.
(315) Seo, J.; Lee, L. P. *Sens. Actuators B Chem.* **2004**, *99* (2–3), 615–622.
(316) Jiang, L.; Pau, S. *Appl. Phys. Lett.* **2007**, *90* (11), 111108–111108.
(317) Watts, B. R.; Zhang, Z.; Xu, C.-Q.; Cao, X.; Lin, M. *Biomed. Opt. Express* **2012**, *3* (11), 2784–2793.
(318) Chang-Yen, D. A.; Eich, R. K.; Gale, B. K. *J. Light. Technol.* **2005**, *23* (6), 2088–2093.

(319) Cai, Z.; Qiu, W.; Shao, G.; Wang, W. *Sens. Actuators Phys.* **2013**, *204*, 44–47.
(320) Mao, X.; Waldeisen, J. R.; Juluri, B. K.; Huang, T. J. *Lab. Chip* **2007**, *7* (10), 1303.
(321) Tang, S. K. Y.; Stan, C. A.; Whitesides, G. M. *Lab. Chip* **2008**, *8* (3), 395.
(322) Rosenauer, M.; Vellekoop, M. J. *Lab. Chip* **2009**, *9* (8), 1040–1042.
(323) Rosenauer, M.; Vellekoop, M. J. In *World Congress on Medical Physics and Biomedical Engineering, September 7-12, 2009, Munich, Germany*; Springer, 2010; pp 185–188.
(324) Song, C.; Nguyen, N.-T.; Asundi, A. K.; Low, C. L.-N. *Opt. Lett.* **2011**, *36* (10), 1767–1769.
(325) Chao, K.-S.; Lin, M.-S.; Yang, R.-J. *Lab. Chip* **2013**, *13* (19), 3886.
(326) Lin, B.-S.; Yang, Y.-C.; Ho, C.-Y.; Yang, H.-Y.; Wang, H.-Y. *Sensors* **2014**, *14* (2), 2967–2980.
(327) Chabinyc, M. L.; Chiu, D. T.; McDonald, J. C.; Stroock, A. D.; Christian, J. F.; Karger, A. M.; Whitesides, G. M. *Anal. Chem.* **2001**, *73* (18), 4491–4498.
(328) Qi, S.; Liu, X.; Ford, S.; Barrows, J.; Thomas, G.; Kelly, K.; McCandless, A.; Lian, K.; Goettert, J.; Soper, S. A. *Lab. Chip* **2002**, *2* (2), 88.
(329) Wu, M.-H.; Cai, H.; Xu, X.; Urban, J. P.; Cui, Z.-F.; Cui, Z. *Biomed. Microdevices* **2005**, *7* (4), 323–329.
(330) Mazurczyk, R.; Vieillard, J.; Bouchard, A.; Hannes, B.; Krawczyk, S. *Sens. Actuators B Chem.* **2006**, *118* (1–2), 11–19.
(331) Irawan, R.; Tjin, S. C.; Fang, X.; Fu, C. Y. *Biomed. Microdevices* **2007**, *9* (3), 413–419.
(332) Ashok, P. C.; Singh, G. P.; Rendall, H. A.; Krauss, T. F.; Dholakia, K. *Lab. Chip* **2011**, *11* (7), 1262–1270.
(333) Sapuppo, F.; Schembri, F.; Fortuna, L.; Llobera, A.; Bucolo, M. *Microfluid. Nanofluidics* **2011**, *12* (1–4), 165–174.
(334) Dugan, C. E.; Cawthorn, W. P.; MacDougald, O. A.; Kennedy, R. T. *Anal. Bioanal. Chem.* **2014**, *406* (20), 4851–4859.
(335) Roper, M. G.; Shackman, J. G.; Dahlgren, G. M.; Kennedy, R. T. *Anal. Chem.* **2003**, *75* (18), 4711–4717.
(336) Harrison, D. J.; Fluri, K.; Seiler, K.; Effenhauser, C. S.; Manz, A. *Science* **1993**, *261* (5123), 895–897.
(337) Jacobson, S. C.; Hergenroder, R.; Moore, A. W. J.; Ramsey, J. M. *Anal. Chem.* **1994**, *66* (23), 4127–4132.
(338) Clark, A. M.; Sousa, K. M.; Jennings, C.; MacDougald, O. A.; Kennedy, R. T. *Anal. Chem.* **2009**, *81* (6), 2350–2356.
(339) Biovision 02/13.
(340) Jin, S.; Anderson, G. J.; Kennedy, R. T. *Anal. Chem.* **2013**, *85* (12), 6073–6079.
(341) Miyaki, K.; Guo, Y.; Shimosaka, T.; Nakagama, T.; Nakajima, H.; Uchiyama, K. *Anal. Bioanal. Chem.* **2005**, *382* (3), 810–816.
(342) Li, H.-F.; Lin, J.-M.; Su, R.-G.; Uchiyama, K.; Hobo, T. *ELECTROPHORESIS* **2004**, *25* (12), 1907–1915.
(343) Lee, K. S.; Lee, H. L. T.; Ram, R. J. *Lab. Chip* **2007**, *7* (11), 1539.
(344) Llobera, A.; Demming, S.; Joensson, H. N.; Vila-Planas, J.; Andersson-Svahn, H.; Büttgenbach, S. *Lab. Chip* **2010**, *10* (15), 1987.

(345) Hofmann, O.; Wang, X.; Cornwell, A.; Beecher, S.; Raja, A.; Bradley, D. D. C.; deMello, A. J.; deMello, J. C. *Lab. Chip* **2006**, *6* (8), 981.
(346) Richard, C.; Renaudin, A.; Aimez, V.; Charette, P. G. *Lab. Chip* **2009**, *9* (10), 1371.
(347) Lin, B.-S.; Yang, Y.-C.; Ho, C.-Y.; Yang, H.-Y.; Wang, H.-Y. *Sensors* **2014**, *14* (2), 2967–2980.
(348) Miyaki, K.; Guo, Y.; Shimosaka, T.; Nakagama, T.; Nakajima, H.; Uchiyama, K. *Anal. Bioanal. Chem.* **2005**, *382* (3), 810–816.
(349) Li, H.-F.; Lin, J.-M.; Su, R.-G.; Uchiyama, K.; Hobo, T. *Electrophoresis* **2004**, *25* (12), 1907–1915.
(350) Lee, K. S.; Lee, H. L. T.; Ram, R. J. *Lab. Chip* **2007**, *7* (11), 1539.
(351) Lee, J. N.; Park, C.; Whitesides, G. M. *Anal. Chem.* **2003**, *75* (23), 6544–6554.
(352) Martens, W. N.; Frost, R. L.; Kristof, J.; Theo Kloprogge, J. *J. Raman Spectrosc.* **2002**, *33* (2), 84–91.
(353) Horrocks, Jr., W. D.; Cotton, F. A. *Spectrochim. Acta* **1961**, *17*, 134–147.
(354) Wang, C.; Vickers, T. J.; Mann, C. K. *J. Pharm. Biomed. Anal.* **1997**, *16*, 87–94.
(355) Kontoyannis, C. G.; Orkoula, M. *Talanta* **1994**, *41* (11), 1981–1984.
(356) Pagliara, S.; Camposeo, A.; Polini, A.; Cingolani, R.; Pisignano, D. *Lab. Chip* **2009**, *9* (19), 2851–2856.
(357) Yao, B.; Luo, G.; Wang, L.; Gao, Y.; Lei, G.; Ren, K.; Chen, L.; Wang, Y.; Hu, Y.; Qiu, Y. *Lab. Chip* **2005**, *5* (10), 1041–1047.
(358) Kamei, T.; Paegel, B. M.; Scherer, J. R.; Skelley, A. M.; Street, R. A.; Mathies, R. A. *Anal. Chem.* **2003**, *75* (20), 5300–5305.
(359) Kendall, C.; Day, J.; Hutchings, J.; Smith, B.; Shepherd, N.; Barr, H.; Stone, N. *The Analyst* **2010**, *135* (12), 3038.
(360) Morris, M. D.; Finney, W. F.; Rajachar, R. M.; Kohn, D. H. *Faraday Discuss.* **2004**, *126*, 159.
(361) Dishinger, J. F.; Reid, K. R.; Kennedy, R. T. *Anal. Chem.* **2009**, *81* (8), 3119–3127.
(362) Nunemaker, C. S.; Dishinger, J. F.; Dula, S. B.; Wu, R.; Merrins, M. J.; Reid, K. R.; Sherman, A.; Kennedy, R. T.; Satin, L. S. *PLoS ONE* **2009**, *4* (12), e8428.